JULLIANE VASCONCELOS JOVIANO DOS SANTOS

ALTERAÇÕES CENTRAIS E PERIFÉRICAS EM MODELO MURINO PARA DOENÇA DE HUNTINGTON: CARACTERIZAÇÃO E UMA NOVA ABORDAGEM TERAPÊUTICA

Instituto de Ciências Biológicas

Universidade Federal de Minas Gerais

Fevereiro/2019

JULLIANE VASCONCELOS JOVIANO DOS SANTOS

ALTERAÇÕES CENTRAIS E PERIFÉRICAS EM MODELO MURINO PARA DOENÇA DE HUNTINGTON: CARACTERIZAÇÃO E UMA NOVA ABORDAGEM TERAPÊUTICA

Tese apresentada ao Programa de Pós-Graduação em Biologia Celular do Departamento de Morfologia, do Instituto de Ciências Biológicas, da Universidade Federal de Minas Gerais, como requisito parcial para obtenção do título de Doutor em Ciências.

Área de concentração: Biologia Celular

Orientadora: Profa. Dra. Cristina Guatimosim

Co-Orientadora: Profa. Dra. Silvia Guatimosim

Instituto de Ciências Biológicas

Universidade Federal de Minas Gerais

Fevereiro/2019

Universidade Federal de Minas Gerais - Instituto de Ciências Biológicas
Programa de Pós-Graduação em Biologia Celular

ATA DA DEFESA DE TESE DE DOUTORADO DE

203/2019
entrada
1º/2015
2015702223

JULLIANE VASCONCELOS JOVIANO DOS SANTOS

Às **treze horas** do dia **28 de fevereiro de 2019**, reuniu-se, no Instituto de Ciências Biológicas da UFMG, a Comissão Examinadora da Tese, indicada pelo Colegiado do Programa, para julgar, em exame final, o trabalho final intitulado: **"ALTERAÇÕES CENTRAIS E PERIFÉRICAS EM MODELO MURINO PARA DOENÇA DE HUNTINGTON: CARACTERIZAÇÃO E UMA NOVA ABORDAGEMN TERAPÊUTICA"**, requisito final para obtenção do grau de Doutora em Biologia Celular. Abrindo a sessão, a Presidente da Comissão, **Dra. Cristina Guatimosim Fonseca**, após dar a conhecer aos presentes o teor das Normas Regulamentares do Trabalho Final, passou a palavra à candidata, para apresentação de seu trabalho. Seguiu-se a arguição pelos examinadores, com a respectiva defesa da candidata. Logo após, a Comissão se reuniu, sem a presença da candidata e do público, para julgamento e expedição de resultado final. Foram atribuídas as seguintes indicações:

Prof./Pesq.	Instituição	Indicação
Dra. Cristina Guatimosim Fonseca	UFMG/ICB	Aprovada
Dr. Silvia Guatimosim Fonseca	UFMG	
Dr. Celio José de Castro Junior	IEP/Santa Casa	APROVADA
Dr. Lucas Kangussu	UFMG	APROVADA
Dra. Daisy Mota Santos	UFMG	Aprovada
Dra. Márcia Gallacci	UNESP	Aprovada

Pelas indicações, a candidata foi considerada: Aprovada

O resultado final foi comunicado publicamente à candidata pela Presidente da Comissão. Nada mais havendo a tratar, a Presidente encerrou a reunião e lavrou a presente ATA, que será assinada por todos os membros participantes da Comissão Examinadora. **Belo Horizonte, 28 de fevereiro de 2019.**

Dra. Cristina Guatimosim Fonseca (Orientadora) _____

Dra. Silvia Guatimosim Fonseca _____

Dr. Celio José de Castro Junior _____

Dr. Lucas Kangussu _____

Dra. Daisy Mota Santos _____

Dra. Márcia Gallacci _____

Obs: Este documento não terá validade sem a assinatura e carimbo do Coordenador

Prof. Erika Cristina Jorge
Coordenadora do Programa de Pós Graduação
em Biologia Celular ICB/UFMG

APOIO INSTITUCIONAL

AGRADECIMENTOS

De acordo com a **RESOLUÇÃO Nº 05/2014** de 13 de Fevereiro de 2014, que estabelece os requisitos e procedimentos para defesa de tese/dissertação, a presente tese de doutorado será apresentada no formato de compilação de artigos científicos.

"RESOLUÇÃO Nº 05/2014
De 13 de fevereiro de 2014
Estabelece os requisitos e procedimentos para
defesa de tese/dissertação e revoga as Resoluções 01/1998, 02/1998, 03/2000, 4/2000 e 01/2002.

Art. 6º. A dissertação e a tese deverão conter introdução, objetivos, material e métodos, resultados, discussão, conclusões e referências bibliográficas. A revisão de literatura poderá integrar a introdução ou constituir tópico separado.

Parágrafo único: Como forma alternativa, a dissertação e a tese de aluno que esteja dentro do prazo regular do curso poderão ser apresentadas no formato de compilação de artigos publicados resultantes diretamente do projeto desenvolvido, desde que obedeça aos requisitos abaixo:

a) para a dissertação exige-se a publicação de pelo menos um (01) artigo completo e para tese, de pelo menos dois (02) artigos completos;

b) o aluno deverá ser primeiro autor em pelo menos um dos artigos;

c) os artigos devem estar publicados em periódico de qualidade compatível ao descrito no artigo 3º. dessa resolução.

d) deverão integrar a dissertação/tese, os seguintes tópicos: introdução, objetivos, artigos resultantes, discussão integradora dos resultados (no caso da tese), conclusões e referências bibliográficas. Opcionalmente, poderão constar: perspectivas, resultados não incluídos nas publicações, anexos com informações adicionais, referências adicionais;

e) todos os tópicos, com exceção dos artigos publicados, deverão estar escritos em português."

SUMÁRIO

LISTA DE ABREVIATURAS

ACh - acetilcolina

AMPA - alfa-amino-3-hidroxil-5-metilisoxazolepropionato

BAC - cromossomo artificial bacteriano

BACHD - BACHD^{Q97}

BDNF - do inglês *Brain-derived neurotrophic factor*

CaMKII - Calmodulina cinase II

CCSV - canais para Ca^{+2} sensíveis à voltagem

DH - Doença de Huntington

EAATs - do inglês *excitatory amino acid transporters*

ECG - Eletrocardiograma

ELA - Esclerose Lateral Amiotrófica

HD - Huntington's disease

HTT - huntingtina

JNMs - junções neuromusculares

KA - cainato, do inglês *Kainate*

KD - *knockdown*

mGluRs - Receptores metabotrópicos de glutamato

MSNs - do inglês *medium spiny neurons*

NMDA - n-metil-D-aspartato

Q97 - 97 repetições poliglutamínicas

SMCs - Síndromes Miastênicas Congênitas

SNA - Sistema Nervoso Autônomo

SNC - Sistema Nervoso Central

SNP - Sistema Nervoso Parassimpático

SNP - Sistema Nervoso Periférico

SNS - Sistema Nervoso Simpático

VAChT - Transportador Vesicular de Acetilcolina

WT - do inglês *Wild Type*

LISTA DE FIGURAS

RESUMO

A Doença de Huntington (DH) é uma desordem neurodegenerativa, com efeitos devastadores que geralmente surgem na idade adulta. Clinicamente, ela é caracterizada por alterações motoras, comportamentais e declínio cognitivo. Contudo, pacientes com DH podem desenvolver também distúrbios cardiovasculares causando morte súbita (segunda causa de morte). Apesar da importância clínica, as alterações cardíacas observadas na DH ainda são pouco compreendidas. Esse projeto de tese de doutorado foi dividido em dois subprojetos. No primeiro subprojeto, utilizando-se um modelo murino para a DH (camundongos BACHD), investigamos possíveis alterações cardíacas (juntamente com o mecanismo de ação) que ainda não foram descritas. Nossos resultados mostraram variações cardíacas significativas tanto *in vivo* como *in vitro*. Os distúrbios de condução do impulso cardíaco observados foram associados com um prolongamento do potencial de ação bem como, a presença de arritmias celulares. Além disso, detectamos prejuízos na fase de relaxamento dos cardiomiócitos, o que foi corroborado com alterações no manejo intracelular de cálcio e em estruturas moleculares. O comprometimento do coração foi desencadeado por um elevado estresse oxidativo, que modulou a atividade de enzimas importantes (por exemplo a CaMKII), sendo caracterizado pela primeira vez por nosso grupo de pesquisa. No segundo subprojeto, utilizamos a isoforma Phα1β do veneno da aranha *Phoneutria nigriventer* como ferramenta farmacológica contra a morte neuronal em camundongos BACHD. Tratamos os camundongos com essa toxina por duas vias diferentes e analisamos seu possível potencial neuroprotetor. Observamos que a toxina promoveu melhora de parâmetros motores, o que pode estar relacionado com a preservação local do número de neurônios além da estrutura muscular, que deixou de apresentar atrofia nos animais BACHD. O mecanismo de ação dessa isoforma, por sua vez, está associado com a diminuição na liberação de glutamato e na expressão de caspase-3 em neurônios da medula espinal. Dessa forma, nesse trabalho descrevemos as alterações cardíacas do modelo BACHD, bem como descrevemos o potencial neuroprotetor da isoforma Phα1β. Os resultados obtidos desse projeto já foram publicados ou submetidos à publicação e poderão contribuir para o desenvolvimento de novas abordagens terapêuticas, fornecendo substratos para o tratamento desta doença que é muito incapacitante.

ABSTRACT

Huntington's disease (HD) is a neurodegenerative disorder, with devastating effects that usually arise in adulthood. Clinically, it is characterized by motor, behavioral, and cognitive decline. However, patients with HD can also develop cardiovascular disorders causing sudden death (the second cause of death). Despite the clinical importance, cardiac alterations observed in HD are still poorly understood. The present thesis was divided into two subprojects. In the first subproject, using a murine model for HD (BACHD line), we investigated possible cardiac changes (along with the mechanisms of action) that have not yet been described. Our results showed significant cardiac variations both *in vivo* and *in vitro*. The observed cardiac impulse conduction disturbances were associated with a prolongation of the action potential, as well as, the presence of cellular arrhythmias. In addition, we detected impairments in the cardiomyocyte relaxation phase, which was corroborated by changes in intracellular calcium handling and in molecular structures. The heart damage was triggered by oxidative stress, which modulated the activity of important enzymes (for example CaMKII), characterized for the first time by our research group. In the second subproject, we used the Phα1β isoform of the venom of the spider *Phoneutria nigriventer* as a pharmacological tool against neuronal death in BACHD mice. We treated the mice with this toxin by two different injections and analyzed its possible neuroprotective action. We observed that the toxin improved motor parameters, which may be related to a local neuronal preservation besides muscles structure, which no longer presented atrophy in BACHD animals. The mechanism of action of this isoform was associated with a decrease in glutamate release and caspase-3 expression in spinal cord neurons. Thus, in this work we describe the cardiac alterations in the BACHD model; moreover, we provide new evidence of a neuroprotective potential of the Phα1β isoform. The results obtained from this thesis have already been published or submitted to publication and may contribute to the development of new therapeutic approaches, providing novel substrates for the treatment of this disabling disease.

1- INTRODUÇÃO GERAL

1.1- A Doença de Huntington

As doenças neurodegenerativas são caracterizadas por uma perda gradual e progressiva de células neuronais, o que pode induzir uma disfunção do sistema nervoso[1]. Alguns exemplos de doenças neurodegenerativas são: Alzheimer, Parkinson, Esclerose Lateral Amiotrófica (ELA) e Doença de Huntington (DH). Essas doenças apresentam diferentes características morfológicas e fisiopatológicas, porém, todas podem desencadear sintomas altamente incapacitantes e gerar gastos financeiros envolvidos no tratamento e cuidados paliativos com os pacientes[2]. Os custos financeiros gerados pelas doenças neurodegenerativas, por exemplo, podem ser diretos (como, gastos com hospitalização, medicamentos e reabilitação) bem como indiretos (gastos com cuidados domiciliares, perda da produtividade, redução da renda familiar e aposentadoria precoce do indivíduo), gerando impacto econômico para toda a sociedade[3,4].

Considerando-se especificamente a DH (muitas vezes confundida com Parkinson ou Alzheimer), sabe-se que ela é um distúrbio caracterizado por alterações motoras progressivas como movimentos involuntários dos membros e da face (coreia), disartria (dificuldade em articular palavras), instabilidade postural, alterações da marcha e alterações de tônus muscular (o que leva a uma limitação da capacidade de realizar movimentos voluntários)[5]. Além disso, essa doença pode causar distúrbios emocionais e demência[6]. É uma doença que geralmente surge na idade adulta, com efeitos devastadores que podem levar à morte entre 15-20 anos após o aparecimento dos sintomas. A insuficiência cardíaca é uma das principais causas de morte dos pacientes.

Classicamente, a DH é uma doença genética, autossômica, dominante[7], caracterizada pela morte de neurônios em várias regiões do cérebro, principalmente no corpo estriado. No entanto, há também perda neuronal em outras regiões tais como córtex, tálamo, hipotálamo e hipocampo[8]. Ela é causada por uma mutação na porção 5' do gene *IT15* ou *Interesting Transcript 15*, no braço curto do cromossomo 4, que codifica a proteína huntingtina (HTT). Tal mutação resulta em uma expansão da sequência dos nucleotídeos citosina, adenina e guanina (CAG - que codifica o aminoácido glutamina), resultando em uma proteína mutante com uma sequência de poliglutaminas no terminal amínico da proteína HTT[9]. A penetrância da doença é variável para alelos que transportam 36-39 repetições CAG, mas já foi observado que, quando há um número $\geq$ 40 de repetições CAG, a doença apresenta penetrância completa[10].

Em relação á prevalência da DH no mundo, sabe-se que a Europa e a América do Norte são regiões de maior prevalência sendo 5,7 por 100.000 indivíduos[11,12]. De forma interessante, na América do Sul, uma pequena região na Venezuela (Lago de Maracaibo) possui altas taxas de prevalência da DH (sendo 7 casos a cada 100 indivíduos)[11,12]. Considerando o Brasil, em 2013 foi criada a Associação Brasil Huntington (ABH, 2013) que busca quantificar o número de pacientes com essa doença. Ainda não há dados oficiais sobre a prevalência da DH no Brasil, no entanto, existem algumas regiões no país que se destacam pelo número de indivíduos com DH. Uma delas é a cidade de Feira Grande, em Alagoas, cuja prevalência estimada é de 1 caso por 1.000 indivíduos. Outro exemplo é o município de Ervália, em Minas Gerais, com essa mesma prevalência[13]. É importante destacar que esses números são 10 vezes maiores do que a prevalência da população mundial. Historicamente, o continente europeu tem sido muito importante no estudo da DH pois, a maioria dos estudos sugerem que a migração europeia foi responsável por levar o gene causador da doença para os outros continentes.

A patogênese da DH está relacionada tanto à perda da função da HTT selvagem como também a toxicidade associada à HTT mutante que provoca disfunções celulares e degeneração. Sabe-se que a proteína selvagem participa no processo de transcrição de muitos genes, por exemplo, o gene que codifica fatores de sobrevivência neuronal como o Fator Neurotrófico Derivado do Cérebro (BDNF, do inglês *Brain-derived neurotrophic factor*), além de atuar na prevenção da cascata apoptótica, auxiliar o transporte axonal e a liberação de vesículas sinápticas[14,15]. Por outro lado, a forma mutante pode interagir com proteínas que estão intimamente associadas aos processos de exocitose e endocitose de vesículas sinápticas em neurônios do Sistema Nervoso Central (SNC) e do Sistema Nervoso Periférico (SNP)[16]. Além das alterações nas sinapses, existem evidências na literatura de que em modelos transgênicos para DH, a mutação na HTT pode causar déficits no transporte axonal[17]. Uma possível explicação para esta alteração é a de que a HTT mutante inibe o transporte axonal via alterações na atividade das quinases envolvidas na fosforilação de proteínas motoras tais como a cinesina e a dineína[18,19]. Essa proteína mutante também pode induzir apoptose, promover disfunção mitocondrial (e com isso distúrbios metabólicos) e interferir nos proteassomos aumentando ainda mais a formação de agregados intracelulares[14]. Além desses eventos citados, danos causados por estresse oxidativo[20] e excitotoxicidade mediada pelo glutamato[21] também estão correlacionados à patogênese da DH, tanto em seres humanos como em modelos animais. Todos esses eventos somados podem desencadear morte neuronal além de alterações na neurotransmissão e consequentemente perda da comunicação entre neurônio/ neurônio e neurônio/ músculo gerando os déficits motores. Algumas funções associadas a HTT selvagem e mutante podem ser visualizadas na Figura 1.
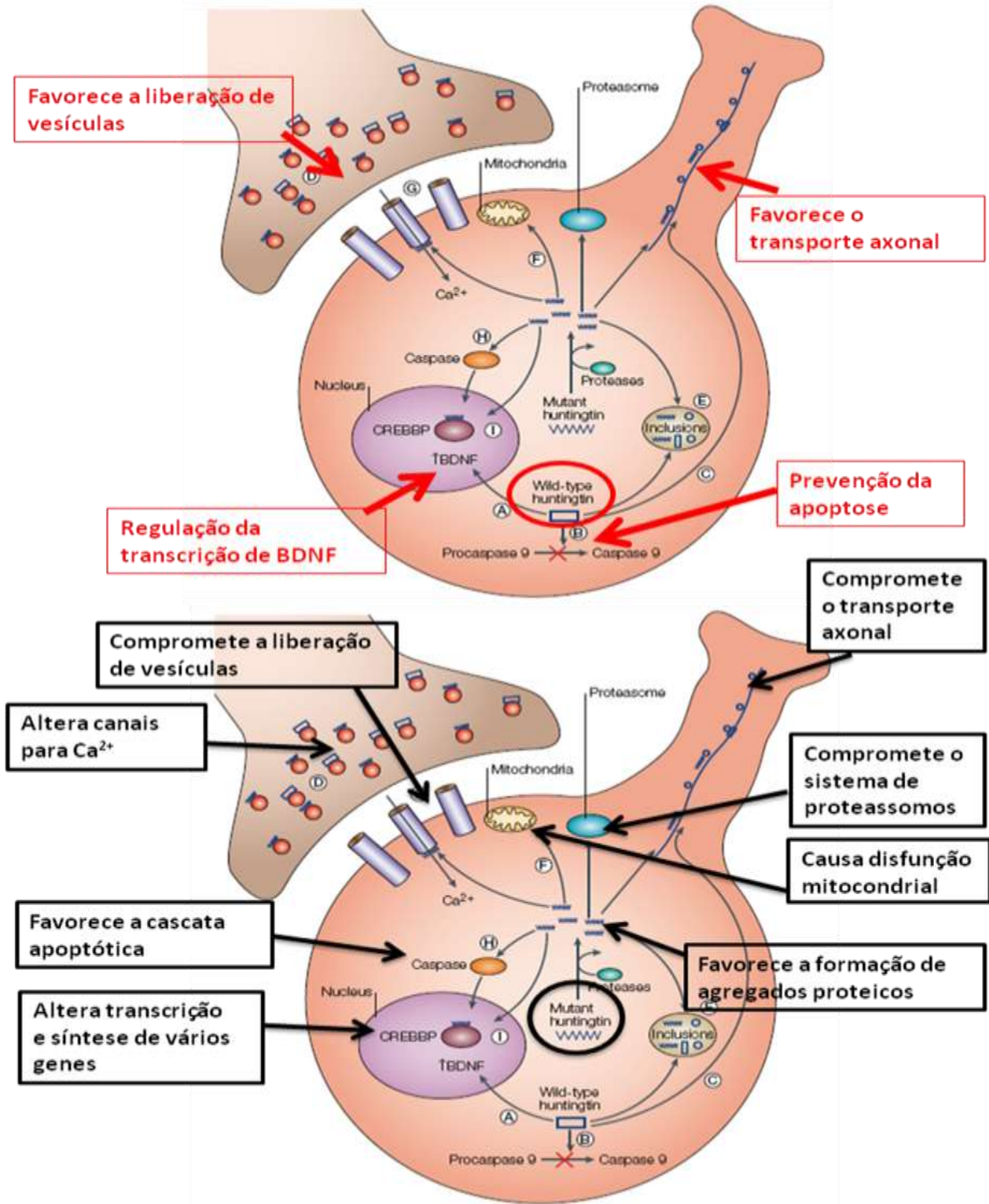
Figura 1: Exemplificação de algumas funções da huntingtina selvagem (em A, destaque em vermelho) e da mutante (em B, destaque em preto). Adaptado de Prospero & Fichbeck, 2005[14].

1.2- Doença de Huntington e excitotoxicidade

Em relação à DH, uma das causas da morte neuronal, que envolve liberação de neurotransmissores, está associada à excitotoxicidade[22,23,24]. Excitotoxicidade refere-se às alterações patológicas geradas pela exposição excessiva a neurotransmissores excitatórios por exemplo, ao glutamato[25]. Os efeitos excitatórios de neurotransmissores liberados por neurônios foram relatados pela primeira vez por Curtis *et al.* (1959)[26], que descreveu o processo de despolarização induzida por glutamato nos neurônios da medula espinal de ratos. É importante destacar que existem outros aminoácidos excitatórios (endógenos ou exógenos), porém o glutamato é o neurotransmissor excitatório mais abundante no SNC dos mamíferos, representando aproximadamente um terço de todas as sinapses excitatórias rápidas no SNC[27] sendo assim, este composto o foco do nosso estudo.

A síntese do glutamato pode ocorrer através de duas vias diferentes. Uma dessas vias envolve a transaminação do α-cetoglutarato (formado intracelularmente durante ciclo de Krebs) nas terminações nervosas do SNC. Alternativamente, a glutamina produzida e secretada por células da glia pode ser internalizada pelas terminações nervosas neuronais e convertida em glutamato pela enzima glutaminase. O glutamato por sua vez, será estocado em vesículas sendo posteriormente liberado na fenda sináptica por exocitose dependente de cálcio[25]. Na membrana pós-sináptica, há receptores para o glutamato do tipo ionotrópico como n-metil-D-aspartato (NMDA), alfa-amino-3-hidroxil-5-metilisoxazolepropionato (AMPA) e cainato (KA), responsáveis pelo transporte iônico de cálcio e sódio pela membrana plasmática, respectivamente. Já os receptores metabotrópicos (mGluRs) são responsáveis por mecanismos de sinalização intracelular via proteína G[25]. Finalmente, o glutamato presente no espaço extracelular é removido da fenda sináptica por transportadores específicos de recaptação. Ao contrário de outros, esse

neurotransmissor, quando no espaço extracelular, possui baixa conversão bioquímica, pois não há nessa região uma enzima que o modifique ou o degrade[28]. Desse modo, o glutamato deve interagir e ser removido do líquido extracelular por transportadores de aminoácidos excitatórios (EAATs, do inglês *excitatory amino acid transporters*) que controlam o tempo de concentração desse neurotransmissor na fenda[29,30]. Existem cinco tipos de EAATs a saber: transportador de aspartato-glutamato (GLAST/EAAT1), transportador de glutamato (GLT/EAAT2), transportador de aminoácido excitatório (EAAC/EAAT3), e os transportadores de aminoácidos excitatórios 4 e 5, (EAAT4 e EAAT5)[30].

O aumento na concentração de glutamato na fenda sináptica pode ocorrer por uma liberação exacerbada desse aminoácido ou comprometimento de sua recaptação, gerando o processo de excitotoxicidade[31]. Esse neurotransmissor no meio extracelular provocará uma hiper estimulação de seus receptores seguida da despolarização do terminal pós sináptico (devido ao influxo de cálcio e sódio para o citoplasma), o que desencadeia a ativação de canais voltagem dependentes e consequente agravamento do desequilíbrio iônico. Exemplos de canais ativados durante esse processo são os canais para Ca^{+2} sensíveis à voltagem (CCSV) que favorecem ainda mais a entrada de cálcio para o meio intracelular[31]. O excesso de Ca^{+2} dentro da célula gera desarranjos metabólicos letais dentre eles ativação de proteases como calpaína e caspases iniciando o processo de apoptose[32,33].

Sendo assim, alterações na via glutamatérgica e variações na expressão e/ou disfunção dos subtipos de CCSV estão relacionados com a injúria neuronal observada em desordens neurológicas como a DH[34]. De fato, vários estudos já demonstraram que a excitotoxicidade mediada por glutamato é um mecanismo importante que leva à morte neuronal nessa doença[35,36,37]. Estudos iniciais comprovaram que injeções de análogos de glutamato diretamente no corpo

estriado de ratos e primatas causaram lesões semelhantes às observadas em pacientes[36,38,39]. Recentemente, foi constatado em encéfalos *post mortem* de pacientes e em modelos transgênicos para a DH (R6/2), uma redução dos transportadores de glutamato (GLAST e GLT tipo 1) no estriado, resultando em uma diminuição da captação e aumento de sua disponibilização na fenda sináptica[40,41,42,43]. Além disso, a HTT mutante foi encontrada em células da glia causando a morte, por exemplo, de astrócitos, células importantes para a remoção do excesso de glutamato[44]. Disfunções nos receptores NMDA, como aumento de sua sensibilidade e permeabilidade ao cálcio, também foram evidenciadas em pacientes e modelos animais[22,45]. Por fim, uma super indução da via de sinalização glutamatérgica, aumentando a liberação desse neurotransmissor, já foi descrita na patogênese da DH[23,25].

1.3- Modelos animais para o estudo da Doença de Huntington

A primeira descrição da DH foi feita no século XIX por George Huntington, contudo apenas em 1993 a mutação genética causadora dessa enfermidade foi descrita[9]. Essa descoberta foi um grande marco para a história da DH, pois a partir desse fato modelos animais geneticamente modificados começaram a ser desenvolvidos. Atualmente, muitos organismos estão sendo utilizados na tentativa de se recapitular o fenótipo da DH. Esses organismos incluem: leveduras (*Caenorhabditis elegans*), insetos (*Drosophila melanogaster*), camundongos, ratos, ovelhas e, mais recentemente, porcos e macacos[46]. Os resultados de estudos feitos em modelos geneticamente modificados ajudam a elucidar vias importantes que são alteradas na DH, fornecem novos aspectos sobre a patogênese desta doença além de serem importantes para o estabelecimento de abordagens terapêuticas (revisado por Pouladi *et al*., 2013)[47].

Levando em consideração os modelos em camundongos, um modelo muito bem consolidado e estudado é o modelo R6/2, onde os camundongos transgênicos exibem uma rápida progressão dos sintomas da DH[48]. Esse modelo foi descrito em 1996, e foi gerado a partir da inserção de somente a região amino-terminal do gene que codifica a proteína HTT. Os animais R6/2 apresentam um fenótipo neuromotor grave caracterizado por hipoatividade, déficit de coordenação motora, equilíbrio, diminuição de força e tônus muscular além de alterações da marcha[49]. Vale destacar que esse modelo apresenta semelhança histológica com cérebros *post-mortem* de indivíduos com DH, apresentando, por exemplo, a presença de inclusões e agregados de HTT[50]. Contudo, o modelo R6/2 possui desvantagens no que diz respeito à progressão da doença, que ocorre de forma muito agressiva e rápida, o que causa uma sobrevida curta (geralmente esses camundongos morrem em aproximadamente 4 meses de idade)[51,52]. Sendo assim, estudos a longo prazo em animais idosos por exemplo, são muitas vezes inviáveis. Além disso, o modelo murino R6/2 apresenta limitações devido à instabilidade de repetições CAG. Já foi comprovado que, em muitas colônias, o número dessas repetições pode variar, comprometendo de forma significativa o fenótipo do camundongo[47]. Um rigoroso monitoramento e quantificação das repetições CAG é fundamental para o uso desses animais durante as pesquisas científicas.

Desta forma, uma boa alternativa é o uso de um novo modelo de camundongos transgênicos para DH produzido por tecnologia de recombinação de DNA. Este modelo utiliza o cromossomo artificial bacteriano (BAC) associado ao gene completo humano da HTT mutante que, ao ser codificado, expressa 97 repetições poliglutamínicas (Q97), estáveis, sendo então denominado BACHD[Q97] (BACHD). Diferente dos outros modelos, o BACHD apresenta progressão da doença de forma mais lenta e por este motivo, torna-se um modelo valioso e único para investigar as alterações decorrentes da DH, mimetizando da melhor maneira seus efeitos em seres humanos[53].

Os camundongos BACHD exibem comprometimento motor progressivo (início aos 2 meses de idade) que aparece antes de alterações neuropatológicas[53]. Sendo assim, o modelo BACHD é muito interessante para estudos longitudinais onde animais de meia idade e idosos podem ser avaliados. É importante mencionar que a DH é uma doença de meia idade sendo então, esses animais considerados como um modelo robusto para a investigação da patogênese e também para o desenvolvimento de novos tratamentos para essa enfermidade.

Outros exemplos de modelos para a DH e suas vantagens/limitações são exemplificados na Figura 2.

Animal model	Name	CAG repeat length	Strengths	Weaknesses
Mouse	R6/2	144	Rapid, progressive behavioral deficits	Limited neuropathology, short lifespan
	N171-Q82	82	Accumulation of mutant *Htt* aggregates	Subtle motor changes
	YAC128	128	Striatal atrophy	Late onset, subtle and transient behavior deficits
	BACHD	97	Striatal atrophy and behavioral deficits	Weight gain, late onset
	Hdh (CAG)150	150	Striatal atrophy and behavioral deficits	Late onset
Rat	TgHD51	51	Progressive behavior deficits	Late-onset and limited neuropathology
	BACHD	97	Striatal atrophy and behavioral deficits	Limited availability and late onset
	Quinolinic acid	N/A	Reproducible behavioral deficits and striatal cell loss	Not progressive, does not have the mutant *Htt* gene or produce mutant protein
	3-nitropropionic acid	N/A	Reproducible behavioral deficits and striatal cell loss	Does not have the mutant *Htt* gene or produce mutant protein
Mini-pig	N208	105	HD-like apoptotic neurons and DNA fragmentation	Limited behavioral tests and availability
Sheep	OVT73	73	Reduction in striatal GABA A receptor	Limited behavioral tests and availability
Nonhuman primate	Exon 1 *HTT*	84	Dystonia, chorea, neuronal inclusions and neuropil aggregates	Extremely limited availability

Figura 2: Modelos animais mais utilizados em pesquisas sobre a DH[54].

1.4- Doença de Huntington: Sistema nervoso *versus* periferia

Já está bem consolidado na literatura que a principal característica neuropatológica da DH é a morte dos neurônios do corpo estriado[55]. O corpo estriado (dorsal e ventral) faz parte dos denominados "núcleos (antigamente gânglios) da base do cérebro". Sabe-se que o corpo estriado (em conjunto com o córtex cerebral, tálamo e núcleos do tronco encefálico) exerce funções na orquestração e execução de comportamentos planejados e/ou motivados do circuito motor[56]. Antigamente, o corpo estriado era mais bem conhecido por suas funções motoras porém, nos últimos anos, essa região deixou de ser classificada como puramente motora passando a exercer funções que medeiam outros comportamentos associados a cognição, emoções e motivação[56]. Nesse sentido, a morte dos neurônios do corpo estriado justifica as alterações motoras da DH, bem como outros sintomas em termos cognitivos e emocionais. De forma bem específica, a degeneração neuronal ocorre principalmente nos neurônios espinhosos médios (MSNs, do inglês *medium spiny neurons*)[57,58]. Os MSNs são neurônios gabaérgicos e compreendem a maior parte do corpo estriado, de onde se projetam para outras regiões[59,60].

Entretanto, apesar da neurodegeneração estar principalmente associada à patologia da DH, não podemos esquecer que os pacientes também sofrem com alterações periféricas. De fato, sabe-se que a HTT é expressa ubiquamente em vários órgãos e tecidos humanos. Tanto a proteína selvagem como a mutante pode ser encontrada em músculos esqueléticos, coração, fígado, pâncreas, rim, estômago e testículos[50,61]. A Figuras 3 mostra algumas alterações periféricas da DH em pacientes.
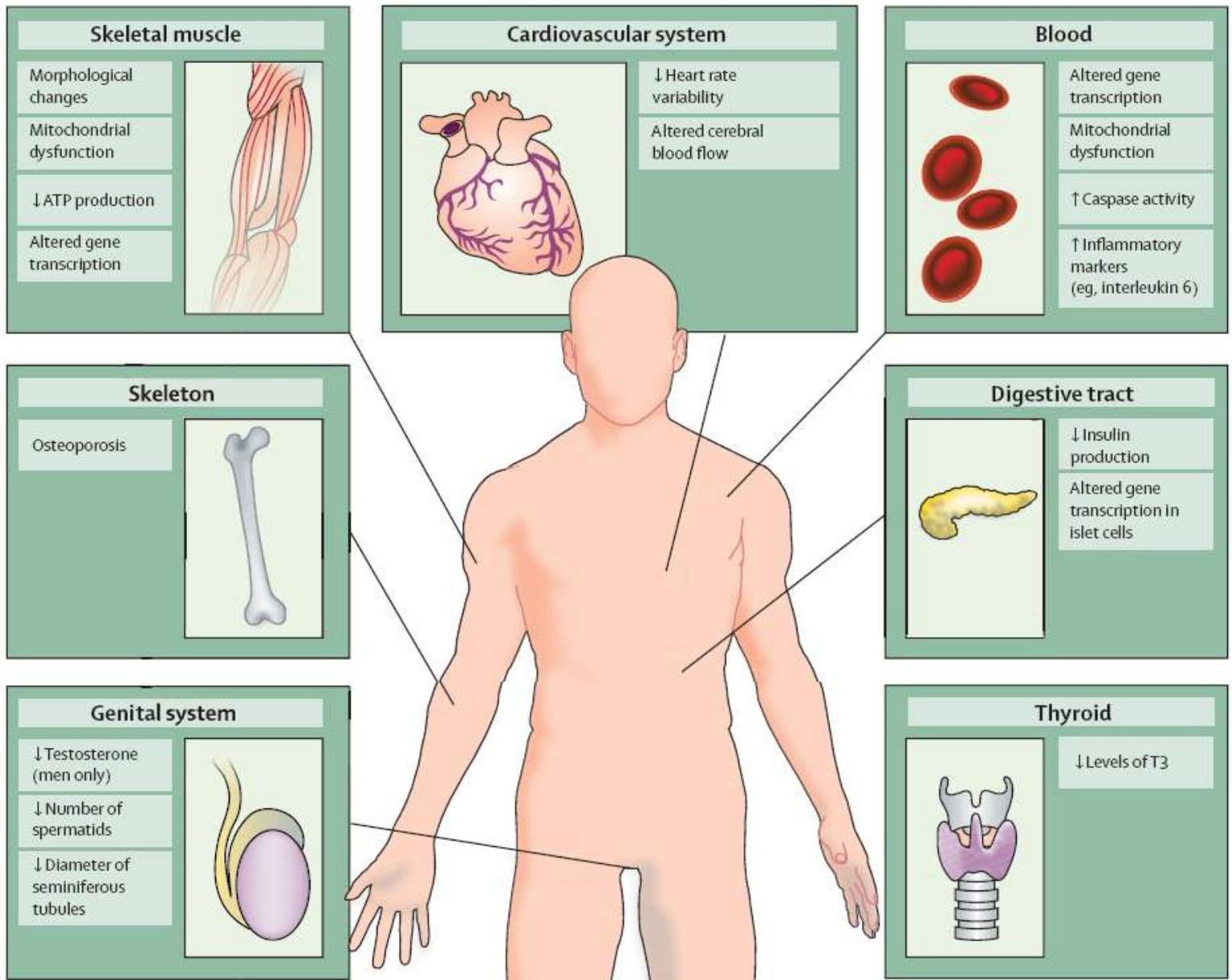
Figura 3: Alterações periféricas em pacientes com a DH[50].

Diante de tantas alterações periféricas, a DH deixou de ser uma condição apenas associada ao SNC. Dessa forma, novos estudos com o objetivo de se entender as modificações em outros órgãos e tecidos são fundamentais. A caracterização periférica é muito importante uma vez que possibilita o desenvolvimento de novas abordagens terapêuticas com o foco no periférico. Uma intervenção em outros órgãos pode ser mais favorável, e com menos riscos ao paciente, quando comparada a uma intervenção específica no SNC. Atualmente pouco se sabe sobre o comprometimento periférico no modelo BACHD, sendo esse modelo o mais próximo aos seres humanos, por expressar a HTT humana completa[53].

1.5- Abordagens terapêuticas para doenças neurodegenerativas: uso de toxinas animais

Venenos e toxinas animais são produtos da seleção natural podendo ser encontrados em inúmeros organismos incluindo moluscos, artrópodes, répteis, cnidários, plantas além de micro-organismos. Normalmente, os venenos contêm uma mistura de moléculas, como íons, proteínas, nucleotídeos e enzimas, e podem desencadear uma ampla variedade de efeitos nos seres humanos, como hemorragia, necrose ou neurotoxicidade[62]. A análise, purificação e síntese de componentes dos venenos animais pode ser útil para o desenvolvimento de novos fármacos para diversos tipos de enfermidades. Realmente, podemos citar muitos medicamentos utilizados na clínica médica com base em toxinas de animais ou em seus compostos. Alguns bem sucedidos exemplos são Prialt (Ziconotida), que é uma versão sintética da conotoxina MVIIA encontrada no veneno do molusco *Conus magus*, e usado para tratamento da dor[63,64]; e o altamente receitado como anti-hipertensivo, Captopril, baseado em compostos presentes no veneno da cobra *Bothrops jararaca*[65,66].

Exemplos de venenos animais e suas ações em diferentes condições neuropatológicas foram revisados e publicados recentemente por de Souza *et al.* 2018[67]. Vale destacar por exemplo, o uso de toxinas derivadas de serpentes africanas do gênero *Dendroaspis*, bem como espécies indianas do gênero *Daboia*, além de abelhas (*Apis mellifera)*, como ferramentas farmacológicas para o tratamento de sintomas do Alzheimer. De forma interessante, o veneno dessa mesma espécie de abelha foi usado em modelos para a Doença de Parkinson. A administração do veneno dessa abelha levou à diminuição da neurodegeneração pela redução de estresse oxidativo (via atenuação dos níveis de espécies reativas de oxigênio e peróxidos lipídicos), neuroinflamação (diminuindo o número e a ativação de astrócitos e microglia, bem como redução na liberação de fatores pró-inflamatórios) e também apoptose (uma vez que esse composto diminui os níveis de expressão do gene *Bax*, a ativação da caspase-3 e a fragmentação do DNA)[67].

Em relação ao uso de toxinas animais na DH, um potencial efeito neuroprotetor do veneno da aranha *Phoneutria nigriventer* foi evidenciado em cultura primaria de neurônios corticostriatais derivados do modelo BACHD[68]. Tal veneno é composto por uma mistura de peptídeos que afetam a função de canais iônicos, diminuindo a morte neuronal e melhorando as alterações na neurotransmissão. As neurotoxinas dessa aranha são reconhecidas como novas fontes de substâncias bioativas, apresentando uma ampla gama de efeitos farmacológicos importantes. Várias frações do veneno dessa aranha já foram identificadas bioquimicamente e serão abordadas na seção que se segue.

1.5.1- O veneno da aranha *Phoneutria nigriventer*

Até o presente momento, ainda não há cura para a DH. As opções terapêuticas para os pacientes envolvem apenas o uso de medicamentos para tratamento dos sintomas já estabelecidos

e assim, tentando melhorar a qualidade de vida desses pacientes. Geralmente, para tratar sintomas como a coreia, são usados medicamentos como bloqueadores dos receptores dopaminérgicos (fármacos neurolépticos) ou agentes depletores de monoaminas (exemplo: Tetrabenazina). São receitadas também drogas antidepressivas e contra distúrbios psicóticos e de ansiedade (como Benzodiazepinas)[69,70]. Diante disso, drogas neuroprotetoras que preservam a função neuronal emergem como candidatas ideais a agentes modificadores do curso da doença ao invés de simplesmente tratar os sintomas já instalados. Nesse contexto, é de grande relevância testar novos agentes neuroprotetores que poderiam minimizar a morte neuronal na DH. Como exemplo, citamos o desenvolvimento de agentes terapêuticos seguros e eficazes direcionados para atuar em etapas específicas da neurotransmissão sináptica, por exemplo, na entrada de cálcio via CCSV. Dados da literatura mostram que em neurônios há uma predominância de CCSV Tipo-N e Tipo P/Q enquanto que em terminações nervosas da musculatura lisa e cardíaca, observa-se marcante predomínio de canais Tipo-L[71].

Uma abordagem interessante para minimizar as desordens neuromotoras da DH poderia ser o uso de toxinas animais como agentes terapêuticos contra excitotoxicidade e neurodegeneração, como as toxinas do veneno da aranha armadeira *Phoneutria nigriventer* que têm um amplo espectro de ação[72]. Essa aranha é uma das espécies mais agressivas da América do Sul[73], sendo responsável pela maioria dos acidentes por picadas de aranha no Brasil. A picada da aranha armadeira causa dor severa e vários sintomas como espasmos, tremores, convulsões, paralisia espástica, priampismo, disritmia, distúrbios visuais e sudorese fria[73]. Esses sintomas presentes em crianças ou idosos podem levar à morte, se não devidamente tratados.

Baseado nos sintomas observados em seres humanos e nos resultados de injeções intracérebro-ventriculares em animais experimentais, viu-se que o veneno da aranha *Phoneutria*

nigriventer é, de fato, neurotóxico. Tal veneno foi então purificado, através de uma combinação de filtração em gel e cromatografia de fase reversa[74], gerando 5 frações distintas (nomeadas PhTx1, PhTx2, PhTx3, PhTx4 e a não neurotóxica fração M)[74,75]. Cada uma das frações é constituída por diferentes isoformas (peptídeos), que quando isolados apresentam diversas ações farmacológicas, como pode ser visto na Figura 4 e evidenciado na seção 4.2 da presente tese.

	PhTx1	PhTx2	PhTx3	PhTx4	M
		FRAÇÕES do veneno			
Isoformas	Única: **Tx1**	9 peptídeos: **Tx2-1 a Tx2-9**	6 peptídeos: **Tx3-1 a Tx3-6**	7 peptídeos: **Tx4-1 a Tx4-7**	Única: **M**
Efeitos (após injeção i.c.v.)	Elevação da cauda; excitação; paralisia espástica	Excitatórios (salivação, lacrimação, convulção); paralisia espástica; atuação em canais de sódio	Inibição da neurotransmissão; paralisia flácida; atuação em canais de cálcio (principalmente) e potássio	Pouco tóxica em camundongos; letal em insetos; ação no sistema glutamatérgico	Sem efeito letal em camundongos, contração do músculo liso em íleo de cobaia

Figura 4: Representação das frações do veneno da aranha armadeira *Phoneutria nigriventer* com suas isoformas e principais ações.

i.c.v: intracérebro-ventricular

As frações são classificadas como PhTx1 a PhTx4 (além da Fração M), as isoformas são peptídeos isolados componentes das frações classificados como Tx ou PnTx (seguido do número da fração e número específico da isoforma)[72,74,75,76,77,78,79,80].

Até o momento essas toxinas ainda não foram testadas como agentes contra a excitotoxicidade (provocada pelo excesso de glutamato) e preservação neuronal no modelo BACHD *in vivo*.

2- JUSTIFICATIVA

De acordo com a associação Brasil Huntington, existem hoje em nosso país cerca de 500 famílias com o gene da doença, e estima-se que existam na população brasileira aproximadamente 100 mil indivíduos com a DH. Apesar de ser uma doença rara, ela apresenta sintomas similares a várias outras doenças neurológicas como ELA, Parkinson e Esclerose (com a vantagem da DH ser uma desordem genética de causa conhecida, mutação no gene *htt*, o que faz dela um excelente modelo para estudo das doenças neurodegenerativas como um todo). Considerando que a DH é uma doença motora, mesmo com os avanços das pesquisas, alterações morfofisiológicas em diferentes tipos musculares ainda não estão elucidadas. Por exemplo, a análise do músculo cardíaco em um importante modelo animal da doença, o BACHD, ainda não foi completamente avaliada. Por fim, o uso de neurotoxinas animais pode ser uma nova alternativa como agente terapêutico contra excitotoxicidade provocada pelo excesso de glutamato e preservação neuronal na DH.

3- OBJETIVOS

Os objetivos gerais desse trabalho de doutorado envolvem a caracterização de possíveis alterações cardíacas no modelo murino para a DH (BACHD) na idade de 12 meses. Além disso, tivemos como objetivo avaliar o potencial de uma neurotoxina derivada do veneno aranha armadeira *Phoneutria nigriventer* em retardar a morte neuronal bem como, a melhora dos parâmetros morfológicos, comportamentais e motores da DH em nosso modelo experimental.

3.1- Objetivos Específicos

Subprojeto 1:

- Investigar o desenvolvimento de alterações na condução do impulso elétrico *in vivo* em camundongos BACHD e WT, utilizando-se a técnica de eletrocardiograma (ECG);

- Caracterizar possíveis alterações na excitabilidade dos cardiomiócitos isolados de camundongos BACHD e WT, utilizando-se a técnica de *whole-cell patch clamp*;

- Caracterizar possíveis alterações na contratilidade de cardiomiócitos isolados de camundongos BACHD e WT;

- Caracterizar possíveis alterações no transiente de cálcio em cardiomiócitos isolados de camundongos BACHD e WT, utilizando-se o sistema de microscopia confocal;

- Caracterizar possíveis alterações moleculares (em proteínas) importantes para o processo de excitação/contração, utilizando-se *western blot*;

- Caracterizar possíveis alterações ultraestruturais de camundongos BACHD e WT, utilizando-se o sistema de microscopia eletrônica;

- Caracterizar possíveis alterações de estresse oxidativo em corações de camundongos BACHD e WT, utilizando-se ensaios da atividade de enzimas antioxidantes e sondas específicas;

- Descrever um potencial mecanismo de ação para as alterações cardíacas utilizando-se um inibidor específico.

Subprojeto 2:

- Avaliar o potencial neuroprotetor *in vivo* após o tratamento com toxina Phα1β em animais BACHD e WT, utilizando-se testes comportamentais e motores;

- Avaliar o potencial neuroprotetor da toxina Phα1β no sistema nervoso central de camundongos BACHD e WT, utilizando-se microscopia óptica;

- Investigar possíveis alterações na morfologia de diferentes músculos esqueléticos de camundongos BACHD e WT após o tratamento com a toxina Phα1β, utilizando-se microscopia óptica;

- Descrever um potencial mecanismo de ação para o tratamento com a toxina Phα1β, utilizando-se a quantificação dos níveis de glutamato no líquor a expressão de caspase-3 em neurônios da medula espinal.

4- RESULTADOS

Os resultados serão apresentados em formato de artigos científicos já publicados ou submetidos para publicação.

4.1- Contextualização do artigo 1

Vários estudos epidemiológicos já mostraram que as doenças cardiovasculares e a insuficiência cardíaca são a segunda principal causa de mortalidade nos pacientes com DH[50,81,82]. Sabe-se que a HTT mutante pode ser também encontrada de forma periférica no organismo no tecido muscular estriado esquelético e cardíaco[8,50,83]. Dessa forma, além das alterações neurológicas e motoras, pacientes com DH podem desenvolver problemas cardiovasculares como insuficiência do coração, doença coronariana e desenvolvimento de arritmias que podem causar morte súbita[84]. Estudos prévios já demonstraram que esses pacientes podem apresentar mudanças no Sistema Nervoso Autônomo (SNA) que são detectadas mesmo antes do aparecimento dos sintomas motores. Em muitos casos acontece uma desregulação do Sistema Nervoso Simpático (SNS) e do Sistema Nervoso Parassimpático (SNP), onde o SNS torna-se hiperativo em pacientes pré-sintomáticos, enquanto a atividade do SNP declina progressivamente[85,86]. Esses tipos de mudanças no SNA estão associadas a um mau prognóstico para eventos cardiovasculares graves que muitas vezes levam à morte súbita[87]. De fato, já foi descrito que camundongos transgênicos para a DH, quando comparados aos controles WT (do inglês *Wild Type*), apresentam alterações baroreflexas, bem como aumento pressão arterial (o que indica uma disfunção autonômica). Apesar disso, esses animais não apresentaram grandes mudanças estruturais no coração, apenas leve hipertrofia[88]. No entanto, mesmo com os avanços das pesquisas possíveis alterações elétricas, arritmias, alterações no potencial de ação, contratilidade do cardiomiócito e alterações no

transiente de cálcio, além de anormalidades moleculares e ultraestruturais não foram descritas no modelo BACHD. Sendo assim, a análise desses parâmetros cardíacos além de uma descrição de um possível mecanismo de ação, é muito importante para patofisiologia da DH (podendo auxiliar no desenvolvimento de novas estratégias clínicas para evitar a incidência de eventos cardiovasculares fatais em pacientes doentes).

De acordo com o exposto acima, a análise cardíaca dos animais BACHD e WT, com 12 meses de idade, foi realizada por nosso grupo de pesquisa. Todos os resultados podem ser visualizados no artigo 1, publicado em 2018 na revista *The FEBS Journal*, que se segue.

ARTIGO 1

Increased oxidative stress and CaMKII activity contribute to electro-mechanical defects in cardiomyocytes from a murine model of Huntington's disease

Julliane Vasconcelos Joviano-Santos[1], Artur Santos-Miranda[2], Ana Flávia Machado Botelho[3], Itamar Couto Guedes de Jesus[4], Jéssica Neves Andrade[1], Tatiane de Oliveira Barreto[2], Matheus Proença S. Magalhães-Gomes[1], Priscila Aparecida Costa Valadão[1], Jader dos Santos Cruz[2], Marília Martins Melo[3], Silvia Guatimosim[4] and Cristina Guatimosim[1]

1 Department of Morphology, Instituto de Ciências Biológicas, Universidade Federal de Minas Gerais, Belo Horizonte, Brazil
2 Department of Biochemistry and Immunology, Instituto de Ciências Biológicas, Universidade Federal de Minas Gerais, Belo Horizonte, Brazil
3 Department of Veterinary Clinic and Surgery, Escola de Veterinária, Universidade Federal de Minas Gerais, Belo Horizonte, Brazil
4 Department of Physiology, Instituto de Ciências Biológicas, Universidade Federal de Minas Gerais, Belo Horizonte, Brazil

Huntington's disease (HD) is a neurodegenerative genetic disorder. Although described as a brain pathology, there is evidence suggesting that defects in other systems can contribute to disease progression. In line with this, cardiovascular defects are a major cause of death in HD. To date, relatively little is known about the peripheral abnormalities associated with the disease. Here, we applied a range of assays to evaluate cardiac electro-mechanical properties *in vivo*, using a previously characterized mouse model of HD (BACHD), and *in vitro*, using cardiomyocytes isolated from the same mice. We observed conduction disturbances including QT interval prolongation in BACHD mice, indicative of cardiac dysfunction. Cardiomyocytes from these mice demonstrated cellular electro-mechanical abnormalities, including a prolonged action potential, arrhythmic contractions, and relaxation disturbances. Cellular arrhythmia was accompanied by an increase in calcium waves and increased Ca^{2+}/calmodulin-dependent protein kinase II activity, suggesting that disruption of calcium homeostasis plays a key part. We also described structural abnormalities in the mitochondria of BACHD-derived cardiomyocytes, indicative of oxidative stress. Consistent with this, imbalances in superoxide dismutase and glutathione peroxidase activities were detected. Our data provide an *in vivo* demonstration of cardiac abnormalities in HD together with new insights into the cellular mechanistic basis, providing a possible explanation for the higher cardiovascular risk in HD.

Introduction

Huntington's disease (HD) is a neurodegenerative genetic disorder clinically characterized by progressive movement alterations, cognitive dysfunction, and psychiatric impairment [1,2]. The disease is an autosomal dominant condition caused by expansion of a CAG trinucleotide repeat sequence present in the *huntingtin* (*Htt*) gene, which results in an abnormally long polyglutamine (polyQ) tract in the N terminus of the huntingtin (HTT) protein [3]. A hallmark of HD is the clustering of mutant HTT (mHTT) as insoluble aggregates, which have been extensively associated with progressive neuronal death [4–6]. Moreover, the loss of normal function and/or the gain of toxicity of mHTT is also associated with the cellular dysfunction and degeneration observed in HD pathogenesis [7].

Cardiac dysfunction contributes to both mortality and morbidity of HD, with cardiovascular disease and heart failure being the second most common cause of death of the patients [8,9]. Studies performed in mice and *Drosophila* show that cardiomyocyte-specific expression of disease-causing HTT-polyQ [83 polyQ repeats (Q83) in mice and different polyQ repeat lengths (Q25, Q46, Q72, and Q103) in *Drosophila*] leads to severe heart failure. This suggests that the cardiovascular disturbances might be a consequence of direct cardiomyocyte abnormalities as well as improper autonomous nervous system input [10,11]. Moreover, it has been described that cardiac mHTT expression inhibited protein complexes such as mechanistic target of rapamycin complex 1 (mTORC1), limiting heart growth and reducing the heart's ability to compensate for chronic stress [12]. BACHD, a new mouse model of HD, showed functional differences between WT and BACHD hearts starting at 3 months of age, and the aged BACHD mice developed cardiac fibrosis and apoptosis [13]. It is important to highlight that these transgenic mice express the human gene of mHTT, and unlike other models, BACHD shows slower disease progression, and for this reason is a valuable and unique model to investigate the HD-like pathology in aged animals [14]. However, despite the clinical importance, the mechanisms involved in cardiac dysfunction in HD remain poorly understood. Indeed, previous studies [13] have not addressed the contribution of the electrical and mechanical function in the heart to the development of HD in 12-month-old animals.

In this work, we investigated electro-mechanical properties such as action potential (AP) and cardiac cell contractility to better understand the mechanisms underlying cardiac malfunction in the BACHD mouse model of HD. We also searched for ultrastructural changes in the cardiomyocytes of these animals. We found that the hearts from the BACHD mice exhibited marked electro-mechanical dysfunction associated with oxidative stress, which might be the trigger for severe arrhythmias. Moreover, we identified ultrastructural changes in the mitochondria and imbalance in the antioxidant system in the cardiomyocytes. Finally, we propose a pathway associated with Ca^{2+}/calmodulin-dependent protein kinase II (CaMKII) activity responsible for the electro-mechanical alterations observed in the BACHD cardiac cells.

Results

BACHD mice present significant changes in electrocardiography recordings

Considering that HD is a disorder of middle age and the main cause of death of the patients is related to cardiovascular defects [8,9], 12-month-old WT and BACHD mice were subjected to electrocardiography (ECG) to investigate the *in vivo* changes in the conduction of cardiac impulses. The spontaneous conduction disturbances seen in the BACHD mice included QT interval prolongation, ST-segment deviation, wandering pacemaker, and 'M'-shaped R wave (Fig. 1A). Additionally, the BACHD mice showed a significant prolongation of the QT interval (WT: 78.3 ± 2.9 ms; BACHD: 85.5 ± 1.9 ms; mean $\pm$ SEM) and ST-segment (WT: 0.08 ± 0.04 mV; BACHD: 0.26 ± 0.07 mV) (Fig. 1B,C). The analysis of the other electrocardiographic parameters revealed no significant difference between the two groups of mice (Table 1).

Ventricular myocytes from BACHD mice show electrical, mechanical, and calcium handling disturbances

In light of the *in vivo* changes in the electrocardiogram observed in the BACHD mice, we next investigated whether the ventricular myocytes from the BACHD mice presented electrical and mechanical abnormalities. To this end, we used three different but complementary approaches: the patch-clamp technique, analyses of cell contraction, and confocal microscopy.

The results obtained with the patch-clamp technique revealed that the BACHD ventricular cardiomyocytes have prolonged AP duration and alternans (Fig. 2A). Figure 2B,C shows that a statistical difference was found between the groups: 90% AP repolarization ($APR_{90\%}$) WT: 107.4 ± 21.9 ms ($n = 22$ cells); BACHD: 226.5 ± 33.2 ms ($n = 27$ cells); standard
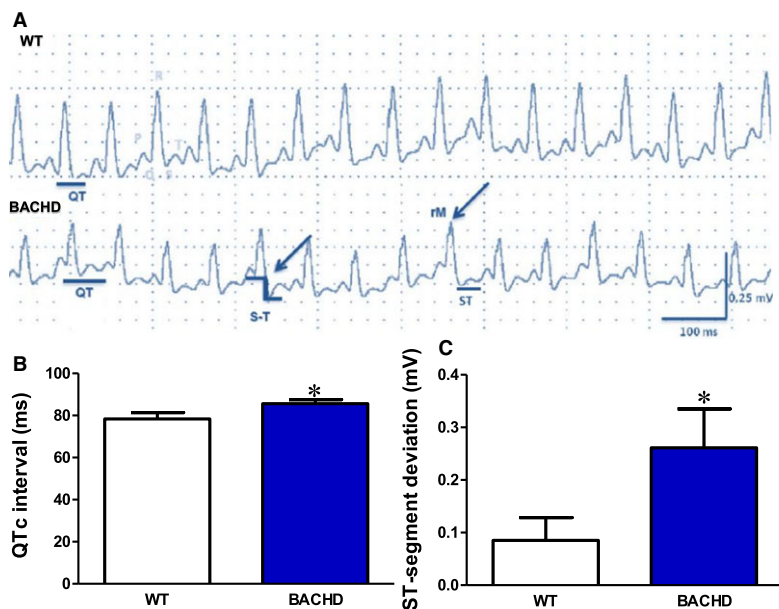
Fig. 1. Huntington's disease transgenic (BACHD) mice present electrocardiographic spontaneous electrical disturbances. (A) Electrocardiogram waveforms of WT ($n = 10$) and BACHD ($n = 15$) mice. BACHD mice presented QT interval prolongation, ST-segment elevation, and 'M'-shaped R wave (rM) (see arrows). (B) Bar graph showing a significant increase in QT interval in BACHD; QT interval was corrected by Van der Waters's formula ($P = 0.04$). (C) Bar graph showing a significant increase in the ST-segment elevation in BACHD compared with WT ($P = 0.02$). *$P < 0.05$, Student's *t* test. Data are expressed as mean $\pm$ SEM.

Table 1. Electrocardiography and cardiomyocyte AP parameters of WT and Huntington's disease transgenic (BACHD) mice. Data are expressed as mean $\pm$ SEM. No significant differences were observed between the groups ($P > 0.05$, Student's *t* test). bpm, beats per minute; HR, heart rate.

Parameter	WT	BACHD
ECG parameters		
P wave duration (ms)	31.9 ± 1.2	32.0 ± 1.2
P wave amplitude (mV)	0.03 ± 0.0	0.03 ± 0.0
PR interval (ms)	32.2 ± 0.9	33.3 ± 2.2
QRS duration (ms)	40.5 ± 0.9	42.5 ± 2.2
R wave amplitude (mV)	0.1 ± 0.01	0.1 ± 0.01
T wave amplitude (mV)	0.02 ± 0.0	0.02 ± 0.0
RR interval (ms)	0.1 ± 0.0	0.1 ± 0.0
HR (bpm)	499 ± 13	506 ± 9
AP parameters		
Maximum rise slope (dV/dt)	82.4 ± 11	81.8 ± 10
Resting membrane potential (mV)	-62.8 ± 0.6	-63.8 ± 0.6
AP amplitude (ms)	113.0 ± 2	110.9 ± 1

deviation of mean AP duration; mean σ for $APR_{90\%}$: WT: 9.1 ± 1.9 ms; BACHD: 64.9 ± 7.8 ms; mean $\pm$ SEM). Despite these changes, we did not find alterations in other AP parameters, i.e. maximum rise slope, resting membrane potential, and AP amplitude (Table 1).

Using the contraction assay, we noted that contraction in the WT cells was homogeneously synchronized with the electrical stimulus whereas the BACHD cardiomyocytes showed changes in the pattern of contraction (Fig. 3A). In fact, we observed a higher number of arrhythmic events (characterized by spontaneous contractions triggered without stimulation) in the BACHD

cells. Figure 3B shows the number of arrhythmic events per 60 s in 50 WT cells and 53 BACHD cells (0.8 ± 0.4 and 4.8 ± 1.3, respectively, mean $\pm$ SEM). There was no alteration in the contractile parameters such as fractional shortening and maximum rate of contraction (Fig. 3C,D). However, we identified significant alterations in the relaxation parameters such as the maximum rate of relaxation, time to relaxation, and time to peak (Fig. 3E–G). Altogether, these data show the presence of arrhythmias at a cellular level and the preservation of contraction in spite of alterations in the relaxation parameters.

Next, we evaluated the Ca^{2+} dynamics in the BACHD ventricular cardiomyocytes. The cells were labeled with Fluo4 acetoxymethyl ester and imaged by confocal microscopy. We investigated the presence of calcium waves, the transient amplitude (F/F_0), and the rate of transient decay. As shown in Fig. 4A,B, BACHD cardiomyocytes presented an increased number of calcium waves when compared with WT. The calcium transient amplitude was maintained in the BACHD cardiomyocytes supporting the lack of alterations observed in the contraction (Fig. 4C). Finally, the decay constant was significantly decreased, corroborating the faster relaxation rate seen in the BACHD cells (Fig. 4D).

Molecular alterations in the ventricular myocardium of BACHD mice

To assess the molecular alterations of proteins involved in the excitation–contraction coupling, we performed
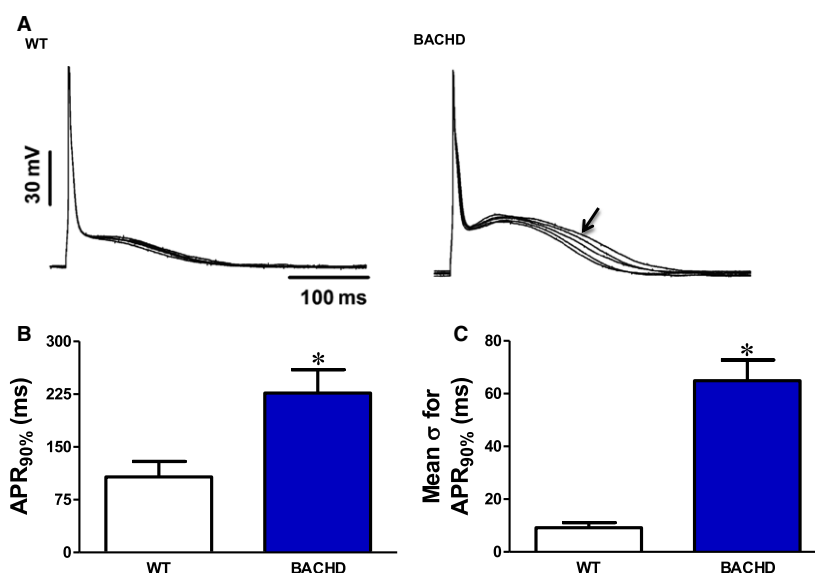
Fig. 2. Huntington's disease transgenic (BACHD) mice show alterations in AP in ventricular cardiomyocytes. (A) Representative AP traces obtained for WT and BACHD cardiomyocytes. In BACHD, the cardiomyocytes present a prolonged AP and AP duration alternans (arrow). (B) Bar graph showing significant increase in AP repolarization (APR) time in BACHD ($P = 0.009$). (C) Bar graph showing significant increase in AP duration alternans in BACHD ($P < 0.0001$). Sigma: Standard deviation of mean AP duration from 30 consecutive analyzed AP. Analyses involved $n = 22$ and $n = 27$ cells from four different WT and BACHD animals, respectively, in 10 consecutive beats. *$P < 0.05$ compared with WT, Student's *t* test. Data are expressed as mean ± SEM.

western blotting of the ventricular myocardium samples (Fig. 5A). Figure 5B reveals that the expression of SERCA did not change between the groups (WT: 1.6 ± 0.2; BACHD: 1.7 ± 0.3; mean ± SEM). However, BACHD samples showed increased phosphorylation of phospholamban (PLN) at Thr17 (WT: 1.0 ± 0.04; BACHD: 1.6 ± 0.2; mean ± SEM) (Fig. 5C) and CaMKII at Thr[286] (WT: 1.0 ± 0.1; BACHD: 2.2 ± 0.5; mean ± SEM) (Fig. 5D).

CaMKII is involved in the mechanical disturbances observed in cardiomyocytes from BACHD mice

Considering our data that showed increased CaMKII phosphorylation in the BACHD hearts and its role during the development of cardiac arrhythmias [15,16], we assessed CaMKII's contribution in the mechanical disturbances observed in the BACHD cardiomyocytes. We incubated the ventricular myocytes with the CaMKII inhibitor KN93 before the contractility assay. Although KN93 blocked cell arrhythmias (Fig. 6A), it did not affect cell fractional shortening and the maximum rate of contraction (Fig. 6B,C), in accordance with our previous results (described in Fig. 3). On the other hand, the maximum rate of relaxation, time to relaxation, and time to peak of BACHD cardiomyocytes were similar when compared with the WT

KN93 group (Fig. 6D–F), indicating there was a reversal of the effects previously observed in these relaxation parameters (shown in Fig. 3). We did not observe such differences when using the inactive analog KN92.

BACHD mice present ultrastructural alterations in the ventricular myocardium associated with oxidative damage

Because CaMKII plays a key role in the development of arrhythmias in BACHD cells, we decided to investigate whether the BACHD cells presented any sign of oxidative damage since reactive oxygen species (ROS) can lead to CaMKII oxidation and consequently its activation. Therefore, we searched for evidence of oxidative stress in the ventricular myocardium using electron microscopy and found mitochondrial ultrastructural abnormalities. Accordingly, based on a qualitative analysis, the mitochondria of the ventricular myocardium were degraded and had absent cristae or were filled by granules (Fig. 7A–E). Although we also detected changes in the WT myocardium, these were less intense than the damage observed in the BACHD myocardium. Additionally, we observed the presence of lipofuscin granules in the cardiac tissue. Because the lipofuscin content may include aggregates of oxidized proteins [17] and, therefore, is indirect evidence of
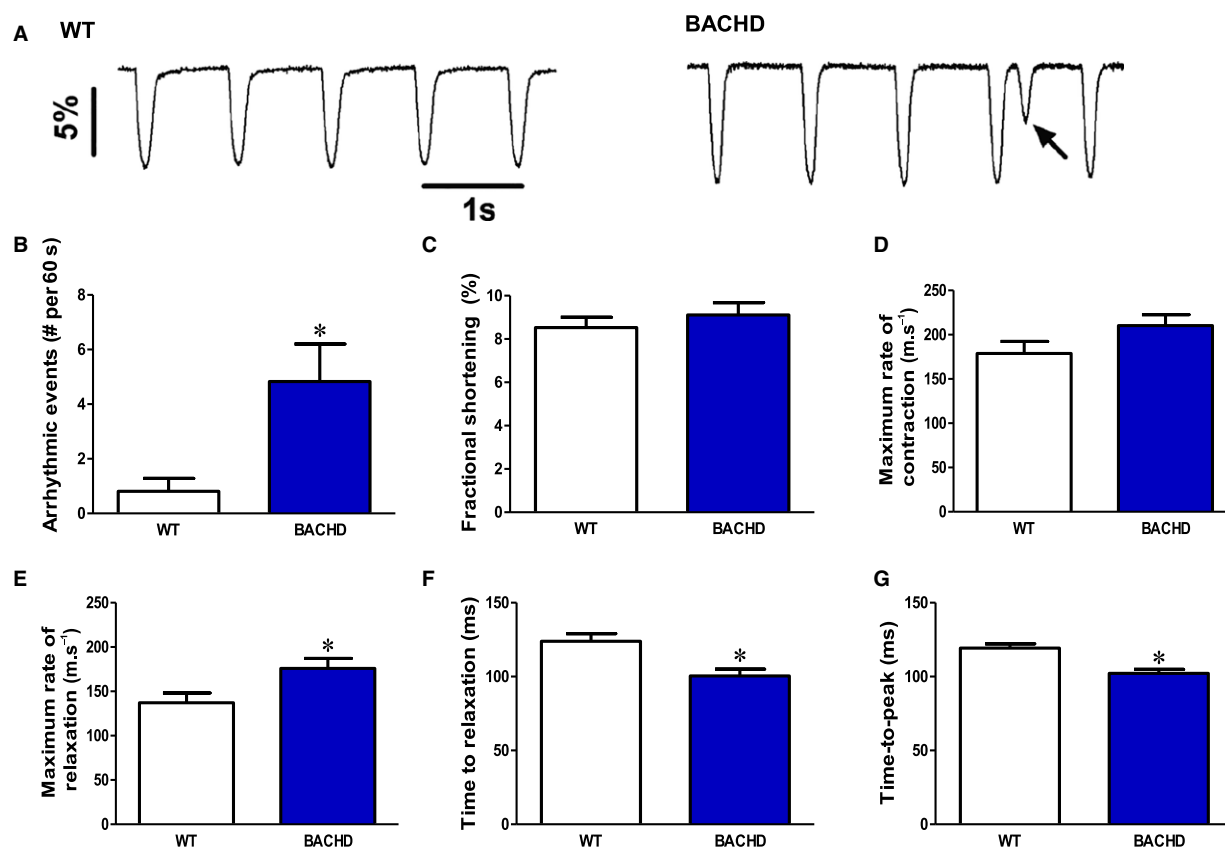
Fig. 3. Huntington's disease transgenic (BACHD) mice show mechanical changes in ventricular cardiomyocytes. (A) Representative contraction traces obtained from ventricular cardiomyocytes of WT and BACHD mice. The arrow shows arrhythmic events in BACHD cells. (B) Bar graph showing a significant increase in arrhythmic events in BACHD cells ($P = 0.004$). (C) Bar graph showing no alterations in fractional shortening ($P = 0.21$). (D) Bar graph showing no alterations in the maximum rate of contraction ($P = 0.37$). (E) Bar graph showing significant increase in the maximum rate of relaxation in BACHD cells ($P = 0.007$). (F) Bar graph showing a significant decrease in the time to relaxation in BACHD cells ($P = 0.0005$). (G) Bar graph showing significant decrease in the time-to-peak in BACHD cells ($P < 0.0001$). Analyses involved $n = 50$ and $n = 53$ cells from four different WT and BACHD animals, respectively. *$P < 0.05$ compared with WT, Student's t test. Data are expressed as mean $\pm$ SEM.

oxidative stress, we quantified these granules and found that the BACHD myocardium presented a higher number of lipofuscin deposits than in the WT myocardium (Fig. 7F).

The analyses of the cardiac antioxidant system revealed an increase in the superoxide dismutase (SOD; Fig. 8A) and glutathione peroxidase (GPx; Fig. 8C) activities and no alteration in the catalase (CAT) activity (Fig. 8B), supporting the hypothesis that oxidative damage is likely to underlie the alterations observed in the BACHD myocardium. And finally, with two different probes we observed a significant increase in the fluorescence of BACHD cells, suggesting oxidative stress [dichlorodihydrofluorescein diacetate (DCF) in Fig. 8D: WT: 13.9 ± 1.0 A.U.; BACHD: 65.3 ± 4.5 A.U.; MitoSOX in Fig. 8E: WT: 21.3 ± 0.9 A.U.; BACHD: 26.3 ± 1.2 A.U.; mean $\pm$ SEM].

Discussion

We investigated the electrical function of middle-aged BACHD mouse hearts as well as excitability, contractility, and Ca^{2+} handling aspects of the freshly isolated ventricular cardiomyocytes from these mice. In this study, we revealed that the mouse model of HD presents electrocardiographic abnormalities (e.g. QT interval prolongation and ST-segment elevation). These ECG parameters are indicative of a delay in ventricular repolarization and ventricular overload that may be caused by hypoxia, myocardial infarction, or oxidative stress [18]. Our results are in accordance with the study of Schroeder *et al.* [13], which showed ST-segment range and elevation in BACHD mice, despite the fact that they used a different background (C57BL6/J). Importantly, many drugs prescribed to

Fig. 4. Huntington's disease transgenic (BACHD) mice showed alterations in the intracellular calcium handling of ventricular cardiomyocytes. (A) Representative images of calcium transients from WT and BACHD mice observed by confocal microscopy. Calcium waves in BACHD cells are indicated by the arrows. (B) Bar graph showing a significant increase in the number of calcium waves in BACHD cells ($P = 0.004$). (C) Bar graph showing no alterations in calcium transient amplitude (F, fluorescence; F_0, basal fluorescence) ($P = 0.31$). (D) Bar graph showing a significant decrease in the decay rate in BACHD cells ($P = 0.01$). Analyses involved $n = 50$ and $n = 69$ cells from four different WT and BACHD animals, respectively. *$P < 0.05$ compared with WT, Student's t test. Data are expressed as mean $\pm$ SEM.
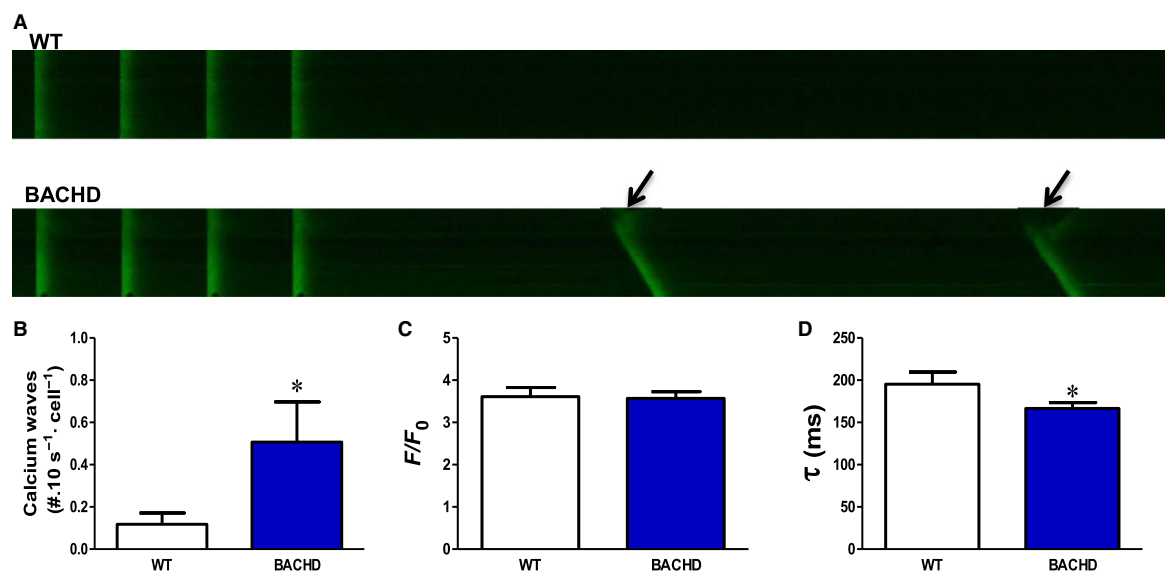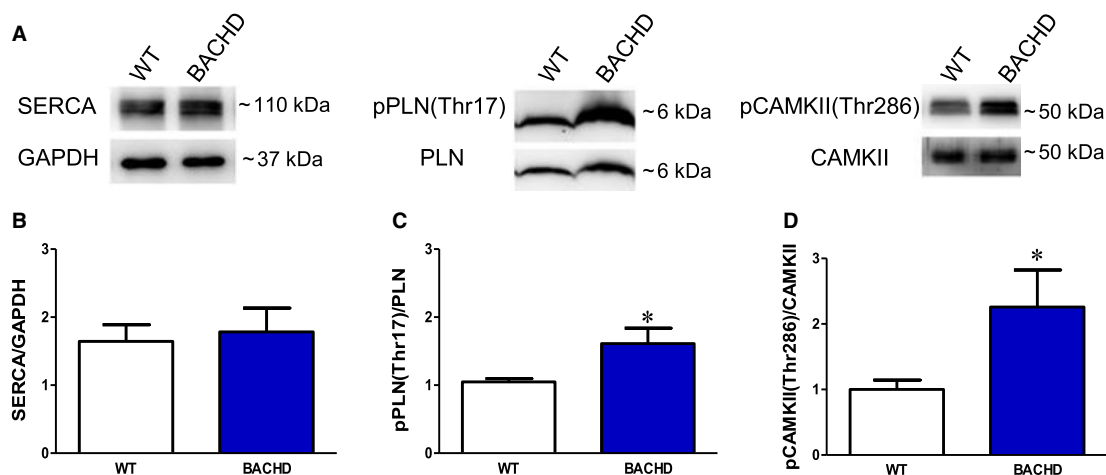

Fig. 5. Huntington's disease transgenic (BACHD) mice showed alterations in key proteins involved in excitation–contraction coupling in ventricular myocardium. (A) Representative western blotting of SERCA, pPLNThr17/PLN, and pCaMKIIThr286/CaMKII immunodetection of ventricular myocardium samples obtained from WT and BACHD mice. (B) Bar graph showing no alterations in SERCA expression ($P = 0.30$). (C) Bar graph showing a significant increase in the expression of pPLNThr17/PLN in BACHD ventricular myocardium ($P = 0.04$). (D) Bar graph showing a significant increase in the expression of pCaMKIIThr286/CaMKII expression in BACHD hearts ($P = 0.03$). The analyses involved eight animals per group. *$P < 0.05$ compared with WT, Student's t test. Data are expressed as mean $\pm$ SEM.

HD patients to treat some symptoms, but not to modify the disease progression (e.g. thioridazine or haloperidol for psychosis), have a well-recognized potential to induce QT prolongation as a side effect [19]. Delayed ventricular repolarization is associated with the development of severe arrhythmias [20], prominently ventricular tachycardia such as torsades de pointes. The association of these drugs with prolonged QT interval might increase the patient's risk of developing severe electrical disturbances and/or sudden
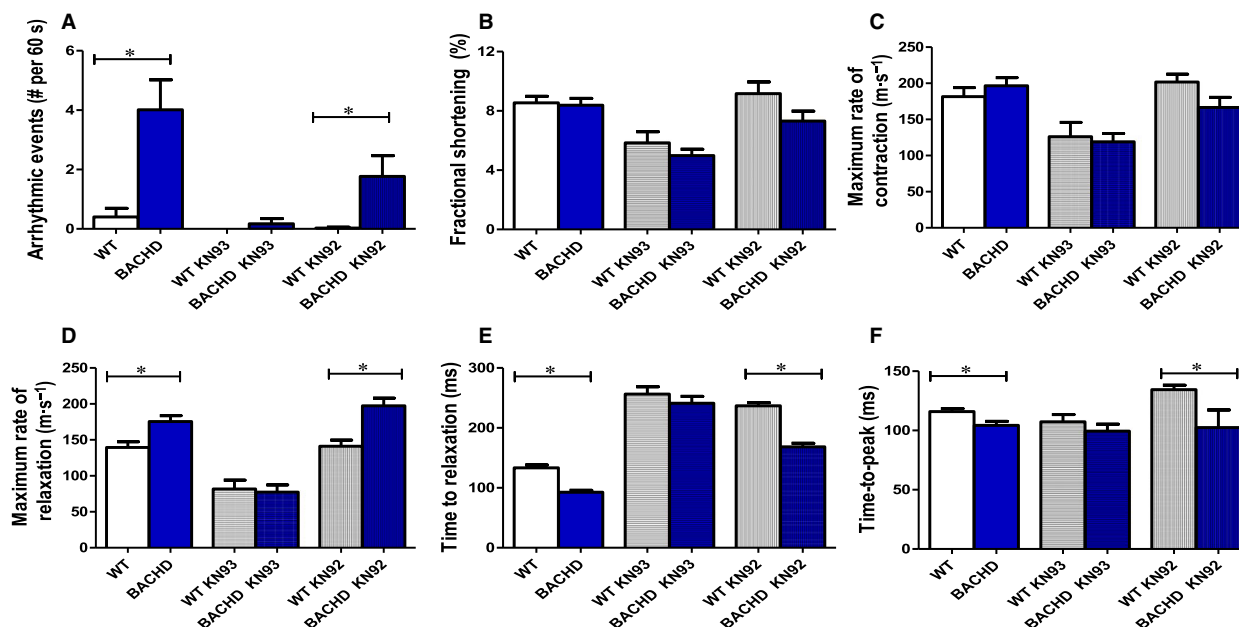
Fig. 6. Mechanical changes in the cardiomyocytes of Huntington's disease transgenic (BACHD) mice are mediated by CaMKII activity. (A) Bar graph showing inhibition of arrhythmic events after incubation of BACHD mouse cardiomyocytes with KN93. (B) Bar graph showing no alterations in fractional shortening after incubation of cardiomyocytes with KN93. (C) Bar graph showing no alterations in the maximum rate of contraction after incubation of cardiomyocytes with KN93. (D) Bar graph showing an increased relaxation in BACHD mouse cardiomyocytes that were not treated with KN93 and the absence of alterations in the cardiomyocytes treated with KN93 in comparison with the respective WT controls. (E,F) Bar graphs showing decreased time to relaxation (E) and time-to-peak (F) in BACHD mouse cardiomyocytes that were not treated with KN93, and the absence of alterations in BACHD mouse cardiomyocytes treated with KN93 in comparison with the respective WT controls. KN92 is an inactive analog and it was used to control for off-target effects of KN93. The same differences between WT and BACHD were also observed when comparing WT KN92 and BACHD KN92 groups. $*P < 0.05$ BACHD, BACHD KN93 and BACHD KN92 groups compared with the respective WT controls. Analyses involved WT $n = 57$, BACHD $n = 70$, WT KN93 $n = 38$, BACHD KN93 $n = 46$, WT KN92 $n = 34$ and BACHD KN92 $n = 30$, cells from four different WT and BACHD animals. One-way ANOVA followed by Newman–Keuls test. Data are expressed as mean $\pm$ SEM.

cardiac death. Interestingly, apart from the above observations, we did not detect abnormalities in the conduction of atrial cardiac impulses and ventricular depolarization.

Following the *in vivo* ECG observations, we evaluated the excitation–contraction properties of the ventricular cardiomyocytes. The AP repolarization phase of the BACHD cardiomyocytes was delayed, in accordance with the observed prolonged QT interval. Furthermore, BACHD cardiomyocytes showed AP duration alternans, which is a risk factor for the development of different types of arrhythmic events [21,22] that can lead to several ventricular arrhythmias and atrial fibrillation [23]. It is possible that the prolongation of AP favors re-entry phenomena that allow repetitively excitable circuits [23]. It is important to highlight that triggered arrhythmias and re-entrant mechanisms likely co-exist, especially in structurally diseased heart tissue. We suggest that, in BACHD cardiomyocytes, prolonged AP together with the increased AP duration alternans provides a favorable substrate for severe arrhythmias, which in turn might contribute to an impaired heart function and finally heart failure [22], known to occur in HD patients [8].

The increase in AP duration alternans led us to investigate the intracellular calcium dynamics because calcium affects the maintenance of excitability and contraction in cardiomyocytes [22]. The BACHD cells presented a higher number of Ca^{2+} waves than those of WT mice, suggesting an increased leak of calcium from ryanodine receptors. Increase in the calcium leak promotes the calcium-dependent depolarization of cardiomyocyte membranes through Na^+/Ca^{2+} exchanger activity, a process that may account for the prolonged AP and could also determine the appearance of the early depolarization events [24,25] corroborating the increased arrhythmia discussed above. Indeed, increased arrhythmic contractions that appear independent of triggered stimulation were detected by the edge detection assay tracking cell contraction, further strengthening this idea.
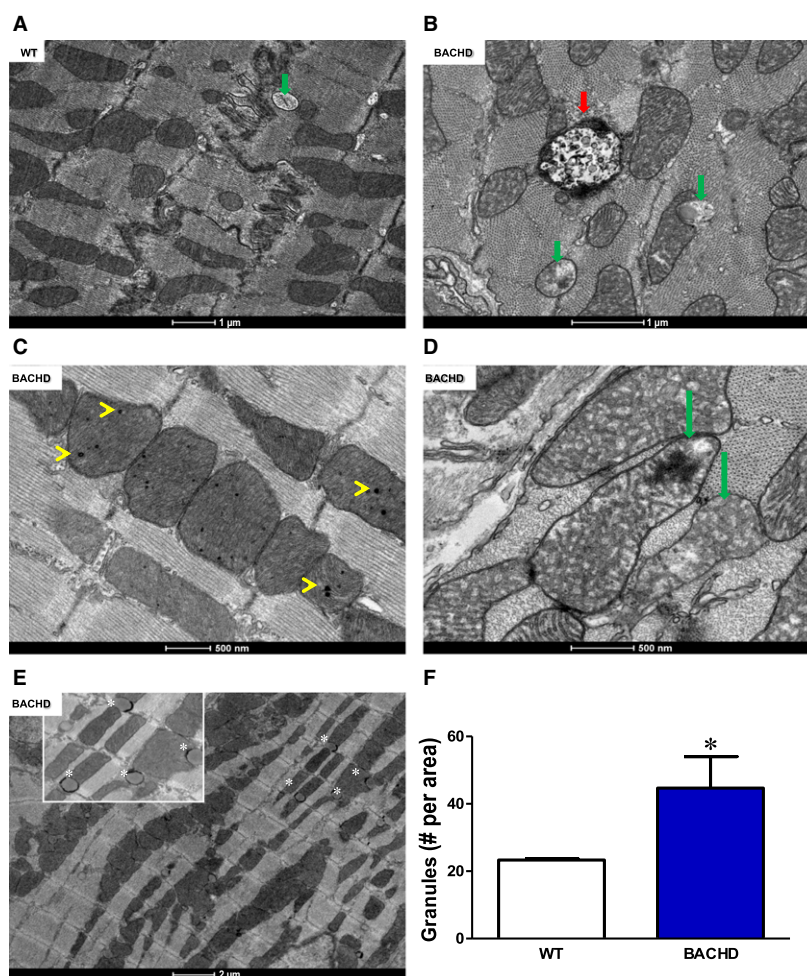
Fig. 7. Ventricular myocardium of Huntington's disease transgenic (BACHD) mice show pronounced mitochondrial ultrastructural abnormalities. (A) Representative electron micrograph of ventricular myocardium of WT mice. (B–E) Representative electron micrographs of ventricular myocardium of BACHD mice revealing ultrastructural abnormalities: severe mitochondrial damage presented by altered or absent cristae (green arrows); presence of lipofuscin granules (red arrows); intramitochondrial granules (yellow arrowheads) and lipid bodies (white asterisks and shown in inset). (F) Bar graph showing a significant increase in number of lipofuscin granules in the ventricular myocardium of BACHD mice ($P = 0.03$). Thirty images obtained from three animals per group were analyzed. $*P < 0.05$ compared with WT, Student's *t* test. Data are expressed as mean $\pm$ SEM.

Despite the strong evidence of increased calcium leak from RyRs, the calcium transient amplitude remained unaltered in accordance with the unchanged cellular fractional shortening. At first glance, such a finding may appear controversial since a reduction in calcium, in response to the increase in calcium leak, impairs the balance between calcium influx and uptake from the sarcoplasmic reticulum (SR) [20,26]. However, we also observed a decrease in the calcium transient decay rate and an increase in the relaxation speed, suggesting a rise of SERCA activity [27] that could compensate for the proposed increase in the calcium leak. Corroborating this assumption, we found a significant increase in PLN^{Thr17} phosphorylation. It is

known that phosphorylation of PLN by protein kinase A and/or CaMKII (in addition to other kinases) progressively removes its ability to inhibit SERCA activity [27]. This finding may determine an increase in SERCA activity, increasing transport of Ca^{2+} to the SR interior, which may reflect an increase in the relaxation rate and calcium reuptake by the SR. In agreement with the aforementioned data, we also observed a rise in the levels of CaMKII protein, determining the increased phosphorylation at the Thr^{17} site of PLN.

CaMKII is a calcium and calmodulin-regulated enzyme and multifunctional serine/threonine protein kinase with widespread expression in the muscle, nervous and immune tissues [27,28]. However, post-
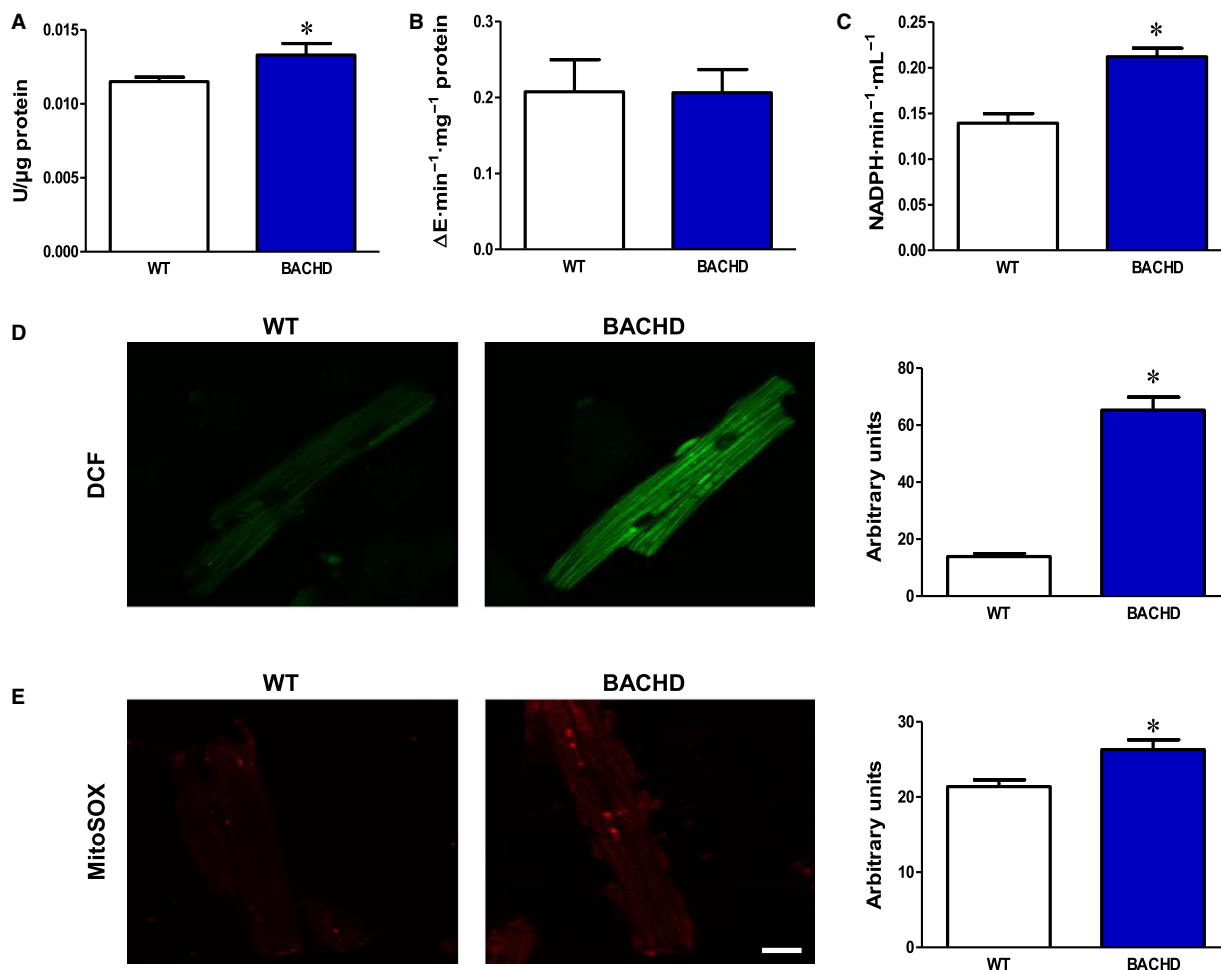
Fig. 8. Ventricular myocardium of Huntington's disease transgenic (BACHD) mice shows changes in antioxidant systems and oxidative stress. (A) Bar graph showing significant increase in SOD activity in BACHD myocardium ($P = 0.01$). (B) Bar graph showing no alterations in CAT activity in both groups ($P = 0.50$). (C) Bar graph showing significant increase in GPx activity in BACHD mouse myocardium ($P = 0.001$). The analyses involved 10 animals per group. (D) Representative cardiomyocytes from WT and BACHD mice, and bar graph showing an increase in DCF labelling ($P < 0.0001$). (E) Representative cardiomyocytes from WT and BACHD mice, and bar graph showing an increase in MitoSOX labelling ($P = 0.001$). DCF, $n = 106$ and $n = 120$ cells, and MitoSOX, $n = 101$ and $n = 103$ cells from three WT animals and three BACHD animals, respectively. Scale bar: 25 μm. *$P < 0.05$ compared with WT, Student's *t* test. Data are expressed as mean ± SEM.

translational modifications can convert CaMKII to a calcium and calmodulin-independent enzyme involved in some cardiovascular disease, including during arrhythmogenic episodes [27]. CaMKII can be super-activated under pathological conditions including acidosis, ischemia, and oxidative stress [28,29]. Moreover, this enzyme mediates arrhythmias in chronic diseases such as during heart failure and in genetic syndromes such as long-QT syndrome [29]. To confirm the involvement of CaMKII in the deleterious effects observed in the function of the BACHD cardiomyocytes, we incubated these cells with KN93, a direct inhibitor of CaMKII [30]. Strikingly, KN93 abolished arrhythmic contractions and restored the rate of

relaxation, time to relaxation, and time to peak to the levels observed in WT KN93-treated cells. It is noteworthy that KN93 promoted a slight reduction in the cell fractional shortening in the cardiomyocytes of WT and BACHD mice, indicating that CaMKII is an important modulator of cellular electro-mechanical properties, in accordance with previous findings [28,29]. We also used the inactive analog KN92 to control for off-target effects of KN93. The same differences between WT and BACHD were also observed when comparing WT KN92 and BACHD KN92 groups, corroborating the KN93 action. As suggested by Mustroph *et al.* [29], strategies aiming to alter CaMKII expression and/or activity could be a new

approach to prevent arrhythmias as well as systolic and diastolic ventricular dysfunctions.

Under oxidative conditions, high ROS can enhance the CaMKII activity by direct or indirect pathways [28]. We investigated the oxidative damage status (associated with ROS) of BACHD myocardium. Based on a qualitative analysis of mitochondria in the ventricular myocardium, mitochondria were degraded in the BACHD group. It is well known that mitochondrial changes and lipofuscin accumulation are important features of aging in non-mitotic cells [31,32], such as neurons and cardiomyocytes. Terman *et al.* [32] showed a positive correlation between the intracellular lipofuscin content and both mitochondrial damage and production of ROS. Thus, considering that mitochondria are significant sources of ROS production and that enhanced lipofuscinogenesis is strongly related to oxidative enzymatic activity, we investigated how some key components of the cellular antioxidant system were operating in HD.

The differences in the oxidative status of the cardiac cells were examined by evaluating the antioxidant defense system through SOD, CAT, and GPx activities. Normally, SOD activity is the first line of defense against the superoxide anion O_2^- leading to the release of H_2O_2 and O_2. Another component responsible for decreasing the H_2O_2 production as well as for reducing the oxidized proteins is CAT. The increase in SOD and GPx activities, in association with the ultrastructural changes seen in the mitochondria, strongly indicates that oxidative disturbances are taking place in the cardiac tissue of the BACHD mice. In fact, oxidative stress in nervous tissue has a critical role in the pathogenesis of HD [8,33,34]. Importantly, using a direct assessment, we confirmed the oxidative stress in HD cardiomyocytes.

In conclusion, in this study, we demonstrated that elderly BACHD mice present abnormalities in cardiac repolarization as observed in the ECG profile, which translate into a prolonged duration of AP with enhanced AP duration alternans in isolated ventricular myocytes. The isolated cardiomyocytes further exhibit arrhythmic contraction and relaxation disturbances that are in accordance with the calcium handling imbalances, such as the increase in the number of calcium waves and Ca^{2+} reuptake, associated with SERCA activity and modulated by phosphorylated PLN. These effects can be explained by the heightened CaMKII expression and stimulation, as a consequence of oxidative stress, evidence that is supported by mitochondrial ultrastructural disorganization associated with the increase in the cellular antioxidant axis function and with the direct analyses of general oxidative stress and mitochondrial superoxide anion production indicators.

Although HD is a neurodegenerative condition, patients die primarily due to pulmonary complications followed by impairment of cardiovascular function [9]. Therefore, research into HD-associated cardiac dysfunctions and the mechanisms associated with them are relevant to a better understanding of HD pathophysiology. Most studies on HD have focused on the changes incurred in the nervous system. HD has a known genetic cause, a mutation in the *Htt* gene, and the BACHD mouse is an excellent model for neurodegenerative research. The findings presented herein may also be important to researchers interested in the cardiac aspects of others neurodegenerative disorders.

Materials and methods

Animals

FVB/NJ (WT) and FVB/N-Tg (HTT*97Q)IXwy/J (BACHD) transgenic mice were purchased from The Jackson Laboratory (Bar Harbor, ME, USA) and used to establish a new colony. For this study, we used 12-month-old wild-type (WT) and BACHD mice, when the HD-related phenotypes were shown to be more developed [14]. The animals were housed in a room with controlled humidity, temperature (23 ± 2 °C), and a 12-h light–dark cycle with free access to food and water. The experimental procedures were approved by the animal welfare committee of the Universidade Federal de Minas Gerais (CEUA-UFMG 25/2015).

In vivo procedures

The *in vivo* heart electrical impulse conduction was analyzed by ECG. A six-channel non-invasive electrocardiograph (ECG-PC version 2.07; TEB, São Paulo, Brazil) was used. WT ($n = 10$) and BACHD ($n = 15$) animals were anesthetized with 1.5–2.0% isoflurane inhalation (VetCase, Brasmed, Brazil) and recordings made at 50 mm·s^{-1} and 2 N. Data analysis of heart rate, segments, and intervals was conducted in lead II (DII).

Isolated ventricular cardiomyocytes

For *in vitro* analyses, ventricular cardiomyocytes from the mice ($n = 4$ mice per group) were isolated as previously described [35]. The animals were euthanized after heparinization (heparin 50 U, i.p.). Then, the heart was quickly dissected out and cannulated in a home-made constant-pressure Langendorff system through the aortic trunk. CIB nurturing solution (in mM: 30 NaCl; 5.4 KCl; 0.5 $MgCl_2$; 0.33 NaH_2PO_4; 25 HEPES; and 22 glucose) was perfused through the coronary system followed by the perfusion of an enzyme mix added to CIB in an increasing calcium concentration gradient. Then, freshly isolated cells were centrifuged, and

the resulting pellet was re-suspended in Tyrode's solution (in mM: 140 NaCl; 5.4 KCl; 0.5 MgCl$_2$; 0.33 NaH$_2$PO$_4$; 1.8 CaCl$_2$; 5 glucose; and 11 HEPES). The isolated ventricular cardiomyocytes were used for electrophysiology, cell contraction assay, and confocal microscopy.

Electrophysiology

Electrophysiological recordings of the cardiomyocyte AP were obtained using an EPC9.2 patch-clamp amplifier (HEKA, Harvard Bioscience, Inc., Holliston, MA, USA) in whole-cell current-clamp mode. The APs of 22 WT and 27 BACHD cardiomyocytes were recorded. After establishing this configuration, the cells were maintained at rest for 3 min for the pipette solution to equilibrate with the intracellular environment. Glass pipettes with tip resistances varying between 1 and 2 MΩ were used. The APs in the isolated ventricular cells were measured by applying a 1000 pA pulse lasting 2–4 ms with 1 Hz frequency.

Cell contractility assay

For the analyses of the cellular arrhythmias and contraction, the ventricular cardiomyocytes obtained from the WT ($n = 50$) and BACHD ($n = 53$) mice were placed on a coverslip coupled to a chamber containing a pair of parallel electrodes and stimulated electrically using 60 V biphasic pulses at 1 Hz for 4 ms [36]. Throughout these experiments, the cells were kept in Tyrode's solution at room temperature (25–30 °C). The cells were monitored through an MCS100 CCD camera (IonOptix, Milton, MA, USA), and the acquired images were used to measure cell shortening (contractility index) in response to the electrical stimulus using an edge detector video system. The images were obtained using an acquisition frequency of 240 Hz. Cell shortening was calculated based on the output obtained from the edge detection converter system IonWizard A/D. In some experiments (in another group of animals), we pretreated the cells with KN93 or KN92 (10 μmol·L^{-1}; Sigma-Aldrich, St Louis, MO, USA) for 20 min without light.

Confocal microscopy

The alterations in the calcium handling were investigated by confocal microscopy using a Zeiss confocal microscope LSM 510 system (Zeiss, Jena, Germany). For these experiments, the cells were labeled with 5 μM Fluo4-AM for 30 min at 25 °C under gentle agitation. The labeled cells were excited with 60 V biphasic pulses at 1 Hz frequency for 4 ms. The scan line (set at 512 pixels) was positioned along the longitudinal axis to avoid nuclear regions. The spatial resolution ranged from 0.1 to 0.3 μm·pixel^{-1}, and the temporal resolution used was 1.92 ms per line. The changes in fluorescence (F) were normalized with the baseline fluorescence (F_0). The

data were recorded and analyzed using the software IMAGE-J (NIH, National Institutes of Health, Bethesda, MD, USA). Ca^{2+} transient amplitudes were taken as the mean between three transient recordings after a train of 10 pulses intended to load the SR. The calcium waves were analyzed by counting the number of waves during the 10 s after the acquisition of calcium transients, maintaining the cell at rest [36].

Western blot analyses

We used western blotting to analyze the protein expression. To this end, the left ventricles from the WT and BACHD mice ($n = 8$ animals per group) were homogenized in ice-cold lysis buffer (in mM: 100 NaCl, 50 Trizma base, 5 Na$_2$-EDTA, 50 Na$_4$P$_2$O$_7$.10 H$_2$O; and 1 MgCl$_2$; pH 8.0) containing 0.3% Triton X-100, 1% NP-40, 0.5% sodium deoxycholate, and enriched with a cocktail of protease and phosphatase inhibitors. Next, 40–60 μg of protein was separated by SDS/PAGE followed by electronic transfer onto a PVDF membrane (Millipore, Darmstadt, Germany). The membranes were incubated with the following primary antibodies: anti-sarco/endoplasmic reticulum Ca^{2+}-ATPase (SERCA) (1 : 2500; Santa Cruz Biotechnology, Dallas, TX, USA), anti-PLN (Abcam, Cambridge, UK, 1 : 1500), anti-p-phospholamban-Thr^{17} (1 : 2500; Santa Cruz Biotechnology), anti-CaMKII (1 : 500; Santa Cruz Biotechnology), anti-pCaMKII Thr^{286} (1 : 500; Santa Cruz Biotechnology) and anti-glyceraldehyde 3-phosphate dehydrogenase (GAPDH) (1 : 3000; Santa Cruz Biotechnology). The immunodetection was carried out using enhanced chemiluminescence (GE Healthcare, Chicago, IL, USA) followed by densitometric analyzes with the software IMAGEQUANTTL (GE Healthcare). The protein levels were expressed as a ratio of the optical densities. GAPDH was used as a control for any variations in the protein loading.

Transmission electron microscopy

For qualitative ultrastructural analyses, the mice were anesthetized and transcardially perfused with sodium phosphate buffer (PB) and Karnovsky fixative solution. Next, the hearts from three animals from the WT and BACHD groups were removed, and the left ventricles were separated. The samples were washed with cacodylate buffer (0.1 M), post-fixed in reduced osmium (1% osmium tetroxide containing 1.6% potassium ferrocyanide), contrasted *en bloc* with uranyl acetate (2% uranyl acetate in deionized water), dehydrated through an ascending series of ethanol solutions, and embedded in EPON. Serial ultrathin sections were collected on 200- or 300-mesh copper grids and contrasted with lead citrate. The sections were viewed with a Tecnai-G2-Spirit FEI/Quanta electron microscope (120 kV; Philips, FEI Company, Hillsboro, OR, USA) maintained at the Microscopy Center – UFMG.

Antioxidant enzyme assays

For the antioxidant enzyme assays, the left ventricle samples obtained from the WT and BACHD mice ($n = 10$ animals per group) were weighed and homogenized (Euro Turrax T20b; IKA LABORTECHNIK, Wilmington, NC, USA) on ice in 0.2 g·mL^{-1} of PB at pH 7.2. The homogenates were centrifuged for 15 min at 10 000 g, and the supernatant was used to quantify the SOD and CAT activities. The left ventricle samples were homogenized in ice-cold Tris/HCl buffer (50 mM, pH 7.5, containing 5 mM EDTA) and centrifuged at 4 °C (10 000 g) for 20 min to measure the GPx activity. The protein concentration was determined using bovine serum albumin as the standard. Then, the following procedures were performed.

Superoxide dismutase activity

Superoxide dismutase activity was determined by measuring the inhibition of pyrogallol autoxidation, where 1 U = 50% pyrogallol inhibition autoxidation [37]. To this end, after the homogenization, the supernatant was collected and combined with PB containing 1.25 mM MTT and 100 mM pyrogallol at pH 7.2. After 5 min of incubation, the reaction was quenched by the addition of DMSO, and the reading was carried out at 570 nm.

Catalase activity

Catalase activity was determined by the decomposition of H_2O_2 following absorbance at 240 nm and expressed as millimoles of H_2O_2 decomposed per minute per milligram of protein ($\Delta E \cdot min^{-1} \cdot mg^{-1}$ protein). To this end, 0.05 mL homogenate supernatant was added to 50 mM PB (2 mL, pH 7.0, 25 °C). The reaction was started by adding H_2O_2 (6 mM) and allowed to proceed for 1 min at room temperature.

Glutathione peroxidase activity

The supernatant (4 μL) was added to 0.2 mL of PB (100 mM, pH7.5), with 2 mM reduced glutathione, 0.1 U·mL^{-1} glutathione reductase, 0.12 mM NADPH, 2 mM H_2O_2, and 1 mM sodium azide. The GPx activity was measured at 340 nm and expressed in nmol NADPH·min^{-1}·mL^{-1}.

Assessment of oxidative stress

For a direct assessment of oxidative stress in cardiac myocytes, confocal imaging was performed using a Zeiss LSM 880 at Center for Acquisition and Image Processing (CAPI, Federal University of Minas Gerais, Brazil). Freshly isolated cardiomyocytes were loaded with (a) DCF, a general oxidative stress indicator (2 μM, incubated for 20 min at room temperature), and (b) MitoSOX, an indicator of mitochondrial superoxide anion production (5 μM, incubated 150 g for 30 s) and bathed in Tyrode solution. The optical slice was set to 2 μm in all recorded images. Fluorescence was quantified on digitized pictures as the average of pixels of single focused cells (DCF, $n = 106$ and $n = 120$ cells, and MitoSOX, $n = 101$ and $n = 103$ cells from three WT and three BACHD animals, respectively). Fluorescence measurements are presented as the subtraction between cell fluorescence, excluding nuclei, and background fluorescence.

Statistical analysis

Data are expressed as mean ± standard error of mean (SEM). After the normality tests, the data were analyzed using Student's t test for comparing two groups and one-way ANOVA followed by the Newman–Keuls test for comparing more than two groups. All analyses were performed using PRISM 6 (GraphPad Software, La Jolla, CA, USA). The significance level was set to 5% ($P < 0.05$).

Conflict of interest

All authors declare no conflict of interest.

Author contributions

JVJ-S, AS-M, AFMB, ICGJ, JNA, TOB, MPSM-G, and PACV participated in acquisition, analysis, or interpretation of data for the work; and wrote the paper. JSC, MMM, SG, and CG participated in conception or design of the work; and drafting the work or revising it critically for important intellectual content.

References

1 Xuereb JH, MacMillan JC, Snell R, Davies P & Harper PS (1996) Neuropathological diagnosis and CAG repeat expansion in Huntington's disease. *J Neurol Neurosurg Psychiatry* **60**, 78–81.
2 Jones L & Hughes A (2011) Pathogenic mechanisms in Huntington's disease. *Int Rev Neurobiol* **98**, 373–418.

3 Yu S, Mulley J, Loesch D, Turner G, Donnelly A, Gedeon A, Hillen D, Kremer E, Lynch M, Pritchard M *et al.* (1993) A novel gene containing a trinucleotide repeat that is expanded and unstable on Huntington's disease chromosomes. *Cell* **72**, 971–983.

4 Moffitt H, McPhail GD, Woodman B, Hobbs C & Bates GP (2009) Formation of polyglutamine inclusions in a wide range of non-CNS tissues in the HdhQ150 knock-in mouse model of Huntington's disease. *PLoS One* **4**, e8025.

5 Ross AC & Tabrizi SJ (2011) Huntington's disease: from molecular pathogenesis to clinical treatment. *Lancet* **10**, 83–98.

6 Bano D, Zanetti F, Mende Y & Nicotera P (2011) Neurodegenerative processes in Huntington's disease. *Cell Death Dis* **2**, e228.

7 Squitieri F, Falleni A, Cannella M, Orobello S, Fulceri F, Lenzi P & Fornai F (2010) Abnormal morphology of peripheral cell tissues from patients with Huntington disease. *J Neural Transm* **117**, 77–83.

8 van der Burg JM, Björkqvist M & Brundin P (2009) Beyond the brain: widespread pathology in Huntington's disease. *Lancet Neurol* **8**, 765–774.

9 Sorensen SA & Fenger K (1992) Causes of death in patients with Huntington's disease and in unaffected first degree relatives. *J Med Genet* **29**, 911–914.

10 Pattison JS, Sanbe A, Maloyan A, Osinska H, Klevitsky R & Robbins J (2008) Cardiomyocyte expression of a polyglutamine pre-amyloid oligomer causes heart failure. *Circulation* **117**, 2743–2751.

11 Melkani GC, Trujillo AS, Ramos R, Bodmer R, Bernstein SI & Ocorr K (2013) Huntington's disease induced cardiac amyloidosis is reversed by modulating protein folding and oxidative stress pathways in the *Drosophila* heart. *PLoS Genet* **9**, e1004024.

12 Child D, Lee J, Pascua C, Chen Y, Mas Monteys A & Davidson B (2018) Cardiac mTORC1 dysregulation impacts stress adaptation and survival in Huntington's disease. *Cell Rep* **23**, 1020–1033.

13 Schroeder AM, Wang HB, Park S, Jordan MC, Gao F, Coppola G, Fishbein MC, Roos KP, Ghiani CA & Colwell CS (2016) Cardiac dysfunction in the BACHD mouse model of Huntington's disease. *PLoS One* **11**, 1–25.

14 Gray M, Shirasaki DI, Cepeda C, Andre VM, Wilburn B, Lu XH, Tao J, Yamazaki I, Li SH, Sun YE *et al.* (2008) Full-length human mutant huntingtin with a stable polyglutamine repeat can elicit progressive and selective neuropathogenesis in BACHD mice. *J Neurosci* **28**, 6182–6195.

15 Zhang P (2017) CaMKII: the molecular villain that aggravates cardiovascular disease (review). *Exp Ther Med* **13**, 815–820.

16 Hund T & Mohler P (2015) Role of CaMKII in cardiac arrhythmias. *Trends Cardiovasc Med* **25**, 392–397.

17 Gilissen EP & Staneva-dobrovski L (2013) Distinct types of lipofuscin pigment in the hippocampus and cerebellum of aged cheirogaleid primates. *Anat Rec* **296**, 1895–1906.

18 Konopelski P & Ufnal M (2016) Electrocardiography in rats: a comparison to human. *Physiol Res* **65**, 717–725.

19 Cubeddu LX (2003) QT prolongation and fatal arrhythmias: a review of clinical implications and effects of drugs. *Am J Ther* **10**, 452–457.

20 Bers DM (2002) Cardiac excitation–contraction coupling. *Nature* **415**, 198–205.

21 Pogwizd SM & Bers DM (2002) Calcium cycling in heart failure: the arrhythmia connection. *J Cardiovasc Electrophysiol* **13**, 88–91.

22 Bers DM & Guo T (2005) Calcium signaling in cardiac ventricular myocytes. *Ann N Y Acad Sci* **1047**, 86–98.

23 Franz MR, Jamal SM & Narayan SM (2012) The role of action potential alternans in the initiation of atrial fibrillation in humans: a review and future directions. *Europace* **14**, 58–64.

24 Zhao Z, Wen H, Fefelova N, Allen C, Baba A, Matsuda T & Xie L-H (2012) Revisiting the ionic mechanisms of early afterdepolarizations in cardiomyocytes: predominant by Ca waves or Ca currents?. *Am J Physiol Heart Circ Physiol* **302**, H1636–H1644.

25 Venetucci LA, Trafford AW, O'Neill SC & Eisner DA (2008) The sarcoplasmic reticulum and arrhythmogenic calcium release. *Cardiovasc Res* **77**, 285–292.

26 Eisner DA, Kashimura T, O'Neill SC, Venetucci LA & Trafford AW (2009) What role does modulation of the ryanodine receptor play in cardiac inotropy and arrhythmogenesis? *J Mol Cell Cardiol* **46**, 474–481.

27 Mattiazzi A & Kranias EG (2014) The role of CaMKII regulation of phospholamban activity in heart disease. *Front Pharmacol* **5**, 1–11.

28 Rokita AG & Anderson ME (2012) New therapeutic targets in cardiology: arrhythmias and CaMKII. *Circulation* **126**, 2125–2139.

29 Mustroph J, Neef S & Maier LS (2016) CaMKII as a target for arrhythmia suppression. *Pharmacol Ther* **176**, 22–31.

30 Hegyi B, Chen-Izu Y, Jian Z, Shimkunas R, Izu LT & Banyasz T (2015) KN-93 inhibits IKr in mammalian cardiomyocytes. *J Mol Cell Cardiol* **89**, 173–176.

31 Brunk UT & Terman A (2002) The mitochondrial-lysosomal axis theory of aging accumulation of damaged mitochondria as a result of imperfect autophagocytosis. *Eur J Biochem* **269**, 1996–2002.

32 Terman A, Dalen H, Eaton JW, Neuzil J & Brunk UT (2004) Aging of cardiac myocytes in culture: oxidative stress, lipofuscin accumulation, and mitochondrial turnover. *Ann N Y Acad Sci* **1019**, 70–77.

33 Johri A & Beal MF (2012) Antioxidants in Huntington's disease. *Biochim Biophys Acta* **1822**, 664–674.

34 Quintanilla RA & Johnson GVW (2009) Role of mitochondrial dysfunction in the pathogenesis of Huntington's disease. *Brain Res Bull* **80**, 242–247.

35 Shioya T (2007) A simple technique for isolating healthy heart cells from mouse models. *J Physiol Sci* **57**, 327–335.

36 Joviano-Santos J, Santos-Miranda A, Joca H, Cruz J & Ferreira A (2016) New insights into the elucidation of angiotensin-(1-7) in vivo antiarrhythmic effects and its related cellular mechanisms. *Exp Physiol* **101**, 1506–1516.

37 Gioda CR, Barreto TDO, Prímola-gomes TN, De Lima DC, Campos PP, Aggunn S, Lauton-santos S, Vasconcelos AC, Coimbra CC, Soares V *et al.* (2013) Cardiac oxidative stress is involved in heart failure induced by thiamine deprivation in rats. *Am J Physiol Heart Circ Physiol* **298**, 2039–2045.

4.2- Contextualização do artigo 2

Como já mencionado, há uma extensa morte neuronal na DH[55]. Uma possível abordagem terapêutica para a preservação neuronal poderia ser o uso de neurotoxinas derivadas do veneno da aranha armadeira *Phoneutria nigriventer*. Tal veneno já foi purificado e suas frações estão exemplificadas na Figura 4 dessa tese. Considerando-se especificamente a fração PhTx3, sabe-se que ela contém seis isoformas de peptídeos denominadas PnTx- ou Tx-3-1 a 6[76]. Essa fração é uma das mais estudadas e caracterizadas sendo que já foram descritas diversas ações de suas isoformas nos canais iônicos acoplados à neurotransmissão[72]. Essas isoformas são consideradas uma excelente ferramenta para bloquear CCSV, levando a uma consequente diminuição na liberação de glutamato dependente de cálcio, além de reduzir o influxo de cálcio bem como a exocitose de vesículas sinápticas em sinaptossomas cerebrocorticais de ratos[77,78,80]. Recentemente, demonstrou-se o potencial neuroprotetor da fração PhTx3 na isquemia induzida em fatias de hipocampo[89]. Posteriormente, foi descrito o efeito neuroprotetor das isoformas Tx3-5 e Tx3-4 nas isquemias cerebral[90] e retiniana (tanto *in vitro*[91] como *in vivo*[92]).

A isoforma Tx3-6, denominada Phα1β, consiste em uma neurotoxina capaz de bloquear CCSV de alta voltagem, com maior especificidade para canais Tipo-N[93]. Essa toxina tem sido utilizada no controle da dor pela sua capacidade de inibição de canais de forma reversível[94], apresentando alta janela terapêutica. Já foi descrito na literatura a sua atuação na prevenção de dor neuropática[95,96], dor somática[97], dor da fibromialgia[98] e dor visceral persistente. Além disso, a utilização da Phα1β foi avaliada na injúria medular aguda em ratos tendo sido observada melhora na preservação morfológica da medula espinal com consequente recuperação funcional (dados ainda não publicados).

A utilização clínica da isoforma Phα1β nativa pode ser dificultada pela sua baixa produção a partir do veneno total da aranha[99]. De forma alternativa, essa isoforma pode ser produzida por meio de tecnologia de DNA recombinante em *Escherichia coli.* A toxina sintética recombinante (CTK 01512-2) já está disponível comercialmente e mimetizou o efeito da forma nativa em estudos experimentais[100,101].

Baseado nos dados que mostraram uma ação neuroprotetora das isotoxinas da fração PhTx3 do veneno da aranha armadeira, nós então avaliamos o potencial da isoforma Phα1β recombinante em retardar a morte neuronal possivelmente provocada por excitotoxicidade (pelo excesso de glutamato) e a melhora de parâmetros motores e comportamentais em camundongos BACHD. Esses resultados serão submetidos para publicação conforme o artigo 2.

ARTIGO 2

Phα1β, a neurotoxin from the armed spider *Phoneutria nigriventer*, prevents neuromuscular abnormalities by modulating glutamate levels and caspase activity in a murine model for Huntington's disease

Joviano-Santos, J.V.[1]; Valadão, P.A.C.[1]; Magalhães-Gomes, M.P.S.[1]; Fernandes, L.F.[2]; Diniz, D.M.[3]; Machado, T.C.G.[1]; Soares, K.B.[1]; Ladeira, M.S.[1]; Miranda, A.S.[4] Massensini, A.R.[2]; Gomez, M.V.[3]Guatimosim, C[1*].

[1]Laboratório de Biologia da Neurotransmissão, Departamento de Morfologia; [2]Núcleo de Neurociências, Departamento de Fisiologia e Biofísica, Instituto de Ciências Biológicas, Universidade Federal de Minas Gerais, Belo Horizonte, MG, Brasil; [3]IEP Santa Casa, Belo Horizonte, MG, Brasil; [4]Laboratório de Neurobiologia, Departamento de Morfologia, Instituto de Ciências Biológicas, Universidade Federal de Minas Gerais, Belo Horizonte, MG, Brasil.

*Corresponding author: Cristina Guatimosim

Associate Professor

Departamento de Morfologia, Instituto de Ciências Biológicas, Universidade Federal de Minas Gerais, Av. Antônio Carlos, 6627, Belo Horizonte, MG, Brazil

Email: cguati@icb.ufmg.br

Abstract

Abnormal calcium influx and glutamatergic excitotoxicity have been extensively associated with neuronal death in Huntington's disease (HD), a genetic neuromuscular disorder. Currently, there is no effective treatment for this fatal condition. Pharmacological approaches focusing on the spinal cord and skeletal muscles might represent a more feasible strategy than targeting neuronal function in brain. The neurotoxin Phα1β has demonstrated therapeutic effects as a calcium channel blocker, for example during pain control. However, little is known about its neuroprotective effect. Herein, we investigated Phα1β action in a 12-months old HD murine model (BACHD), and whether spinal cord neurons might represent potential therapeutic targets. We performed intrastriatal and intrathecal injections of Phα1β in WT and BACHD mice, chronically. No side effects or unusual behaviors were observed upon toxin administration. Both treatments greatly improved BACHD mice locomotor changes as revealed by Wire-hang and Open Field tests. Using NeuN labeling, we visualized that Phα1β toxin prevented neuronal cell loss in striatum, cortex and spinal cord when injected locally. The intrathecal injection of Phα1β was also able to revert muscle atrophy in BACHD mice. Finally, we observed that Phα1β might, at least in part, exert its protective effect by decreasing glutamate release, measured in liquor, and by inhibiting neuronal apoptosis as revealed by a reduction in caspase-3 expression in the spinal cord. Our data provide evidence of a novel neuroprotector effect of Phα1β, paving a path for the development of new approaches to treat HD motor symptoms beyond the brain.

Keywords

Huntington's disease; Phα1β; calcium blocker; glutamate; spinal cord; BACHD.

1- INTRODUCTION

Huntington's disease (HD) is a fatal neurodegenerative disorder caused by an expansion of a CAG nucleotides in the *Huntingtin (Htt)* gene, which results in a polyglutamine stretch in HTT protein (The Huntington's Disease Collaborative Research Group, 1993). HD pathogenesis is related to both loss of wild-type (WT) HTT function, as well as, a gain of toxicity associated with the mutant one (Bano et al., 2011), (Squitieri et al., 2010). A hallmark of HD is the insoluble aggregates formation and glutamatergic excitotoxicity, that has been extensively associated with a progressive neuronal death (Moffitt et al., 2009), (Ross and Tabrizi, 2011), (Zeron et al., 2002), (Graham et al., 2009). The neuronal death mainly occurs in the striatum region (but there is also neuron loss in cortex, thalamus, hypothalamus and, hippocampus) (Margolis and Ross, 2003). Furthermore, recently it has also been described some alterations in spinal cord, neuromuscular junctions and skeletal muscles in an important model for HD, the BACHD mice line (Valadão et al., 2017).

Since the major HD symptoms are primarily characterized by involuntary movements (i.e. rigidity, bradykinesia, dystonia, and choreatic movements) (Haddad and Cummings, 1997), analyses of other region of the nervous system (like the spinal cord) in addition to the muscles, are essential. This leads to the question of whether a primary defect in the motor units (MUs) *per se* contributes to motor deterioration, separately of

the striatal degeneration (van der Burg et al., 2009). It is noteworthy that, once the peripheral neuromuscular symptoms are characterized, one might propose a new therapeutic intervention focusing on MUs, independently of a high-risk brain intervention for patients. In fact, there are still no drugs available for specific treatment of HD (Frank, 2014). Neuroprotective drugs that preserve neuronal function emerge as ideal candidates for the disease-modifying progress, rather than simply treating symptoms already installed. In this context, it is of great relevance to test new neuroprotective agents that could minimize neuronal loss. Given that the glutamate-excitotoxicity process is most related with neuronal injury in HD (Simms and Zamponi, 2014), a novel interesting approach could be the use of animal toxins against to this phenomenon and consequently, lessen the neurodegeneration.

Many studies strongly suggest that toxins present in the venom of the South America armed spider *Phoneutria nigriventer* have a broad spectrum of action (Gomez et al., 2002). Such venom was purified generating four distinct neurotoxic fractions (namely PhTx1, PhTx2, PhTx3, PhTx4) (Rezende Júnior et al., 1991). Each one of these fractions is constituted by different peptides with several pharmacological actions. For example, PhTx3-3 and PhTx3-4 (isoforms from the PhTx3 fraction), have a therapeutic potential for managing neurodegenerative retinopathies reducing the glutamate release and excitotoxic events *in vitro* (Agostini et al., 2011) and *in vivo* (Binda et al., 2016). Also, within the PhTx3 fraction, there is the PhTx3-6 isoform, namely as Phα1β, which is capable of blocking the voltage-gating calcium channels (VGCCs), with high specificity for the N-type (Vieira et al., 2005). Data from literature have shown that this toxin has been used for pain control, like in neuropathic, somatic and/or persistent visceral types of

pain (de Souza et al., 2011), (Rigo et al., 2013), (Rosa et al., 2014), (Diniz et al., 2014). Despite the N-type channels blocking property and reduction in neuronal calcium influx, little is known about the Phα1β isoform effect on glutamate-induced excitotoxicity in neurodegenerative conditions, such as in HD.

In this present investigation, we set out to determine if Phα1β is effective in inhibiting neuronal cell death in a mouse model for HD, and whether spinal cord neurons might represent potential therapeutic targets. To this end, we tested two types of treatment routes directly in striatum or in the spinal cord, and then performed behavior along with morphofunctional analyses. This is the first report of Phα1β isoform neuroprotective effect, with a local site of action. Our treatments provided preservation in neurons from the spinal cord and in muscles structure, beyond to a reduction in glutamate release and caspase-3 activity, which may help to contribute to new approaches to treat HD motor symptoms beyond the brain.

2- MATERIALS AND METHODS

2.1- Animals

We used 12-month old wild-type (WT) and BACHD mice [FVB/NJ and FVB/N-Tg (HTT*97Q)IXwy/J, Jackson Laboratory (Bar Harbor, ME, USA)]. This age was chosen due to the HD-related phenotypes being more pronounced (Gray et al., 2008). All animals were housed in a facility with controlled humidity, temperature, and a 12-h light-dark cycle with food and water *ad libitum*. All experimental procedures were approved by our animal ethics committee (CEUA-UFMG 25/2015).

2.2- Surgical procedures

Animals were divided into four experimental groups: WT (saline), WT (toxin), BACHD (saline) and BACHD (toxin). The recombinant version of Phα1β was synthesized and was expressed in *E. coli.* (CTK 01512-2, Giotto Biotech S.r.l., Florence, Italy). It was purified through a proprietary production process, with a mixture of ion exchange and size exclusion chromatography (Wormwood et al., 2018). Then, the lyophilized recombinant Phα1β isoform was diluted in sterile saline (100 pmol/site). The toxin dose used was based on previous dose-responses findings from literature (Diniz et al., 2014), (Rigo et al., 2017). To note, it was already provided essential structural information and disulfide assignment of Phα1β isoform with a 55 amino acid sequence (ACIPRGEICTDDCECCGCDNQCYCPPGSSLGIFKCSCAHANKYFCNRKKEKCKKA) (Wormwood et al., 2018). Treatments were performed two times per week for one month. Two administration routes were used:

1 – An intrastriatal route, aiming to analyze the toxin effects directly on the main region affected by HD (Margolis and Ross, 2003). A surgical procedure was performed using stereotaxic apparatus. Animals were anesthetized with a ketamine and xylazine mixture (90 / 30; mg/kg, respectively, i.p.). After complete sedation, they were positioned and a skull incision was made (approximately 2 cm in length, exposing the cranial bone sutures). Two guide cannulas were inserted following these coordinates: Antero-posterior -0.5; Medium-lateral- ±3.0; Dorso-ventral- +6.0 (Paxinos and Watson, 2013). After the cannulas incision, an acrylic resin helmet was placed over the skull for the complete guide cannulas' fixation, allowing the injection of the toxin or saline in a volume of 2 µl/site (1 µl per hemisphere). An occlusive cannula was placed inside each cannula guide to prevent clogging. Toxin or saline were administered bilaterally with an injection

cannula (30 G, 8 mm) coupled to a polyethylene tube attached to a Hamilton 701LT syringe.

2 - An intrathecal route, aiming to access the effects of the toxin Phα1β directly in spinal cord and muscles. In this case, the injections were performed according to the technique described by Hylden & Wilcox (1980) (Hylden and Wilcox, 1980), in a volume of 5 μl/site. The Phα1β toxin and saline were administered in subarachnoid space by puncture between the fifth and sixth lumbar vertebrae (L5-L6) with a Hamilton syringe 701LT coupled to a 26 G needle. The correct perforation was indicated behaviorally by a rapid mouse tail movement.

2.3- Behavior analyses

The following animal behavior tests were performed in the experimental groups ((Prado et al., 2006), with small modifications):

i) Wire-hang for muscle coordination and strength evaluation. In this test the hanging time (in seconds corrected by the body weight) was recorded, when the animals were placed on an inverted grid and kept 45 cm above surface. Values of three trials were averaged and then used for quantification (waiting for a 10 min period interval between each trial).

ii) Rotarod test for motor coordination, balance and motor skill learning. Animals were trained for 2 min in five trials at an accelerated rate (4 to 40 RPM in 300 s) for three consecutive days. On the third day, the latency to fall was measured (in seconds) in three trials waiting for a 10 min interval between each one.

iii) Open field for general activity analyses (mean velocity and distance traveled by the mouse during 20 min of experiment). This test consists of an automatic locomotor box system (LE 8811 IR Motor Activity Monitors PANLAB, Harvard Apparatus; Spain), made of acrylic (450 x 450 x 200 mm), where mice were placed in the center of the apparatus and allowed to freely explore the environment.

For all tests, mice were habituated in behavior room for at least 60 min prior to records initiation ($n = 5$ animals per group, per treatment).

2.4- Histological analysis of the central nervous system

For histological analysis, mice ($n = 5$ animals per group, per treatment) were anesthetized with isoflurane and transcardially perfused with 4% paraformaldehyde solution (PFA) in phosphate buffered saline 1x (PBS). Brain and spinal cord were removed and dissected for evaluation of the following regions: cortex, striatum, cervical (C1-C3) and lumbar (L1-L5) segments of the spinal cord. Samples were maintained incubated in PFA overnight at 4 ºC and then were processed in 30% sucrose solution in PBS overnight at 4 ºC, for cryopreservation. Samples were then fresh frozen in isopentane and liquid nitrogen and kept in -80 ºC to be sectioned. Free-floating coronally brains sections (40 µm thickness) were performed using the Leica VT1000S vibratome. Regarding the spinal cord, the segments were frozen in Tissue-tek medium O.C.T. compound and subsequently sectioned using a Leica CM3050S cryostat (30 µm thickness).

After, immunohistochemistry (using a peroxidase-based protocol, and the Vector Elite Kit) was performed in both brain and spinal cord (Doria et al., 2015). Briefly,

peroxidase activity was quenched using 0.3% H_2O_2 (for 30 min, in dark), followed by washing two times for 5 min in PBS. Then, membranes permeabilization were taken using 1% Triton X-100 for 10 min. Samples were blocked using 1.5% horse serum for 30 min and incubated with mouse anti-NeuN (1:500; Cat # MAB377, Millipore, USA) primary antibody, with 2% horse serum and 3% bovine serum albumin (BSA) in PBS overnight at 4 °C. In the second day, sections were washed in PBS three times for 5 min and next incubated in secondary antibody (biotinylated horse anti-mouse, 1:200, Vector Elite ABC kit) for 90 min at 4 °C. Finally, sections were incubated in avidin-biotin enzyme reagent complex for 90 min at 4 °C, according to manufacturer's instructions. Immunostaining was visualized using a chromogen (Vector SG substrate). The number of NeuN positive puncta per image was counted using the cell counter tool from ImageJ (NIH, USA).

2.5- Histological analysis of muscles

For morphological analysis of muscles fibers, sternomastoid (STM) and tibialis anterior (TIB) muscles were dissected and immediately fixed according to the protocol already established in our laboratory (Valadão et al., 2017) ($n = 5$ animals per group, per treatment). After the fixation, muscles were dehydrated in alcohols (70%, 80%, 90%, 95%), embedded in glycolmethacrylate resin and sectioned (5 μm thickness) in a microtome (model HM335E; Microm, Inc., Minneapolis, MN, USA). Sections from the STM and TIB muscles were stained with toluidine blue, and the cross-sectional area (CSA) of individual myofibers was analyzed using a light microscope (Leica DM2500) coupled to a CCD camera (Leica DFC345FX).

2.6- Glutamate analyses

To evaluate glutamate levels in spinal cords, another cohort of animals (n = 5 animals per group, per treatment), were treated and euthanized. For glutamate quantification, the cerebrospinal fluid was collected using cistern magna punction technique. As already described (Souza et al., 2008), the neurotransmitter measurements were performed enzymatically by analyzing the increase in fluorescence triggered to NADPH production in presence of glutamate dehydrogenase (50 U) and NADP$^+$ (1.0 mM). Excitation and emission wavelengths were 360 nm and 450 nm, respectively and experiments were performed using a Schimadzu RF-5301PC spectrofluorimeter.

2.7- Caspase-3 expression

For caspase-3 analyses (n = 5 animals per group, per treatment), cervical and lumbar segments were again collected and immediately immersed in neutral-buffered formalin overnight. Then, samples were dehydrated in alcohols (70%, 80%, 90%, 95%, and 100%), cleared in xylene, embedded in paraffin and cut (5 µm thickness sections) in a microtome. Nonspecific antibody binding was blocked by incubation in a solution containing 2% BSA, 0.1% Tween-20 in PBS for 60 min. After, samples were incubated with the primary antibody (1:100 polyclonal rabbit anti-caspase-3, CAT# C8487 Sigma-Aldrich, Saint Louis, MO, USA) diluted in blocking solution and maintained overnight at 4 °C. Samples were washed three times in PBS and incubated with a secondary antibody (1:1000, Alexa Fluor 488 goat anti-rabbit; Invitrogen, Eugene, OR) for 60 min. Subsequently, sections were washed three times in PBS and prepared for imaging.

2.8- Statistical Analysis

All data were expressed as mean ± standard error of mean (S.E.M.). After the normality tests, the results were analyzed using One-way ANOVA test followed by the Newman-Keuls post-test or Two-way ANOVA followed by the Bonferroni post-test. The GraphPad Prism 6 program was used and a p value < 0.05 was considered significant.

3- RESULTS

3.1- Treatments with the toxin Phα1β prevent motor changes in BACHD mice

In order to unravel an original neuroprotective action of Phα1β from the venom of the *Phoneutria nigriventer,* this recombinant isoform was injected trough two different routes; intrastriatal or intrathecal. No side effects or unusual behaviors were observed upon toxin administration.

Firstly, considering the intrastriatal route, we noticed that BACHD toxin group (when comparing with BACHD saline group) presented: 1- significant increase in hanging time considering the Wire-hang test (Figure 1A); 2- absence of differences in all groups in the Rotarod test (Figure 1B); 3- increase in mean velocity in the Open field test (Figure 1C) and also 4- increase in the distance traveled by the animal in the same test (Figure 1D). All of these changes were reverted to the WT level.

Secondly, using the intrathecal route, we found no difference between BACHD saline and BACHD toxin treatment groups regarding the Wire-hang test (Figure 1E). Also, considering these same two groups, we did not detect any statistical difference in the Rotarod test. It is worth mentioning that, in general, BACHD animals performed worse in

the latency to fall comparing with WT (Figure 1F). On the other hand, in Figure 1G-H we can see an improvement in the Open field parameters (mean velocity and distance traveled, respectively)

Moreover, toxin treatment also affected the mice body weight, mainly in the BACHD intrastriatal injection group. The body weight during the treatments periods can be seen in Supplementary Figure 1.
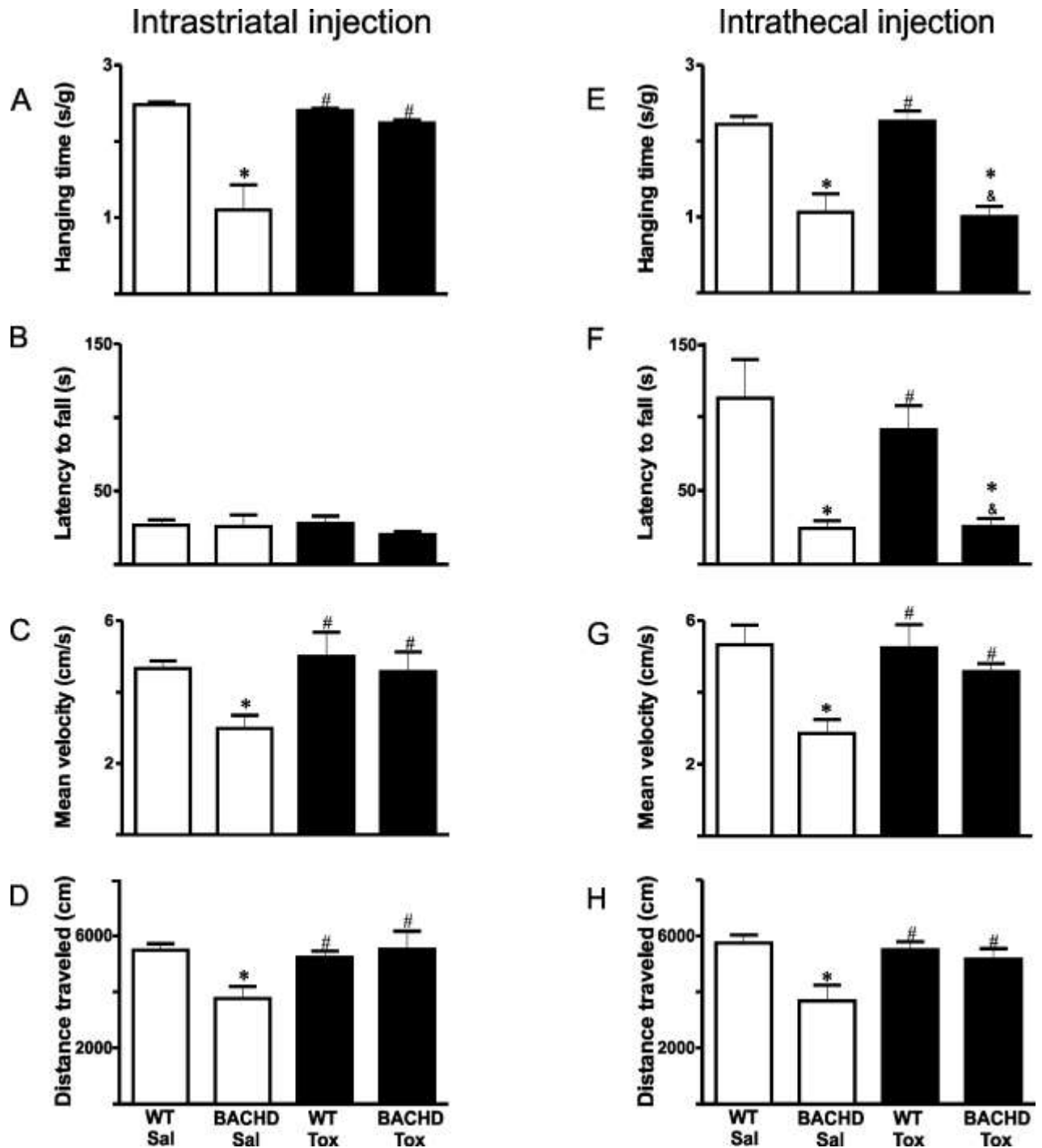
Figure 1: Phα1β treatments ameliorate behavioural performance in BACHD mice. Intrastriatal injection: A. Hanging time in Wire Hang test, B. Latency to fall in Rotarod test, C. Mean velocity in Open Field test, D. Distance traveled in Open Field test. Intrathecal injection: E. Hanging time in Wire Hang test, F. Latency to fall in Rotarod test, G. Mean

velocity in Open Field test, H. Distance traveled in Open Field test. *N* = 5 animals per group, per treatment, *p < 0.05 comparing with WT Sal, #p < 0.05 comparing with BACHD Sal, &p < 0.05 comparing with WT Tox. One-way ANOVA followed by the Newman-Keuls post-test. Sal: Saline; Tox: Toxin. Data are expressed as mean ± S.E.M.

3.2- Neuroprotective effect of Phα1β isoform in the cortex and striatum regions of BACHD mice

Data from the literature showed that the striatum is severely affected in HD, mainly justifying the motor symptoms observed in patients (Margolis and Ross, 2003). Therefore, we decided to evaluate a possible neuronal protection associated with the Phα1β toxin effect directly in this region. Figures 2A and 2B show the quantification of several neurons from striatum and cortex areas stained for NeuN. We observed that BACHD-saline group presented a reduction in the number of NeuN-labeled when compared with WT-saline in striatum and cortex. After treatment with the Phα1β toxin by intrastriatal injection, the number of neurons stained for NeuN in both regions in BACHD-treated animals was higher compared to BACHD-saline, suggesting neuroprotection. Noteworthy, we did not detect significant differences between the WT saline and WT toxin groups (for both brain regions) suggesting a possible non-toxic effect of Phα1β isoform.

In order to investigate whether the neuroprotection might be associated with spinal cord, another central nervous system key region in motor function, the toxin was injected intrathecally. Figure 2C and 2D show the results obtained after injecting BACHD and WT

mice with Phα1β toxin by intrathecal route. We observed that the treatment was not efficient in preserving the number of neurons in the striatum and cerebral cortex. Again, there was a significant reduction in the amount of neurons stained with NeuN in the BACHD-saline when compared to WT-saline. We did not detect statistical differences between the groups WT saline and WT toxin, as well as, BACHD saline and BACHD toxin. This result suggests, in the latter case, that the toxin, when injected in the spinal cord, was not able to protect neurons from death in the brain areas.
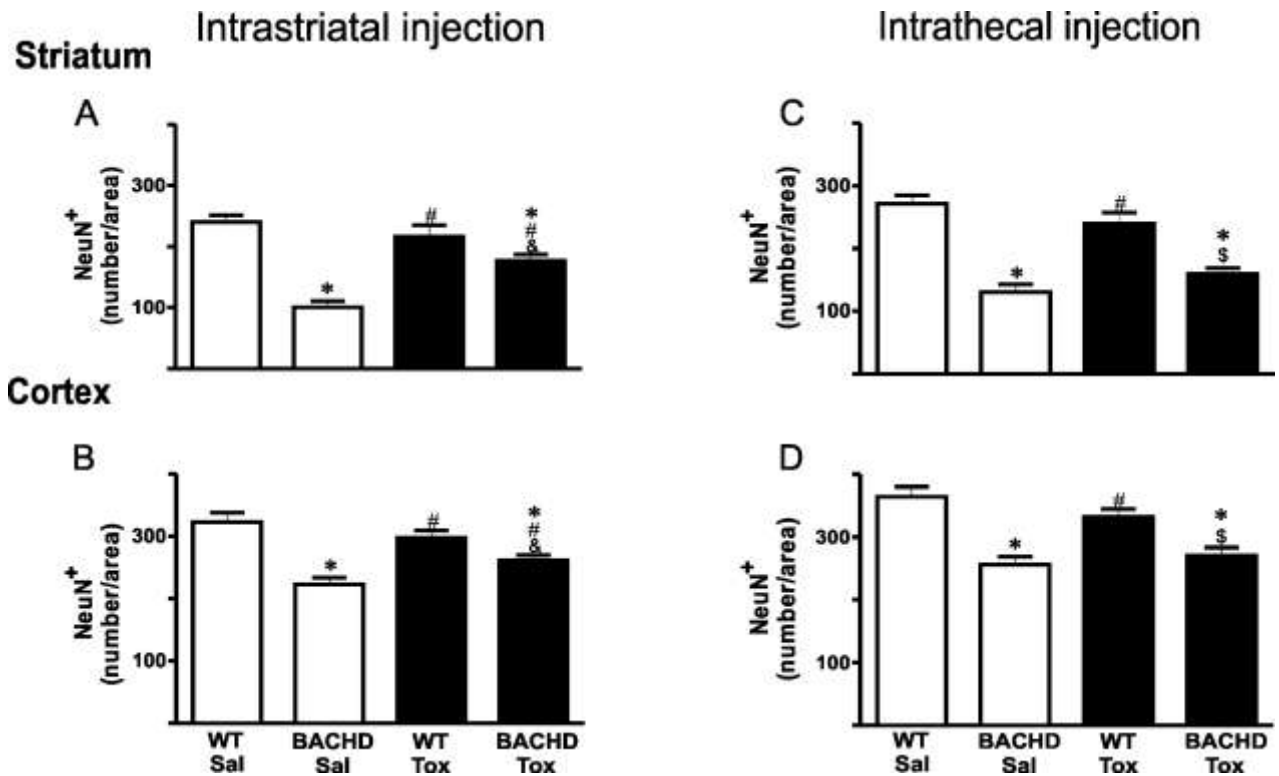
Figure 2: Neuroprotection in BACHD mice after Phα1β treatments. <u>Intrastriatal injection</u>: A. Bar graph showing neuronal quantification in striatum, B. Bar graph showing neuronal quantification in cortex. <u>Intrathecal injection:</u>, C. Bar graph showing neuronal quantification in striatum, D. Bar graph showing neuronal quantification in cortex. $N = 5$ animals per group, per treatment. Twenty four images per animal were analyzed in 3 different sections (total area ~ 114.000 μm^2). *p < 0.05 comparing with WT Sal, #p < 0.05 comparing with BACHD Sal, &p < 0.05 comparing with WT Tox. One-way ANOVA followed by the Newman-Keuls post-test. Sal: Saline; Tox: Toxin. Data are expressed as mean ± S.E.M.

3.3- Neuroprotective effect of Phα1β isoform in the spinal cord of BACHD mice

A recent work published by our research group showed significant alterations in the anterior horn of the spinal cord, and MUs in BACHD model (Valadão et al., 2017), opening possibility of new therapeutic approaches for HD beyond the brain. Therefore, we analyzed the neuroprotective effect of Phα1β in different segments of spinal cord. Figure 3A and 3B display the quantification of NeuN stained neurons in cervical and lumbar segments after intrastriatal injections of Phα1β. We can observe that, in this case, the treatment was not efficient in protecting neurons from the spinal cord. These results suggest that the toxin, when injected into a brain region, might not reach the spinal cord and therefore did not cause neuroprotection.

However, when we performed the same analyzes in the animals that were injected with Phα1β isoform directly in the spinal cord (by intrathecal route), we observed that the toxin caused neuroprotection in the anterior horn of the spinal cord (in both cervical and lumbar segments) by increasing the number of NeuN+ neurons (Figure 3C and 3D). There was a significant reduction in the number of neurons of the BACHD-saline animals compared with WT-saline. Corroborating our findings in the brain region, we also did not visualize differences between the WT groups (saline and toxin), suggesting low toxicity. With these data we can suggest that neuroprotection seems to occur in a route dependent manner, opening a road for the hypothesis that this toxin isoform may display a local action.
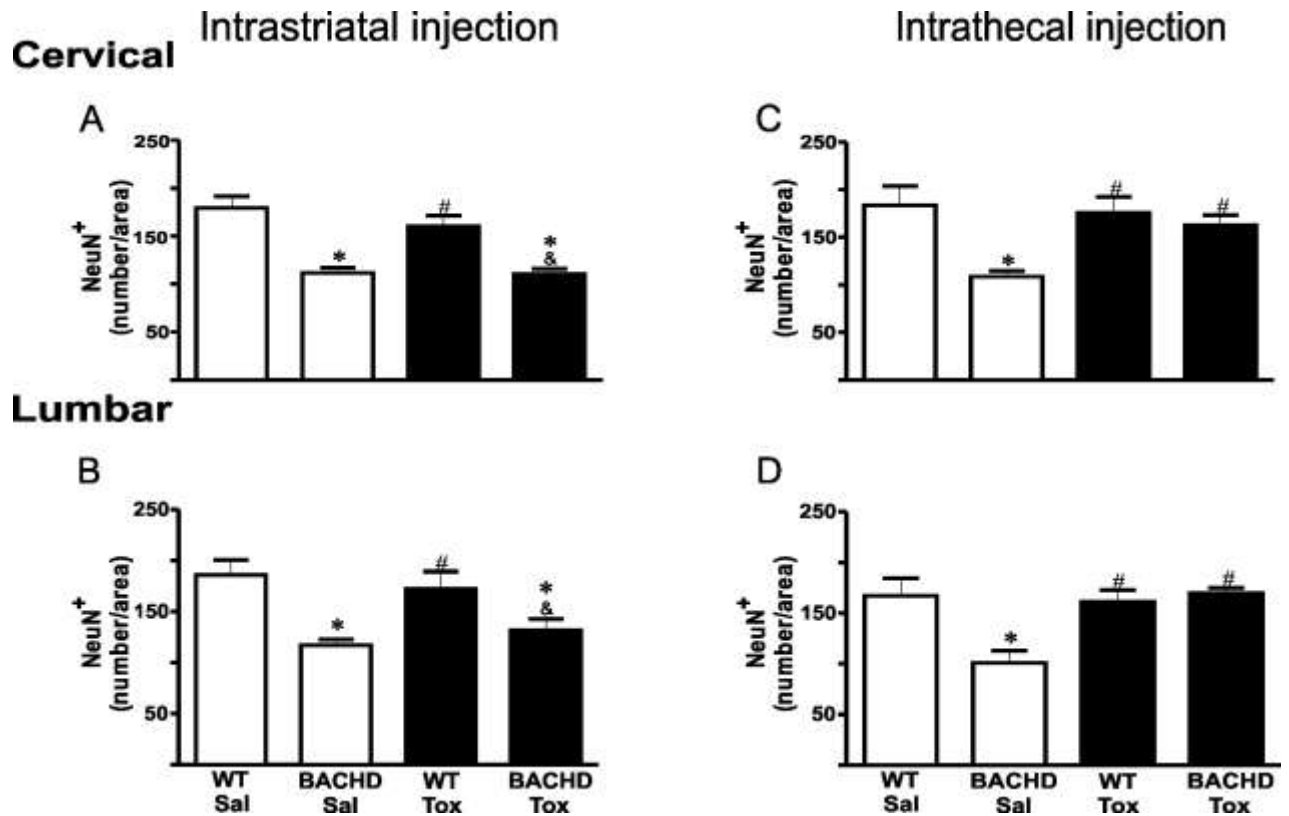
Figure 3: Neuronal preservation in spinal cords from BACHD mice after Phα1β treatments. <u>Intrastriatal injection</u>: A. Bar graph showing neuronal quantification in the cervical segment, B. Bar graph showing neuronal quantification in the lumbar segment. <u>Intrathecal injection</u>: C. Bar graph showing neuronal quantification in the cervical segment, D. Bar graph showing neuronal quantification in the lumbar segment. $N = 5$ animals per group, per treatment, 12 images per animal were analyzed in 3 different sections (total area ~ 57.000 μm^2), *$p < 0.05$ comparing with WT Sal, #$p < 0.05$ comparing with BACHD Sal, &$p < 0.05$ comparing with WT Tox. One-way ANOVA followed by the Newman-Keuls post-test. Sal: Saline; Tox: Toxin. Data are expressed as mean ± S.E.M.

3.4- *Phα1β isoform intrathecal injection reverts muscle atrophy in BACHD mice*

Our research group has described several changes in skeletal muscles such as in STM and Diaphragm from BACHD mouse line (de Aragão et al., 2016), (Valadão et al., 2017), (Valadão et al., 2018). Considering that intrathecal route is less invasive, we performed additional analyses only in this group of injection in order to answer whether a protection in neurons from the spinal cord could reverse muscle atrophy. Therefore, we conducted histological analysis in STM and TIB muscles (mainly innervated by motoneurons from the cervical and lumbar segments of the spinal cord) from BACHD mice treated and non-treated with Phα1β. The representative images in figure 4A show that in BACHD mice, these two skeletal muscles presented muscle fibers that were smaller compared to WT. The quantification of STM and TIB muscles fibers CSA in Figures 4B and 4C confirm this observation. After Phα1β treatment, there was a significant increase in CSA when comparing BACHD-saline and BACHD-toxin groups. Also, there were no statistical differences between the groups: BACHD-toxin, WT-toxin and WT-saline, for both muscles analyzed. In all, these data suggest that the preservation in the number of neurons at the anterior horn of spinal cord might be important for skeletal muscles innervations, reversing the atrophy described in BACHD animals.
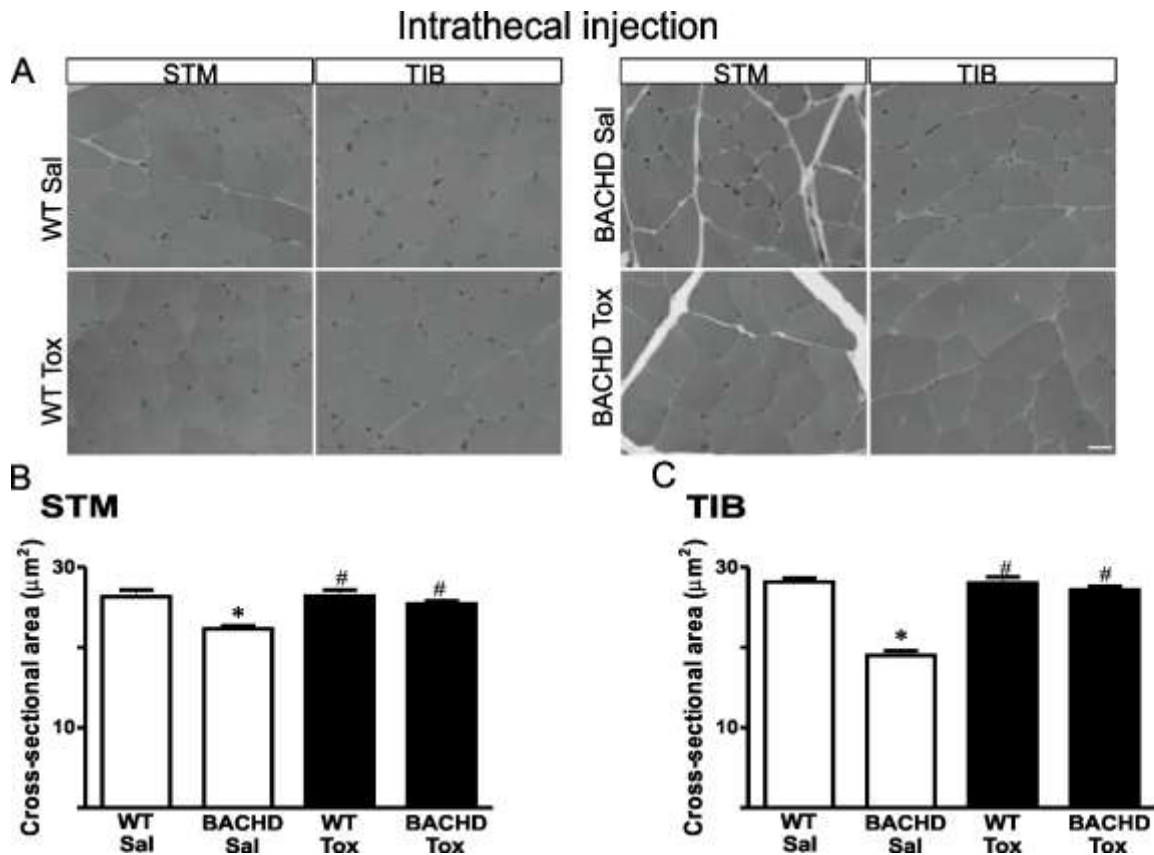
Figure 4: Phα1β treatment increase the cross-sectional area in myofibers from BACHD mice. Intrathecal injection: A. Representative skeletal muscles images, sternomastoid (STM) and tibial (TIB), B. Bar graph showing cross-sectional area (CSA) in STM, C. Bar graph showing cross-sectional area (CSA) in TIB. $N = 5$ animals per group, per treatment, 400 myofibers analyzed per group in 3 different sections, $*p < 0.05$ comparing with WT Sal, $\#p < 0.05$ comparing with BACHD Sal, $\&p < 0.05$ comparing with WT Tox. One-way ANOVA followed by the Newman-Keuls post-test. Sal: Saline; Tox: Toxin. Data are expressed as mean ± S.E.M. Scale bar: 20 μm.

3.5- Reductions in glutamate release in liquor and caspase-3 expression are associated with Phα1β effects in BACHD animals

Next, considering the neuroprotective potential of Phα1β in neurons of the spinal cord, we asked whether Phα1β can modulate a glutamate-excitotoxicity effect in the spinal cord of BACHD mice. To address this question, we measured glutamate levels in the liquor of BACHD and WT mice treated and non-treated with Phα1β isoform. Analysis in Figure 5A revealed glutamate levels in the cerebrospinal fluid from BACHD-saline group was increased compared to WT counterparts. After the intrathecal injection of Phα1β isoform in BACHD mice, we observed a significant reduction in the levels of this neurotransmitter comparing the BACHD-treated mice to the BACHD non-treated group. Finally, to gain further insight into the mechanisms underlying Phα1β action, we also performed caspase-3 immunofluorescence. Figure 5B displays representative immunofluorescence images of the spinal cord segments. We observed an intense caspase-3 expression in BACHD animals, a suggestion of neuronal death by apoptosis. After Phα1β administration, there was a decrease in caspase-3 labelling, seen in Figure 5C, for cervical segment, and Figure 5D, for lumbar segment of the spinal cord. Altogether, these data suggest that glutamate and caspase-3 activation have an important role in Phα1β mechanisms of action.
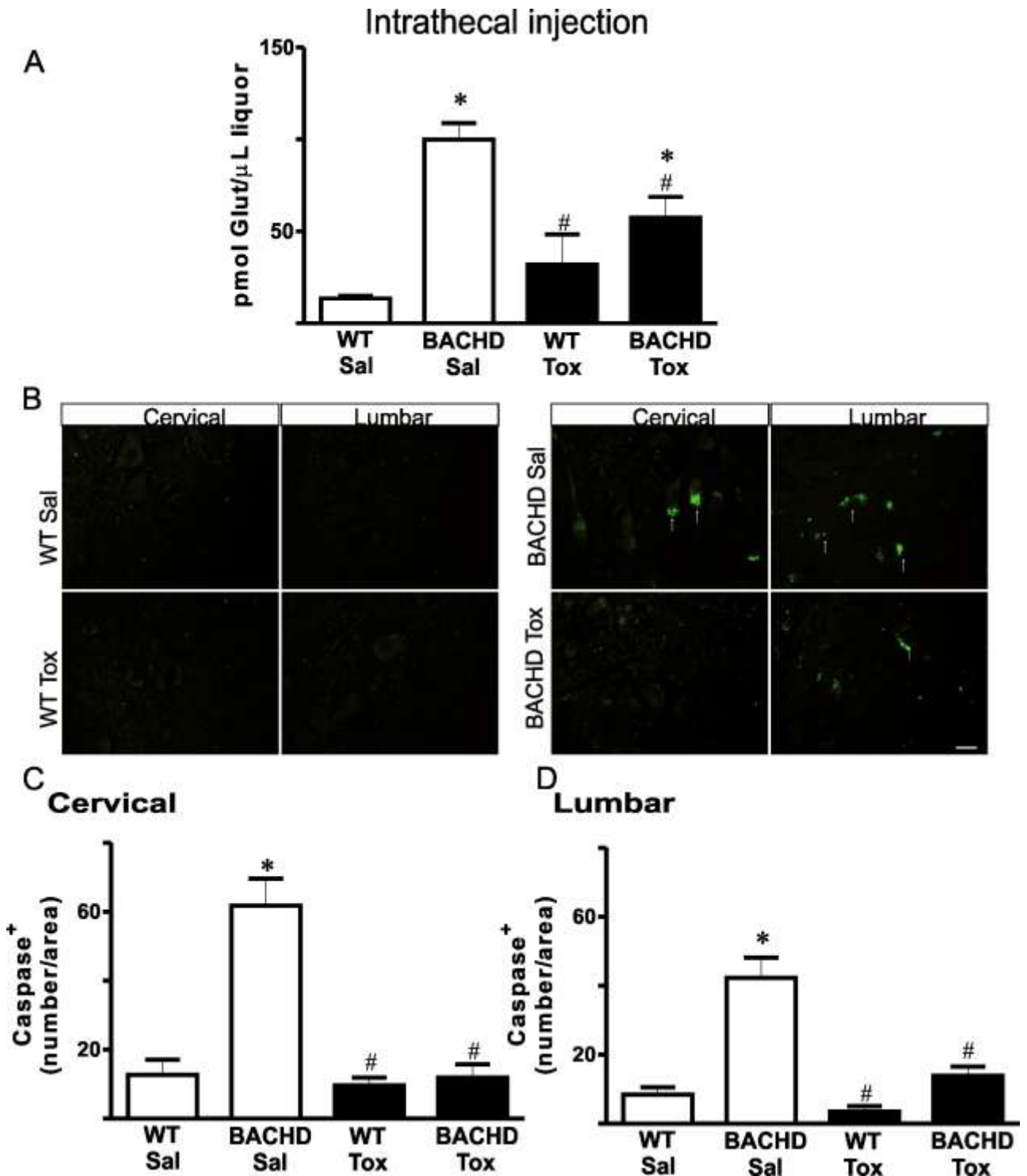
Figure 5: Reduction in glutamate levels and caspase-3 expression after Phα1β treatment in BACHD mice. Intrathecal injection: A. Bar graph showing Glutamate levels in the in the cerebrospinal fluid, B. Representative immunofluorescence images showing caspase[+]

neurons in cervical and lumbar segments of spinal cord, C. Bar graph showing caspase-3 quantification in the cervical segment, D Bar graph showing caspase-3 quantification in the lumbar segment. The arrows show caspase-3 labelling. $N = 5$ animals per group, per treatment, 100 images were analyzed in 5 different sections (total area ~ 300.000 μm^2) for cervical segment and 50 images were analyzed in 5 different sections (total area ~ 150.000 μm^2) for lumbar segment , *p < 0.05 comparing with WT Sal, #p < 0.05 comparing with BACHD Sal, &p < 0.05 comparing with WT Tox. One-way ANOVA followed by the Newman-Keuls post-test. Sal: Saline; Tox: Toxin. Data are expressed as mean ± S.E.M. Scale bar: 20 µm.

4- DISCUSSION

In this study, we provided evidence of a novel neuroprotective action for Phα1β peptide from the spider *Phoneutria nigriventer* venom. Using two routes of injections, we observed that this isoform improved behavior and morphological parameters from BACHD mice, a transgenic murine model for HD, which highly resembles the human condition (Gray et al., 2008).

In terms of motor behavior analyses, the motor tests provide a good read-out of neuromuscular function. Notably, the toxin ameliorated some behavior abnormalities in BACHD model (seen in Figure 1). The BACHD-toxin animals performed better in the Wire-hang test only in the intrastriatal delivery group. This test is very useful for measuring, for example, muscle coordination, which has a strong relationship with specific brain areas (Hoffman and Winder, 2016). Compelling data support a critical role

of the striatum in terms of movement control and historically, this area underlies the neurobiology basis of some movement-neurodegenerative disorders, such as HD and Parkinson's disease (Haber, 2016). The striatum is also involved in processes that lead to movement including motivation, emotion, and cognition (Haber, 2016). In this context, the toxin Phα1β, when injected directly in this area, may affect other central circuits, and projections that might explain the increase in hanging time only in the intrastriatal route.

No differences were detected in the Rotarod test regarding the two types of routes. First of all, with the intrastriatal one, all groups did not perform well in this test. A possible explanation for these findings is the presence of the acrylic resin helmet for the guide cannulas' fixation over animal's head. These structures might affect mice motor coordination, balance and motor skill learning, which are main parameters measured by Rotarod test. Therefore, the presence of the resin helmet may have hampered the results, since unexpectedly the BACHD saline did not differ from WT mice in the test. Secondly, BACHD groups (treated or not by intrathecal route) had worse latency to fall, which is in accordance with previous publications that showed a reduction in this parameter considering the transgenic mice (Menalled et al., 2010). As described above, the striatum displays a wide range of actions affecting motor and cognitive functions and importantly, the motor skill learning process is associated with neuronal changes in this region (Hikosaka et al., 1999), (Lehéricy et al., 2005), (Poldrack et al., 2005). The motor skill learning on the Rotarod, for instance, requires striatal and also cortical ensemble functions (Jeljeli et al., 1999), (Costa et al., 2004), (Kishioka et al., 2009). Then, the toxin, when delivered in the spinal cord, might not be able to modulate striatal motor learning

skill, explaining why we did not visualize improvements in the Rotarod test after intrathecal injections.

In the Open field test, we observed improvement in BACHD-toxin group after both types of injection routes (in the striatum or in the spinal cord). This is the simplest behavior test performed by us, which measures animal general locomotor activity (Brooks and Dunnett, 2009). This might explain why Phα1β promoted an increase in mean velocity and distance traveled regardless of the injection route. As already published, although differences in the Open field test started at 28 weeks of age in the BACHD animals, changes in this type of test are less severe (compared to the Rotarod test where the animals showed a severe decrease in the latency to fall at 4 weeks of age) (Gray et al., 2008), (Menalled et al., 2010). Thus, we can hypothesize that the first test to be improved by a non-striatal injection would be the Open field, which has been proven by our experiments considering the intrathecal route. It is important to emphasize that this type of test is widely used to validate the HD phenotype, whereas the BACHD mice model is amenable to drug testing (Menalled et al., 2010). New treatments should be done to validate the improvement of the other behavioral tests.

We next investigated morphological aspects regarding to a putative neuronal protection induced by Phα1β in central nervous system. Using NeuN immunohistochemistry, we detected an increase in NeuN+ neurons, and therefore neuroprotection, after treatment of BACHD mice with Phα1β isoform. After intrastriatal toxin injection in BACHD mice, the neurons from striatum and cortex regions were preserved, whereas the neurons of the spinal cord were not in the BACHD-treated group. Contrarily, using the intrathecal route, the neurons from spinal cord (in cervical or lumbar

segments) were maintained, and this was not visualized in striatum and cortex regions. We can speculate that the toxin was not able to be transported efficiently between brain and spinal cord in the cerebrospinal fluid. Indeed, this isoform molecular mass is about 6044 Da (Cordeiro et al., 1993) and this transport can actually be impaired. Another data that supports this local site action of Phα1β action is the body weight graph (see below and in Supplementary Figure).

It has been postulated that BACHD animals have metabolic alterations associated with a body mass gain (Gray et al., 2008), (Hult et al., 2011), (Lundh et al., 2012). Confirming these findings, we also observed that BACHD animals presented higher body weight when compared with WT (regardless of the administration route). Nevertheless, we visualized that all animals that were injected by intrastriatal route lost weight between weeks 1 and 2 of the treatment. It is worth mentioning that to perform the injections weekly, it was necessary to implant a resin helmet with cannulas to direct access the striatum. This procedure is highly invasive which can cause a change in the metabolism of the animal as a whole, and consequently loss of body mass. From week 2, the animals started to recover the body mass, and the BACHD saline group showed a significant increase in relation to WT saline. However, we observed that the BACHD-toxin group did not return to this body mass gain, continuing to lose weight (until reaching values similar to WT mice). This may suggest that the presence of the toxin directly in the central nervous system of BACHD animals could also influence other regions, for example, the hypothalamus. Recently, the hypothalamus emerged as an important area affected in HD (Hult et al., 2011), and changes in its neuroendocrine circuits can play an important role in the development of non-motor symptoms (such as metabolic changes, i.e. insulin and

leptin resistance, beyond mood alterations and anxiety). Thus, it is possible that the toxin also acts in others brain areas, which might justify the weight loss in BACHD animals. Intriguingly, when injected intrathecally, the toxin did not have any effect in body weight (and BACHD treated or not remained with higher body weight compared to WT animals). Over again, Phα1β, when injected in the spinal cord, seems not to accurately be transported to the brain.

Considering the local effect of Phα1β isoform, and the fact that an intrathecal intervention is less invasive than a striatal one, we proceeded with the analysis of the neurons from the spinal cord and Phα1β mechanisms of action only in this group. Indeed, we observed a spinal cord neuronal preservation in BACHD mice that was important to keep muscles innervations and we observed an increase in CSA in the treated-HD transgenic animals. The choice of the skeletal muscles used (STM and TIB) was due to the observation that patients with HD present involuntary movements of the neck as well as lower limbs. Also, it is important to highlight that STM is innerved by motoneurons manly from the cervical portion of the spinal cord and TIB by motoneurons from the lumbar segment. As the toxin was injected between L5-L6 it is essential to analyze muscles from upper areas, such as the cervical segment. The preservation of muscles CSA is possibly associated with a spinal cord neuroprotection.

Finally, glutamate levels in BACHD were reduced in the cerebrospinal fluid after the intrathecal toxin delivery. The decreasing in glutamate overflow in cerebrospinal fluid by the *Phoneutria nigriventer* venom was also observed in a series of previous studies (Agostini et al., 2011), (Souza et al., 2008), (Pinheiro et al., 2009). The Ca^{2+} channels blocking property by Phα1β might be associated with this reduction in glutamate levels,

which in turn, could be related to caspase down-regulation. Corroborating with this hypothesis, we observed a reduction in caspase-3 labeling in BACHD Phα1β treated-animals (seen in Figure 5). The reduction in caspase activity can further be linked to the spinal cord neuroprotection in the BACHD-toxin group. As already mentioned, the isoform used in this study has large specificity for the N-type VGCCs (Vieira et al., 2005). Of note, despite the highest density of N-type channels that can be found in the dorsal horn of the spinal cord, the N-type VGCC is also presented on the cell bodies and dendrites of motoneurons in the anterior horn (Westenbroek et al., 1998), (Cizkova et al., 2002). Interestingly, von Lewinski and Keller, 2005 (von Lewinski and Keller, 2005) reported that, in general, motoneurons have low calcium buffering capacity and are particularly sensitive to intracellular Ca^{2+} challenges. Probably, the toxin, when injected in the BACHD spinal cord favorably blocked the VGCCs, and in consequence, it modulated the deleterious effects of an intense calcium influx through the motoneurons. Electrophysiological experiments are required to understand the exact role of this isoform on the VGCCs and calcium currents from motoneurons at the spinal cord.

To date, there is no effective treatment for HD. New approaches targeting the mutant HTT are very difficult to be developed and the creation of a successful therapy only focusing on this protein may take a long time and considerable resources (Bezprozvanny, 2010). So, the use of novel agents that modulate the calcium signaling in neurons is promising target for the development of a therapy that could delay onset of symptoms. The isoform Phα1β as a Ca^{2+} blocker represent a good possibility to preserve some motor functions and neuromuscular structure. We can list, for instance, the following advantages of Phα1β peptide: 1- A local site of action with no adverse motor

side effects (seen by us when comparing the WT mice treated or not, and by others researchers (Souza et al., 2008), (Dalmolin et al., 2011)) and 2- The recombinant form of the toxin is already commercially available and it exhibits the same effects as the native form (Souza et al., 2008), (Rigo et al., 2017). In conclusion, our data provide a novel neuroprotector effect of Phα1β isoform, decreasing glutamate release in addition to caspase activity, and also protecting neurons and muscles structure/function, which may help to contribute to new approaches to treat HD motor symptoms.

5- ACKNOWLEDGMENTS

All authors declare no conflict of interest.

6- REFERENCES

Agostini, R.M., do Nascimento Pinheiro, A.C., Binda, N.S., Romano Silva, M.A., do Nascimento Cordeiro, M., Richardson, M., Sena Guimarães, A.L., Gomez, M. V, 2011. Phoneutria spider toxins block ischemia-induced glutamate release and neuronal death of cell layers of the retina. Retina 31, 1392–1399. https://doi.org/10.1097/IAE.0b013e318205b249

Bano, D., Zanetti, F., Mende, Y., Nicotera, P., 2011. Neurodegenerative processes in Huntington's disease. Cell Death Dis 2, e228. https://doi.org/10.1038/cddis.2011.112

Bezprozvanny, I.B., 2010. Calcium signaling and neurodegeneration. Acta Naturae 2, 72–82.

Binda, N.S., Carayon, C.P., Agostini, R.M., Pinheiro, A.C., Cordeiro, M.N., Silva, M.A., Silva, J.F., Pereira, E.M., da Silva Junior, C.A., de Castro Junior, C.J., Guimarães, A.L., Gomez, M. V, 2016. PhTx3-4, a Spider Toxin Calcium Channel Blocker, Reduces NMDA-Induced Injury of the Retina. Toxins (Basel). 8, 1–14. https://doi.org/10.3390/toxins8030070

Brooks, S.P., Dunnett, S.B., 2009. Tests to assess motor phenotype in mice: a user's guide. Nat Rev Neurosci 10, 519–529. https://doi.org/10.1038/nrn2652

Cizkova, D., Marsala, J., Lukacova, N., Marsala, M., Jergova, S., Orendacova, J., Yaksh, T.L., 2002. Localization of N-type Ca2+ channels in the rat spinal cord following chronic constrictive nerve injury. Exp Brain Res 147, 456–463. https://doi.org/10.1007/s00221-002-1217-3

Cordeiro, M.N., de Figueiredo, S.G., Valentim, A.C., Diniz, C.R., von Eickstedt, V.R., Gilroy, J., Richardson, M., 1993. Purification and amino acid sequences of six Tx3 type neurotoxins from the venom of the Brazilian "armed" spider Phoneutria nigriventer (Keys). Toxicon 31, 35–42.

Costa, R.M., Cohen, D., Nicolelis, M.A., 2004. Differential corticostriatal plasticity during fast and slow motor skill learning in mice. Curr Biol 14, 1124–1134. https://doi.org/10.1016/j.cub.2004.06.053

Dalmolin, G.D., Silva, C.R., Rigo, F.K., Gomes, G.M., Cordeiro, M.N., Richardson, M., Silva, M.A., Prado, M.A., Gomez, M. V, Ferreira, J., 2011. Antinociceptive effect of Brazilian armed spider venom toxin Tx3-3 in animal models of neuropathic pain. Pain 152, 2224–2232. https://doi.org/10.1016/j.pain.2011.04.015

de Aragão, B.C., Rodrigues, H.A., Valadão, P.A., Camargo, W., Naves, L.A., Ribeiro, F.M., Guatimosim, C., 2016. Changes in structure and function of diaphragm neuromuscular junctions from BACHD mouse model for Huntington's disease. Neurochem Int 93, 64–72. https://doi.org/10.1016/j.neuint.2015.12.013

de Souza, A.H., Lima, M.C., Drewes, C.C., da Silva, J.F., Torres, K.C., Pereira, E.M., de Castro Junior, C.J., Vieira, L.B., Cordeiro, M.N., Richardson, M., Gomez, R.S., Romano-Silva, M.A., Ferreira, J., Gomez, M., 2011. Antiallodynic effect and side effects of Phα1β, a neurotoxin from the spider Phoneutria nigriventer: comparison with ω-conotoxin MVIIA and morphine. Toxicon 58, 626–633. https://doi.org/10.1016/j.toxicon.2011.09.008

Diniz, D.M., de Souza, A.H., Pereira, E.M., da Silva, J.F., Rigo, F.K., Romano-Silva, M.A., Binda, N., Castro, C.J., Cordeiro, M.N., Ferreira, J., Gomez, M. V, 2014. Effects of the calcium channel blockers Phα1β and ω-conotoxin MVIIA on capsaicin and acetic acid-induced visceral nociception in mice. Pharmacol Biochem Behav 126, 97–102. https://doi.org/10.1016/j.pbb.2014.09.017

Doria, J.G., de Souza, J.M., Andrade, J.N., Rodrigues, H.A., Guimaraes, I.M., Carvalho, T.G., Guatimosim, C., Dobransky, T., Ribeiro, F.M., 2015. The mGluR5 positive allosteric modulator, CDPPB, ameliorates pathology and phenotypic signs of a mouse model of Huntington's disease. Neurobiol Dis 73, 163–173. https://doi.org/10.1016/j.nbd.2014.08.021

Frank, S., 2014. Treatment of Huntington's disease. Neurotherapeutics 11, 153–160. https://doi.org/10.1007/s13311-013-0244-z

Gomez, M. V, Kalapothakis, E., Guatimosim, C., Prado, M.A., 2002. Phoneutria nigriventer venom: a cocktail of toxins that affect ion channels. Cell Mol Neurobiol 22, 579–588. https://doi.org/10.1023/A:1021836403433

Graham, R.K., Pouladi, M.A., Joshi, P., Lu, G., Deng, Y., Wu, N., Figueroa, B.E., Metzler, M., André, V., Slow, E., Raymond, L., Friedlander, R., Levine, M.S., Leavitt, B.R., Hayden, M.R., 2009. Differential susceptibility to excitotoxic stress in YAC128 mouse models of Huntington disease between initiation and progression of disease. J Neurosci 29, 2193–2204. https://doi.org/10.1523/JNEUROSCI.5473-08.2009

Gray, M., Shirasaki, D.I., Cepeda, C., Andre, V.M., Wilburn, B., Lu, X.H., Tao, J., Yamazaki, I., Li, S.H., Sun, Y.E., Li, X.J., Levine, M.S., Yang, X.W., 2008. Full-length human mutant huntingtin with a stable polyglutamine repeat can elicit progressive and selective neuropathogenesis in BACHD mice. J Neurosci 28, 6182–6195. https://doi.org/10.1523/JNEUROSCI.0857-08.2008

Haber, S.N., 2016. Corticostriatal circuitry. Dialogues Clin Neurosci 18, 7–21. https://doi.org/10.1007/978-1-4939-3474-4_135

Haddad, M.S., Cummings, J.L., 1997. Huntington's disease. Psychiatr Clin North Am 20, 791–807.

Hikosaka, O., Nakahara, H., Rand, M.K., Sakai, K., Lu, X., Nakamura, K., Miyachi, S., Doya, K., 1999. Parallel neural networks for learning sequential procedures. Trends Neurosci 22, 464–471. https://doi.org/10.1016/S0166-2236(99)01439-3

Hoffman, E., Winder, S.J., 2016. A Modified Wire Hanging Apparatus for Small Animal Muscle Function Testing. PLoS Curr 8, pii: ecurrents.md.1e2bec4e78697b7b0ff80ea25a1d38be. https://doi.org/10.1371/currents.md.1e2bec4e78697b7b0ff80ea25a1d38be

Hult, S., Soylu, R., Bjorklund, T., Belgardt, B.F., Mauer, J., Bruning, J.C., Kirik, D., 2011. Mutant huntingtin causes metabolic imbalance by disruption of hypothalamic neurocircuits. Cell Metab 13, 428–439. https://doi.org/10.1016/j.cmet.2011.02.013

Hylden, J.L., Wilcox, G.L., 1980. Intrathecal morphine in mice: a new technique. Eur J Pharmacol 67, 313–316.

Jeljeli, M., Strazielle, C., Caston, J., Lalonde, R., 1999. Effects of electrolytic lesions of the lateral pallidum on motor coordination, spatial learning, and regional brain variations of cytochrome oxidase activity in rats. Behav Brain Res 102, 61–71. https://doi.org/10.1016/S0166-4328(98)00162-4

Kishioka, A., Fukushima, F., Ito, T., Kataoka, H., Mori, H., Ikeda, T., Itohara, S., Sakimura, K., Mishina, M., 2009. A novel form of memory for auditory fear conditioning at a low-intensity unconditioned stimulus. PLoS One 4, e4157. https://doi.org/10.1371/journal.pone.0004157

Lehéricy, S., Benali, H., Van de Moortele, P.F., Pélégrini-Issac, M., Waechter, T., Ugurbil, K., Doyon, J., 2005. Distinct basal ganglia territories are engaged in early and

advanced motor sequence learning. Proc Natl Acad Sci U S A 102, 12566–12571. https://doi.org/10.1073/pnas.0502762102

Lundh, S.H., Soylu, R., Petersén, A., 2012. Expression of mutant huntingtin in leptin receptor-expressing neurons does not control the metabolic and psychiatric phenotype of the BACHD mouse. PLoS One 7, e51168. https://doi.org/10.1371/journal.pone.0051168

Margolis, R.L., Ross, C.A., 2003. Diagnosis of Huntington disease. Clin Chem 49, 1726–1732.

Menalled, L., El-khodor, B.F., Patry, M., Suarez-farinas, M., Zahasky, B., Leahy, C., Wheeler, V., Yang, X.W., Macdonald, M., Morton, A.J., Bates, G., Leeds, J., Park, L., Signer, E., Tobin, A., Brunner, D., 2010. Systematic behavioral evaluation of Huntington's disease transgenic and knock-in mouse models. Neurobiol Dis 35, 319–336. https://doi.org/10.1016/j.nbd.2009.05.007.Systematic

Moffitt, H., McPhail, G.D., Woodman, B., Hobbs, C., Bates, G.P., 2009. Formation of polyglutamine inclusions in a wide range of non-CNS tissues in the HdhQ150 knock-in mouse model of Huntington's disease. PLoS One 4, e8025. https://doi.org/10.1371/journal.pone.0008025

Paxinos, G., Watson, C., 2013. The rat brain in stereotaxic coordinates. https://doi.org/10.1016/0143-4179(83)90049-5

Pinheiro, A.C., da Silva, A.J., Prado, M.A., Cordeiro, M.N., Richardson, M., Batista, M.C., de Castro Junior, C.J., Massensini, A.R., Guatimosim, C., Romano-Silva, M A Kushmerick, C., Gomez, M. V, 2009. Phoneutria spider toxins block ischemia-induced glutamate release, neuronal death, and loss of neurotransmission in hippocampus. Hippocampus 19, 1123–1129. https://doi.org/10.1002/hipo.20580

Poldrack, R.A., Sabb, F.W., Foerde, K., Tom, S.M., Asarnow, R.F., Bookheimer, S.Y., Knowlton, B.J., 2005. The neural correlates of motor skill automaticity. J Neurosci 25, 5356–5364. https://doi.org/10.1523/JNEUROSCI.3880-04.2005

Prado, V.F., Martins-Silva, C., de Castro, B.M., Lima, R.F., Barros, D.M., Amaral, E., Ramsey, A.J., Sotnikova, T.D., Ramirez, M.R., Kim, H.G., Rossato, J.I., Koenen, J., Quan, H., Cota, V.R., Moraes, M.F., Gomez, M. V, Guatimosim, C., Wetsel, W., Kushmerick, C., Pereira, G.S., Gainetdinov, R.R., Izquierdo, I., Caron, M.G., Prado, M.A., 2006. Mice deficient for the vesicular acetylcholine transporter are myasthenic and have deficits in object and social recognition. Neuron 51, 601–612. https://doi.org/10.1016/j.neuron.2006.08.005

Rezende Júnior, L., Cordeiro, M.N., Oliveira, E.B., Diniz, C.R., 1991. Isolation of neurotoxic peptides from the venom of the "armed" spider Phoneutria nigriventer. Toxicon 29, 1255–1233.

Rigo, F.K., Dalmolin, G.D., Trevisan, G., Tonello, R., Silva, M.A., Rossato, M.F., Klafke, J.Z., Cordeiro, M.D.N., Castro Junior, C.J., Montijo, D., Gomez, M. V, Ferreira, J.,

2013. Effect of ω-conotoxin MVIIA and Phα1β on paclitaxel-induced acute and chronic pain. Pharmacol Biochem Behav 114–115, 16–22. https://doi.org/10.1016/j.pbb.2013.10.014

Rigo, F.K., Trevisan, G., De Prá, S.D.T., Cordeiro, M.N., Borges, M.H., Silva, J.F., Santa Cecilia, F.V., de Souza, A.H., de Oliveira Adamante, G., Milioli, A.M., de Castro Junior, C.J., Ferreira, J., Gomez, M.V., 2017. The spider toxin Phα1β recombinant possesses strong analgesic activity. Toxicon 133, 145–152. https://doi.org/10.1016/j.toxicon.2017.05.018

Rosa, F., Trevisan, G., Rigo, F.K., Tonello, R., Andrade, E.L., Cordeiro, M.D.N., Calixto, J.B., Gomez, M. V, Ferreira, J., 2014. Phα1β, a peptide from the venom of the spider Phoneutria nigriventer shows antinociceptive effects after continuous infusion in a neuropathic pain model in rats. Anesth Analg 119, 196–202. https://doi.org/10.1213/ANE.0000000000000249

Ross, C.A., Tabrizi, S.J., 2011. Huntington's disease: from molecular pathogenesis to clinical treatment. Lancet Neurol 10, 83–98. https://doi.org/10.1016/S1474-4422(10)70245-3

Simms, B.A., Zamponi, G.W., 2014. Neuronal voltage-gated calcium channels: structure, function, and dysfunction. Neuron 82, 24–45. https://doi.org/10.1016/j.neuron.2014.03.016

Souza, A.H., Ferreira, J., Cordeiro, M.N., Vieira, L.B., De Castro, C.J., Trevisan, G., Reis, H., Souza, I.A., Richardson, M., Prado, M.A., Prado, V.F., Gomez, M. V, 2008. Analgesic effect in rodents of native and recombinant Ph alpha 1beta toxin, a high-voltage-activated calcium channel blocker isolated from armed spider venom. Pain 140, 115–126. https://doi.org/10.1016/j.pain.2008.07.014

Squitieri, F., Falleni, A., Cannella, M., Orobello, S., Fulceri, F., Lenzi, P., Fornai, F., 2010. Abnormal morphology of peripheral cell tissues from patients with Huntington disease. J Neural Transm 117, 77–83. https://doi.org/10.1007/s00702-009-0328-4

The Huntington's Disease Collaborative Research Group, 1993. A novel gene containing a trinucleotide repeat that is expanded and unstable on Huntington's disease chromosomes. The Huntington's Disease Collaborative Research Group. Cell 72, 971–983.

Valadão, P.A., de Aragão, B.C., Andrade, J.N., Magalhães-Gomes, M.P., Foureaux, G., Joviano-Santos, J. V, Nogueira, J.C., Ribeiro, F.M., Tapia, J.C., Guatimosim, C., 2017. Muscle atrophy is associated with cervical spinal motoneuron loss in BACHD mouse model for Huntington's disease. Eur J Neurosci 45, 785–796. https://doi.org/10.1111/ejn.13510

Valadão, P.A.C., Gomes, M.P.S.M., Aragão, B.C., Rodrigues, H.A., Andrade, J.N., Garcias, R., Joviano-Santos, J. V, Luiz, M.A., Camargo, W.L., Naves, L.A., Kushmerick, C., Cavalcante, W.L.G., Gallacci, M., de Jesus, I.C.G., Guatimosim, S., Guatimosim, C., 2018. Neuromuscular synapse degeneration without muscle

function loss in the diaphragm of a murine model for Huntington's Disease. Neurochem Int 116, 30–42. https://doi.org/10.1016/j.neuint.2018.05.002

van der Burg, J.M., Björkqvist, M., Brundin, P., 2009. Beyond the brain: widespread pathology in Huntington's disease. Lancet Neurol 8, 765–774. https://doi.org/10.1016/S1474-4422(09)70178-4

Vieira, L.B., Kushmerick, C., Hildebrand, M.E., Garcia, E., Stea, A., Cordeiro, M.N., Richardson, M., Gomez, M. V, Snutch, T.P., 2005. Inhibition of high voltage-activated calcium channels by spider toxin PnTx3-6. J Pharmacol Exp Ther 314, 1370–1377. https://doi.org/10.1124/jpet.105.087023

von Lewinski, F., Keller, B.U., 2005. Ca2+, mitochondria and selective motoneuron vulnerability: Implications for ALS. Trends Neurosci 28, 494–500. https://doi.org/10.1016/j.tins.2005.07.001

Westenbroek, R.E., Hoskins, L., Catterall, W.A., 1998. Localization of Ca2+ channel subtypes on rat spinal motor neurons, interneurons, and nerve terminals. J Neurosci 18, 6319–6330.

Wormwood, K.L., Gatien, A., Wetie, N., Gomez, M.V., Ju, Y., Kowalski, P., Mihasan, M., Darie, C.C., 2018. Structural Characterization and Disulfide Assignment of Spider Peptide Phα1β by Mass Spectrometry. J Am Soc Mass Spectrom 29, 827–841. https://doi.org/10.1007/s13361-018-1904-3

Zeron, M., Hansson, O., Chen, N., Wellington, C., Leavitt, B., Brundin, P., Hayden, M., Raymond, L., 2002. Increased sensitivity to N-methyl-D-aspartate receptor-mediated excitotoxicity in a mouse model of Huntington's disease. Neuron 33, 849–860.

Supplementary Figure

A

Intrastriatal injection
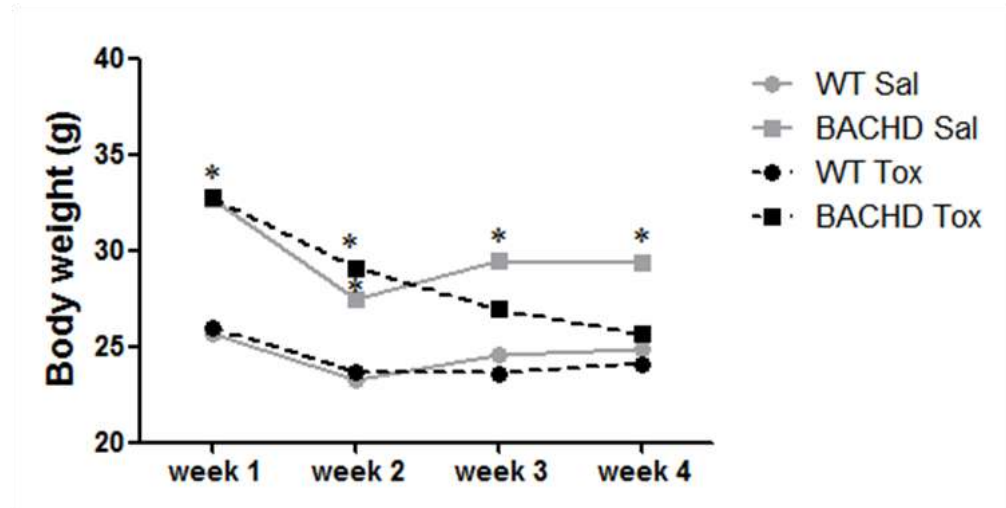
B

Intrathecal injection
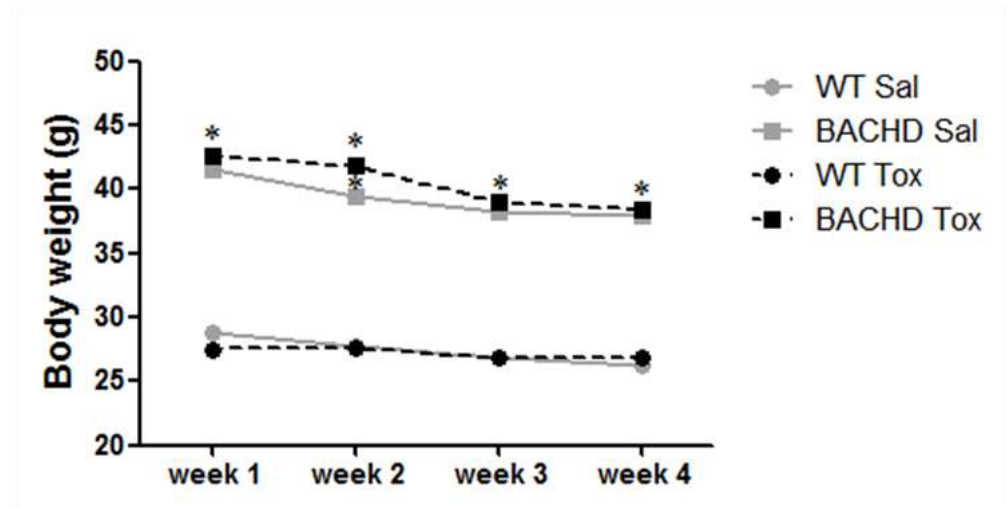
Supplementary Figure: Body weight quantification during Phα1β treatments. <u>Intrastriatal injection:</u> A. Graph showing body weight during the treatments. <u>Intrathecal injection</u>: B. Graph showing body weight during the treatments. $N = 5$ animals per group, per treatment, *$p < 0.05$ comparing with WT Sal. Two-way ANOVA followed by the Bonferroni post-test. Sal: Saline; Tox: Toxin. Data are expressed as mean ± S.E.M.

5- DISCUSSÃO INTEGRADORA

Como a presente tese foi apresentada em formato de artigos científicos é importante destacar que a discussão específica para cada subprojeto está disposta em seu respectivo artigo. A discussão geral e integradora pode ser vista nos próximos parágrafos.

A DH é uma desordem neurodegenerativa progressiva fatal, cujos sintomas são graves e incluem comprometimento motor além de déficits cognitivos e psiquiátricos. A doença se inicia a partir da morte de neurônios da região do corpo estriado[102], e por causa disso a maioria dos estudos sobre novas abordagens terapêuticas estão focados em intervenções nessa região. De fato, esses estudos são muito importantes para a vida dos pacientes, no entanto, não podemos esquecer que existe um comprometimento periférico na DH o que abre novas possibilidades de tratamento (além do SNC). Sendo assim, a caracterização periférica de modelos animais que mimetizam a DH dos seres humanos, como o modelo BACHD, é fundamental.

Nosso grupo de pesquisa descreveu pela primeira vez (artigo 1 dessa tese), que animais BACHD apresentam disfunções cardíacas (tanto elétricas como contráteis). A descrição e a explicação dos fenômenos elétricos e contráteis observados podem ser vistas na discussão original do artigo. Extrapolando o que já discutimos nessa publicação, é importante destacar que todas as disfunções relatadas estão associadas a um elevado estresse oxidativo no miocárdio dos camundongos BACHD. Em nosso trabalho foram descritas evidências indiretas que justificam o estresse oxidativo como as alterações nas mitocôndrias, a presença de grânulos de lipofuscina (grânulos descritos como resultantes de uma modificação no status redox das células[103]), além de distúrbios no sistema antioxidante do coração. Somado a isso, também observamos diretamente utilizando-se sondas específicas (uma sonda como indicador geral de estresse oxidativo e outra

como um indicador da produção de ânions superóxidos mitocondriais), um aumento desse parâmetro nos animais transgênicos para a DH. Nesse contexto, podemos sugerir que a HTT mutante pode estar comprometendo de forma direta a função mitocondrial (uma vez que tal organela é a principal fonte geradora de radicais livres e espécies reativas de oxigênio por meio da cadeia respiratória). Sabe-se que, além dos agregados intracelulares, essa proteína mutante é capaz de interagir fisicamente com as mitocôndrias[104]. Essa associação pode provocar alterações no manejo intramitocondrial de cálcio, distúrbios no tráfico dessa organela além de danos na cadeia respiratória (o que aumenta a liberação de espécies reativas de oxigênio contribuindo para o estresse oxidativo mencionado)[105,106,107,108]. O estresse oxidativo por sua vez, desencadeou uma alta expressão da enzima Calmodulina cinase II (CaMKII), que também justifica as alterações observadas. A CAMKII é uma serina/treonina cinase ativada pela interação com Ca^{2+} e Calmodulina. Comprovamos, de forma inédita, a participação da CaMKII nos efeitos deletérios no coração dos animais BACHD, através da detecção de um aumento da expressão dessa proteína utilizado a técnica de *western blot*. Além disso, com o uso de um inibidor específico da CaMKII (o KN93) detectamos uma reversão das arritmias e dos efeitos mecânicos observados. Com o análogo inativo (o KN92) não observamos inibição dessa enzima (e os mesmos efeitos foram observados quando comparamos WT e BACHD). Muitas evidências apoiam a capacidade do eixo Ca^{2+}/Calmodulina/CaMKII em modular a atividade de diversos canais iônicos, bem como a sua hiperativação contribuir para a arritmogênese, distúrbios e contratilidade e apoptose[109,110]. Além disso, o aumento da expressão da CaMKII pode promover um cenário de desajuste no manejo intracelular de Ca^{2+}[111,112], o que também foi observado em nosso modelo. Os resultados publicados nesse artigo abrem novas possibilidades para o tratamento dos sintomas cardíacos da DH. Uma nova possibilidade que podemos citar é o uso de medicamentos antioxidantes que

podem afetar a expressão ou atividade dessa enzima, o que já ocorre por exemplo em estudos clínicos que utilizam inibidores ou silenciadores da CaMKII[113,114,115].

Vale destacar que uma nova linha de pesquisa que envolve o uso de antioxidantes, como o fulerol, foi introduzida em nosso laboratório como outra possibilidade terapêutica para a DH, que também tem como patogênese estresse oxidativo celular em regiões do SNC[116]. Além das novas terapias que abordam uso de antioxidantes[117], é importante analisar também outras drogas como possível atenuadoras de estresse oxidativo e também da excitotoxicidade mediada por glutamato (uma vez que ambos os fenômenos podem coexistir[118]). A neurotoxina Phα1β, por exemplo, derivada do veneno da aranha *Phoneutria nigriventer*, foi descrita como capaz de promover redução de espécies reativas de oxigênio além da liberação de glutamato em modelos de dor[119].

Quando consideramos o artigo 2 apresentado nessa tese, observamos que o tratamento com essa isoforma foi capaz de promover uma preservação neuronal tanto no corpo estriado como na medula espinal dos animais BACHD. Essa preservação foi fundamental para a manutenção do tamanho das fibras musculares esqueléticas além de uma melhora de parâmetros *in vivo*. Também comprovamos pela primeira vez, que os níveis de glutamato estão elevados no líquor desses animais e a isoforma Phα1β foi capaz de promover uma redução nesses valores. O principal mecanismo de ação para os efeitos dessa isoforma está associado a uma redução da expressão da caspase-3 em neurônios da medula espinal.

Complementando o que já foi discutido no artigo 2, gostaríamos de enfatizar e sugerir possíveis mecanismos de ação da isoforma Phα1β. Sabe-se que o veneno da aranha *Phoneutria nigriventer* contém um coquetel de toxinas que afetam os canais iônicos, sendo que a maioria desses peptídeos são bloqueadores de canais de cálcio[120]. O principal canal de cálcio inibido por

essa isoforma é o do Tipo- N[93], sendo esse subtipo de canal mais prevalente em terminais nervosos periféricos[121]. Foi sugerido por Vieira *et al*. 2005 que a Phα1β pode se ligar firmemente ao orifício externo do canal e promover uma oclusão física do poro, desencadeando o seu bloqueio. Em seu trabalho foi mostrado que tal isoforma não promoveu alteração na dependência de voltagem e nem na cinética dos canais de cálcio Tipo- N[93]. De forma geral, já se sabe que as neurotoxinas do veneno da aranha armadeira são capazes de se ligar a regiões próximas aos sensores de voltagem dos canais (o que pode promover alteração na dependência de voltagem e cinética de *gating*). Esses fenômenos não foram observados no trabalho de Vieira *et al*. 2005[93] sendo por fim sugerido um possível mecanismo de bloqueio físico dos canais de cálcio. O que também corrobora com a ação de bloqueio físico feito pela Phα1β, é a sua similaridade de sequência de aminoácidos com outras toxinas, como as Agatoxinas (já comprovadas como bloqueadoras físicas de canais de Ca^{2+})[76,122]. Nesse contexto, nós também sugerimos uma ação de bloqueio físico feita pela Phα1β sobre os canais de cálcio dos neurônios da medula espinal. Novos experimentos de eletrofisiologia são importantes para confirmar essa ideia.

Por fim, o bloqueio dos CCSV desencadeado pela Phα1β pode estar diretamente associado á queda na liberação de glutamato, como já foi descrito em outros estudos[90,91,123,100]. Ao diminuir a exposição excessiva ao glutamato o fenômeno de excitotoxicidade pode ser modulado[25] resultando em diminuição da apoptose e por fim morte neuronal. Em um estudo anterior feito por nosso grupo de pesquisa foi demonstrado que os motoneurônios da medula espinal dos animais BACHD estão atrofiados e possivelmente morrem após significativa ativação da caspase-3[124]. Novamente, nós confirmamos a ativação dessa via em nosso modelo, e de forma importante, constatamos que a isoforma Phα1β foi capaz de reduzir a expressão da caspase, provavelmente via diminuição do

influxo anormal de cálcio (íon importante para ativação dessa enzima[125]) desencadeado por uma menor excitotoxicidade mediada por glutamato (que se encontrou reduzido após o tratamento).

6- CONCLUSÕES

De forma geral podemos concluir que animais transgênicos para a DH apresentam anormalidades cardíacas, como observado no perfil eletrocardiográfico *in vivo*. Tal fato se relaciona com alterações *in vitro* como uma duração prolongada do potencial de ação dos cardiomiócitos, além de distúrbios arrítmicos de contração e relaxamento que estão de acordo com os desequilíbrios no manejo intracelular de cálcio, e também aumento na expressão de proteínas importantes para a maquinaria cardíaca. Esses efeitos podem ser explicados pelo aumento da expressão da CaMKII, como consequência do estresse oxidativo, evidência que é apoiada pela desorganização ultraestrutural das mitocôndrias associada ao aumento da função do eixo antioxidante celular e com as análises diretas de estresse oxidativo.

Além disso, também concluímos que a isoforma Phα1β apresenta efeito neuroprotetor a partir da diminuição da liberação de glutamato e da expressão de caspase-3 em neurônios da medula espinal. Essas mudanças podem ser associadas á preservação do número dos neurônios além da estrutura muscular, que deixou de apresentar hipotrofia nos animais BACHD. Por fim, houve melhora de parâmetros motores após o tratamento com essa neurotoxina.

A caracterização cardíaca somada a nova abordagem terapêutica, utilizando-se toxinas animais, podem contribuir para o avanço das pesquisas relacionas a essa doença, fatal e altamente incapacitante.

7- ANEXOS

Outros artigos foram publicados por nosso grupo de pesquisa considerando a caracterização do modelo transgênico BACHD, para a DH. Esses artigos estão dispostos a seguir.

7.1- Contextualização do artigo 3

Juntamente com as alterações cardíacas, outros fatores que podem causar morte dos pacientes com a DH são: pneumonia aspirativa (sendo a primeira causa de morte), associada à disfunção respiratória, diminuição da força muscular respiratória e disfagia[126,127]. Existem evidências na literatura que a DH, tanto em modelos animais como nos seres humanos, é capaz de promover atrofia da musculatura estriada esquelética[50]. Ainda não se sabe se essa atrofia ocorre de forma independente ou não do prejuízo do SNC. Realmente, a HTT mutante já foi encontrada em diferentes músculos[50] sugerindo uma possível ação local dessa proteína que poderia causar impactos musculares negativos de forma direta. No entanto, não podemos excluir o fato de que disfunções no SNC podem levar à desenervação seguida de alterações nas junções neuromusculares (JNMs) e por fim, distúrbios entre a comunicação neurônio/músculo[128], com comprometimento, por exemplo, da liberação de acetilcolina (principal neurotransmissor da contração muscular de mamíferos). A análise de um importante músculo respiratório, o diafragma, ainda não foi realizada no modelo BACHD. Além disso, não se sabe se existem alterações morfológicas e sinápticas no nervo frênico (responsável pela inervação desse músculo). Nesse contexto, nosso grupo de pesquisa também analisou aspectos morfológicos do nervo frênico, do músculo diafragma, de suas JNMs, e também a liberação de vesículas colinérgicas nos animais BACHD com 12 meses de idade.
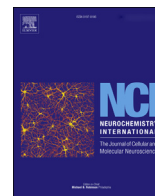
Esses resultados foram publicados em 2018 na *Neurochemistry International* e podem ser visualizados do artigo 3.

ARTIGO 3

Neuromuscular synapse degeneration without muscle function loss in the diaphragm of a murine model for Huntington's Disease

Priscila A.C. Valadão [a], Matheus P.S.M. Gomes [a], Bárbara C. Aragão [a],
Hermann A. Rodrigues [d], Jéssica N. Andrade [a], Rubens Garcias [a],
Julliane V. Joviano-Santos [a], Murilo A. Luiz [a], Wallace L. Camargo [b], Lígia A. Naves [b],
Christopher Kushmerick [b], Walter L.G. Cavalcante [c], Márcia Gallacci [e],
Itamar C.G. de Jesus [b], Silvia Guatimosim [b], Cristina Guatimosim [a, *]

[a] Departamento de Morfologia, Universidade Federal de Minas Gerais, Belo Horizonte, MG, Brazil
[b] Departamento de Fisiologia e Biofísica, Universidade Federal de Minas Gerais, Belo Horizonte, MG, Brazil
[c] Departamento de Farmacologia, Universidade Federal de Minas Gerais, Belo Horizonte, MG, Brazil
[d] Departamento de Ciências Básicas da Vida, Instituto de Ciências da Vida, Universidade Federal de Juiz de Fora, Campus Governador Valadares, UFJF, GV, MG, Brazil
[e] Departamento de Farmacologia, Instituto de Biociências, UNESP, Distrito de Rubião Jr., Botucatu, 18618-970 São Paulo, Brazil

ARTICLE INFO

ABSTRACT

Huntington's disease (HD) is an autosomal dominant neurodegenerative disease characterized by chorea, incoordination and psychiatric and behavioral symptoms. The leading cause of death in HD patients is aspiration pneumonia, associated with respiratory dysfunction, decreased respiratory muscle strength and dysphagia. Although most of the motor symptoms are derived from alterations in the central nervous system, some might be associated with changes in the components of motor units (MU). To explore this hypothesis, we evaluated morphofunctional aspects of the diaphragm muscle in a mouse model for HD (BACHD). We showed that the axons of the phrenic nerves were not affected in 12-months-old BACHD mice, but the axon terminals that form the neuromuscular junctions (NMJs) were more fragmented in these animals in comparison with the wild-type mice. In BACHD mice, the synaptic vesicles of the diaphragm NMJs presented a decreased exocytosis rate. Quantal content and quantal size were smaller and there was less synaptic depression whereas the estimated size of the readily releasable vesicle pool was not changed. At the ultrastructure level, the diaphragm NMJs of these mice presented fewer synaptic vesicles with flattened and oval shapes, which might be associated with the reduced expression of the vesicular acetylcholine transporter protein. Furthermore, mitochondria of the diaphragm muscle presented signs of degeneration in BACHD mice. Interestingly, despite all these cellular alterations, BACHD diaphragmatic function was not compromised, suggesting a higher resistance threshold of this muscle. A putative resistance mechanism may be protecting this vital muscle. Our data contribute to expanding the current understanding of the effects of mutated huntingtin in the neuromuscular synapse and the diaphragm muscle function.

© 2018 Elsevier Ltd. All rights reserved.

1. Introduction

Huntington's disease (HD) is an autosomal dominant neurodegenerative disease clinically characterized by chorea, incoordination, motor impersistence, psychiatric and behavioral symptoms (Finkbeiner, 2011; Walker, 2007). The worldwide prevalence of HD is 5–10 cases per 100,000 people (Baig et al., 2016). It is caused by an excessive number of CAG repeats ($\geq$37) in the Huntingtin gene (*IT15*), which translates into an elongated polyglutamine (polyQ) tail in the Huntingtin (HTT) protein (McNeil et al., 1997; Rubinsztein et al., 1996; The Huntington's Disease Collaborative Research Group, 1993).

The leading cause of death in HD patients is pneumonia (Roos,

2010), which is mainly due to dysphagia and aspiration (Heemskerk and Roos, 2011). Respiratory dysfunction, decreased respiratory muscle strength and lung volumes, as well as swallow dysfunction, are some of the factors underlying respiratory failure and dysphagia (Heemskerk and Roos, 2011; Jones et al., 2016).

The main cause of motor symptoms is the death of striatal medium spiny and cortical pyramidal neurons (DiFiglia et al., 1995; Vonsattel and DiFiglia, 1998). Mutant HTT (mHTT) with expanded polyQ are prone to aggregate, thereby affecting several key neuronal processes such as nuclear transcription, apoptosis, mitochondrial function, axonal transport and neurotransmitter release, all eventually leading to neuronal death (Harjes and Wanker, 2003; Li and Li, 2004). Other possible explanations are: i) the mutation of the protein confers a new function to HTT that is toxic to the cell (gain of toxic function); and ii) the normal protein is sequestered in clusters formed by mHTT, thus leading to loss of normal protein function (Browne and Beal, 2004; Imarisio et al., 2008; Zuccato et al., 2010).

The HTT is a 348 kDa multiple domain protein that is usually expressed at high levels in the central nervous system (CNS) of humans and rodents (Difiglia et al., 1997; Ferrante et al., 1997). Both the normal and mutated forms are also expressed in tissues outside the CNS such as in the skeletal muscle, heart, liver, pancreas, kidney, testis and stomach (Van Der Burg et al., 2009). Although normal HTT can be found in the cell nucleus, the protein is primarily found in the cytoplasm associated to organelles such as the Golgi complex, mitochondria, endoplasmic reticulum, synaptic vesicles, and cytoskeletal components (Hoffner et al., 2002). Interestingly, a large number of proteins interact with HTT to help axonal transport by microtubules (Schulte and Troy Littleton, 2011). Gauthier et al. (2004) showed that normal HTT is capable of improving vesicular transport by interacting with huntingtin-associated protein 1 (HAP1), which is attached to the p150 subunit of dynactin. The HAP 1 is also found associated with motor proteins such as dynein and kinesin that are proteins involved with retrograde and anterograde axonal transport (Caviston and Holzbaur, 2009; Wu and Zhou, 2009; Schulte and Troy Littleton, 2011).

Although several studies have focused on elucidating the mechanisms of neurodegeneration in the brain, the expression of the *IT15* gene and HTT are not restricted to this organ, as they occur in many peripheral tissues, including skeletal muscles (Farrar et al., 2011; Sassone et al., 2009; Smith et al., 2006; Yuen et al., 2012). Previous studies have shown contractility reduction, muscle atrophy, dysregulation of contractile proteins, changes in NMJs, and electrophysiological alterations in skeletal muscles of HD mouse models (Mielcarek, 2015; Sathasivam et al., 1999). However, these studies are limited to the early stages of the disease in mice, which correspond to the pre-clinical manifestation of the disease in humans. There are a few reports considering HD in the skeletal muscles of patients with the late stages of the disease. For example. the sternomastoid muscle, a skeletal neck muscle important for head stability, was investigated by Valadão et al. (2017).

One feature of HD is the progressive weakness and uncoordinated movements of the face, neck, lips and diaphragm muscle, which underlie the chewing and swallowing difficulties that arise in patients later in their life, when the first symptoms of the disease appear (Brotherton et al., 2012). However, the structural and functional alterations in the diaphragm of HD patients remains poorly understood. We have previously described neuromuscular synaptic defects in the diaphragm of 3-months-old BACHD mouse model for HD, which corresponds to the pre-clinical stage in humans. We found morphological alterations in the shape and circumference of synaptic vesicles, decreased exocytosis and a reduction in the amplitude of miniature endplate potentials (MEPPs) in diaphragm NMJs from BACHD mice (de Aragão et al.,

2016). However, the main impairments in diaphragm function occur at later stages of the disease and virtually nothing is known about the changes in this muscle in patients with advanced HD.

To further understand the mechanisms underlying HD progression, we investigated the motor pathology of the diaphragm nerve-muscle communication in the 12-months-old BACHD mouse model, which corresponds to the late clinical manifestation of the disease in humans. The BACHD mouse is a particularly attractive model because it shows symptoms that closely resemble human HD such as progressive motor and cognitive impairment, psychiatric-like disturbances and striatal neuronal loss. Moreover, it allows for the study of the later stages of the disease (Gray et al., 2008).

2. Materials and methods

2.1. Drugs and chemicals

FM1–43, FM1–43fx, α-bungarotoxin (α-btx) and ProLong® Gold antifade were purchased from Invitrogen™; D–tubocurarine and ADVASEP-7 were purchased from Sigma–Aldrich. All other chemicals and reagents were of analytical grade.

2.2. Animals and ethical procedures

The experimental procedures were carried out in accordance with the protocol approved by the local Ethics Committee on Animal Experimentation - CEUA/UFMG − protocol 036/2013. All efforts were made to minimize animal suffering and to reduce the number of animals used. This study was not pre-registered. The experimental procedures in this work were performed at Departments of Morphology and Physiology of Universidade Federal de Minas Gerais (UFMG) and the Department of Pharmacology, Institute of Biosciences of the Universidade do Estado de São Paulo (UNESP). We used the male mouse from the strains FVB/NJ wild-type (WT) and FVB/N-Tg (HTT*97Q) IXwy/J (BACHD) (RRID: SCR #008197). These transgenic animals were purchased from the Jackson Laboratory (Bar Harbor, ME, USA) and were housed at the animal care facility of the Department of Physiology and Biophysics at the Universidade Federal de Minas Gerais (UFMG). Upon arrival, the animals were housed at 23 °C on a 12 h light/12 h dark cycle with food (Nuvilab CR-1) and water provided *ad libitum*. All animals used in this study were genotyped 10 days after birth using multiplex PCR (HTT-Forward: CCGCTCAGGTTCTGCTTTTA/ HTT-Reverse: GGTCGGTGCAGCGGCTCCTC.

Actin- Forward: TGGAATCGTGTGGCATCCATCA/Actin- Reverse: AATGCCTGGGTA CATGGGGTA).

All animals used in this study were appropriately identified by numbers according to their genotype (WT or BACHD) and separated into mini-isolator cages (length: 48.3 cm; width: 33.7 cm; height: 21.4 cm) with a maximum of four animals per cage. The mice were randomly divided into two groups using a table of random numbers. The number of experiments is provided in the figure legends/results section. The experimental groups remained constant from the beginning to the end of the study. For all experiments involving morphology and electrophysiology techniques, mice from both genotypes (WT and BACHD) were deeply anesthetized with ketamine/ xylazine (0.1 mL/20 g) in accordance with the CEUA/UFMG protocol. All surgical procedures are described in the appropriate following sections. The experimental procedures were performed in the afternoon and by the end of each surgical procedure, animals were euthanized by a super-dosage of anesthetics.

2.3. Nerve-muscle preparation

The phrenic nerve was processed following the transmission

electron microscopy (TEM) protocol (see below, topic 2.8). The semi-thin cross sections (300 nm) obtained and stained with to-luidine blue as described were used to capture images of whole phrenic nerve cross-sections from WT and BACHD mice using a 20x objective in a ZEISS Axio Lab. A1 microscope. The cross-sectional area of the nerve was measured using ImageJ plugins (NIH). To quantify axonal myelination we used the G-ratio, which was calculated measuring the axonal inner diameter and dividing it by the outer diameter following the formula: $G = d/D$, where G is the G-ratio, d is the inner diameter, and D is the outer diameter (Chau et al., 2000).

For FM1-43 experiments, the diaphragm muscle was dissected out, split in two hemi diaphragms and bathed in mouse Ringer solution (135 mM NaCl, 5 mM KCl, 2 mM CaCl$_2$, 1 mM MgCl$_2$, 12 mM NaHCO$_3$, 1 mM Na$_2$HPO$_4$, and 11 mM D-glucose) that was bubbled with a mixture of 95% O$_2$—5% CO$_2$ and the pH adjusted to 7.4.

For Transmission Electron Microscopy (TEM) experiments, the diaphragm muscles were fixed in ice-cold modified Karnovsky solution fixative (4.0% paraformaldehyde and 2.5% glutaraldehyde in 0.1 M sodium cacodylate buffer).

2.4. Staining of pre and post-synaptic elements

Experiments were performed as described previously (Rodrigues et al., 2013). Briefly, immediately after dissection, the diaphragm muscles were labeled with α-btx- Alexa Fluor 555 (12 μM) for 20 min to visualize the clusters of nicotinic receptors in the postsynaptic membrane. FM1-43fx (8 μM) was added to stain recycling synaptic vesicles during stimulus with a high-K$^+$ solution (60 mM KCl) for 10 min. After stimulation, the diaphragm muscle preparations were maintained at rest in normal Ringer solution with FM1-43fx for 10 min to guarantee maximal dye uptake during compensatory endocytosis. Excess of FM1-43fx adhering to the muscle plasma membrane and nerve terminal membrane was removed during a 40 min washing period in mouse Ringer solution devoid of FM1-43fx. To reduce the background fluorescence, we added Advasep-7 (1 mM) during the washing step (after FM1-43fx staining). Diaphragms were fixed with 4% paraformaldehyde for 40 min and then mounted onto slides using ProLong® Gold (Invitrogen, SP, Brazil) mounting medium.

2.5. Confocal microscopy and image analysis

Confocal microscopy experiments followed the steps described in previous works published by our group (Valadão et al., 2017; Rodrigues et al., 2013). Images of NMJs stained with FM1-43fx and α-btx - Alexa Fluor 555 were acquired with a confocal laser scanning microscope (Zeiss LSM 880 - located at Center of Acquisition and Processing of Images (CAPI) − ICB/UFMG), using an oil immersion objective (63x/NA 1.4) for quantification of pre and post-synaptic elements. The excitation light came from an argon laser (488 nm) and the emission spectrum was set from 507 to 564 nm to FM 1-43fx. To visualize the α-btx - Alexa Fluor 555 staining, we used a helium-neon laser (543 nm) and the emission light was collected (577—697 nm). Optical sections in Z series mode were collected at 2.0 μm intervals. During image acquisition, whole hemi diaphragms were scanned and the images were obtained from muscle areas with stained pre and post-synaptic terminals. Quantitative analyses of nerve terminals were carried out with Image J software (Wayne Rasband, National Institutes of Health, USA). For each set of experiments, the images were converted to a gray scale format of 8 bits. All marked synaptic elements were individually evaluated and the mean fluorescence intensity was considered for comparisons between genotypes. The nerve terminals were identified considering their colocalization with nicotinic acetylcholine receptors (nAChR) clusters.

We used the method of particles analysis to obtain the NMJs fragmentation index based on the pixels presented in each image (Pratt et al., 2013). Briefly, the images were converted into a binary image pattern and then skeletonized. Next, to describe the connectivity for each pixel in the image, a histogram was generated using the Binary Connectivity Class plugin from ImageJ (Pratt et al., 2013). We analyzed the degree of fragmentation in pre- and post-synaptic elements comparing muscle samples obtained from WT and BACHD mice. The parameters adopted for fragmentation were defined according to evaluation criteria that establish fragmentation by five or more islands both in the presynaptic and postsynaptic membranes, as described by Valdez et al. (2010).

2.6. Monitoring exocytosis with FM1—43

These experiments were performed as described in de Aragão et al. (2016) and Rodrigues et al. (2013). The fluorescent dye FM1-43 binds reversibly to the outer leaflet of biological membranes membrane without permeating them, being a powerful tool to track exocytosis, endocytosis and recycling of secretory granules or vesicles (Betz and Bewick, 1992). FM1-43 binds to the synaptic membrane and after a stimulus that causes exocytosis of synaptic vesicles and consequently a compensatory endocytosis, the fluorescent dye is incorporated. This results in a typical staining pattern of the synaptic vesicles (Betz and Bewick, 1992). When the nerve terminals are subjected to a new round of stimulation in the absence of FM1-43 in the external medium, the dye is released into the hydrophilic medium, leading to a decrease in the fluorescence intensity, which represents the exocytosis of synaptic vesicles (Rizzoli and Betz, 2004; Betz et al., 1996; Betz and Bewick, 1992). The neuromuscular preparations were stimulated by the addition of a saline solution containing a high concentration of potassium (60 mM KCl) in the presence of the vital dye FM1-43 (4 μm) for 10 min. After stimulation, the preparation was left for 10 min to rest in Ringer solution containing FM1-43. Then, the preparation was washed in Ringer solution devoid of FM1-43 for at least 20 min to allow the excess of labeled FM1- 43 adhered to the membrane of the synaptic terminal and the muscle cell membrane to be removed. The preparations were incubated in the presence of D-tubocurarine (16 μM) to prevent muscle contractions during the entire experimental procedure. For each animal, we used only one presynaptic terminal for monitoring the destaining process (exocytosis).

2.7. Optical imaging and analyses

Images of NMJs stained with FM1-43 were acquired using a fluorescence microscope (Leica DM2500) coupled to a Leica DFC 345FX camera and visualized in a microcomputer with the Leica Application Suite software (LAS). The microscope was equipped with a water immersion objective (63x, 0.95NA). Excitation light came from a 100-W Hg lamp and passed through filters (505/530 nm) to select the fluorescence spectrum appropriate to the excitation of the FM1-43. All image adjustment variables such as binning and the exposure time were maintained constant for images acquired in the same experiment. Image analyses were performed using the software Image J allowing quantification of the brightness of several regions of interest. The mean fluorescence intensity was determined for each group of fluorescent spots and plotted as a percentage of its mean initial fluorescence using Microsoft Excel and Graph Pad Prism 4.0.

2.8. Transmission electron microscopy

These experiments were performed as described in Rodrigues
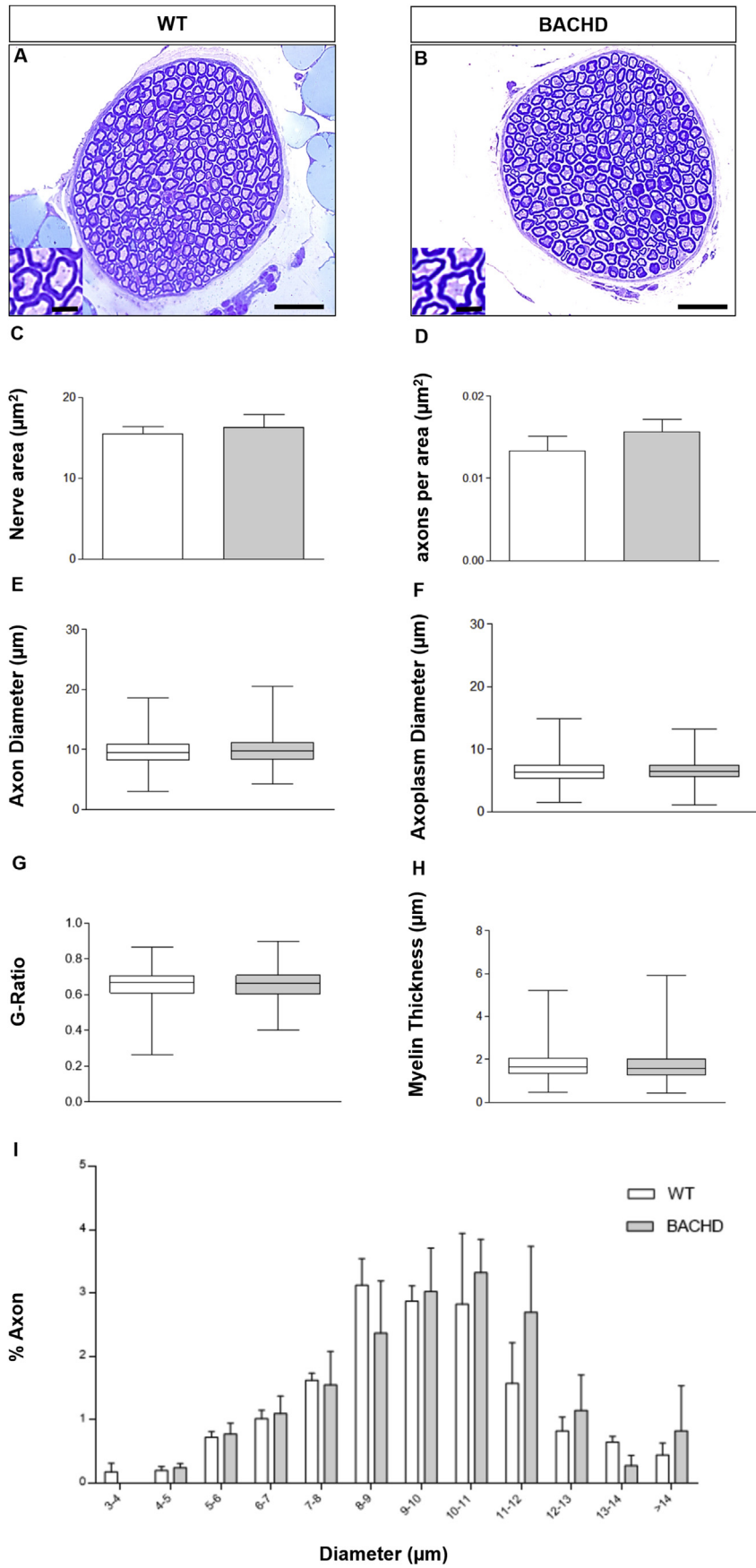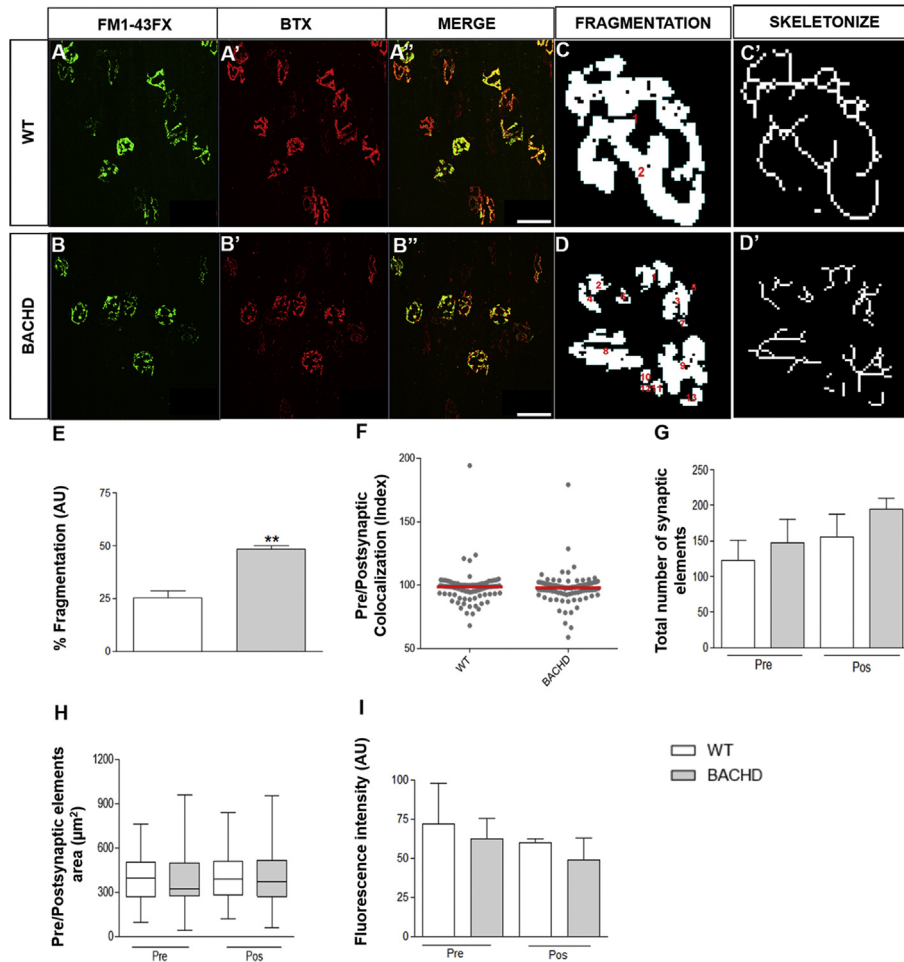
Fig. 2. BACHD mice show fragmentation of diaphragm neuromuscular junctions (NMJ). A-B'': Representative images of diaphragm NMJs of 12-months-old WT and BACHD mice. A and B: Presynaptic terminals labeled with FM1-43fx (green). A' and B': Postsynaptic acetylcholine receptors (AChRs) labeled with Alexa-555 α-bungarotoxin (red). A'' and B'': Merged images. C and D: Representation of the particle analysis for both genotypes (red numbers indicate the number of fragments in each NMJ). C' and D': Skeletonization rendering of fragmentation in endplates from WT and BACHD. E—I: Graphs showing fragmentation of NMJs (E), the index of co-localization (F), total number of synaptic elements (G), pre- and postsynaptic elements area (H) and fluorescence intensity (I). Results are presented as mean ± SD of 55 NMJs per genotype. Mann-Whitney test (F and H); unpaired Student's t-test (E, G and I); **p = 0,0031; n = 3 animals per genotype. Scale bar = 50 μm. (For interpretation of the references to colour in this figure legend, the reader is referred to the Web version of this article.)

et al. (2013). For ultrastructural analysis, diaphragm muscles were fixed overnight in a modified Karnovsky solution at 4 °C. After fixation, the samples were washed with cacodylate buffer (0.1 M). The preparations were cut into several pieces, post-fixed in reduced osmium (1% osmium tetroxide containing 1.6% potassium ferrocyanide) for 90 min at 4 °C, washed with water, contrasted *en bloc* with uranyl acetate (2% uranyl acetate in deionized water) and dehydrated through an ascending series of ethanol solutions. After dehydration, the samples were embedded in EPON resin. Then, the blocks were sectioned in semi-thin sections (300 nm) that were placed onto glass slides and stained with toluidine blue to aid the selection of regions of interest. Ultra-thin sections (50 nm) were collected on 300 mesh copper grids and contrasted with lead citrate. The sections were viewed with a Tecnai-G2- Spirit-FEI/Quanta electron microscope (120 kV Philips) located at the UFMG's

Microscopy Center.

2.9. TEM imaging analysis

NMJs were selected based on the presence of mitochondria and junctional folds in the postsynaptic membrane. Single sections through terminals of interest were traced and the cross-section area of each nerve terminal and the number of synaptic vesicles were determined. Analyses were performed as described in Rodrigues et al. (2013).

Vesicle circumference was measured using equation $2\pi [(d2 + d2)/2] 0.5$ considering the longest diameter (d) and the diameter at right angles (d_2) (Van der Kloot et al., 2002). Synaptic vesicles shape was determined using the equation: shape factor = $(4 \times \pi \times area)/(perimeter)^2$. This parameter reaches a maximum of

Fig. 1. BACHD mice do not present alterations in phrenic nerve morphology. A—B: Representative images of axons from 12-months-old WT and BACHD mice, respectively. Note the typical axons with preserved structure in both genotypes (inserts in A and B). Axons were stained with toluidine blue. Scale bar: 10 μm. C—H: Quantification of nerve area (C), number of axons per nerve area (D), axon's diameter (E), axoplasm diameter (F), G-ratio [G = d/D, where G is the G-ratio, d is the inner diameter, and D is the outer diameter] (G), and myelin thickness (H). I: Histogram of the axonal size. *n* = 3 animals per group. We analyzed one semi-thin section per animal; 659 axons in WT and 708 in BACHD. Mann-Whitney test (E, F, G and H); unpaired Student's t-test, p > 0.05 (C, D and I). (For interpretation of the references to colour in this figure legend, the reader is referred to the Web version of this article.)
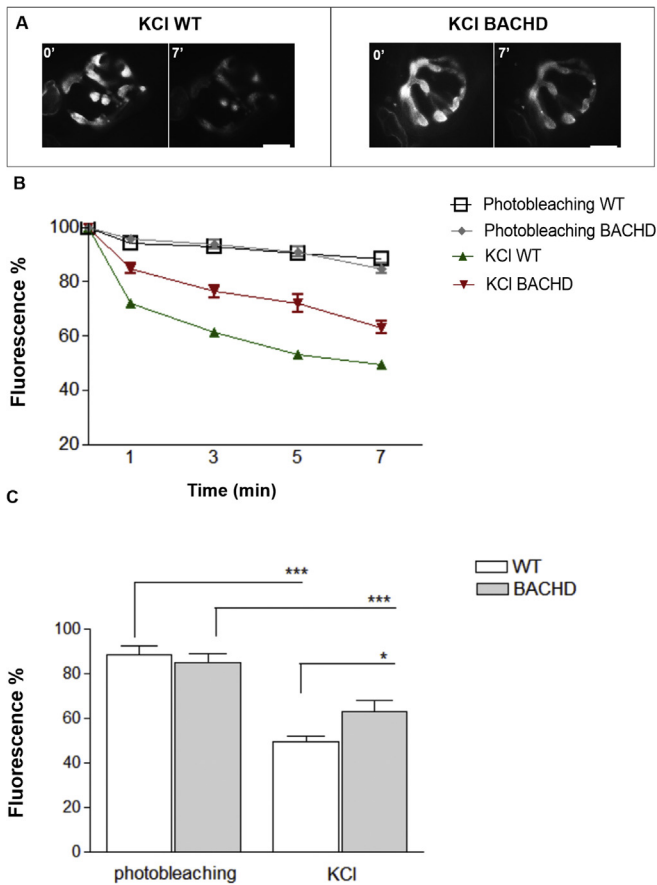
Fig. 3. BACHD mice show decreased synaptic vesicles exocytosis in the diaphragm nerve terminals. A: Representative images of the axon terminal of WT and BACHD diaphragm labeled with FM1-43 before (time 0′) and 7 min (time 7′) after the depolarizing stimulus. B: Fluorescent signal decay during 7 min following the depolarizing stimulus in WT (green) and BACHD (red) nerve terminals. Black and gray curves represent fluorescence decay control due to photobleaching. C: Graph showing fluorescence decay due to photobleaching and exocytosis evoked by KCl stimulus in WT (white) and BACHD (gray) animals. Five fluorescent points per nerve terminal were analyzed and four animals per genotype were used for quantification. The results express the mean ± SEM of 20 fluorescent points for each experimental group. Unpaired Student's t-test; *p < 0.05, ***p < 0.0001. Scale bar = 10 μm. (For interpretation of the references to colour in this figure legend, the reader is referred to the Web version of this article.)

1 for a circular object (Croft et al., 2005). The values for circumference and shape factor are shown by a histogram and a cumulative probability plot and compared using the Mann Whitney test. The graphs were plotted using the software Minitab and Sigma Plot 10.0 0 (SyStat Software) Graph Pad Prism 4.0. While determining the average circumference of the synaptic vesicles, we did not correct for variability in the plane of the section through which the vesicles were cut. Although this is likely to underestimate vesicle diameter and lead to variability in size and shape, we did not expect this to change the interpretation of our results. Indeed, these effects should be similar for the identically prepared samples from WT and BACHD mice. Van der Kloot et al. (2002) used a similar approach.

2.10. Electrophysiology

Hemi-diaphragm nerve-muscle preparations were prepared as described above and maintained in Ringer solution bubbled with carboxygen (5%CO2/95% O2) at room temperature (22–24C). For recordings, muscles were pinned onto a bed of silicon rubber (Sylgard; DowCorning, Midland, MI) in a 5 mL chamber on the stage

of a dissecting microscope and perfused with carboxygenated Ringer at 1–2 mL/min. Microelectrodes were fabricated from borosilicate glass using a Narishige puller (PN-30) and had resistances of 8–15 MΩ when filled with 3M KCl. Recordings were made with an Axoclamp 2A 10-X preamplifier (Molecular Devices) connected to a CyberAmp 380 (Molecular Devices) that filtered the signal at a band with of 0.1–5 kHz and then applied further amplification by 20–100 times, as needed. A second channel recorded the DC-coupled 10 times Vm signal which was used to correct for resting potential and non-linear summation (see below). Data was sampled at 100 kHz by a digital-to-analog converter (National Instruments) in a PC computer controlled by the program WinEDR (kindly provided by John Dempster, University of Strathclyde).

Microelectrodes were inserted into the muscle fibers in the endplate region as verified by the presence of miniature endplate potential (MEPP) with rise time < 1 ms. To measure quantal size, tetrodotoxin (100 nM) was included in some experiments to avoid action potentials and movement artifacts. In experiments with nerve stimulation, we used the cut-fiber method (Barstad and Lilleheil, 1968) which depolarizes the nerve fiber thus preventing muscle contraction. For stimulation, the nerve was drawn into a suction electrode and suprathreshold 0.1 ms voltage pulses were applied. Amplitudes of EPPs and MEPPs were corrected to a standard resting potential of −70 mV for intact fibers or −36 mV for cut fiber experiments. EPP amplitudes were further corrected for non-linear summation (McLachlan and Martin, 1981).

To measure quantal size in intact fibers, we sampled >100 MEPPS from each of 5 fibers from 5 animals of each genotype. For measurements of EPP, quantal content, tetanic depression and readily-releasable pool, measurements were from 4 to 7 fibers per animal from 3 different animals per genotype. The nerve stimulation protocol consisted of 90 stimuli applied at 0.3 Hz followed by 1500 stimuli at 30 Hz. MEPP amplitudes were captured during the intervals between stimuli. Quantal content was calculated by the direct method and expressed in units of EPP/MEPP, for which quantal size (i.e. MEPP amplitude) was determined separately for each fiber. Synaptic depression was calculated as the average of 30 EPP amplitudes at the end of a 50 s train at 30 Hz, normalized to the amplitude of the first EPP in the train. Readily-releasable pool was estimated by fitting a line to the relationship of QC vs ΣQC (Elmqvist and Quastel, 1965). For these calculations, the linear fit started at the second EPP, to allow for facilitation and 10 EPPs were used for the fit. Estimates of RRP are expressed in units of EPP/MEPP (i.e. quanta).

2.11. Neuromuscular preparation and recording of muscle contractions

The phrenic nerve-diaphragm muscle preparation was removed and mounted for myographic recording "*in vitro*", as described by Gallacci and Oliveira (1994). Briefly, the preparation was mounted vertically in a conventional isolated organ-bath chamber containing 15 mL of Ringer's solution. This solution was gassed with O2 (95%) + CO2 (5%) and maintained at 35 °C. Muscle contractions were recorded by isometric force transducer (FT03, Grass) coupled to an AcquireLab Data Acquisition System (Gould). Indirect contractions were evoked by supramaximal strength pulses delivered from an electronic stimulator (S88K, Grass) and applied to the phrenic nerve using a suction electrode. Once mounted in the test apparatus, muscles were allowed to stabilize for 30 min, and an indirect stimulation (0.2 Hz, 5 ms) was used to establish the muscle viability.
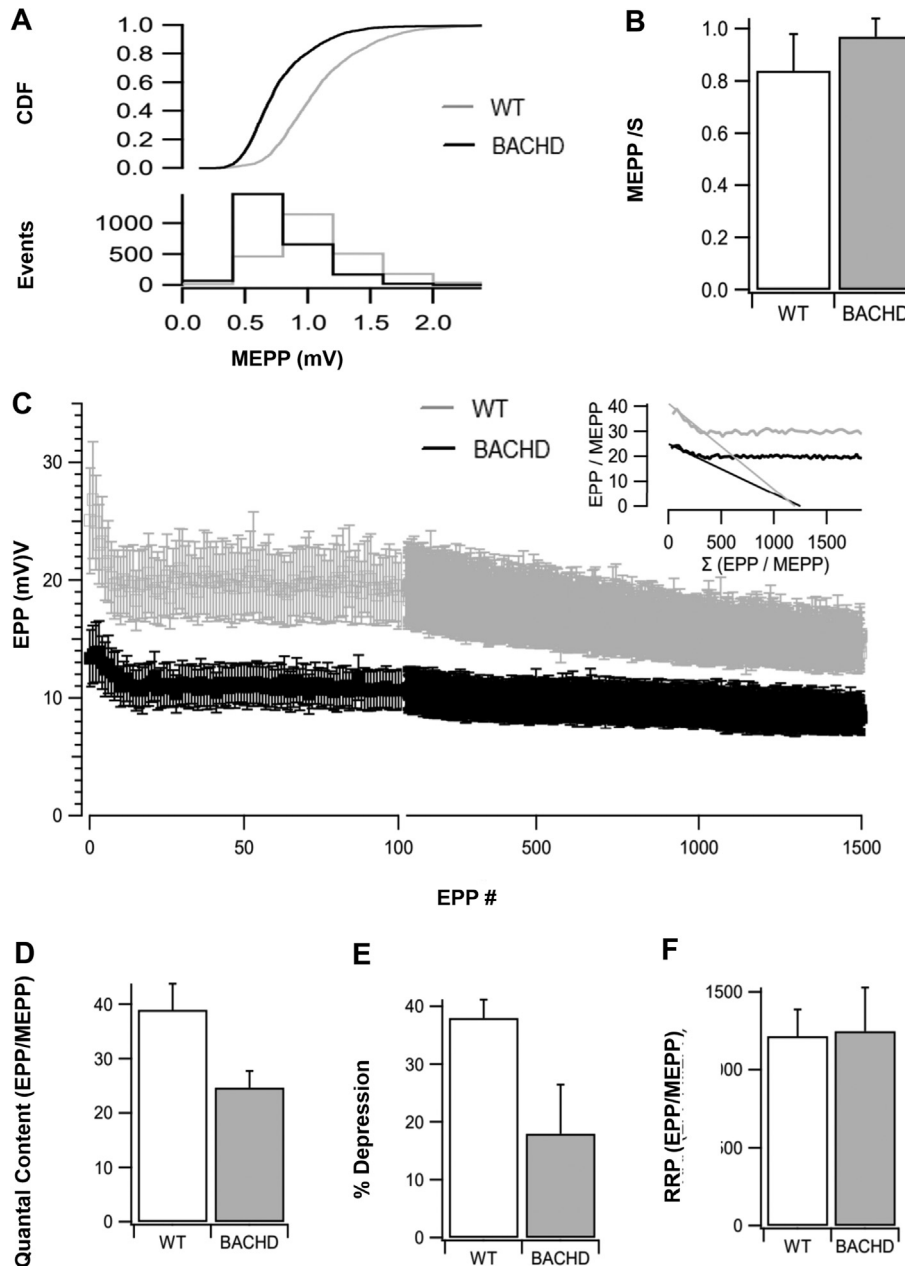
Fig. 4. Reduced quantal release at BACHD NMJs. A: Amplitude cumulative distribution function (CDF) and histogram for MEPPs recorded from WT NMJ (grey lines) or BACHD NMJ (black lines). Groups are pooled from 5 animals of each genotype. For each group, 4–5 fibers were sampled from each animal, resulting in 24 fibers in each group. B. Frequency of MEPPs measured in WT or BACHD NMJ. Data are from the same groups as shown in panel A. C. Average EPP amplitudes during 30 Hz stimulation. Data are pooled from 3 animals of each genotype, 4–7 fibers per animal, resulting in N = 14 fibers (WT) and 20 fibers (BACHD). Note change in horizontal scale after EPP# 100. Insert: Average quantal content of each EPP in the stimulus train plotted against the cumulative quantal content. Quantal content was determined as EPP/MEPP where quantal size was determined for each fiber by recording MEPPs in the intervals between evoked events. Lines indicate extrapolation of the initial linear phase of depression to the horizontal axis to estimate RRP. D. Average quantal content of EPPs recorded during low frequency stimulation (0.3 Hz). E. Extent of depression induced by 50 s of 30 Hz stimulation. For each fiber, the average amplitude of 15 events at the end of a 50 s train were normalized to the amplitude of the first EPP in the train. F. Readily reliable pool, determined for each fiber using the method illustrated in the inset to Panel C. Experimental groups for Panel C insert, Panel D and Panel E are the same as described above for Panel C. For determination of RRP, fibers that exhibited less than 15% depression generated unreliable estimates and were excluded from analysis, resulting in N = 12 fibers for WT and 14 fibers for BACHD.

2.12. Safety margin of synaptic transmission

The overall safety margin of the synaptic transmission was evaluated from the susceptibility of indirectly evoked contractions of the diaphragm muscle to the blockade induced by the addition of increasing concentrations of pancuronium bromide or magnesium to the organ bath, allowing 10 min between each concentration. The ratio of muscle tension in the presence and absence of

pancuronium or magnesium was used to estimate the safety margin of neuromuscular transmission.

Other preparations were submitted to a gradual increase of tetanic stimulation, starting at 70 Hz and ending at 220 Hz, with a gradual increase of 10 Hz. Each tetanus lasted 5 s with an interval of 10 min between them. During this interval, supramaximal pulses (0.2 Hz; 0.5 ms) evoked indirect contractions. The ability of the preparation to support the different tetanus was assessed by the
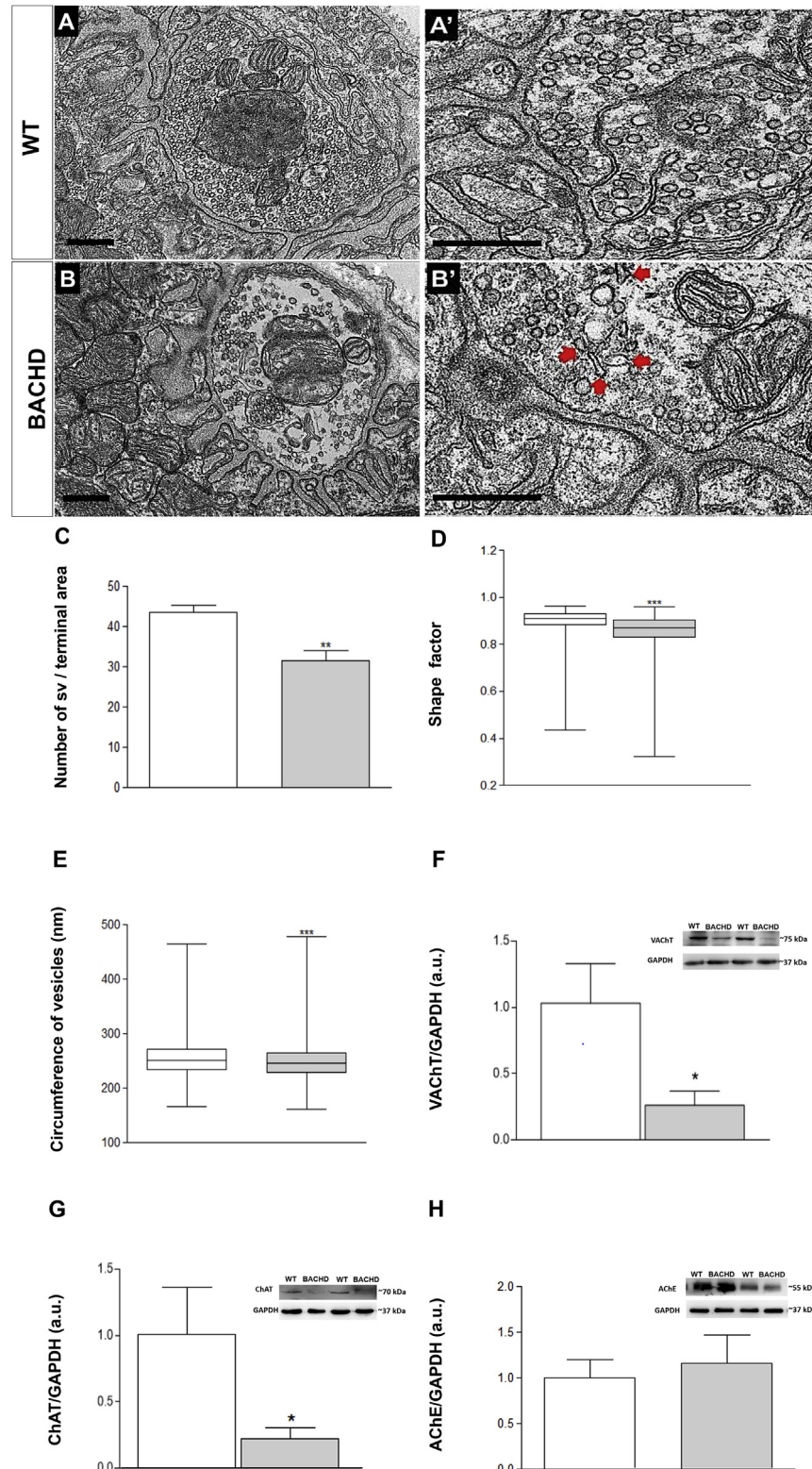
Fig. 5. **BACHD mice present ultrastructural changes in the morphology of the synaptic vesicles of diaphragm NMJs**. A: Representative image of a WT diaphragm nerve terminal. B: Representative images of a BACHD nerve terminal presenting synaptic vesicles with heterogeneous sizes. Scale bar = 500 nm. A' and B': Representative images showing nerve terminals with changes in the size and shape of the synaptic vesicles (red arrows). Scale bar = 500 nm. C: Graph representing the number of synaptic vesicles per terminal area (Unpaired student's t-test; *$p = 0.0286$). D: Boxplot comparing the synaptic vesicles shape in WT and BACHD mice (Mann Whitney test, ***$p < 0.0001$). E: Boxplot comparing synaptic vesicles circumference in WT and BACHD mice (Mann Whitney test, ***$p < 0.0001$). We analyzed at least 15 NMJs profiles from three animals per genotype. All integrally visualized synaptic vesicles were used for the quantification of shape and circumference. A total of 3723 synaptic vesicles were analyzed for WT and 2343 for BACHD F–H: Western blot analysis of VAChT (F), ChAT (G) and AChE (H) proteins in diaphragm muscle of WT and BACHD. GAPDH was used as a control of protein loading between experiments. GAPDH protein levels are similar between WT and BACHD. Data are presented as a percentage of WT (Unpaired student's t-test; ***$p = 0.0286$, *$p = 0.04$). (For interpretation of the references to colour in this figure legend, the reader is referred to the Web version of this article.)

relationship between the amplitude of the initial tetanic peak amplitude and the moment at which the stimulus was ended.

2.13. Fatigue resistance

After the diaphragm muscle was stabilized, the preparations were submitted to a repeat sequence of 30 tetanic contractions, with 5 s long, 130 Hz and an interval of 20 s. Fatigue resistance was defined as the amplitude of the last contraction of the series relative to the first, expressed as a percentage. Results were expressed as mean ± S.E. Data were analyzed by ANOVA complemented by the Tukey-Kramer test. Values of $p < 0.05$ were considered significant.

2.14. Western blot

To detect the vesicular ACh transporter (VAChT), Choline acetyltransferase (ChAT) and Acetylcholinesterase (AChE) in diaphragm muscles, 50 μg of protein were separated by SDS-PAGE. The antibodies used and their sources are as follow: anti-VAChT (1:2000; Sigma-Aldrich Cat# V5387 RRID: AB_261875), anti-ChAT (1:1000; Abcam Cat#ab70219 RRID: AB_1209541) and anti-AChE (1:1000; Thermo Fisher Scientific Cat#MA3-042 RRID: AB_325478) Glyceraldehyde-3-phosphate dehydrogenase (GAPDH; 1:3000; Santa Cruz Biotechnology Cat#sc- 20356 RRID: AB_641103). Validation data for each antibody were obtained from the data-sheet provided by the company. Immunodetection was carried out using enhanced chemiluminescence (Amersham Biosciences). Protein levels were expressed as a ratio of optical densities. GAPDH was used as a protein loading control.

2.15. Statistical analysis

All data were registered using Microsoft Excel and were plotted using the program GRAPHPAD PRISM 6. For data with normal distribution, values were represented as the mean ± standard deviation (mean ± SD) and statistical significance was evaluated using the unpaired Student's t-test. When data were not normally distributed, the values were represented as the median and the Man-Whitney test was used to assess statistical significance. Values of $p < 0.05$ were considered significant. Exact p-values are provided in the figure legends. During the analyses, the investigators were blinded to the genotypes and experimental groups. Each genotyped animal was assigned a number that was revealed to the investigator only after the analyses ended.

In this work, we used a minimum of three animals per genotype for each data set to detect a difference at 95% confidence ($a = 0.05$) and 0.8 statistical power. The exact n for each experimental procedure is described in the figure legends. All data points were treated as outliers and excluded from the data analysis outside the 95% confidence interval.

3. Results

We previously described neuromuscular synaptic defects in the diaphragm of adult (3-months-old) BACHD mice (de Aragão et al., 2016). Herein, we asked if aging would exacerbate those defects. We initially looked at the structure of the phrenic nerve that is responsible for innervation of the diaphragm muscle in 12-months-old BACHD and WT mice. Histological analysis of this nerve showed that, in both genotypes, the phrenic nerve was preserved (Fig. 1A–B), with no alterations in the analyzed parameters: i) nerve area (C) ii) number of axons per area (D); iii) axon diameter (E); iv) axoplasm diameter (F); v) G-ratio (G); and vi) size of the axons (H).

Labeling the nerve-muscle preparations with the activity-dependent fluorescent marker FM1-43fx and the postsynaptic nicotinic receptors for ACh with the α-btx conjugated to Alexa Fluor 555, revealed significant alterations in the motor nerve terminals during depolarizing stimulus. Fig. 2 shows representative images of pre- and postsynaptic elements of the diaphragm NMJs of WT (Fig. 2A–A″) and BACHD (Fig. 2B- B″) mice. Fragmentation analysis showed that diaphragm NMJs from 12-month-old BACHD mice are more fragmented than diaphragm NMJs of WT animals (Fig. 2C–C′, D-D′ and E). The quantitative analysis of the pre- and postsynaptic elements showed no statistically significant differences in the following morphological parameters: i) co-localization of pre- and postsynaptic elements (Fig. 2F); ii) total number of elements (Fig. 2G); iii) area of the elements (Fig. 2H). Measuring endocytic activity through fluorescence intensity of the presynaptic elements did not reveal significant differences between the genotypes (Fig. 2I). Next, using FM1-43, we measured the exocytosis of synaptic vesicles in the diaphragm NMJs of BACHD and WT animals. The fluorescence intensity was reduced in the diaphragm NMJs of both BACHD and WT mice, especially in the later (Fig. 3B). The KCl-evoked decrease in the fluorescent signal in the nerve terminals was greater in the WT in comparison with the BACHD mice (Fig. 3C). Diaphragm NMJs of WT mice showed a decrease in fluorescence of approximately 50% whereas the diaphragm NMJs of BACHD mice lost about 35% of their fluorescent signal (Fig. 3C). No significant differences were observed between WT and BACHD photobleaching values (Fig. 3C).

Electrophysiological recordings show that MEPPs of BACHD mice have smaller amplitudes when compared with WT (Fig. 4A). In contrast, there was no significant difference in MEPPs frequency between the two genotypes. (Fig. 4B).

Since we found that BACHD animals have a decreased rate of destaining, which suggests an imparment in the exocytosis, we measured evoked release during low frequency (0.3 Hz) and high frequency (30 Hz) stimulation. In between evoked events, we captured MEPPs to calculate quantal content by the direct method (EPP/MEPP). Both EPP amplitude and quantum content were significantly reduced in BACHD animals (WT: EPP = 26.6 ± 5.5 mV, QC = 39 ± 4.8; BACHD: EPP = 14.0 ± 2.5 mV QC = 24.7 ± 3.1, $p < 0.05$). During high frequency stimulation, average EPP amplitude declined in both WT and BACHD groups, however tetanic depression was stronger in WT groups (Fig. 4E). At the end of a 50 s train at 30 Hz, EPP amplitudes in WT fibers had declined by 38 ± 3.2% of compared to a decline of only 18 ± 8.5% in the BACHD Group ($p < 0.05$).

We estimated the size of the Releasable pool using a calculation based on the method of Elmqvist and Quastel (1965). EPPs were measured during 30 Hz stimulation and the QC of each EPP in the train plotted as a function of the cumulative release (Fig. 4C, insert) and a line fit to the initial, linear phase of depression and extrapolating to the horizontal axis. These data indicate an available pool of about 1200 quanta, with no significant difference between WT and BACHD animals. Based on these results, we conclude that, although the pool of vesicles available is similar in WT and BACHD NMJ, the BACHD group have a lower release probability, resulting in fewer quantal released. These findings explain the reduction in FM-143 destaining as described above. A consequence of the reduced release probability is that BACHD exhibit less synaptic depression during 30 Hz stimulation.

Since we observed a decrease of quantal size in the diaphragm NMJs of BACHD, we investigated whether there were ultrastructural changes in the size and shape of the synaptic vesicles in the diaphragm NMJs of these mice. The qualitative analysis of the electron micrographs of the diaphragm NMJs showed that the nerve terminals of both genotypes presented similar morphology of the terminal area and post-junctional folds (Fig. 5A–B). We also
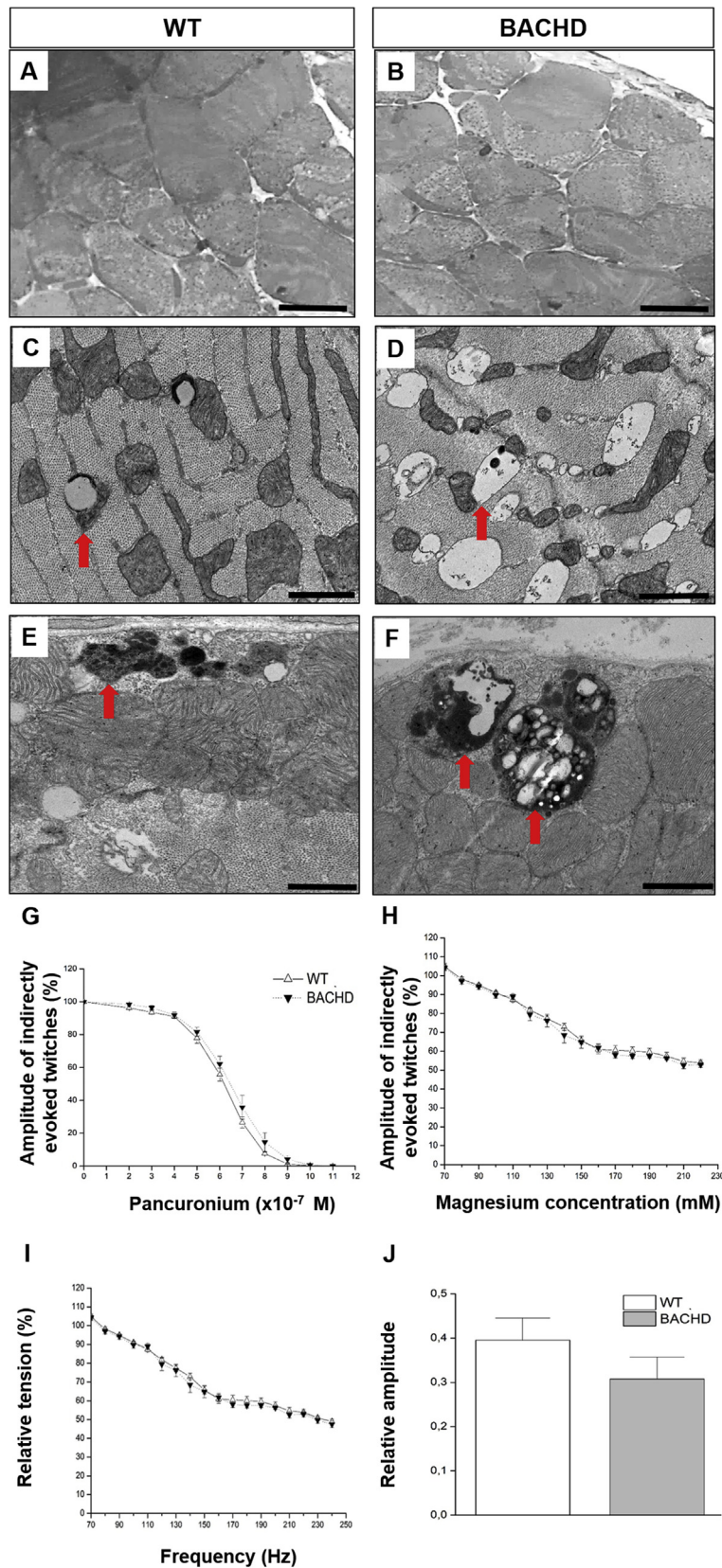
Fig. 6. BACHD mice present ultrastructural changes in the mitochondrial of diaphragm muscle fiber, despite having normal functional parameters. A—B: Representative images of diaphragm skeletal muscle fibers from 12- month-old old WT and BACHD mice, respectively. C—E: Representative electron micrographs of diaphragm fibers from WT (C and E) and BACHD mice (D and F). Note morphological alterations such as abnormal mitochondria in different stages of degeneration in both genotypes (red arrows in C-F). G—H: Time course of indirectly evoked twitches in phrenic-diaphragm preparations of WT and BACHD animals in the presence of Pancuronium (G) and Magnesium (H). Twitch amplitudes were expressed as a percentage from the control situation (without pancuronium or magnesium). I: Time course of tetanic fade of indirectly evoked contractions induced

observed that the nerve terminals of BACHD animals contained less synaptic vesicles in their interior (Fig. 5 B′-C). Moreover, the diaphragm NMJs of BACHD mice presented vesicles with irregular morphology (varying sizes, flattened or with elliptical shape) (Fig. 5D). Additionally, the circumference and shape of the synaptic vesicles of the diaphragm NMJs of BACHD animals were smaller than that found in the diaphragm NMJs of WT mice (Fig. 5E). Given that the expression of cholinergic neuronal markers such as ChAT, AChE and VAChT is reduced in transgenic mice for HD (Aquilonius et al., 1975; Smith et al., 2006; Massouh et al., 2008), we also examined VAChT, ChAT and AChE protein expression levels in the diaphragm NMJs of 12—months-old BACHD animals. We found a significant reduction in the expression of VAChT and ChAT, but AChE was not reduced in the diaphragm NMJs of BACHD compared to WT mice (Fig. 5F—H).

In light of the above-reported observations, we investigated the general morphology of the diaphragm muscle fibers. The qualitative analysis showed no morphological changes in the diaphragm muscle fibers of both genotypes (Fig. 6A—B). However, ultrastructural analysis revealed abnormal mitochondria with vacuoles in the diaphragm NMJs of WT and BACHD animals, as shown in the representative images displayed in Figs. 6C—F. Lastly, we asked if all the presynaptic and muscle alterations described above could compromise diaphragm function in BACHD mice. We found no differences between the genotypes with regards to the susceptibility of neuromuscular blockade induced by pancuronium bromide (Fig. 6G) or excess of magnesium (Fig. 6H), indicating that the safety margin of diaphragm's synaptic transmission is preserved in 12-months-old BACHD mice. In addition, experiments with increasing frequencies of tetanic stimulation also showed no differences between the experimental groups (Fig. 6I). The fatigue resistance test revealed similarities between WT and BACHD animals (Fig. 6J). These data indicate that despite all morphological changes, the diaphragm muscle maintains its functional capacity in the BACHD mice.

4. Discussion

One of the main pathological features of HD is brain neurodegeneration, although cellular dysfunctions have also been reported in other structures such as the spinal cord motor neurons, nerves, NMJs and the skeletal muscles (Valadão et al., 2017; Mielcarek, 2015; Zielonka et al., 2014; Ribchester et al., 2004). Previous work from our group showed that 3-months-old BACHD mice exhibit: i) decreased number of synaptic elements in diaphragm NMJs; ii) reduced synaptic vesicle exocytosis; iii) changes in the form and sizes of the synaptic vesicles; and iv) decreased spontaneous ACh release, thus suggesting a deficit of neuromuscular function (de Aragão et al., 2016). To better understand the progression mechanisms of HD, we investigated the advance of motor pathology in the diaphragm of 12-months-old BACHD mice.

In BACHD, the NMJs from phrenic nerve, which innervates the diaphragm muscle, did not differ from the WT mice regarding the index of co-localization, the total number and area of pre- and postsynaptic elements and the endocytosis process. However, diaphragm NMJs of BACHD were more fragmented compared with WT, indicating that diaphragm NMJs of BACHD mice are undergoing a neurodegenerative process. These results are in agreement with previous morphological evaluations showing an increase of NMJ fragmentations of different models for neurodegenerative

diseases such as HD and ALS (Valadão et al., 2017; Valdez et al., 2010, 2012).

The decreased FM1-43 destaining rate and smaller synaptic depression observed in BACHD mice argue in favor of a decreased vesicular exocytosis rate. This indicates that middle-aged (12-months-old) BACHD present alterations in exocytosis of synaptic vesicles similar to previous observations in younger animals (3-month-old BACHD) (de Aragão et al., 2016). Abnormal interactions between mHTT and proteins that are involved with the exocytosis process may influence the release of neurotransmitters (Sari, 2011; Saudou and Humbert, 2016; Zuccato et al., 2010). Also, several studies demonstrated the reduction of synaptic proteins involved in synaptic vesicle exocytosis in the postmortem brain of WT animals and in HD mice. These proteins include complexin II, V-SNARE (synaptobrevin 2), and Rab3A (Morton and Edwardson, 2001; Smith et al., 2005, 2007). These reports show that mHTT interacts with key proteins of the exocytosis process of synaptic vesicles, which may explain the lower rate of exocytosis seen in the BACHD in relation to WT mice.

Diaphragm NMJs of BACHD mice had a reduced quantal size, when compared with WT animals. Reduction in MEPPs' size in the 3-months-old BACHD mice has been reported by de Aragão et al. (2016), indicating that the deficit in the quantal size in BACHD mice remains at more advanced ages. This could be due to less ACh per vesicle since we observed here a decrease in ChAT and VAChT expression levels in BACHD diaphragms.

We observed no differences in the frequency of MEPPs between BACHD and WT mice, showing similarity in the rate of spontaneous release in both genotypes. On the other hand, we observed less EPPs depression. Data from the literature regarding neurotransmission are divergent, with two reports showing increased synaptic vesicles exocytosis and neurotransmitter release (Rozas et al., 2010, 2011), decreased release (Khedraki et al., 2017; and a report showing no differences in the neurotransmission mechanism (Ribchester et al., 2004). The differences between some of these studies and our observations may be due to the different transgenic models used.

We found changes in the morphological aspect of synaptic vesicles. Electron micrographs revealed that the presynaptic terminals of the diaphragm NMJs of BACHD mice possessed altered synaptic vesicles shape (elliptic and flattened) and circumference compared with the WT counterparts. de Aragão et al. (2016), also observed a similar result in 3-months-old BACHD. The mHTT binds more strongly to the synaptic vesicles compared with the normal HTT, thus altering the structure of the vesicle and affecting neurotransmitter release (Li et al., 2003), which could explain the alterations observed in the structure of the synaptic vesicles.

Reduction in VAChT protein expression can lead to reduced vesicular content of ACh, which can be seen as changes in both MEPPs and synaptic vesicle size in KD VAChT mice (Rodrigues et al., 2013). The reduction in quantal size we observed in the present study could be due to smaller vesicular content of ACh due to less VAChT to fill the vesicles. Moreover, transgenic HTT mice have reduced expression of cholinergic neuronal markers such as ChAT (Aquilonius et al., 1975; Massouh et al., 2008), AChE, and VAChT (Smith et al., 2006). These findings may also be related to smaller quantal size we observed. Considering that the synaptic vesicles morphology seems to correlate with the level of their filling with neurotransmitters (Budzinski et al., 2009; Rodrigues et al., 2013; Van der Kloot et al., 2002), we suggest that the changes in the

by increasing frequency of stimulus in mouse phrenic-diaphragm preparations of WT and BACHD animals. Each point represents the relation between the initial and the 44 final peak of the tetanic stimulation. J: Relative amplitude of indirectly evoked tetanic contractions in rat phrenic-diaphragm preparations of WT and BACHD animals after a series of 30 stimulus (130 Hz, 5 s long at each 20 s). X-axis represents the amplitude of the last contraction of the series relative to the first. Values are expressed as mean ± SEM. (For interpretation of the references to colour in this figure legend, the reader is referred to the Web version of this article.)

circumference of the synaptic vesicles described here may be a consequence of decreased filling with ACh. Further research will be needed to verify this hypothesis.

Ultrastructural changes were observed in the diaphragm muscle of 12-months-old BACHD animals, including mitochondria at different stages of degeneration. However, these changes were also found in the control muscles. According to Regmi et al. (2014), mitochondrial degeneration may be related to age. Biopsies of human muscle reveal that characteristics such as decreased activities of tricarboxylic acid cycle enzymes and those related to oxidative phosphorylation and ATP synthesis may be related to factors such as mitochondrial volume decrease, increased oxidative stress, mitochondrial DNA (mtDNA), and/or altered mitochondrial morphology observed during aging of muscle cells (Bua et al., 2002; Marzetti et al., 2013). Valadão et al. (2017) also described similar ultrastructural changes in the mitochondria of the sternomastoid muscle of 12-months-old BACHD mice. In addition, several studies support the hypothesis that mitochondria dysfunction is involved in the pathophysiological process of several neurodegenerative diseases, particularly HD (Browne and Beal, 2004; Reddy et al., 2009).

In light of the morphological changes observed in the diaphragm NMJs of 12-months-old BACHD animals, we hypothesized that the neuromuscular function would also be affected in these mice. Therefore, we evaluated the overall safety margin of the synaptic transmission regarding the resistance to the neuromuscular blockade induced by pancuronium bromide or magnesium (del Castillo and Engbaek, 1954). No differences in the susceptibility of the neuromuscular blockade induced by pancuronium bromide or excess of magnesium were found between both genotypes, indicating that the safety margin of synaptic transmission was preserved in the diaphragm NMJs of BACHD mice. This suggests that the phrenic nerve of the diaphragm muscle of BACHD animals may be adapted to the period of exposure to HD or that the pre- or postsynaptic alterations were not enough to alter the neurotransmission process observed in our methodology.

Physiological tetanic stimulation induces depletion of ACh output, which is balanced by increased synthesis and transfer of neurotransmitter from mobilization stores (Padmaja and Mantha, 2002). However, the progressive increase of tetanic frequency can disrupt this balance and preparations with compromised safety margin will be more susceptible to such changes, presenting an absence of sustained tetanic stimulation, which is known as tetanus fade (Gissen and Katz, 1969). We used a tetanic protocol and evaluated the fatigue resistance of the phrenic-diaphragm preparation from BACHD and WT mice. Diaphragm muscle resistance to fatigue animals was not significantly different between the BACHD and WT mice. Importantly, the diaphragm muscle is vital for survival since it is involved in the respiratory process. Therefore, it is likely that even if morphological changes are present, the diaphragm probably has a higher resistance threshold than some other muscles when it undergoes functional tests. Future studies characterizing the contractile properties of other muscles may allow comparisons and provide insights on the mechanisms of diaphragm resistance.

5. Conclusions

In summary, here we provide evidence that aging maintains alterations in the diaphragm NMJs (i.e: reduced exocytosis and ACh release, and altered shape and size of synaptic vesicles) of 12-months-old BACHD mice. Further, aging does not lead to further changes (i.e: in endocytosis, or muscle ultrastructure) in the BACHD mice diaphragm. Additionally, we noted that WT mice presented losses in the parameters analyzed, probably due to aging. This may

have masked the effects of HD in the 12-months-old BACHD mice. Our functional analysis suggested that the phrenic nerve might be less affected by the neurodegeneration processes occurring in HD. Therefore, we propose that putative resistance mechanisms may be protecting this vital muscle to allow for survival. The results presented herein contribute to expand the current understanding of the effects of mHTT in the neuromuscular synapse and in the diaphragm muscle function.

Conflicts of interest

We have no conflict of interest to declare.

Appendix A. Supplementary data

Supplementary data related to this article can be found at https://doi.org/10.1016/j.neuint.2018.03.007.

References

Aquilonius, S.M., Eckernäs, S.A., Sundwall, A., 1975. Regional distribution of choline acetyltransferase in the human brain: changes in Huntington's chorea. J. Neurol. Neurosurg. Psychiatry 38, 669–677.

Baig, S.S., Strong, M., Quarrell, O.W., 2016. The global prevalence of Huntington's disease: a systematic review and discussion. Neurodegener. Dis. Manag. 6 (4), 331–343.

Barstad, J.A., Lilleheil, G., 1968. Transversally cut diaphragm preparation from rat. An adjuvant tool in the study of the physiology and pharmacology of the myoneural junction. Arch. Int. Pharmacodyn. Ther. 175, 373–390.

Betz, W.J., Bewick, G.S., 1992. Optical analysis of synaptic vesicle recycling at the frog neuromuscular junction. Science 255, 200–203.

Betz, W.J., Mao, F., Smith, C.B., 1996. Imaging exocytosis and endocytosis. Curr. Opin. Neurobiol. 6 (3), 365–371.

Brotherton, A., Campos, L., Rowell, A., Zoia, V., Simpson, S.A., Rae, D., 2012. Nutritional management of individuals with Huntington's disease: nutritional guidelines. Neurodegener. Dis. Manag. 2 (1), 33–43.

Browne, S.E., Beal, M.F., 2004. The energetics of Huntington's disease. Neurochem. Res. 29 (3), 531–546.

Bua, E.A., McKiernan, S.H., Wanagat, J., McKenzie, D., Aiken, J.M., 2002. Mitochondrial abnormalities are more frequent in muscles undergoing sarcopenia. J. Appl. Physiol. 92, 2617–2624.

Budzinski, K.L., Allen, R.W., Fujimoto, B.S., Kensel-Hammes, P., Belnap, D.M., Bajjalieh, S.M., Chiu, D.T., 2009. Large structural change in isolated synaptic vesicles upon loading with neurotransmitter. Biophys. J. 97 (9), 2577–2584.

Caviston, J.P., Holzbaur, E.L.F., 2009. Caviston, J. P., Holzbaur, E. L. Huntingtin as an essential integrator of intracellular vesicular trafficking. Trends Cell Biol. 19 (4), 147–155.

Chau, W.K., So, K.F., Tay, D., Dockery, P., 2000. A morphometric study of optic axons regenerated in a sciatic nerve graft of adult rats. Restor. Neurol. Neurosci. 16, 105–116.

Croft, B.G., Fortin, G.D., Corera, A.T., Edwards, R.H., Beaudet, A., Trudeau, L.E., Fon, E.A., 2005. Normal biogenesis and cycling of empty synaptic vesicles in dopamine neurons of vesicular monoamine transporter 2 knockout mice. Mol. Biol. Cell 16, 306–315.

de Aragão, B.C., Rodrigues, H.A., Valadão, P.A.C., Camargo, W., Naves, L.A., Ribeiro, F.M., Guatimosim, C., 2016. Changes in structure and function of diaphragm neuromuscular junctions from BACHD mouse model for Huntington's disease. Neurochem. Int. 93, 64–72.

del Castillo, J., Engbaek, L., 1954. The nature of the neuromuscular block produced by magnesium. J. Physiol. 124, 370–384.

DiFiglia, M., Sapp, E., Chase, K., Schwarz, C., Meloni, A., Young, C., Reeves, S.A., 1995. Huntingtin is a cytoplasmic protein associated with vesicles in human and rat brain neurons. Neuron 14, 1075–1081.

Difiglia, M., Sapp, E., Chase, K.O., Davies, S.W., Bates, G.P., Vonsattel, J.P., Aronin, N.,

1997. Aggregation of huntingtin in neuronal intranuclear inclusions and dystrophic neurites in brain. Science 277 (5334), 1990—1993.

Elmqvist, D., Quastel, D.M., 1965. A quantitative study of end-plate potentials in isolated human muscle. J. Physiol. 178 (3), 505—529.

Farrar, A.M., Callahan, J.W., Abercrombie, E.D., 2011. Reduced striatal acetylcholine efflux in the R6/2 mouse model of Huntington's disease: an examination of the role of altered inhibitory and excitatory mechanisms. Exp. Neurol. 232, 119—125.

Ferrante, R.J., Gutekunst, C.A., Persichetti, F., Mcneil, S.M., Kowall, N.W., Gusella, J.F., Macdonald, M.E., Beal, M.F., Hersch, S.M., 1997. Heterogeneous topographic and cellular distribution of huntingtin expression in the normal human neo-striatum. J. Neurosci. 17, 3052—3063.

Finkbeiner, S., 2011. Huntington's disease. CSH. Perspect. Biol. 3 (6), a007476.

Gallacci, M., Oliveira, A.C., 1994. Pre-and postsynaptic mechanisms involved in tetanic fade induced by pancuronium in the isolated rat muscle. Pharmacol 49 (4), 265—270.

Gauthier, L.R., Charrin, B.C., Borrell-Pagès, M., Dompierre, J.P., Rangone, H., Cordelières, F.P., De Mey, J., MacDonald, M.E., Lessmann, V., Humbert, S., Saudou, F., 2004. Huntingtin controls neurotrophic support and survival of neurons by enhancing BDNF vesicular transport along microtubules. Cell 118 (1), 127—138.

Gissen, A.J., Katz, R.L., 1969. Twitch, tetanus and posttetanic potentiation as indices of nerve—muscle block in man. Anesthesiol 30 (5), 481—487.

Gray, M., Shirasaki, D.I., Cepeda, C., Andre, V.M., Wilburn, B., Lu, X.H., Yang, X.W., 2008. Full-length human mutant huntingtin with a stable polyglutamine repeat can elicit progressive and selective neuropathogenesis in BACHD mice. J. Neurosci. 28 (24), 6182—6195.

Harjes, P., Wanker, E.E., 2003. The hunt for huntingtin function: interaction partners tell many different stories. Trends Biochem. Sci. 28 (8), 425—433.

Heemskerk, A.W., Roos, R.A., 2011. Dysphagia in Huntington's disease: a review. Dysphagia 26 (1), 62—66.

Hoffner, G., Kahlem, P., Djian, P., 2002. Perinuclear localization of huntingtin as a consequence of its binding to microtubules through an interaction with β-tubulin: relevance to Huntington's disease. J. Cell Sci. 115 (5), 941—948.

Imarisio, S., Carmichael, J., Korolchuk, V., Chen, C.W., Saiki, S., Rose, C., Krishna, G., Davies, J.E., Ttofi, E., Underwood, B.R., Rubinsztein, D.C., 2008. Huntington's disease: from pathology and genetics to potential therapies. Biochem. J. 412 (2), 191—209.

Jones, K., Pitceathly, R.D., Rose, M.R., McGowan, S., Hill, M., Badrising, U.A., Hughes, T., 2016. Interventions for dysphagia in long-term, progressive muscle disease. Cochrane Database Syst. Rev. 2, CD004303.

Khedraki, A., Reed, E.J., Romer, S.H., Wang, Q., Romine, W., Rich, M.M., Talmadge, R.J., Voss, A.A., 2017. Depressed synaptic transmission and reduced vesicle release sites in Huntington's disease neuromuscular junctions. J. Neurosci. 37 (34), 8077—8091.

Li, H., Wyman, T., Yu, Z.X., Li, S.H., Li, X.J., 2003. Abnormal association of mutant huntingtin with synaptic vesicles inhibits glutamate release. Hum. Mol. Genet. 12 (16), 2021—2030.

Li, S.H., Li, X.J., 2004. Huntingtin-protein interactions and the pathogenesis of Huntington's disease. Trends Genet. 20 (3), 146—154.

Marzetti, E., Calvani, R., Cesari, M., Buford, T.W., Lorenzi, M., Behnke, B.J., Leeuwenburgh, C., 2013. Mitochondrial dysfunction and sarcopenia of aging: from signaling pathways to clinical trials. Int. J. Biochem. Cell Biol. 45, 2288—2301.

Massouh, M., Wallman, M.J., Pourcher, E., Parent, A., 2008. The fate of the large striatal interneurons expressing calretinin in Huntington's disease. Neurosci. Res. 62 (4), 216—224.

McLachlan, E.M., Martin, A.R., 1981. Non-linear summation of end-plate potentials in the frog and mouse. J. Physiol. 311, 307—324.

McNeil, S.M., Novelletto, A., Srinidhi, J., Barnes, G., Kornbluth, I., Altherr, M.R., Myers, R.H., 1997. Reduced penetrance of the Huntington's disease mutation. Hum. Mol. Genet. 6 (5), 775—779.

Mielcarek, M., 2015. Huntington's disease is a multi-system disorder. Rare Dis. 3 (1), e1058464.

Morton, A.J., Edwardson, J.M., 2001. Progressive depletion of complexin II in a transgenic mouse model of Huntington's disease. J. Neurochem. 76 (1), 166—172.

Padmaja, D., Mantha, S., 2002. Monitoring of neuromuscular junction. Indian J. Anaesth. 46 (4), 279—288.

Pratt, S.J., Shah, S.B., Ward, C.W., Inacio, M.P., Stains, J.P., Lovering, R.M., 2013. Effects of in vivo injury on the neuromuscular junction in healthy and dystrophic muscles. J. Physiol. 591, 559—570.

Reddy, P.H., Mao, P., Manczak, M., 2009. Mitochondrial structural and functional dynamics in Huntington's disease. Brain Res. Rev. 61 (1), 33—48.

Regmi, S.G., Rolland, S.G., Conradt, B., 2014. Age-dependent changes in mitochondrial morphology and volume are not predictors of lifespan. Aging (Albany NY) 6 (2), 118—130.

Ribchester, R.R., Thomson, D., Wood, N.I., Hinks, T., Gillingwater, T.H., Wishart, T.M., Morton, A.J., 2004. Progressive abnormalities in skeletal muscle and neuro-muscular junctions of transgenic mice expressing the Huntington's disease mutation. Eur. J. Neurosci. 20, 3092—3114.

Rizzoli, S.O., Betz, W.J., 2004. The structural organization of the readily releasable pool of synaptic vesicles. Science 303 (5666), 2037—2039.

Rodrigues, H.A., Fonseca, M.D.C., Camargo, W.L., Lima, P.M.A., Martinelli, P.M., Naves, L.A., Guatimosim, C., 2013. Reduced expression of the vesicular acetyl-choline transporter and neurotransmitter content affects synaptic vesicle dis-tribution and shape in mouse neuromuscular junction. PLoS One 8 (11), e78342.

Roos, R.A., 2010. Huntington's disease: a clinical review. Orphanet J. Rare Dis. 5, 40—48.

Rozas, J.L., Gomez-Sanchez, L., Tomas-Zapico, C., Lucas, J.J., Fernandez-Chacon, R., 2011. Increased neurotransmitter release at the neuromuscular junction in a mouse model of polyglutamine disease. J. Neurosci. 31 (3), 1106—1113.

Rozas, J.L., Gómez-Sánchez, L., Tomás-Zapico, C., Lucas, J.J., Fernández-Chacón, R., 2010. Presynaptic dysfunction in Huntington's disease. Biochem. Soc. Trans. 38 (2), 488—492.

Rubinsztein, D.C., Leggo, J., Coles, R., Almqvist, E., Biancalana, V., Cassiman, J.J., Hayden, M.R., 1996. Phenotypic characterization of individuals with 30-40 CAG repeats in the Huntington disease (HD) gene reveals HD cases with 36 repeats and apparently normal elderly individuals with 36-39 repeats. Am. J. Hum. Genet. 59 (1), 16—22.

Sathasivam, K., Hobbs, C., Turmaine, M., Mangiarini, L., Mahal, A., Ber-taux, F., Wanker, E.E., Doherty, P., Davies, S.W., Bates, G.P., 1999. Formation of poly-glutamine inclusions in non-CNS tissue. Hum. Mol. Genet. 8, 813—822.

Sari, Y., 2011. Huntington's disease: from mutant huntingtin protein to neurotrophic factor therapy. Int. J. Biomed. Sci. 7 (2), 89—100.

Sassone, J., Colciago, C., Cislaghi, G., Silani, V., Ciammola, A., 2009. Huntington's disease: the current state of research with peripheral tissues. Exp. Neurol. 219 (2), 385—397.

Saudou, F., Humbert, S., 2016. The biology of huntingtin. Neuron 89 (5), 910—926.

Smith, R., Brundin, P., Li, J.Y., 2005. Synaptic dysfunction in Huntington's disease: a new perspective. Cell. Mol. Life Sci. 62 (17), 1901—1912.

Smith, R., Chung, H., Rundquist, S., Maat-Schieman, M.L.C., Colgan, L., Englund, E., Li, J.Y., 2006. Cholinergic neuronal defect without cell loss in Huntington's disease. Hum. Mol. Genet. 15 (21), 3119—3131.

Smith, R., Klein, P., Koc-Schmitz, Y., Waldvogel, H.J., Faull, R.L.M., Brundin, P., Li, J.Y., 2007. Loss of SNAP- 25 and rabphilin 3a in sensory-motor cortex in Hunting-ton's disease. J. Neurochem. 103 (1), 115—123.

Schulte, J., Troy Littleton, J., 2011. The biological function of the Huntingtin protein and its relevance to Huntington's Disease pathology. Curr. Trends Neurol. 1 (5), 65—78.

The Huntington's Disease Collaborative Research Group., 1993.

Valadão, P.A.C., de Aragão, B.C., Andrade, J.N., Magalhães-Gomes, M.P.S., Foureaux, G., Joviano-Santos, J.V., Guatimosim, C., 2017. Muscle atrophy is associated with cervical spinal motoneuron loss in BACHD mouse model for Huntington's disease. Eur. J. Neurosci. 45 (6), 785—796.

Valdez, G., Tapia, J.C., Kang, H., Clemenson, G.D., Gage, F.H., Lichtman, J.W., Sanes, J.R., 2010. Attenuation of age- related changes in mouse neuromuscular synapses by caloric restriction and exercise. Proc. Natl. Acad. Sci. U. S. A 107 (33), 14863—14868.

Valdez, G., Tapia, J.C., Lichtman, J.W., Fox, M.A., Sanes, J.R., 2012. Shared resistance to aging and als in neuromuscular junctions of specific muscles. PLoS One 7 (4), e34640.

Van Der Burg, Jorien, M.M., Björkqvist, M., Brundin, P., 2009. Beyond the brain: widespread pathology in Huntington's disease. Lancet Neurol. 8, 765—774.

Van der Kloot, W., Molgo, J., Cameron, R., Colasante, C., 2002. Vesicle size and transmitter release at the frog neuromuscular junction when quantal acetyl-choline content is increased or decreased. J. Physiol. 541, 385—393.

Vonsattel, G.J.P., DiFiglia, M., 1998. Huntington disease. J. Neuropathol. Exp. Neurol. 57 (5), 369—384.

Walker, F.O., 2007. Huntington's disease. Lancet 369 (9557), 218—228.

Wu, L.L., Zhou, X.F., 2009. Huntingtin associated protein 1 and its functions. Cell Adhes. Migrat. 3 (1), 71—76.

Yuen, E.Y., Wei, J., Zhong, P., Yan, Z., 2012. Disrupted GABAAR trafficking and syn-aptic inhibition in a mouse model of Huntington's disease. Neurobiol. Dis. 46 (2), 497—502.

Zielonka, D., Piotrowska, I., Marcinkowski, J.T., Mielcarek, M., 2014. Skeletal muscle pathology in Huntington's disease. Front. Physiol. 5, 380—385.

Zuccato, C., Valenza, M., Cattaneo, E., 2010. Molecular mechanisms and potential therapeutical targets in Huntington's disease. Physiol. Rev. 90 (3), 905—981.

7.2- Contextualização dos artigos 4 e 5

A DH é considerada uma desordem neuromotora e a análise dos músculos esqueléticos pode ser fundamental para o desenvolvimento de novas abordagens terapêuticas com o foco no sistema periférico. Não somente os músculos devem ser devidamente caracterizados, mas também é importante o estudo da unidade motora. Sabe-se que a unidade motora é a via final do sistema motor, sendo formada pelo motoneurônio (localizado no corno anterior da medula espinal), por seus prolongamentos que vão compor o nervo, por suas terminações na JNM e por fim as pelas fibras musculares esqueléticas inervadas por esses elementos[129]. A detecção de possíveis alterações nas unidades motoras, mais especificamente nos motoneurônios e músculos inervados por eles, durante o desenvolvimento da DH, é uma questão de grande relevância e que ainda não foi completamente elucidada nos animais BACHD. A análise da unidade motora nos segmentos superiores desses animais (segmento cervical) foi realizada e está descrita no artigo 4, publicado em 2017 na *European Journal of Neuroscience*. Além disso, considerando que a DH traz um alto comprometimento para a marcha e equilíbrio dos pacientes, também fizemos o estudo dos segmentos inferiores (segmento lombar). Esse artigo foi submetido para a revista *ASN Neuro* em 2019.

ARTIGO 4

CLINICAL AND TRANSLATIONAL NEUROSCIENCE

Muscle atrophy is associated with cervical spinal motoneuron loss in BACHD mouse model for Huntington's disease

Priscila Aparecida Costa Valadão,[1] Bárbara Campos de Aragão,[1] Jéssica Neves Andrade,[1] Matheus Proença S. Magalhães-Gomes,[1] Giselle Foureaux,[1] Julliane Vasconcelos Joviano-Santos,[1] José Carlos Nogueira,[1] Fabíola Mara Ribeiro,[2] Juan Carlos Tapia[3] and Cristina Guatimosim[1] (iD)

[1]Departamento de Morfologia, ICB, Universidade Federal de Minas Gerais, Av. Antônio Carlos, 6627, Belo Horizonte, MG 31270-901, Brazil
[2]Departamento de Bioquímica e Imunologia, ICB, Universidade Federal de Minas Gerais, Belo Horizonte, MG, Brazil
[3]Department of Biomedical Sciences, University of Talca, Talca, Chile

Abstract

Involuntary choreiform movements are clinical hallmark of Huntington's disease, an autosomal dominant neurodegenerative disorder caused by an increased number of CAG trinucleotide repeats in the huntingtin gene. Involuntary movements start with an impairment of facial muscles and then affect trunk and limbs muscles. Huntington's disease symptoms are caused by changes in cortex and striatum neurons induced by mutated huntingtin protein. However, little is known about the impact of this abnormal protein in spinal cord motoneurons that control movement. Therefore, in this study we evaluated abnormalities in the motor unit (spinal cervical motoneurons, motor axons, neuromuscular junctions and muscle) in a mouse model for Huntington's disease (BACHD). Using light, fluorescence, confocal, and electron microscopy, we showed significant changes such as muscle fibers atrophy, fragmentation of neuromuscular junctions, axonal alterations, and motoneurons death in BACHD mice. Noteworthy, the surviving motoneurons from BACHD spinal cords were smaller than WT. We suggest that this loss of larger putative motoneurons is accompanied by a decrease in the expression of fast glycolytic muscle fibers in this model for Huntington's disease. These observations show spinal cord motoneurons loss in BACHD that might help to understand neuromuscular changes in Huntington's disease.

Introduction

Huntington's disease (HD) is a progressive, autosomal dominant, debilitating, and neurological disease caused by an increased CAG trinucleotide repetition at the short arm of chromosome 4 that leads to a polyglutamine expansion in the huntingtin (Htt) protein (Huntington's Disease Collaborative Research Group, 1993; Bates, 2005). Its symptoms include cognitive and psychiatric disturbances and progressive motor decline with involuntary movements, rigidity, bradykinesia, and dystonia starting with motor impairment in facial muscles and then progressing to trunk and limb muscles (Bates *et al.*, 2002).

It has been described that Htt interacts with more than two hundred proteins and it is involved in many functions, such as regulating gene transcription, cell signaling, vesicular transport, exocytosis, endocytosis, etc. (Harjes & Wanke, 2003; Zuccato *et al.*, 2010). Furthermore, Htt plays a critical role in cell survival by regulating

apoptotic pathways (Ona *et al.*, 1999). For example, synthesis of Htt protects striatal neurons from apoptotic stimuli (Rigamonti *et al.*, 2000).

Previous reports have shown that mutated Htt (mHtt) leads to the generation of insoluble toxic protein aggregates, which accumulate inside the striatum, causing cellular dysfunction, degeneration and neuronal death, all hallmarks of HD neuropathology (Sathasivam *et al.*, 1999; Moffitt *et al.*, 2009). In mammals, besides the Central Nervous System (CNS), Htt is expressed in a number of tissues and organs, including skeletal muscles (Hoogeveen *et al.*, 1993; Li *et al.*, 1993; Trottier *et al.*, 1995). Indeed, Sathasivam *et al.* (1999), using R6/2 mouse model for HD, observed force and contractility reduction and deregulation in the transcription of contractile proteins that are directly related to the presence of protein aggregates in muscles. Ribchester *et al.* (2004), used the same mouse model to demonstrate peripheral disorders, including muscle atrophy as well as morphological and electrophysiological changes in neuromuscular junctions (NMJs). Recently, Mielcarek (2015) also observed muscle contractile dysfunction and progressive loss of functional motor

units in R6/2 mice. However, these studies only speculated the possibility of changes in motoneurons from the spinal cord. Thus, even though several groups have been investigating alterations induced by mHtt (Sathasivam *et al.*, 1999; Ribchester *et al.*, 2004; Zielonka *et al.*, 2014; Mielcarek, 2015), to our knowledge, little is known about motor unit changes induced by mHtt.

In this study, we investigated by a combination of methods (optical, confocal, and transmission electron microscopy) putative abnormalities in muscle fibers, neuromuscular junctions, spinal roots, and spinal cord motoneurons in a transgenic model for HD (BACHD). This murine HD model expresses the complete human *Htt* gene (Gray *et al.*, 2008), with a mutant full length sequence coding for a polyglutamine strech (CAA-CAG) that is more stable through generations compared to the R6/1 and R6/2 mice models (Mangiarini *et al.*, 1996; Kazantsev *et al.*, 1999; Yang *et al.*, 1997). In addition, BACHD mice present robust motor deficits (such as decreased rotarod performance and hypolocomotion) and a slow progression of the disease, allowing to conduct more detailed longitudinal studies when compared to other models of fast progression like the R6/2 (Menalled *et al.*, 2009; Yang & Gray, 2011). The rational for this study relies upon recent evidence indicating that muscle wasting in HD might occur independently of the cortex and basal ganglia dysfunction (Van Der Burg *et al.*, 2009; Mantovani *et al.*, 2016).

Materials and methods

BACHD mice

FVB/NJ (wild type) and FVB/N-Tg (HTT*97Q)IXwy/J (BACHD) male transgenic mice were generated by Gray *et al.* (2008) introducing 170 kb human Htt in 240 kb RP11-866L6 BAC. Htt locus was altered by inserting an exon1 with 97 mixed CAA-CAG repeats into the human *Htt* gene. The animals were purchased from Jackson Laboratory (Bar Harbor, ME, USA) and used to establish a new colony where 12 months old (mo) WT and BACHD mice were obtained.

Our experiments were done in 12 months WT and BACHD animals as previous studies using this mouse model demonstrated morphological changes in the brain, like atrophy of the cerebral cortex (Gray *et al.*, 2008). Furthermore, Holmes *et al.* (2002), showed that changes in behavior tests were more pronounced in 12 months BACHD mice (For a detailed review see Yang & Gray, 2011).

Mice were held in a place with controlled temperature (23 °C) in a 12 h light/12 h dark cycle and with food and water provided *ad libitum*. Animal care was in accordance with the Universidade Federal de Minas Gerais Ethics Committee on Animal Experimentation (CEUA) under approved protocol #036/2013.

Skeletal muscle and spinal roots morphology

Animals from both genotype (WT and BACHD) were deeply anesthetized with ketamine/xylazine (0.1 mL/20 g) in accordance with CEUA/UFMG protocol. The sternomastoid (STM) muscle were dissected out and fixed in 4% glutaraldehyde diluted in phosphate-buffered saline (0.2 M) for 24 h at room temperature. After dehydration in an ascending series of alcohols (70, 80, 90, 95% 2X), samples were embedded in glycolmethacrylate resin (Leica) and sectioned in a microtome (Reichert Jung) where 5 µm thick sections were obtained. Sections from muscle samples were stained with toluidine blue (EMS), to determine the cross-sectional area (CSA) of individual myofibers. Images were acquired using a microscope (Leica DM2500) coupled to a CCD camera (Leica DFC345FX). Muscles sections were imaged with 10× objective.

Samples containing cervical ventral roots were processed following Transmission electron microscopy (TEM) protocol (see below). Semi-thin cross-sections (300 nm) were obtained and stained with toluidine blue. Images of whole ventral roots cross-sections from WT and BACHD mice were captured using a 20× objective in a ZEISS Axio Lab.A1 microscope. The cross-sectional area of the ventral roots was measured using ImageJ plugins (NIH), and the total number of axons counted. To quantify axonal myelination we used the G-ratio, which was calculated measuring the axonal inner diameter and dividing it by the outer diameter following the formula: $G = d/D$, where G is the G-ratio, d is the inner diameter and D is the outer diameter (Chau *et al.*, 2000). The size adopted to classify large myelinated fibers was >4.5 µm, according to the evaluation criteria described by Kong & Xu (1999).

Skeletal muscle fiber typing

The STM muscle fiber typing was performed according to the protocol described by Valdez *et al.* (2012). Mice were sacrificed and the STM muscles were dissected. Samples were put in freezing molds covered with OCT freezing medium (Easy Path) and was fresh frozen in isopentane (Sigma-Aldrich) cooled in liquid nitrogen and stored at −80 °C. The muscle was cut on a cryostat (Leica CM3050S) and the cross-sections (10 µm) were collected on glass slides coated with gelatin (Sigma-Aldrich). First, slides containing muscle sections passed through blockade step with 3% BSA, 5% goat serum and 0.1% Triton X-100, 30 min at room temperature. The muscle sections were then incubated overnight at 4 °C with the following primary antibodies all diluted in 3% BSA, 5% goat serum: anti-MyHC I (NCL-Novocastra, Leica 1 : 250); anti-MyHC IIA (SC-71, Developmental Studies Hybridoma Bank, DSHB 1 : 100), anti-MyHC IIX (BF-35 which recognizes all types of muscles fibers except fast IIX, DSHB 1 : 100) and anti-MyHC IIB (BF-F3, DSHB 1 : 100). Slides were washed three times with PBS 1× and incubated for 1 h at room temperature with secondary antibodies Alexa 488 goat anti-mouse IgG1 (recognizes type I, IIA and IIX antibodies) and Alexa 488 goat anti-mouse IgM (recognizes IIB antibody). The slides were then washed three times with PBS 1× and coverslipped using ProLong® Gold antifade (Thermo Scientific). Images were acquired in a fluorescence microscope (Leica DM2500) coupled to a Leica DFC 345FX camera and visualized in a microcomputer using the Leica Application Suite software (LAS). The microscope was equipped with air objective (10×, 0.25 NA). Excitation light came from a 100W Hg lamp and a FITC filter was used to collect emitted light. We imaged the whole STM muscle cross-sections. Each fiber type was expressed as a percentage of the total number of fibers counted.

Cervical spinal cord immunofluorescence

To evaluate the expression of caspase-3 in BACHD spinal cords, cervical segments (C1–C3) were dissected, and immediately immersed in neutral-buffered formalin (NBF) for 24 h. Thereafter, samples were dehydrated in increasing concentrations of ethanol (70, 80, 90, 95, and 100%), cleared in xylene and embedded in paraffin. Sections (5 µm) were obtained using a microtome (model HM335E; Microm, Inc., Minneapolis, MN). Nonspecific antibody binding was blocked by incubation of the samples in a solution of 2% BSA with 0.1% Tween-20 for 1 h in a moist chamber. Sections were incubated with primary antibody (polyclonal rabbit anti-caspase-3, 1 : 100; Sigma-Aldrich, Saint Louis, MO) diluted in blocking solution overnight at 4 °C in a moist chamber. Sections were then washed 3 Xs with PBS

and incubated with secondary antibody (Alexa Fluor 488 goat anti-rabbit 1 : 1000; Invitrogen, Eugene, OR) for 1 h. Subsequently, sections were washed 3 Xs with PBS, and in the last wash, stained with DAPI to allow identification of cells nuclei (1 : 1000; Invitrogen, Eugene, OR). The stained slides were imaged using NIKON ECLIPSE Ti microscope (100× objective, N.A: 1.49). All digital images were quantitatively analyzed using IMAGE J software (Wayne Rasband, National Institutes of Health, USA).

For specific labeling of putative motoneurons, cervical spinal cord segments (C1–C3) were removed and fixed with 4% PFA for 48 h. Subsequently these segments were kept in 30% sucrose for 24 h. Then, the samples were oriented in freezing molds covered with freezing medium OCT (Easy Path) and were fresh frozen in isopentane (Sigma-Aldrich) cooled in liquid nitrogen and stored at −80 °C. The cervical spinal cords were cut on a cryostat (Leica CM3050S) and the cross sections (30 μm) were collected on gelatin coated slides. The slides containing sections of the cervical segments were blocked 60 min at room temperature with 3% BSA, 5% donkey serum and 0.1% Triton X-100. Then, the sections were incubated overnight at 4 °C with the following primary antibody diluted in 3% BSA, 5% donkey serum: ChAT anti-goat, AB 144P Millipore Corporation (1 : 100).

Slides were washed 3 Xs with PBS 1× and incubated for 2 h at room temperature with secondary antibody Alexa 488 donkey anti-goat IgG1 (1 : 800). The slides were washed again 3Xs with PBS 1× and mounted using ProLong® Gold antifade (Thermo Scientific Invitrogen™). Images were acquired using a 63× oil immersion (N.A: 1.4) objective attached to a laser-scanning confocal microscope (Zeiss LSM 510 Meta, Zeiss GmbH, Jena, Germany). An Argon (488 nm) laser was used for excitation of motor neurons marked with anti-ChAT and Alexa 488. The Z series optical sections were collected at 2.0 μm intervals. All digital images were quantitatively analyzed using IMAGE J software (Wayne Rasband, National Institutes of Health, USA), to determine both the number and Ferret diameter of putative motoneurons. The total number of putative motoneurons located in the ventral horn of the cervical spinal cord segments (C1–C3) were counted and had their diameter measured.

NMJ immunofluorescence and confocal microscopy analysis

Mice were anesthetized with ketamine/xylazine (0.1 mL/20 g) and left ventricular transcardiac perfused with ice-cold 4% paraformaldehyde in 0.1M phosphate-buffered saline (PBS; pH 7.4). Muscles were dissected and blocked in 3% BSA + 5% goat serum + 0.5% Triton X-100 for 30 min at room temperature. Next, primary antibody anti-synaptotagmin was added (Anti-synaptotagmin, anti-mouse, IgG2A, DSHB, 1 : 250) in the blocking solution, and incubated overnight at 4 °C. Muscles were washed 3× with PBS and incubated 1 h at room temperature with Alexa 555-α-bungarotoxin (α-btx) 1 : 1000 (Molecular Probes, Eugene, OR) together with secondary antibody 1 : 1000 (Alexa-488 goat anti-mouse IgG2A; Invitrogen). Muscles were then washed 3× with PBS and whole-mounted slides using Vectashield (Vector Laboratories, Eching, Germany).

Images of NMJs stained with anti-synaptotagmim and bungarotoxin (α-btx) were acquired using a 63× oil immersion (N.A: 1.4) objective attached to a laser-scanning confocal microscope (Zeiss LSM 510 Meta, Zeiss GmbH, Jena, Germany. Argon (Ar 488 nm) and helium-neon (He–Ne, 543 nm) lasers were used for excitation of terminals stained with anti-synaptotagmin and acetylcholine receptors (nAChR) clusters marked with (α-btx), respectively. The Z series optical sections were collected at 2.0 μm intervals and the whole STM muscle samples were scanned. The nerve terminals

were identified considering their colocalization with nAChR clusters. Images were converted to gray scale format (8 bits) and each synaptic element was individually evaluated. We used the method of particles analysis to obtain the NMJs fragmentation index, based on the pixels presented in each image. Briefly, the images were converted into a binary image pattern and were skeletonized. Next, to describe the connectivity for each pixel in the image, a histogram was generated using the BinaryConnectivityClass plugin from IMAGEJ (Pratt et al., 2013). We analyzed the degree of fragmentation in pre- and postsynaptic elements comparing the muscle samples from WT and BACHD mice. The parameters adopted for fragmentation were defined according to the evaluation criteria described by Valdez et al. (2010), which establishes fragmentation by five or more islands both in the presynaptic and postsynaptic membranes.

Transmission electron microscopy (TEM)

For ultrastructure analyses, we used the protocol previously described by our research group (Rodrigues et al., 2013). Briefly, mice were anesthetized with ketamine/xylazine (0.1 mL/20 g), left ventricular transcardiac perfused with ice-cold modified Karnovsky fixative (4% paraformaldehyde and 2.5% glutaraldehyde in 0.1 M sodium cacodylate buffer at 4 °C) and maintained in this solution for at least 24 h at 4 °C. Cervical spinal cord segments (C1–C3) and the STM muscles from WT and BACHD mice were then removed. After fixation, samples were washed with cacodylate buffer (0.1 M), cut into several fragments, post-fixed in reduced osmium (1% osmium tetroxide containing 1.6% potassium ferrocyanide), contrasted en bloc with uranyl acetate (UA, 2% in deionized water), dehydrated through an ascending series of ethanol solutions and embedded in EPON. Blocks were sectioned (50 nm) and collected on 200 or 300 mesh copper grids and contrasted with lead citrate. Sections were viewed with a Tecnai- G2-Spirit FEI/Quanta electron microscope (120 kV Philips). The same protocol was used to obtain semi-thin sections of cervical ventral roots. Images of the semi-thin sections encompassing whole ventral roots were acquired using ZEISS Axio Lab.A1 (20× objective, N.A: 0.45) and analyzed qualitatively and quantitatively as described previously. We analyzed a total of 3.222 axons in WT animals and 1.937 in BACHD.

For the quantification of lipofuscin granules, 30 electron micrographs of the motoneurons from the cervical spinal cord were used for each genotype. The counting of beads was performed using the software IMAGEJ plugins (NIH). Data are presented as granules/area using the GRAPHPAD PRISM 6.

Statistical analysis

All Data were analyzed using Microsoft Excel and plotted using the program GRAPHPAD PRISM 6. Statistical significance was evaluated using the un-paired Student's t-test and represent the mean ± Standard deviation (mean ± SD) or (median), as described in the text. When data were not normally distributed, we applied the Man–-Whitney test, as described in the text. Values of $P < 0.05$ were considered significant.

Results

Changes in BACHD STM muscle fibers area, MyHC expression and ultrastructure

Previous studies suggested that limb and trunk muscle of HD patients are affected during disease progression, causing significant postural

instability (Tian *et al.*, 1992; Brožová *et al.*, 2011). Based on this observation, we began our investigation by searching for morphology changes in a neck muscle directly involved in head posture, the STM muscle, in a mouse model for HD disease (BACHD).

Figure 1(A–B) shows representative transverse section images of STM muscle fibers from 12 months control (WT) and diseased (BACHD) mice. An initial analysis of the STM muscle fiber show no signs of degeneration in both genotypes at the age indicated. However, when compared to WT muscles fiber CSA, BACHD mice presented a reduction in approximately 40% in CSA suggesting a possible muscle fibers atrophy (BACHD: 1333 μm^2 vs. 2772 μm^2 for WT (Median); $P = 0.0001$; We have analyzed ~3000 muscle fibers per genotype, $n = 3$ individual animals per genotype; Mann–Whitney test) (Fig. 1H).

As we noted atrophy of the STM muscle, our next step was to investigate whether this atrophy was associated to shifts in MyHC isoforms expression. Skeletal muscle fibers are characterized as slow-twitch fiber (type I) and three types of fast-twitch fibers (type IIA, type IIX and type IIB) (reviewed by Wang & Pessin, 2013). For this purpose, we performed an immunostaining for fiber types using specific monoclonal antibodies against the different MyHC isoforms. The representative images in Fig. 1C show cross-sections of the STM muscle fibers from WT. Figure 1C–C‴ shows the staining for type I, IIA, IIX, and IIB muscle fibers respectively. Figure 1D–D‴ shows the same staining for BACHD muscle fibers. Compared to WT, we observed more fibers stained for the IIA fibers in BACHD (Fig. 1D′). Indeed our quantification showed that the percentage of IIA fibers were in fact increased in BACHD STM muscle fibers [BACHD: 44.0 ± 4.0% vs. WT: 34.2 ± 1.7% (Mean ± SD); $t_4 = 3.8$; $P = 0.01$; We counted each fiber type in one muscle section in $n = 3$ individual animals per genotype; unpaired student *t*-test]. In addition, BACHD mice presented less staining for the IIX muscle fibers in STM compared to WT (Fig. 1D″). Quantification of several muscle fibers from both genotypes stained for IIX showed a reduction in the percentage of these fibers in the BACHD STM muscle [BACHD: 18.7 ± 4.0% vs. WT: 28.0 ± 4.1% (Mean ± SD); $t_4 = 2.8$; $P = 0.04$; $n = 3$ individual animals per genotype; unpaired student *t*-test]. These data showed that there was a significant fiber-typing switch in BACHD STM muscles.

We next performed a qualitative ultrastructure analysis of STM muscle fibers from BACHD mice (Fig. 1E–G, 90 images analyzed per genotype from 3WT and 3 BACHD animals). In comparison to WT muscle (Fig. 1E), analysis of the ultrastructure of the STM in BACHD mice revealed: (i) sarcoplasmic reticulum (SR) significantly enlarged, invading spaces (demarcated area in F) that were previously occupied by myofibrils (Fig. 1G, red arrows); (ii) Mitochondria containing abnormal vacuoles within the mitochondria matrix (Fig. 1G, blue arrow); (iii) increase in inter-myofibrilar glycogen deposits (Fig. 1G, yellow arrows) and (iv) areas with dramatic decrease in myofibrils (Fig. 1F, asterisk). Together, the ultrastructure

alterations can be an indicative that muscle fibers are under a degenerative process, corroborating the muscle histology data.

NMJs alterations in BACHD mice

Given the degree of STM- muscle atrophy and the pronounced changes observed in BACHD muscle fibers, our next step was to investigate whether muscle damage could be related to alterations at neuromuscular junctions. To address this question, STM- muscle whole mounts from WT and BACHD mice were stained with pre- (synaptotagmin) and postsynaptic (α-btx) markers and the NMJs morphology were examined by confocal microscopy.

Figure 2 shows representative images of presynaptic nerve terminals from 12 months WT (Fig. 2A) and BACHD (Fig. 2 C) STM muscles. Figure 2A′ and C′ shows the postsynaptic AChRs stained with α-btx in the same WT and BACHD muscle fibers respectively. The Fig. 2B and D shows representations of the particle analysis of NMJs of WT and BACHD. Figure 2B′ and D′ shows the skeletonization of NMJs of WT and BACHD. Our analyzes showed normal structure and synaptic elements colocalization in the NMJs from WT animals. In contrast, we observed that in BACHD STM muscles the presynaptic axon terminals did not completely co-localized with the postsynaptic AChRs [BACHD: 87.3 ± 2.0% for vs. 98.4 ± 1.6% for WT (mean ± SD); $t_4 = 8.0$; **$P = 0.001$ unpaired student *t*-test] (Fig. 2C and C′ and 2E for quantification), supporting the view of an ongoing degenerative process like denervation. We next analyzed the degree of denervation in NMJs and observed that many NMJs from BACHD STM muscles were partially denervated [BACHD: 20.0 ± 4.0% vs. 2.7 ± 2.3% for WT (mean ± SD); $t_4 = 6.5$; **$P = 0.002$ unpaired student *t*-test] (Fig. 2F for quantification and 2C″), with patches of postsynaptic AChRs showing no presynaptic partner associated to them (arrow). Additionally, we found that the areas of the pre- and postsynaptic terminals in the BACHD NMJs were smaller than WT [Presynaptic area- BACHD: 923 μm^2 vs. 1655 μm^2 for WT (median); ***$P = 0.0001$ (Fig. 2G); Postsynaptic area- BACHD: 1011 μm^2 vs. 1669 μm^2 for WT (median); ***$P = 0.0005$ (Fig. 2H)]. In general, the pre- and postsynaptic elements were significantly fragmented in BACHD but not in WT [BACHD: 81.7 ± 4.7% vs. 58.0 ± 2.6% for WT (mean ± SD); $t_4 = 7.6$; **$P = 0.001$ unpaired student *t*-test (Fig. 2I)]. We have analyzed 75 NMJs per genotype in $n = 3$ individual animals per genotype.

Axonal abnormalities in BACHD mice

We next evaluated whether the changes described here in BACHD NMJs could be a consequence of damage in motor axons close to the spinal cord. Thus, our next set of experiments aimed to investigate axons exiting the ventral roots. Semi-thin cross-sections of the cervical ventral roots were obtained and stained with toluidine blue (see methods). Qualitative analysis showed that, compared to WT (Fig. 3A), axons from BACHD mice presented severe morphology

---

FIG. 1. Decreased CSA, reduction in IIB fiber typing and ultrastructure abnormalities in BACHD STM muscle fibers. (A–B) Representative images of STM skeletal muscle fibers from 12 months old WT and BACHD mice. Scale bar: 50 μm: C–C‴ to D–D‴: Representative images of STM fiber typing from 12 months old WT and BACHD mice. Note that the STM from BACHD presented less staining for the IIX fibers in comparison to WT (C″ and D″). The IIA fibers are also increased in this muscle (C′ and D′). Scale bar: 50 μm. (E–F) Representative electron micrographs of STM fibers from WT and BACHD animals. Observe a normal triad in WT (red box). Note a reduction in the number of myofibrils in the sarcomere (asterisk) in BACHD. (G) High magnification view of the area shown in F depicting enlargement and invasion of the sarcoplasmic reticulum (demarcated area). Also note the presence of vacuoles within the inner space of mitochondrial organelles (blue arrow), abnormal deposition of glycogen in inter-myofibrilar space (yellow arrows) and atypical SR (red arrows). Scale bar: 500 nm. We have analyzed 90 images for WT and 90 images for BACHD from three individual animals per genotype). (H) The box plot shows the CSA median values for WT and BACHD STM muscle fibers. These results represent the median ± SD of more than 3.000 muscle fibers per genotype (***$P < 0.0001$; Man–Whitney test; $n = 3$ individual animals per genotype). (I) Quantitative analysis of the fiber typing showing decreased expression of IIX isoform and an increase in the expression of the IIA in 12 months old BACHD STM muscle fibers compared to WT. The results represent the mean ± SD (unpaired Student's *t*-test, *$P < 0.05$, $n = 3$ animals per genotype). [Colour figure can be viewed at wileyonlinelibrary.com].
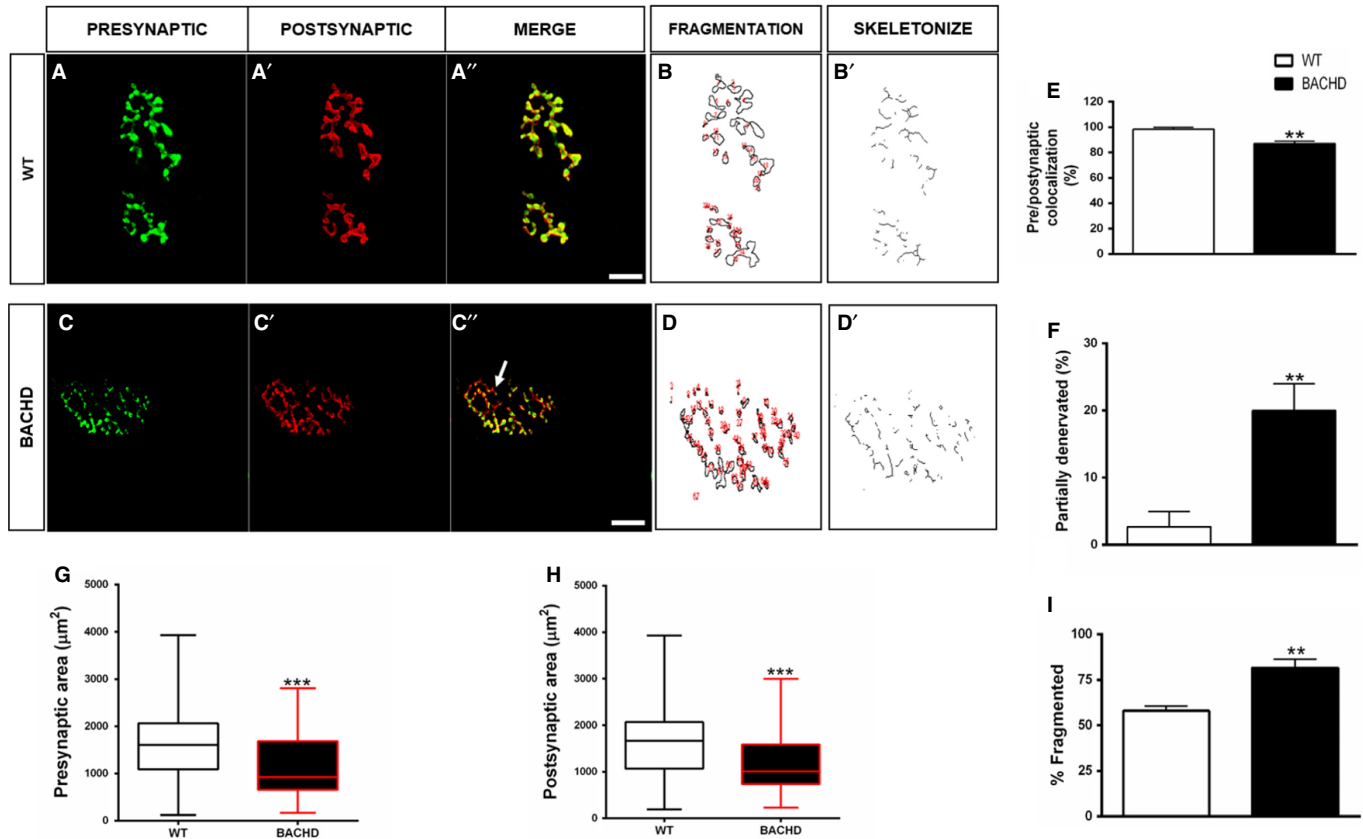
*IIX: unstained
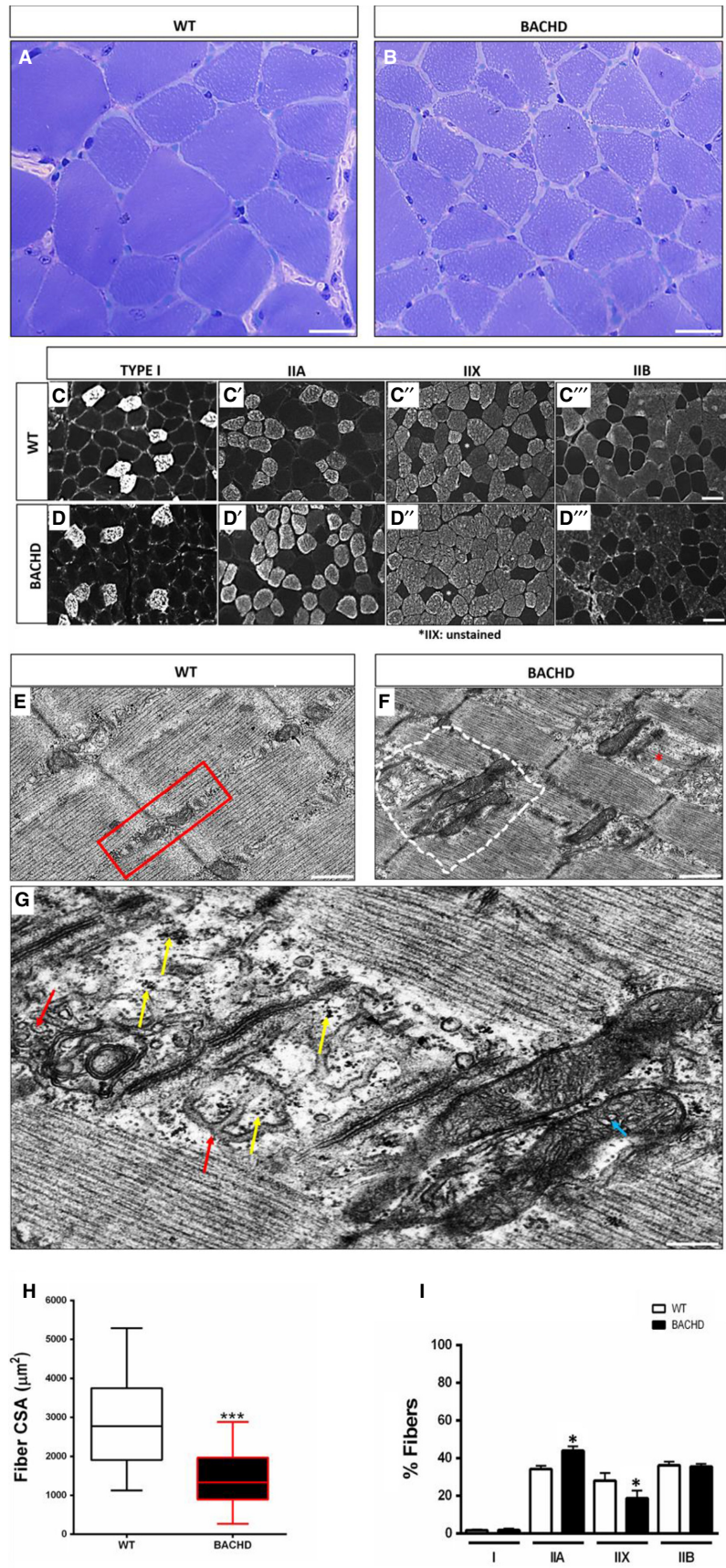
FIG. 2. Fragmentation and denervation in NMJs from BACHD. (A–C″) Representative images of STM- NMJs from 12 months WT and BACHD mice. (A and C) Presynaptic terminals labeled with Alexa-488 anti-synaptotagmin antibody (green). (A′ and C′) Postsynaptic AChRs labeled with Alexa-555 α-bungarotoxin (red). (A″ and C″) Overlapping images showing partial denervation (arrow). Scale bar: 10 μm. (B and D) Representation of particle analysis for both genotypes (red numbers). (B′ and D′) Skeletonization rendering of fragmentation in endplates from WT and BACHD. (E–I) Graphs showing the degree of colocalization (E) **$P = 0.001$ unpaired student *t*-test], partial denervation (F) **$P = 0.002$ unpaired student *t*-test], pre-synaptic area (G) ***$P = 0.0001$), post-synaptic area (H) ***$P = 0.0005$] and fragmentation of the endplates (I) **$P = 0.001$ unpaired student *t*-test]. The results represent the mean ± SD from 75 NMJs per genotype ($n = 3$ individual animals per genotype). [Colour figure can be viewed at wileyonlinelibrary.com].

changes (Fig. 3B red arrows). The quantitative analysis of the ventral roots demonstrated a reduction in the number of axons per area in BACHD [BACHD: 0.08 ± 0.03 axons/μm^2 vs. 0.2 ± 0.02 axons/μm^2 for WT (mean ± SD); $t_4 = 5.7$; **$P = 0.004$ unpaired student *t*-test] (Fig. 3E). The histogram in Fig. 3F shows a reduction in the number of larger myelinated fibers (>4.5 μm) in BACHD [Interval between 5–6 microns-BACHD: 48.7 ± 3.8 μm vs. 90.7 ± 12.7 μm for WT (mean ± SD); $t_4 = 5.5$; **$P = 0.005$ unpaired student *t*-test; interval between 6–7 microns- BACHD: 41.3 ± 3.0 μm vs. 84.3 ± 6.1 μm for WT (mean ± SD); $t_4 = 10.1$; ***$P = 0.0004$ unpaired student *t*-test; interval between 7–8 microns- BACHD: 40.0 ± 6.5 μm vs. 70.3 ± 6.0 μm for WT (mean ± SD); $t_4 = 6.0$; **$P = 0.004$ unpaired student *t*-test and interval between 8 and 9 microns- BACHD: 20.7 ± 4.1 μm vs. 33.3 ± 5.0 μm for WT (mean ± SD); $t_4 = 3.3$; *$P = 0.02$ unpaired student *t*-test, $n = 3$ individual animals per genotype (Fig. 3F)]. However, the *G*-ratio (relationship between axonal inner and outer diameter) [BACHD: 0.6 ± 0.1 vs. 0.7 ± 0.1 for WT (mean ± SD); $t_4 = 0.7$; $P = 0.5$ unpaired student *t*-test] and the thickness of the myelin sheath ratio [BACHD: 1.5 ± 0.1 μm vs. 1.5 ± 0.1 μm for WT (mean ± SD); $t_4 = 0.4$; $P = 0.7$ unpaired student *t*-test, $n = 3$ individual animals per genotype] were not different from control, (Fig. 3G–H). We have analyzed one semi-thin section per animal in $n = 3$ mice per genotype. Ultrastructure analyses confirmed the histological observations and showed that axons from BACHD presented

various degenerative features such as structural breakdown of the myelin sheath with lamellar separations (Fig. 3D, yellow arrows) and vacuoles within the axoplasm (blue arrows). We have qualitatively analyzed 30 images for each animal in $n = 3$ mice per genotype.

Motoneurons loss and atrophy in the spinal cord from BACHD mice

We next looked at the morphology and number of cervical spinal cord motoneurons. To identify putative spinal cord motoneurons we used an antibody that recognizes the enzyme ChAT. We found that there were ChAT- positive neurons clustered in the ventral horn of the cervical spinal cord segments in both genotypes. Figure 4 shows representative images of cervical segments stained with anti-ChAT from WT (Fig. 4A) and BACHD (Fig. 4B). Figure 4C shows an example of an atrophic ChAT-positive putative motoneuron in BACHD (white arrow). Confirming this observation, quantitative analysis of putative motoneurons′ diameters showed statistically significant reduction in this parameter in BACHD compared to WT [BACHD: 26.4 ± 1.4 μm vs. 32.8 ± 2.8 μm for WT (mean ± SD); $t_4 = 3.5$; *$P = 0.02$; $n = 3$ individual animals per genotype; unpaired student *t*-test] (Fig. 4L). In addition, we detected a reduction in the number of putative ChAT-positive motoneurons in sections of the cervical spinal cord segments [BACHD: 270 ± 22.6 vs. 342.3 ± 29 for WT; (mean ± SD); $t_4 = 3.4$;
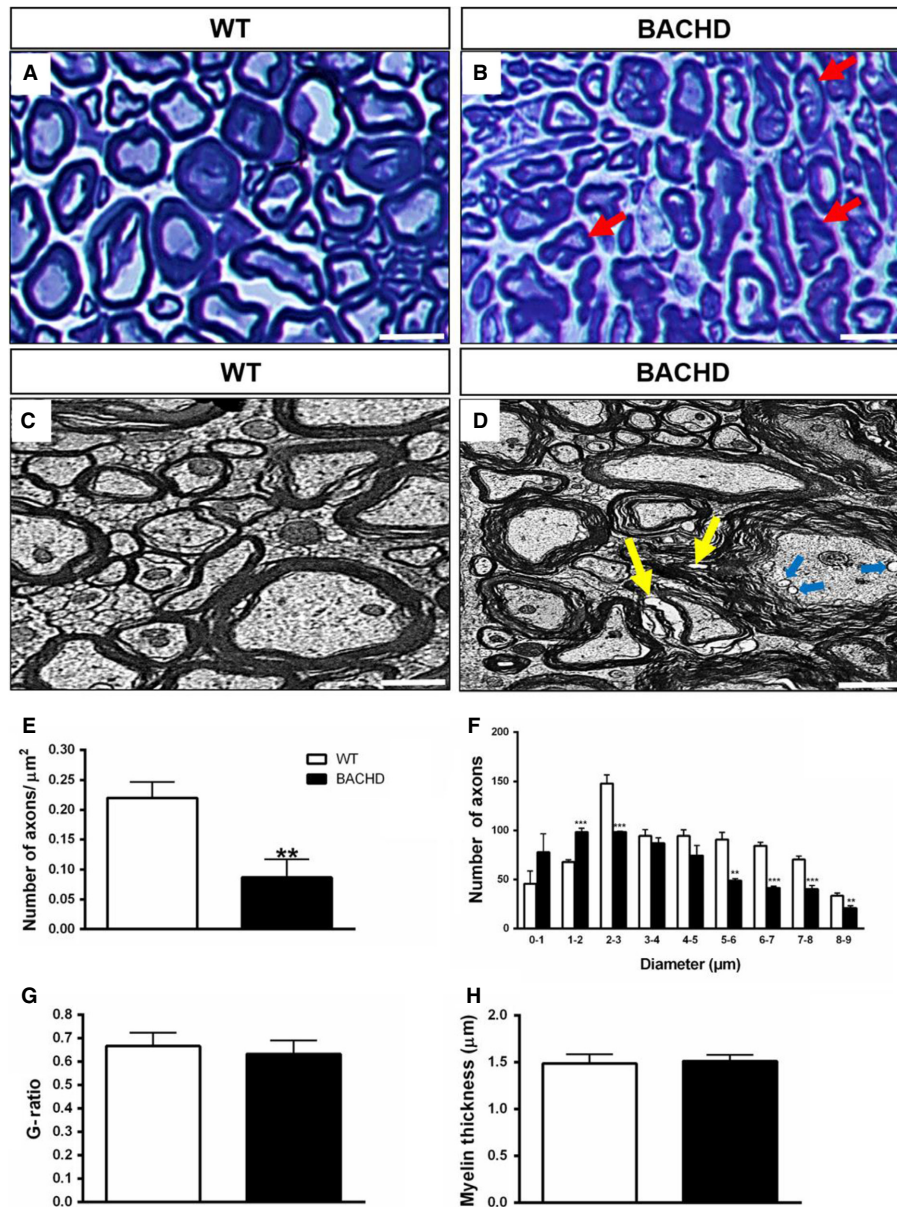
FIG. 3. Axonal changes in BACHD. (A–B) Representative images of axons from 12 months WT and BACHD respectively. Note in A typical axons with preserved structure and shape whereas in B note the presence of atypical axons in degeneration with morphological abnormalities (red arrows). The axons were stained by toluidine blue. Scale bar: 40 μm. (C–D) Electron micrograph of the axons from WT and BACHD. Note in D axons with signs of degeneration like lamellar separation (yellow arrows) and vacuolization in the axoplasm (blue arrows). We analyzed 90 electron micrographs per genotype. Scale bar: 2 μm. (E–H). Quantification of the number of axons by nerve area, number of large axons (>4.5 μm), G-ratio and myelin thickness, respectively. We have analyzed 9 semi-thin sections per genotype and a total of 3.222 axons in WT and 1.937 in BACHD (*, **, ***P < 0.05, unpaired Student's t-test, n = 3 individual animals per genotype). [Colour figure can be viewed at wileyonlinelibrary.com].

*P = 0.02; n = 3 individual animals per genotype; unpaired student t-test] (Fig. 4K). A similar reduction in the total number of cells was observed in cervical spinal cord segments stained with toluidine blue [BACHD: 128.7 ± 11.7 vs. 177.0 ± 26.5 for WT (mean ± SD); t_4 = 2.9; *P = 0.04; n = 3 individual animals per genotype; unpaired student t-test] (Fig. 4M).

Comparing to WT motoneurons, qualitative analysis of TEM micrographs showed atypical atrophic nuclei in a BACHD motoneuron (Fig. 4H-white arrow). We also observed an increase in the number of lipofuscin granules in BACHD motoneurons (Fig. 4G – red arrows) compared to WT (Fig. 4F – red arrows) [BACHD: 0.2 ± 0.1 granules/area vs. 0.1 ± 0.03 granules/area for WT (mean ± SD); t_4 = 2.5;*P = 0, 03; n = 3 individual animals per genotype.

We have analyzed 30 motomeurons per genotype, unpaired student's t-test]. Furthermore, we observed vacuolated mitochondria in BACHD motoneurons (Fig. 4J) that were not observed at WT counterparts (Fig. 4I).

To test whether putative motoneurons were undergoing apoptosis, we immunostained sections that contained C1–C3 cervical segments from WT and BACHD spinal cords with an antibody against caspase-3, a marker of cell death. Figures 4D–E show representative images of the caspase-3 in the cervical segments from BACHD and WT mice. Compared to WT, we observed approximately three times more putative motoneurons positive for caspase-3 in BACHD spinal cords (Fig. 4O) [BACHD: 126 ± 10.6 cells vs. 42 ± 13.1 for WT (mean ± SD); t_4 = 8.6; **P = 0.001; n = 3 individual animals per
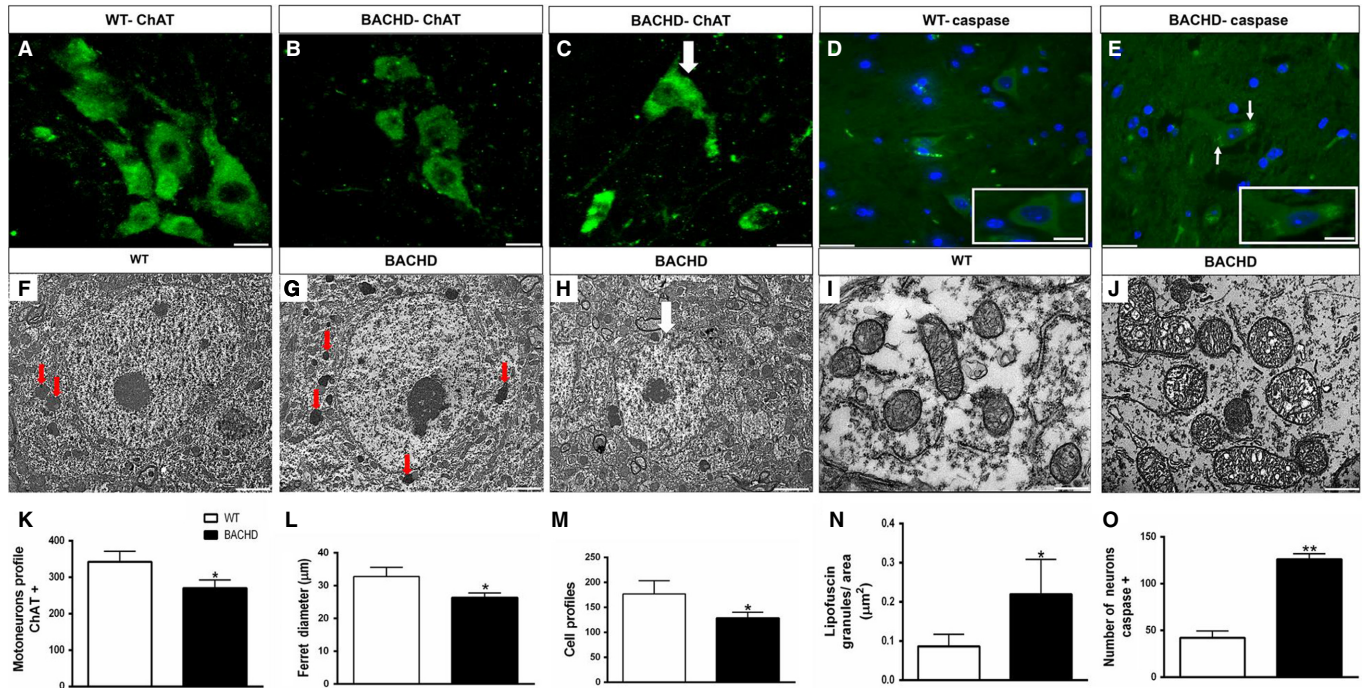
FIG. 4. Motoneurons atrophy in BACHD cervical spinal cords. (A–C) Representative images of putative motoneurons from cervical spinal cord sections stained for ChAT from 12 months WT (A) and BACHD (B). (C) Atypical motoneuron. Scale bar: 50 μm. (D–E) Fluorescence images of motoneurons stained for caspase-3 in WT (D) and BACHD (arrow). Nuclei were stained with DAPI. Inset: putative motoneuron positive for caspase-3 in BACHD. Scale bar: 50 μm. (F–G) Ultrastructural images showing motoneuron with more lipofuscin granules (red arrows) in BACHD compared to WT. (H) Representative images of an atrophic motoneuron from BACHD spinal cords. Scale bar: 5 μm. (I–J) Representative images normal and vacuolated mitochondria in WT and BACHD respectively. Scale bar: 500 nm. (K) Quantification of ChAT-positive motoneurons profiles in WT and BACHD cervical spinal cords (~150 neurons analyzed per genotype). (L) Ferret diameter. (M) Number of cell profiles in spinal cord sections from WT and BACHD stained with toluidine blue (~2.000 cells analyzed per genotype; unpaired student's t-test; *P < 0.05; n = 3 animals per genotype). (N) Quantification of the number of lipofuscin granules/area in WT and BACHD motoneurons (Total analyzed 87 granules in WT and 224 granules in BACHD from 30 motoneurons per genotype; unpaired student's t-test; *P < 0.05; n = 3 animals per genotype). (O) Graphical quantification of motoneurons stained positively for caspase-3 in WT and BACHD (~150 neurons analyzed per genotype; unpaired student's t-test; **P < 0.001; n = 3 animals per genotype). All results described here are from n = 3 individual animals per genotype and were expressed as mean ± SD. [Colour figure can be viewed at wileyonlinelibrary.com].

genotype; unpaired student's t-test]. This result indicates that the activation of apoptotic cascades may be responsible for the putative motoneuron degeneration observed in BACHD spinal cords.

Discussion

Most scientific investigations on HD disease focused their studies mainly in the brain pathology and the neurological symptoms that arise from such alterations. From this perspective, and taking advantage of BACHD murine model for HD, we investigated putative alterations caused by mHtt in the motor unit (NMJs, axons and spinal cord motoneurons) that control muscle contraction.

We first investigated the impact of the mHtt on the last component of the MU: the skeletal muscle. It is well described that the motor symptoms in HD involve involuntary movements of the face and limbs and postural instability of the neck and trunk (Bates et al., 2002). In this study, we evaluated possible changes in the STM, a neck muscle important for head control and posture (Kim, 2015). We found that many of the STM muscle fibers were significantly smaller in the HD mice than in the age-matched control fibers (WT mice) (Fig. 1 and schematic representation in Fig. 5). Consistent with our results, atrophy of skeletal muscles has been considered a hallmark for HD in humans (Farrer, 1985; Farrer & Meaney, 1985; Ribchester et al., 2004; Trejo et al., 2004). Mielcarek (2015) observed in R6/2 mice significant physiological alterations in the contractile properties of the extensor longus digitorum (EDL) and tibialis anterior (TA)

muscles, as well as a reduction in muscle mass. Although it has been suggested that mHtt has deleterious effects on muscles in R6/2 mice, via accumulation of poly-glutamine aggregates (Sathasivam et al., 1999; Moffitt et al., 2009) and formation of inclusions in myoblasts and myotubes (Orth et al., 2003), the subjacent mechanism(s) of muscle atrophy is (are) not yet elucidated.

The ultrastructure analyses of STM muscle fibers from BACHD showed enlargement of the sarcoplasmic reticulum, invading the myofibrils region. We also observed the presence of vacuoles inside the mitochondria. Moreover, we observed the presence of inter-myofibrillar glycogen and disorganization of the triads (Fig. 1). These changes suggested a pathological ongoing process during muscle atrophy in BACHD mice. Furthermore, the mitochondrial defects reported here might be a key factor to the degenerative process seen in HD animal models and patients with this disease. Indeed, mHtt protein has been found to interfere with the normal function of mitochondria (Chaturvedi et al., 2009; Chandra et al., 2016).

Another ultrastructure change that caught our attention was the great amount of glycogen granules accumulated at the inter-myofibrillar spaces in the BACHD STM muscle fibers. It is known that glycogen accumulation at these spaces and in the intra-myofibrillar compartments are normal events and the deposits are used depending on the muscle energy demand (Marchand et al., 2002). However, we cannot exclude the fact that the abnormally high levels of glycogen may be a consequence of energy imbalance caused by putative mitochondrial dysfunction. In addition, areas of degraded
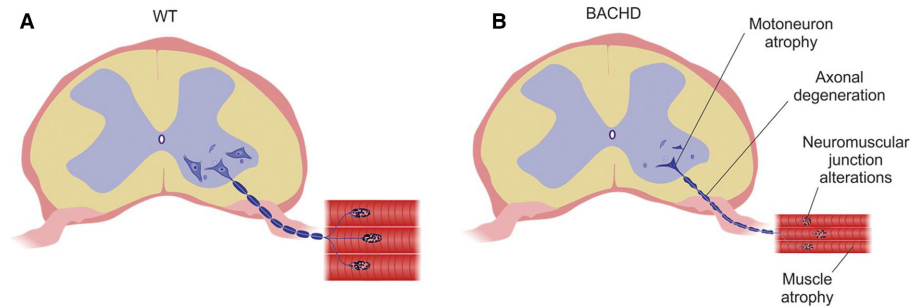
Fig. 5. Schematic representation of cervical spinal cords from WT and BACHD (A) Motor unit of WT mice showing preservation of all structures. (B) Changes seen in the motor unit of BACHD such as motoneurons atrophy, axonal degeneration, neuromuscular junctions fragmentation and muscle fiber atrophy. [Colour figure can be viewed at wileyonlinelibrary.com].

contractile structures together with invaded portions of the sarcoplasmic reticulum were described in denervated muscles (Pellegrino & Franzini, 1963). The authors also reported that, during atrophy, there was a reduction in the number of the contractile filaments similar to what we have reported here for BACHD STM muscle fibers (Fig. 1F). Here, we have also observed changes in sarcoplasmic reticulum and myofibrils. Moreover, it has been reported that there is a close relationship between the accumulation of inter-myofibrillar glycogen and SR function (Nielsen et al., 2009).

We next performed the muscle fiber typing to confirm that the BACHD STM muscle fibers atrophy could be related to a decrease in the proportion of the largest IIX fiber type. We observed that STM muscles from BACHD mice presented a decrease in large fibers (IIX) and partial increase in smaller fibers (IIA) (Fig. 1). Such reduction in fast-twitch fibers (IIX) is in accordance with previous works from the literature showing that they are more vulnerable than slow-twitch fibers under a variety of atrophic conditions (reviewed by Wang & Pessin, 2013). Data from the literature have shown that motoneurons and their NMJs differ drastically in sizes with the biggest ones, with largest NMJs, innervating fast muscle fibers (Burke et al., 1971; Mantilla et al., 2007). We therefore hypothesized that the reduction in IIX muscle fibers in BACHD might also be associated to other alterations described here such as decrease in the area of pre- and postsynaptic elements (Fig. 2) and decreased size of putative motoneurons in BACHD (Fig. 4) (see also the cartoon in Fig. 5). However, we cannot rule out the possibility that the reduction in ChAT-positive cells diameter observed in BACHD spinal cords reflects putative motoneurons shrinkage before they die. Decrease in neuron's size has been recognized in other degenerative disorders such as Alzheimer's, Parkinson's diseases and in ALS patients, where there is a depletion of large pyramidal neurons from the primary motor cortex (Betz cells) and large spinal cord motoneurons compared to control subjects (Kiernan & Hudson, 1991). Additional experiments are necessary to clarify if larger motoneurons selective die in BACHD spinal cords.

Our next experiments were designed to investigate whether BACHD mice showed alterations in the NMJs. STM-NMJs from BACHD presented several degenerative signs such as loss of colocalization between the pre- and postsynaptic elements, reduction in the synaptic area, endplates fragmentation and partial denervation (Fig. 2 and schematic representation in Fig. 5).

Many morphological studies on NMJs in neurodegenerative diseases (Sarantseva et al., 2011; Valdez et al., 2012; Xia et al., 2012) or in age-related degenerative processes (Balice-Gordon, 1997; Courtney & Steinbach, 1981; Gutmann et al., 1971; Valdez et al., 2010) correlated similar alterations to the axonal denervation

process. For example, Ribchester et al. (2004) observed changes in NMJs from R6/2 mice such as denervation, reduction in the area of presynaptic terminals, increased acetylcholine sensitivity, and reduction in the sensitivity to μ-conotoxin (Ribchester). Therefore, it has been suggested that mHtt might alter synaptic components and then interfere with its structure affecting neurotransmission (Smith et al., 2005). The results presented here are in line with this view.

After observing abnormalities in key components of the motor unit such as skeletal muscle and NMJs, we analyzed the ventral roots of the cervical spinal cord. The ultrastructural analysis of the ventral roots of the cervical segment of BACHD spinal cords showed lamellar separation and vacuoles in the myelin sheath and axoplasm (Fig. 3 and schematic representation in Fig. 5). Furthermore, we observed an intense process of axonal degeneration with decrease in diameter and number per area. We also observed that the myelinated fibers that were most affected in BACHD animals were of the highest caliber. Previous work demonstrated similar changes in ultrastructure preferable seen in large-caliber fibers in the sciatic nerve of the R6/2 mice (Wade et al., 2008). Sobue et al. (1981) also found higher incidence of large-caliber fibers at the expense of smaller caliber in cervical ventral roots of patients with ALS. These data suggested that large myelinated fibers, corresponding to α-motoneurons fibers, were selectively affected and that the small myelinated fibers, corresponding to γ-motor neurons fibers, were preserved to some extent (Sobue et al., 1981; Biscoe et al.,1982).

Previous studies performed in R6/2 mice models for HD showed marked atrophy of skeletal muscles like TA and EDL and they related these findings on skeletal muscle atrophy to possible alterations in the α-motoneurons. However, none of these studies investigated what might be happening to α-motoneurons (Ribchester et al., 2004; Mielcarek, 2015). Furthermore, Mielcarek (2015) showed, through functional tests, that the physiological evaluation of the motor unit of the R6/2 mice presented a progressive loss in the number of motor units in the EDL muscle. Our findings mighte contribute to a better understanding of muscle atrophy in this mice model for HD as we observed death and atrophy of putative motoneurons.

As we demonstrated neuronal loss in the cervical segment of the spinal cord, our next experiments aimed to investigate whether these neurons were undergoing apoptosis. A quantitative analysis of the number of caspase-3 positive neurons revealed that cervical spinal cords from BACHD mice had three times more neurons positive for Caspase-3 than their WT counterparts (Fig. 4). Our data suggest that the reported neuronal death in the cervical spinal cord in BACHD might be occurring by an activation of the apoptotic cascade.

These data are in accordance to previous studies using mouse models for HD that showed neuronal death by apoptosis in other regions of the CNS (Dragunow *et al.*, 1995). Other works also suggested that the Htt could be a substrate to caspase-3, leading to an increase in the cleavage rate of Htt, causing additional stress to the cell and consequently the cell death by apoptosis (Wellington *et al.*, 2002). Furthermore, Toulmond *et al.* (2004) showed that the inhibition of the activity of caspase-3 by its reversible inhibitor (M-826), resulted in a significant reduction in the neuronal death in rat models for HD.

We next investigated through TEM possible alterations at the ultrastructural level in motoneurons from cervical spinal cords of BACHD mice. Mitochondria are vital organelles that generate energy to all cellular processes and regulate cell function, thus, any impairment in these structures can lead to generation of reactive oxygen species that can induce cell death by necrosis or apoptosis (Benard *et al.*, 2007). It has been shown that mitochondria dysfunction plays an important role in the pathogenesis of HD (Browne & Beal, 2004; Reddy *et al.*, 2009). In our study, we observed cristae disruption and vacuoles in mitochondria (Fig. 4). Previous *in vivo* studies showed that N-terminals Htt fragments could directly interfere with mitochondria functioning, resulting in calcium related-abnormalities and subsequent energy deficit (Panov *et al.*, 2002). It is interesting to note that neurons are the first cells to be affected by mitochondria alterations as they are very sensitive to oxidative stress, excitotoxic stress, expression of inflammatory signals, pro-apoptotic signals and energy depletion that might play a role in the observed neuronal death in HD (Kim *et al.*, 2010a, b).

Another feature that we observed in the EM images was the presence of lipofuscin granules (Fig. 4H) in BACHD motoneurons. It is well-described that the accumulation of these granules in neurons during aging is a normal process (Samorajski *et al.*, 1965). However, there are evidences that this deposition may also be related to neurodegenerative diseases such as Alzheimer's disease and Amyotrophic Lateral Sclerosis (Mcholm *et al.*, 1984; Cataldo *et al.*, 1994). Furthermore, it is known that oxidative stress caused by mitochondrial damage in brain of HD patients leads to the increase in lipofuscin granules (Brown, 1999). Based on these evidences, we suggested that the accumulation of lipofuscin granules observed in motoneurons from BACHD might be a sign of degeneration. In addition, we suggested that the mitochondria observed in motoneurons at the ultrastructure level might be related to cell atrophy and death by apoptosis in cervical spinal cord from BACHD mice.

In conclusion, our study provides evidences of significant alterations at the spinal cord motoneurons, ventral roots, NMJs, and STM muscle in a mouse model for HD (see Fig. 5). We suggest that although this disease is caused by damage in the upper CNS structures that control movement, the motor unit, which is the final pathway of the motor system, also suffers significant changes in BACHD. Further experiments are necessary to identify mechanisms involved in these alterations. Therefore, our data may open new routes of investigation and could help in establishing new directions in the therapeutics of HD.

Acknowledgements

Abbreviations

ALS, amyotrophic lateral sclerosis; CNS, central nervous system; CSA, cross-sectional area; EDL, extensor longus digitorum; FF, fast fatigable; HD, Huntington's disease; htt, Huntingtin; mHtt, mutated huntingtin; MU, motor unit; nAChR, nicotinic acetylcholine receptor; NMJs, neuromuscular junctions; PGC-1α, proliferator-activated receptor γ co activator 1 alpha; RT, room temperature; SR, sarcoplasmic reticulum; STM, sternomastoid; TA, tibialis anterior; TEM, transmission electron microscopy; WT, wild type; α–btx, α-bungarotoxin.

References

Balice-Gordon, R.J. (1997) Age-related changes in neuromuscular innervation. *Muscle Nerve Suppl.*, **5**, S83–S87.

Bates, G.P. (2005) History of genetic disease: the molecular genetics of Huntington disease – a history. *Nat. Rev. Genet.*, **6**, 766–773.

Bates, G.P., Harper, P.S. & Jones, A.L. (2002) *Huntington's Disease*. Oxford University Press, Oxford, UK, pp. 429–472.

Benard, G., Bellance, N., James, D., Parrone, P., Fernandez, H., Letellier, T. & Rossignol, R. (2007) Mitochondrial bioenergetics and structural network organization. *J. Cell Sci.*, **120**, 838–848.

Biscoe, T.J., Nickels, S.M. & Stirling, C.A. (1982) Numbers and sizes of nerve fibres in mouse spinal roots. *Exp. Physiol.*, **67**, 473–494.

Brown, G.C. (1999) Nitric oxide and mitochondrial respiration. *BBA-Bioenergetics*, **1411**, 351–369.

Browne, S.E. & Beal, M.F. (2004) The energetics of Huntington's disease. *Neurochem. Res.*, **29**, 531–546.

Brožová, H., Štochl, J., Klempíř, J., Kuchařík, M., Růžička, E. & Roth, J. (2011) A sensitivity comparison of clinical tests for postural instability in patients with Huntington's disease. *Gait Posture.*, **34**, 245–247.

Burke, R.E., Levine, D.N., Zajac, F.E.D., Tsairis, P. & Engel, W.K. (1971) Mammalian motor units: physiological-histochemical correlation in three types in cat gastrocnemius. *Science*, **174**, 709–712.

Cataldo, A.M., Hamilton, D.J. & Nixon, R.A. (1994) Lysosomal abnormalities in degenerating neurons link neuronal compromise to senile plaque development in Alzheimer disease. *Brain Res.*, **640**, 68–80.

Chandra, A., Sharma, A., Calingasan, N.Y., White, J.M., Shurubor, Y., Yang, X.W. & Johri, A. (2016) Enhanced mitochondrial biogenesis ameliorates disease phenotype in a full-length mouse model of Huntington's disease. *Hum. Mol. Genet.*, **25**, 2269–2282.

Chaturvedi, R.K., Adhihetty, P., Shukla, S., Hennessy, T., Calingasan, N., Yang, L., Starkov, A., Kiaei, M. *et al.* (2009) Impaired PGC-1alpha function in muscle in Huntington's disease. *Hum. Mol. Genet.*, **18**, 3048–3065.

Chau, W.K., So, K.F., Tay, D. & Dockery, P. (2000) A morphometric study of optic axons regenerated in a sciatic nerve graft of adult rats. *Restor. Neurol. Neuros.*, **16**, 105–116.

Courtney, J. & Steinbach, J.H. (1981) Age changes in neuromuscular junction morphology and acetylcholine receptor distribution on rat skeletal muscle fibres. *J. Physiol.*, **320**, 435–447.

Dragunow, M., Faull, R.L.M., Lawlor, P., Beilharz, E.J., Singleton, K., Walker, E.B. & Mee, E. (1995) In situ evidence for DNA fragmentation in Huntington's disease striatum and Alzheimer's disease temporal lobes. *NeuroReport*, **6**, 1053–1057.

Farrer, L.A. (1985) Diabetes mellitus in Huntington disease. *Clin. Genet.*, **27**, 62–67.

Farrer, L.A. & Meaney, F.J. (1985) An anthropometric assessment of Huntington's disease patients and families. *Am. J. Phys. Anthropol.*, **67**, 185–194.

Gray, M., Shirasaki, D.I., Cepeda, C., André, V.M., Wilburn, B., Lu, X.H. & Li, X.J. (2008) Full-length human mutant huntingtin with a stable polyglutamine repeat can elicit progressive and selective neuropathogenesis in BACHD mice. *J. Neurosci.*, **28**, 6182–6195.

Gutmann, E., Hanzlikova, V. & Vysokocil, F. (1971) Age changes in cross striated muscle of the rat. *J. Physiol.*, **216**, 331–343.

Harjes, P. & Wanke, E.E. (2003) The hunt for huntingtin function: interaction partners tell many different stories. *Cell Press*, **28**, 425–433.

Holmes, A., Yang, R.J., Murphy, D.L. & Crawley, J.N. (2002) Evaluation of antidepressant-related behavioral responses in mice lacking the serotonin transporter. *Neuropsychopharmacology*, **27**, 914–923.

Hoogeveen, A.T., Willemsen, R., Meyer, N., De Roolj, K.E., Roos, R.A., Van Ommen, G.J.B. & Galjaard, H. (1993) Characterization and localization of the Huntington disease gene product. *Hum. Mol. Genet.*, **2**, 2069–2073.

Huntington's Disease Collaborative Research Group (1993) A novel gene containing a trinucleotide repeat that is expanded and unstable on Huntington's disease chromosomes. *Cell*, **72**, 971–983.

Kazantsev, A., Preisinger, E., Dranovsky, A., Goldgaber, D. & Housman, D. (1999) Insoluble detergent-resistant aggregates form between pathological and nonpathological lengths of polyglutamine in mammalian cells. *Proc. Natl. Acad. Sci.*, **96**, 11404–11409.

Kiernan, J.A. & Hudson, A.J. (1991) Changes in sizes of cortical and lower motor neurons in amyotrophic lateral sclerosis. *Brain*, **114**, 843–853.

Kim, M.S. (2015) Neck kinematics and sternocleidomastoid muscle activation during neck rotation in subjects with forward head posture. *J. Phys. Ther. Sci.*, **27**, 3425.

Kim, J., Moody, J.P., Edgerly, C.K., Bordiuk, O.L., Cormier, K., Smith, K., Beal, M.F. & Ferrante, R.J. (2010a) Mitochondrial loss, dysfunction and altered dynamics in Huntington's disease. *Hum. Mol. Genet.*, **19**, 3919–3935.

Kim, J., Moody, J.P., Edgerly, C.K., Bordiuk, O.L., Cormier, K., Smith, K. & Ferrante, R.J. (2010b) Mitochondrial loss, dysfunction, and altered dynamics in Huntington's disease. *Hum. Mol. Genet.*, **19**, 3919–3935.

Kong, J. & Xu, Z. (1999) Peripheral axotomy slows motoneuron degeneration in a transgenic mouse line expressing mutant SOD1 G93A. *J. Comp. Neurol.*, **412**, 373–380.

Li, S.H., Schilling, G., Young, W., Margolis, R.L., Stine, O.C., Wagster, M.V. & Hedree, N.J.C. (1993) Huntington's disease gene (IT15) is widely expressed in human and rat tissues. *Neuron*, **11**, 985–993.

Mangiarini, L., Sathasivam, K., Seller, M., Cozens, B., Harper, A., Hetherington, C. & Bates, G.P. (1996) Exon 1 of the HD gene with an expanded CAG repeat is sufficient to cause a progressive neurological phenotype in transgenic mice. *Cell*, **87**, 493–506.

Mantilla, C.B., Rowley, K.L., Zhan, W.Z., Fahim, M.A. & Sieck, G.C. (2007) Synaptic vesicle pools at diaphragm neuromuscular junctions vary with motoneuron soma, not axon terminal, inactivity. *Neuroscience*, **146**, 178–189.

Mantovani, S., Gordon, R., Li, R., Christie, D.C., Kumar, V. & Woodruff, T.M. (2016) Motor deficits associated with Huntington's disease occur in the absence of striatal degeneration in BACHD transgenic mice. *Hum. Mol. Genet.*, **25**, 1780–1791.

Marchand, I., Chorneyko, K., Tarnopolsky, M., Hamilton, S., Shearer, J., Potvin, J. & Graham, T.E. (2002) Quantification of subcellular glycogen in resting human muscle: granule size, number, and location. *J. Appl. Physiol.*, **93**, 1598–1607.

Mcholm, G.B., Aguilar, M.J. & Norris, F.H. (1984) Lipofuscin in amyotrophic lateral sclerosis. *Arch. Neurol.*, **41**, 1187.

Menalled, L., El-Khodor, B., Patry, M. & Suarez-Farinas, M. (2009) Systematic behavioral evaluation of transgenic and knock-in mouse models of Huntington's disease. *Neurobiol. Dis.*, **35**, 319–336.

Mielcarek, M. (2015) Huntington's disease is a multi-system disorder. *Rare Dis.*, **3**, e1058464.

Moffitt, H., McPhail, G.D., Woodman, B., Hobbs, C. & Bates, G.P. (2009) Formation of polyglutamine inclusions in a wide range of non-CNS tissues in the HdhQ150 knock-in mouse model of Huntington's disease. *PLoS One*, **30**, e8025.

Nielsen, J., Schrøder, H.D., Rix, C.G. & Ørtenblad, N. (2009) Distinct effects of subcellular glycogen localization on tetanic relaxation time and endurance in mechanically skinned rat skeletal muscle fibres. *J. Physiol.*, **587**, 3679–3690.

Ona, V.O., Li, M., Vonsattel, J.P., Andrews, L.J., Khan, S.Q., Chung, W.M., Frey, A.S., Menon, A.S. *et al.* (1999) Inhibition of caspase-1 slows disease progression in a mouse model of Huntington's disease. *Nature*, **399**, 263–267.

Orth, M., Cooper, J.M., Bates, G.P. & Schapira, A.H. (2003) Inclusion formation in Huntington's disease R6/2 mouse muscle cultures. *J. Neurochem.*, **87**, 1–6.

Panov, A.V., Gutekunst, C.A., Leavitt, B.R., Hayden, M.R., Burke, J.R., Strittmatter, W.J. & Greenamyre, J.T. (2002) Early mitochondrial calcium defects in Huntington's disease are a direct effect of polyglutamines. *Nat. Neurosci.*, **5**, 731–736.

Pellegrino, C. & Franzini, C. (1963) An electron microscope study of denervation atrophy in red and white skeletal muscle fibres. *J. Cell Biol.*, **17**, 327–349.

Pratt, S.J., Shah, S.B., Ward, C.W., Inacio, M.P., Stains, J.P. & Lovering, R.M. (2013) Effects of in vivo injury on the neuromuscular junction in healthy and dystrophic muscles. *J. Physiol.*, **591**, 559–570.

Reddy, P.H., Mao, P. & Manczak, M. (2009) Mitochondrial structural and functional dynamics in Huntington's disease. *Brain Res. Rev.*, **61**, 33–48.

Ribchester, R.R., Thomson, D., Wood, N.I., Hinks, T., Gillingwater, T.H., Wishart, T.M., Court, F.A. & Morton, A.J. (2004) Progressive abnormalities in skeletal muscle and neuromuscular junctions of transgenic mice expressing the Huntington's disease mutation. *Eur. J. Neurosci.*, **20**, 3092–3114.

Rigamonti, D., Bauer, J.H., De-Fraja, C., Conti, L., Sipione, S., Sciorati, C., Clementi, E., Hackam, A. *et al.* (2000) Wild-type huntingtin protects from apoptosis upstream of caspase-3. *J. Neurosci.*, **20**, 3705–3713.

Rodrigues, H.A., Fonseca, M.D.C., Camargo, W.L., Lima, P.M., Martinelli, P.M., Naves, L.A. & Guatimosim, C. (2013) Reduced expression of the vesicular acetylcholine transporter and neurotransmitter content affects synaptic vesicle distribution and shape in mouse neuromuscular junction. *PLoS One*, **8**, e78342.

Samorajski, T., Ordy, J.M. & Keefe, J.R. (1965) The fine structure of lipofuscin age pigment in the nervous system of aged mice. *J. Cell Biol.*, **26**, 779–793.

Sarantseva, S.V., Kislik, G.A., Tkachenko, N.A., Vasil'ev, A.N. & Shvartsman, A.L. (2011) [Morphological and functional abnormalities in neuromuscular junctions of Drosophila melanogaster induced by the expression of human APP gene]. *Tsitologiia*, **54**, 421–429.

Sathasivam, K., Hobbs, C., Turmaine, M., Mangiarini, L., Mahal, A., Bertaux, F., Wanker, E.E., Doherty, P. *et al.* (1999) Formation of polyglutamine inclusions in non-CNS tissue. *Hum. Mol. Genet.*, **8**, 813–822.

Smith, R., Brundin, P. & Ly, J.Y. (2005) Synaptic dysfunction in Huntington's disease: a new perspective. *Cell. Mol. Life Sci.*, **62**, 1901–1912.

Sobue, G., Matsuoka, Y., Mukai, E., Takayanagi, T. & Sobue, I. (1981) Pathology of myelinated fibers in cervical and lumbar ventral spinal roots in amyotrophic lateral sclerosis. *J. Neurol. Sci.*, **50**, 413–421.

Tian, J.R., Herdman, S.J., Zee, D.S. & Folstein, S.E. (1992) Postural stability in patients with Huntington's disease. *Neurology*, **42**, 1232.

Toulmond, S., Tang, K., Bureau, Y., Ashdown, H., Degen, S., O'donnell, R., Tam, J., Han, Y. *et al.* (2004) Neuroprotective effects of M826, a reversible caspase-3 inhibitor, in the rat malonate model of Huntington's disease. *Brit. J. Pharmacol.*, **141**, 689–697.

Trejo, A., Tarrats, R.M., Alonso, M.E., Boll, M.C., Ochoa, A. & Velásquez, L. (2004) Assessment of the nutrition status of patients with Huntington's disease. *Nutrition*, **20**, 192–196.

Trottier, Y., Lutz, Y., Stevanin, G., Imbert, G., Devys, D., Cancel, G. & Agid, Y. (1995) Polyglutamine expansion as a pathological epitope in Huntington's disease and four dominant cerebellar ataxias. *Nature*, **378**, 403–406.

Valdez, G., Tapia, J.C., Kang, H., Clemenson, G.D.J.R., Gage, F.H., Lichtman, J.W. & Sanes, J.R. (2010) Attenuation of age-related changes in mouse neuromuscular synapses by caloric restriction and exercise. *Proc. Natl. Acad. Sci. USA*, **107**, 14863–14868.

Valdez, G., Tapia, J.C., Lichtman, J.W., Fox, M.A. & Sanes, J. (2012) Shared resistance to aging and ALS in neuromuscular junctions of specific muscles. *PLoS One*, **7**, e34640.

Van Der Burg, J.M., Björkqvist, M. & Brundin, P. (2009) Beyond the brain: widespread pathology in Huntington's disease. *Lancet Neurol.*, **8**, 765–774.

Wade, A., Jacobs, P. & Morton, A.J. (2008) Atrophy and degeneration in sciatic nerve of presymptomatic mice carrying the Huntington's disease mutation. *Brain Res.*, **1188**, 61–68.

Wang, Y. & Pessin, J.E. (2013) Mechanisms for fiber-type specificity of skeletal muscle atrophy. *Curr. Opin. Clin. Nutr.*, **16**, 243–250.

Wellington, C.L., Ellerby, L.M., Gutekunst, C.A., Rogers, D., Warby, S., Graham, R.K., Loubser, O., Van Raamsdonk, J. *et al.* (2002) Caspase cleavage of mutant huntingtin precedes neurodegeneration in Huntington's disease. *J. Neurosci.*, **22**, 7862–7872.

Xia, R., Liu, Y., Yang, L., Gal, J., Zhu, H. & Jia, J. (2012) Motor neuron apoptosis and neuromuscular junction perturbation are prominent features in a Drosophila model of Fus-mediated ALS. *Mol. Neurodegener.*, **7**, 10.

Yang, X.W. & Gray, M. (2011) Mouse models for validating preclinical candidates for Huntington's disease. In Lo, D.C. & Hughes, R.E. (Eds),

Neurobiology of Huntington's Disease: Applications to Drug Discovery. CRC Press/Taylor & Francis, Boca Raton, FL. Chapter 7.

Yang, X.W., Model, P. & Heintz, N. (1997) Homologous recombination based modification in *Esherichia coli* and germline transmission in transgenic mice of a bacterial artificial chromsome. *Nature Biotechnol.*, **15**, 859–865.

Zielonka, D., Piotrowska, I., MarcinkowskI, J.T. & Mielcarek, M. (2014) Skeletal muscle pathology in Huntington's disease. *Front. Physiol.*, **5**, 1–5.

Zuccato, C., Valenza, M. & Cattaneo, E. (2010) Molecular mechanisms and potential therapeutical targets in Huntington's disease. *Physiol Ver.*, **90**, 905–981.

ARTIGO 5

ASN Neuro

Abnormalities in the motor unit of a fast-twitch lower limb skeletal muscle in Huntington's disease.

Abstract:	Huntington's disease (HD) is a disorder characterized by chronic involuntary movements, dementia, and psychiatric symptoms. It is caused by a mutation in the gene that encodes for huntingtin protein (HTT), leading to the formation of mutant proteins expressed in various tissues. Although brain pathology has become the hallmark for HD, recent studies suggest that damage of peripheral structures also contributes to HD progression. We previously identified severe alterations in the motor units (MUs) that innervate cervical muscles in 12 months old BACHD mice, a well-established mouse model for HD. Here, we studied lumbar motoneurons and their projections onto hind limb fast-twitch skeletal muscles (Tibialis Anterior, TA), which control balance and gait in HD patients. We found that lumbar motoneurons were altered in the HD mouse model; the number and size of lumbar motoneurons were reduced in BACHD. Structural alterations were also present in the sciatic nerve, and neuromuscular junctions (NMJs). Acetylcholine receptors (AChRs) were organized in several small patches (AChR fragmentation), many of which were partially innervated. In BACHD mice, we observed atrophy of TA muscles, decreased expression of glycolytic fast type IIB fibers, and at the ultrastructural level, alterations of sarcomeres and mitochondria. Corroborating all these findings, BACHD animals performed worse on motor behavior tests. Our results provide additional evidences that nerve-muscle communication is impaired in HD and that motoneurons from distinct spinal cord locations are similarly affected in the disease.

SCHOLARONE™
Manuscripts

Abnormalities in the motor unit of a fast-twitch lower limb skeletal muscle in Huntington's disease.

Priscila Aparecida Costa Valadão[a]; Bárbara Campos de Aragão[a]; Jéssica Neves Andrade[a]; Matheus Proença S. Magalhães-Gomes[a]; Giselle Foureaux[a]; Julliane Vasconcelos Joviano-Santos [a]; José Carlos Nogueira[a]; Thatiane Cristina Gonçalves Machado[a], Luisa Peixoto [a]; Fabíola Mara Ribeiro[b]; Juan Carlos Tapia[c]; Cristina Guatimosim[a*]

[a]Departamento de Morfologia, Universidade Federal de Minas Gerais, Belo Horizonte – MG, Brasil.

[b]Departamento de Bioquímica e Imunologia, Universidade Federal de Minas Gerais, Belo Horizonte – MG, Brasil.

[c] Department of Biomedical Sciences, University of Talca, Talca, Chile.

Motor unit and Huntington's disease

*Corresponding author

Cristina Guatimosim, Associate Professor

Departamento de Morfologia, ICB

Universidade Federal de Minas Gerais

Av. Antônio Carlos, 6627

Belo Horizonte, MG 31270-901 Brazil
email: cguati@icb.ufmg.br

Abbreviations: BSA: bovine serum albumin; ChAT: Choline Acetyltransferase; CNS: Central Nervous System; CSA: Cross-Sectional Area; HTT: Huntingtin; HD: Huntington´s Disease; mHTT : mutant huntingtin; MUs: Motor Units; MyHC: Myosin Heavy Chain; NMJs: Neuromuscular Junctions; nAChR: Nicotinic Acetylcholine receptor; OCT : optimum cutting temperature; OPN: osteopontin ; PFA**:** paraformaldehyde; RT: Room Temperature; SR: Sarcoplasmic Reticulum; STM: Sternomastoid;TA: Tibialis Anterior; TEM: Transmission Electron Microscopy; WT: Wild Type; α –btx: α-bungarotoxin.

1

1
2
3
4
5
6
7
8
9
10
11
12
13
14
15
16
17
18
19
20
21
22
23
24
25
26
27
28
29
30
31
32
33
34
35
36
37
38
39
40
41
42
43
44
45
46
47
48
49
50
51
52
53
54
55
56
57
58
59
60

Abstract

42
43   Huntington's disease (HD) is a disorder characterized by chronic involuntary
44   movements, dementia, and psychiatric symptoms. It is caused by a mutation in
45   the gene that encodes for huntingtin protein (HTT), leading to the formation of
46   mutant proteins expressed in various tissues. Although brain pathology has
47   become the hallmark for HD, recent studies suggest that damage of peripheral
48   structures also contributes to HD progression. We previously identified severe
49   alterations in the motor units (MUs) that innervate cervical muscles in 12 months
50   old BACHD mice, a well-established mouse model for HD. Here, we studied
51   lumbar motoneurons and their projections onto hind limb fast-twitch skeletal
52   muscles (Tibialis Anterior, TA), which control balance and gait in HD patients. We
53   found that lumbar motoneurons were altered in the HD mouse model; the number
54   and size of lumbar motoneurons were reduced in BACHD. Structural alterations
55   were also present in the sciatic nerve, and neuromuscular junctions (NMJs).
56   Acetylcholine receptors (AChRs) were organized in several small patches (AChR
57   fragmentation), many of which were partially innervated. In BACHD mice, we
58   observed atrophy of TA muscles, decreased expression of glycolytic fast type IIB
59   fibers, and at the ultrastructural level, alterations of sarcomeres and
60   mitochondria. Corroborating all these findings, BACHD animals performed worse
61   on motor behavior tests. Our results provide additional evidences that nerve-
62   muscle communication is impaired in HD and that motoneurons from distinct
63   spinal cord locations are similarly affected in the disease.

64

65

Summary statement

67   This study evaluates the morphology of the motor unit of the tibilais anterior
68   muscle. The main finding is that Huntington's disease can affect the motor unit in
69   all its components, from the motoneuron to the skeletal muscle.

70
71
72
73
74
75
76
77
78
79
80
81
82
83
84
85
86
87
88
89

2

Introduction

Skeletal muscle loss and dysfunction are found in Huntington's disease (HD), which is a progressive neurodegenerative disorder caused by an autosomal dominant condition leading to motor, cognitive, and psychiatric impairment. In 1993, the Huntington's Disease Collaborative Research Group identified a mutation in the short arm of chromosome 4, an unstable expansion in the number of CAG repeats in the Huntingtin (HTT) protein (The Huntington's Disease Collaborative Research Group, 1993). Historically, HD has been studied in the central nervous system (CNS), mainly in neurons from the basal ganglia and cerebral cortex (Reiner et al., 1988; Novak and Tabrizi, 2010; Reinius et al., 2015).

The discovery of HTT gene mutation opened a new scenario for scientific research enabling the generation of numerous animal models for the disease (Menalled and Chesselet, 2002; Heng et al., 2008; Menalled et al., 2009; Yang and Gray, 2011). Experiments performed in these animal models allowed the identification of mutant Huntingtin protein (mHTT) not only in the CNS but also in peripheral structures, such as skeletal muscles (Van der Burg et al., 2009; Zielonka et al., 2014; Mielkarek et al., 2017). In fact, mouse HD models exhibited pronounced skeletal muscle atrophy, a pathophysiological finding that could be due to accumulation of mHTT in skeletal muscles, motoneurons or both (Khedraki et al., 2017). This prompted the question of whether a primary defect in the neuromuscular system contributes to the motor deterioration observed in patients with HD, independently of the striatal degeneration (Van der Burg et al., 2009). Consistent with this hypothesis, Ribchester et al., (2004), using the R6/2 mouse model, identified physiological and morphological alterations on neuromuscular junctions (NMJs), a result that suggested a progressive disruption of the communication between motoneurons and skeletal muscles. However, it is important to note that these authors did not investigate whether there is denervation in the NMJs of R6 / 2 mice.

Recently, using a different mouse model for HD (BACHD), which expresses the full-length human mHTT in a BAC vector, we reported alterations in cervical motor units (MUs), such as the reduction in the number and size of motoneurons, axonal degeneration, and fragmentation of NMJs. Furthermore, marked muscle atrophy and fiber-type switching were observed in BACHD-sternomastoid (STM) muscles (Valadão et al., 2017). In addition, we also described abnormal neuromuscular junctions in the diaphragm of BACHD mice (Valadão et al.,2018). Nonetheless, the hypothesis that HD may have a more direct connection with progressive disruption of communication between motoneurons and skeletal muscles remains poorly explored.

Following the trail initiated in our previous studies, we investigated whether mHTT-mediated alterations were restricted to cervical motoneurons, or spread over other spinal cord segments like the lumbar segment. This comparison has clinical importance, since in Amyotrophic lateral sclerosis (ALS), which is a disease that affects the motoneurons, there are evidences that upper and lower motor neurons are differently affected during the course of the disease (Eisen et al., 1992;Fischer et al., 2004, reviewed by Van den Bos et al., 2019). Thus, studying two different segments of the spinal cord in the BACHD animal model, which shows clear loss of motoneurons, is an important study in the sense of identifying possible differences in these two regions (cervical and lumbar segments) in this HD model. To this end, we chose to look at the lumbar spinal

cord segment and the MU of the lower hindlimb muscle Tibialis Anterior (TA). This muscle controls movement and balance that are severely impaired in HD such as decreased walking speed, difficulties in starting the steps and variable pattern of step. In addition, motor neurons of the lumbar spinal cord segment and TA muscle are also involved in gait, which is considered to be one of the main factors of disability in patients with HD (Piira et al., 2013). It is noteworthy that, with the progression of the disease, the mobility is affected, increasing the risk of falls and directly impacting the functionality of the patients who end up needing constant help in their daily living activities (Bilney et al., 2005; Carroll et al., 2015; Cruickshank et al., 2015; Koller and Trimble, 1985; Thaut et al., 1999; Wheelock et al., 2003).

In this way, this study adds to our previous work, since the focus now is to examine another segment of the spinal cord, with motoneurons that are involved in the innervation of muscle groups with function (TA is dorsiflexion and inversion of the foot) and composition (predominantly a fast contraction muscle) different from the STM muscle previously studied by us.

Materials and methods
BACHD mice

All experiments were performed according to the rules established by the local animal care committee (Ethics Committee on Animal Experiments of the Universidade Federal de Minas Gerais - CEUA / UFMG); approved protocol #036/2013. All efforts were made to minimize animal suffering and to reduce the number of animals used. This study was not pre-registered.

The FVB/NJ (wild-type) and FVB/N-Tg (HTT*97Q)IXwy/J (BACHD) transgenic mice (male) were purchased from Jackson Laboratory (Barl Harbor, ME, USA) (JAX stock #008197) and used to establish a new colony. Mice were held in a place with controlled temperature (23 °C) in a 12-12h light-dark cycle. Food and water were provided *ad libitum* in an animal care facility of the Department of Physiology and Biophysics, UFMG. All animals used in this study were genotyped ten days after birth using multiplex Polymerase Chain Reaction (PCR) (HTT-Forward: CCGCTCAGGTTCTGCTTTTA/HTT-Reverse: GGTCGGTGCAGCGGCTCCTC; Actin-Forward: TGGAATCGTGTGGCATCCATCA/Actin-Reverse: AATGCCTGGGTACATGGGGTA).

The BACHD mouse model, unlike the R6 / 2 model, expresses the total length of human mHtt inserted into the BAC (Bacterial Artificial Chromosome (Gray et al.,2018). Compared to the R6 / 2 model, BACHD has an expressive vantage, because in addition to presenting behavioral and pathological characteristics of the disease, it also has the polyglutamine sequence "CAA / CAG" in a more stable form, thus the length of the CAA / CAG repeat in BACHD mice is stable in 97 replicates over several generations (Yang et al., 1997). In this way, this model is reliability for the study of long-term phenotypic characteristics as we did in 12-month-old animals (Kazantsev et al., 1999.; Yang et al., 1997). In addition to these characteristics, this model has a normal life span with slow disease progression, allowing more detailed longitudinal studies when compared to other rapid progression models, such as R6 / 2, for example (Yang and Gray, 2011).

4

187   Animals were identified by numbers according to their genotype (WT or BACHD).
188   They were separated into mini-isolator cages with a maximum of 4 animals per
189   cage. In this study, we used WT and BACHD mice (24 grams). Using a table of
190   random numbers, animals were randomly divided into two groups. Our
191   experiments were performed on 12 months old WT and BACHD animals, as
192   previous studies using this model demonstrated pronounced neurodegenerative
193   signals in the cerebral cortex and deficits in motor behavior in mice of this age
194   (Gray et al., 2008); for review see (Yang and Gray, 2011). Also, this age
195   corresponds to middle age in humans, when it is supposed to appear HD
196   symptoms. In addition, previous work from our research group have shown that
197   12 months old BACHD mice present alterations in cardiac cells and other
198   muscles such as sternomastoid and diaphragm (Joviano-Santos et al., 2019;
199   Valadão et al., 2017b); Valadão et al., 2018).

200   For all experiments involving morphology and immunofluorescence
201   techniques, mice from both genotypes (WT and BACHD) were deeply
202   anesthetized with ketamine/xylazine (0.1mL/20g) in accordance to the
203   CEUA/UFMG protocol. All surgical procedures were described in the
204   appropriated sections. The experimental procedures were performed in the
205   afternoon and, by the end of each surgical procedure, the animals were
206   euthanized by an over-dosage of anesthetics.

207   The experimental procedures were performed in the Departments of
208   Morphology and Pharmacology at the UFMG. The experimental groups
209   remained constant from the beginning to the end of the study, and the exact
210   numbers for all experiments are provided in the figure captions/results section.

211

Lumbar Spinal Cord immunofluorescence

213   All immunofluorescence experiments were performed according to the
214   protocol described by Valadão et al., (2017). For the identification of alpha-
215   motoneurons, lumbar spinal cords slices were stained with Choline
216   Acetyltransferase (ChAT) antibody (1:100, Cat #AB1582 RRID: AB_11211009)
217   and with osteopontin (OPN) (1:100, R&D Systems Cat #MAB14331
218   RRID:AB_2194980) Lumbar spinal cord (L1-L5 segments) were removed and
219   fixed with 4% PFA for 48 hours. Next, the spinal cord segments were kept in 30%
220   sucrose for 24 hours. Samples were then frozen in isopentane (Sigma-Aldrich),
221   cooled with liquid nitrogen, and stored at -80°C. The lumbar spinal cords cross-
222   sections (30μm) were cut on a cryostat (Leica CM3050S), and collected on
223   gelatin-coated slides. The sections were blocked (60 minutes, room temperature)
224   in solution containing 3% bovine serum albumin (BSA), 5% donkey serum, and
225   0.1% Triton X-100. Samples were then incubated overnight at 4°C with the
226   following primary antibodies diluted in 3% BSA, 5% donkey serum, 5% goat
227   serum: goat anti-ChAT and mouse anti-OPN. Slides were washed three times
228   with PBS 1x, and incubated for 2 hours at room temperature with the secondary
229   antibodies Alexa 488 donkey anti-goat IgG1 for anti-CHAT (1:800, Molecular
230   Probes Cat.#A-11055 RRID: AB_142672) and Alexa 488 goat anti-mouse for
231   anti-OPN (1:1000;Thermo Fisher Scientific Cat. #A-21042 RRID: AB_2535711).
232   Samples were washed three times with PBS 1x and mounted using ProLong®
233   Gold antifade (Thermo Scientific Invitrogen^{TM}). Images were acquired using a 63x
234   oil immersion (NA 1.4) objective attached to a laser-scanning confocal

5

235 microscope (Zeiss LSM 510 Meta, Zeiss GmbH, Jena, Germany). An Argon (488
236 nm) laser was used for excitation of lumbar spinal cord slides marked with anti-
237 ChAT and anti-OPN. The Z series of optical sections were collected at 2.0μm
238 intervals. All digital images were quantitatively analyzed using Image J software
239 (Wayne Rasband, National Institutes of Health, USA).

240 Caspase-3 staining in BACHD mice spinal cords lumbar segments (L1-L5)
241 was performed by immersing the spinal cord in neutral-buffered formalin (NBF)
242 for 24 hours. The samples were then dehydrated in ethanol (70%, 80%, 90%,
243 95%, and 100%), cleared in xylene, embedded in paraffin and cut (thin sections
244 -5μm) using a microtome (model HM335E; Microm, Inc., Minneapolis, MN).
245 Nonspecific blockade was performed by incubation of the samples in a solution
246 containing 2% BSA, 0.1% Tween-20 for 1 hour in a moist chamber. Samples
247 were incubated with the primary antibody (1:100 polyclonal rabbit anti-caspase-
248 3, Sigma-Aldrich, Saint Louis, MO) diluted in blocking solution (overnight at 4°C
249 in a moist chamber)and then washed 3 times with PBS following incubation with
250 the secondary antibody (1:1000, Alexa Fluor 488 goat anti-rabbit; Invitrogen,
251 Eugene, OR) for 1 hour. To allow nuclei identification, sections were washed 3
252 times with PBS and stained with DAPI (1:1000; Invitrogen, Eugene, OR). The
253 stained sections were imaged using a NIKON ECLIPSE Ti microscope (100X
254 objective, N.A: 1.49). All digital images were quantitatively analyzed using Image
255 J software (Wayne Rasband, National Institutes of Health, USA).

256 To perform the counting of motoneurons marked with CHAT, OPN and
257 caspase-3, only those with evident nuclei were measured. Since the
258 motoneurons are variable and not perfect circles, we chose to use the "Feret
259 diameter" present in the Image J software (Feret diameter) to measure the
260 diameter of these cells. This tool uses mathematical calculations to correct the
261 diameter of figures that are not totally spherical. In general, it can be defined as
262 the common base of a group of diameters derived from the distance of two
263 tangents to the particle contour in a well-defined orientation (Yap et al., 2012).

NMJ immunofluorescence and confocal microscopy analysis

265 Six mice were anesthetized (three per genotype) as previously described
266 with ketamine/xylazine (0.1mL/20g) and transcardially perfused with iced-cold
267 4% PFA (paraformaldehyde) in 0.1M PBS (phosphate-buffered saline; pH 7.4).
268 The TA muscles were dissected, blocked in 3% BSA + 5% goat serum + 0.5%
269 Triton X-100 for 30 minutes at room temperature and stained with anti-
270 synaptotagmin antibody (1:250, Anti-synaptotagmin, anti-mouse, IgG2A, DSHB;
271 Cat #3H2 2D7 RRID: AB_528483) in the blocking solution. The samples were
272 then incubated overnight at 4°C, washed three times with PBS and incubated for
273 1 hour at room temperature with Alexa 555-α-bungarotoxin (α-btx) (1:1000; Cat#
274 T1175 Molecular Probes, Eugene, OR; T1175 RRID: AB_2313931) together with
275 secondary antibody (1:1000, Alexa-488 goat anti-mouse IgG2A; Invitrogen; Cat
276 #A-21141 also A21141 RRID: AB_141626). The Muscles were washed three
277 times with PBS and whole-mounted using Vectashield (Vector Laboratories,
278 Eching, Germany). Images of NMJs were acquired using a 63x oil immersion
279 (N.A: 1.4) objective attached to a laser-scanning confocal microscope (Zeiss
280 LSM 510 Meta, Zeiss GmbH, Jena, Germany. We used an argon (488 nm) and

6

281 helium-neon (He-Ne, 543 nm) lasers to excite the samples. The Z series optical
282 sections were collected at 2.0 μm intervals, and the whole TA muscle samples
283 were scanned. The nerve terminals were identified considering their
284 colocalization near the AChR clusters. Images were converted to a grayscale
285 format (8 bits), and each synaptic element was individually evaluated. The
286 NMJs- fragmentation index was obtained using the particles analysis method
287 described in Valadão et al. (2017). Briefly, the images were converted into a
288 binary image pattern and were skeletonized. Next, to describe the connectivity
289 for each pixel in the image, a histogram was generated using the
290 BinaryConnectivityClass plugin from IMAGEJ (Pratt et al., 2013). We analyzed
291 the degree of fragmentation in pre- and postsynaptic elements comparing the
292 muscle samples from WT and BACHD mice. The parameters adopted for
293 fragmentation were defined according to the evaluation criteria described by
294 (Valdez et al., 2010), which establishes fragmentation by five or more islands
295 both in the presynaptic and postsynaptic membranes. We analyzed 50 NMJs for
296 each animal.

Morphology and morphometric analysis of sciatic nerve and TA muscle fibers

299 The TA muscle was dissected-out and fixed in 4% glutaraldehyde diluted
300 in PBS (0.2 M) for 24 hours at room temperature. After dehydration in an
301 ascending series of alcohols (70%, 80%, 90%, 95% 2X), samples were
302 embedded in glycolmethacrylate resin (Leica) and sectioned (5μm) in a
303 microtome (Reichert Jung). Sections from the TA muscle were stained with
304 toluidine blue (EMS), and the cross-sectional area (CSA) of individual myofibers
305 imaged using a light microscope (10X oil objective -Leica DM2500) coupled to
306 a CCD camera (Leica DFC345FX).

307 Samples containing the sciatic nerve were histologically analyzed. Semi-
308 thin cross sections (300 nm) were obtained and stained with toluidine blue.
309 Images of whole sciatic nerve cross-sections from WT and BACHD mice were
310 captured using a 20x objective in a ZEISS Axio Lab.A1 microscope. The total
311 CSA of the nerve was measured using ImageJ plugins (NIH), and the total
312 number of axons was counted. Like the motoneurons, the axons are not perfect
313 circles and we also used the Feret diameter (described above) for the calculation
314 of the total diameter (axon diameter). To quantify axonal myelination, we used
315 the G-ratio, which was calculated measuring the axonal inner diameter and
316 dividing it by the outer diameter following the formula: G=d/D, where G is the G-
317 ratio, d is the inner diameter and D is the outer diameter (Chau et al., 2000).

TA muscle fiber typing

319 TA muscle fiber typing was performed according to the protocol described
320 by Valdez et al., (2012). TA samples were put in freezing molds covered with
321 *optimum cutting temperature* (OCT) freezing medium (Easy Path), and fresh
322 frozen in isopentane (Sigma-Aldrich) cooled with liquid nitrogen and stored at -
323 80ºC. The mid-belly region of the TA muscle was cut on a cryostat (Leica
324 CM3050S), and the cross-sections (10μm) collected on gelatin-coated slides.
325 Slides containing muscle sections were then blocked for 30 minutes at room
326 temperature (RT) with 3% BSA (Sigma-Aldrich), 5% goat serum (Sigma-Aldrich)

7

327 and 0.1% Triton X-100 (Sigma-Aldrich) diluted in PBS 1x. Muscle sections were
328 incubated overnight at 4°C with the following primary antibodies: type 1 (1:250,
329 Leica Microsystems Cat# NCL-MHCs RRID: AB_563898); type 2A (1:100, DSHB
330 Cat# SC-71 RRID:AB_2147165), type 2X (1:100, DSHB Cat# BF-35
331 RRID:AB_2274680, which recognizes all types of muscles fibers except 2X), and
332 type 2B (1:100, DSHB Cat# BF-F3 RRID:AB_2266724). All antibodies were
333 diluted in 3% BSA, 5% goat serum prepared in PBS 1x. Slides were washed three
334 times with PBS 1x and incubated for 1 hour at room temperature with secondary
335 antibodies Alexa 488 goat anti-mouse IgG1 (Thermo Fisher Scientific Cat # A-
336 21121 RRID: AB_2535764. It recognizes type 1, 2A and 2X antibodies) and Alexa
337 488 goat anti-mouse IgM (Thermo Fisher Scientific Cat #A-21042 RRID:
338 AB_2535711 It recognizes type 2B antibody). The samples were washed three
339 times with PBS 1x and mounted using VectaShield antifade solution (Vector
340 Laboratories Cat #H-1000 RRID: AB_2336789). Images were acquired using an
341 air objective (10x, 0.25NA) in an epi-fluorescence microscope (Leica DM2500)
342 equipped with a Leica DFC 345FX camera and visualized in a computer. The
343 excitation light came from a 100W Hg lamp, and a FITC filter cube was used to
344 collect the emitted light. Whole muscle cross-sections were imaged for analysis.
345 Each fiber type was expressed as a percentage of the total number of fibers.
346 Validation for each antibody was obtained from the datasheets provided by the
347 company. The CSA of individual myofibers from each fiber type was measured.

Transmission electron microscopy (TEM)

349 For the ultrastructural studies, we used the protocol previously described
350 by us (Rodrigues et al., 2013). Briefly, mice were anesthetized with
351 ketamine/xylazine (0.1mL/20 g), and the heart left ventricle perfused with ice-cold
352 modified Karnovsky fixative (4% PFA and 2.5% glutaraldehyde in 0.1 M sodium
353 cacodylate buffer at 4°C), and maintained in the solution for at least 24 hours at
354 4ºC. Lumbar spinal cord segments (L1-L5) and TA muscles from WT and BACHD
355 transgenic mice were then collected. After fixation, samples were washed with
356 cacodylate buffer (0.1 M), cut into several fragments (300 nm), post-fixed in
357 reduced osmium (1% osmium tetroxide containing 1.6% potassium ferrocyanide),
358 contrasted en bloc with uranyl acetate (UA, 2% in deionized water), dehydrated
359 through an ascending series of ethanol solutions and embedded in EPON. After
360 several days in the oven at 60ºC, the resin blocks were sectioned (50 nm), and
361 the ultra-thin sections collected on 200 or 300 mesh copper grids and contrasted
362 with lead citrate. The ultra-thin sections were viewed with a Tecnai- G2-Spirit
363 FEI/Quanta electron microscope (120 kV Philips).
364 To quantify the lipofuscin granules in the motoneurons, we used 30
365 electron micrographs of the lumbar spinal cord motoneurons for each genotype
366 (WT, BACHD). The counting was performed using the ImageJ software plugins
367 (NIH). Data were presented as granules/area using the GraphPad Prism 6.

Motor behavioral tests

371 We used the test paw print test to examine the pattern of steps of mice
372 hind limbs during the locomotion (adapted from de Lagrán et al., 2004). Briefly,
373 the apparatus consisted of a narrow wooden tunnel (10x10x70cm), lined with
374 white paper, containing a dark box at one of its ends (positive reinforcement) and
375 positioned in an illuminated room (aversive stimulus). Rodents naturally seek to

8

376 be lodged in safer and dimly lit environments, so when the animal were placed at
377 the end of the corridor opposite the box, they naturally tended to walk towards it.
378 The hind legs of the animals were previously painted with non-toxic black ink, so
379 that when walking on paper, the footprints of their legs were printed / recorded.
380 This procedure was repeated at least three times (3 trials) for each animal.
381   The gait pattern of each animal was recorded through four gait cycles
382 for each trial and data were expressed as the mean of at least three trials. A
383 complete gait cycle was previously defined by de Lagrán et al., (2004), as the
384 distance from one pair of hind legs to the next pair of hind legs. Three parameters
385 were evaluated: the length and the width of the step and the size of the step (right
386 and left). The length of the pitch was measured as the average distance of
387 locomotion between one leg and the next immediately ahead. The width was
388 measured as the mean distance between the right and left hind legs. The length
389 of the stride was considered as the distance between each cycle (right and left).
390 These variables were expressed in centimeters.
391   The data obtained through the behavioral tests were plotted in Microsoft
392 Excel® and converted to graphical representations through the program
393 GraphPad Prisma 7.0 (San Diego, CA, USA).
394
395   Spontaneous locomotor activity was evaluated by means of a automatic
396 open field (LE 8811 IR Motor Activity MonitorsPANLAB /HARVARD
397 APPARATUS), with acrylic box dimensions 450x450x200mm (width x depth x
398 height) (Pereira et al., 2014). The WT and BACHD animals were habituated in
399 the behavioral testing room for the minimum time of 60 minutes. The activities
400 detected in the horizontal plane (distance traveled and mean velocity) was
401 measured for 60 min. The measure of activity total was calculated using the
402 ACTITRACK program and the statistical analyzes were performed using
403 GraphPad Prism 6 software.
404   For the wire hang test is a measure of the force muscle (fore and hind
405 limbs) analysis in rodents and the experiments were conducted according to
406 protocol described by (Sango et al., 1996) and (Prado et al., 2006). The animals
407 were accustomed to the experimental room and manipulated by the researcher
408 at least 2 hours before of the test. The apparatus used consisted of a metal grid
409 with spacing of 1 cm between the 0.8 mm diameter bars. The test was conducted
410 in a single session, in which the animal was individually placed on the grid until
411 the hold. The grid was then inverted and maintained at 20 cm above a foam. It is
412 important to note that this height is sufficient for the animal to remain attached to
413 the grid, however is unable to injure it in the event of fall. The latency, which is
414 the time until the animal disengaged and fell off the inverted grid for 60 seconds
415 observation, was measured, and three observations per animal were considered.
416 It is important to emphasize that we use Time/weight (time corrected for weight),
417 since the BACHD mice presented weight gain and for this reason we corrected
418 the time spent in the apparatus by the weight of the animal. The time was counted
419 in seconds and the weight in grams.
420   The grip strength test was performed according to Fowler et al., 2002.
421 To this end, the power transducer was connected to a small metal bracket that
422 could be grasped by the mouse. The force transducer was coupled to a computer
423 that recorded the maximum grip force in fore limbs exerted by the mouse. The
424 animals were used to the test room and handled by only one researcher.

9

425   During the test, the experimenter gently manipulated the animals by the
426 tail to allow adhesion of the animal with the front legs to the apparatus maintaining
427 the body of the animal parallel to the surface. After holding for two seconds in this
428 position, the experimenter continuously increased the force until the animals lost
429 their grip. The peak of the force automatically recorded at the time the animals
430 lost their adhesion was recorded and expressed in grams / force (g / f). The test
431 was performed three times for each animal for a maximum period of 60 seconds.
432 The mean values of three trials were calculated for each animal and used for
433 further analysis.

434

435 **Statistical Analysis**

436   We used Microsoft Excel for analyzes and all data were plotted using the
437 program GRAPHPAD PRISM 6. For data with normal distribution, values were
438 represented as the standard error of the mean (S.E.M.). Statistical significance
439 was evaluated using the unpaired Student's t-test. As described in the text, when
440 data were not normally distributed, values were represented as the median, and
441 the Mann-Whitney test was used to evaluate statistical significance. Values of p
442 < 0.05 were considered statistically significant. Exact p-values were provided in
443 the figure captions. During analysis, the investigators were blinded for both
444 animal genotype and experimental group. A specific number was assigned to
445 each of the genotyped animals, and the identifier was announced to the
446 researchers only all the analyses were completed.
447   In this work, we used a minimum of three animals per genotype for each
448 data set to obtain statistical difference with 95% of confidence (a = 0.05) and 0.8
449 power. The exact *n* for each experimental procedure is described in the figures'
450 captions.

451

452 **Results**

453 **Lumbar spinal cord motoneurons are reduced in size, number and are**
454 **caspase-positive in BACHD mice**

455   Reduced lower limb muscle strength has been described in HD patients
456 and this contribute significantly to mobility and balance problems in HD (Busse et
457 al., 2008; Cruickshank et al., 2014). Herein, we investigated if the lumbar spinal
458 cord motoneurons that innervate lower limb muscles are affected in 12 months
459 old BACHD mouse model for HD.

460   We began by investigating the number, size, and morphology of the
461 motoneurons from the ventral spinal cord lumbar segments (L1-L5). Figure 1 A-
462 B shows representative images of ChAT-positive (a motoneuron marker) neurons
463 located in the ventral portion of the lumbar segments of the spinal cord of WT and
464 BACHD animals, respectively. Quantitative analysis of ChAT-positive neurons
465 showed a significant decrease in the total number of ChAT-positive cells in the
466 lumbar segments of BACHD animals when compared to WT animals (BACHD:
467 142.0 ± 8.0 number; WT: 178.0 ± 17.6 number (mean ± SD); T_4= 3.3; *p<0.02)
468 (Figure 1E). We also noticed a significant decrease in the diameter of these
469 neurons, with ChAT positive-BACHD neurons being smaller than WT (BACHD:
470 23.7 ± 2.0 μm; WT: 28.3 ± 1.4 μm (mean ± SD); T_4= 3.1; *p<0.03) (Figure 1F). A
471 similar trend in number and size was observed when the antibody against OPN
472 (a specific marker for alpha motoneuron type) was used in the lumbar spinal cord

10

segments. A statistically significant decrease in the number (BACHD: 80.5 ± 25.3 number; WT: 131.0 ± 31.4 number (mean ± SD); T_6=2.5; *p<0.02) and diameter (BACHD: 30.2 ± 2.3 µm; WT: 35.1 ± 0.6 µm; T_4=3.5 *p<0.02) of OPN-positive neurons was observed in BACHD mice compared to WT (Figure 1 G-H).

It is possible that BACHD ChAT/OPN- positive neurons were dying at 12 months old. Thus, we immunostained lumbar spinal cord sections (40µm) of BACHD and WT animals for caspase-3 to investigate if these motoneurons were undergoing apoptosis. Figure 1C shows representative images of WT lumbar segments incubated with the antibody anti-caspase-3. Very little caspase staining was observed in all WT lumbar sections. On the other hand, lumbar spinal cord sections of BACHD animals showed a clear presence of caspase-3 labeling with the majority was in ventral horn neurons, mostly in motoneurons (white arrows) (Figure 1D). These observations were confirmed by quantitative analyses of several lumbar spinal cord sections for both genotypes (BACHD: 65.6 ± 8.3 number; WT: 27.0 ± 4.3 number (mean ± SD); T_4=7.1; **p<0.002) (Figure 1M). Overall, these results indicate that the activation of the apoptotic cascade can be part of the degenerative changes seen in motoneurons of BACHD animals.

We next asked if motoneurons from BACHD lumbar spinal cord presented any abnormal feature at the ultrastructure level. Qualitative analysis of electron micrographs showed that typical motoneurons in WT animals were large in size (Figure 1I), whereas motoneurons from BACHD animals looked significantly smaller (Figure 1J, compare to 1I). At the subcellular level, we observed abnormalities in the mitochondria from BACHD lumbar spinal cord motoneurons, such as cristae disruption and presence of vacuoles (Figure 1L, yellow arrows), whereas in WT animals this organelle was well preserved (Figure 1K). We also identified the presence of lipofuscin granules in motoneurons from BACHD (Figure 1J) and WT (Figure 1I) animals (red arrows). However, the number of these granules was not significantly different between the genotypes (BACHD: 0.17 ± 0.05 µm^2; WT: 0.17 ± 0.03 µm^2 (mean ± SD); T_4= 0.08; p= 0.4) (Figure 1N).

Abnormities in sciatic nerve and NMJs from BACHD mice

We next performed histological analysis of the sciatic nerve, which projects to the lower hind limb TA muscle (Figure 2A and B). We found statistically significant differences in the following morphological parameters between BACHD and WT mice: i) axon diameter (BACHD: 10.9 ± 3.5 µm; WT: 11.4 ± 4.02 µm (median); **p<0.001) (E); ii) axoplasm diameter (BACHD: 6.8 ± 2.6 µm; WT: 7.5 ± 2.8 µm (median); ***p<0.0001) (F) and iii) G-ratio (BACHD: 0.6 ± 0.07; WT: 0.6 ± 0.07 (median); ****p<0.0001) (H). However, no significant differences were observed between WT and BACHD sciatic nerves in terms of nerve area (C), number of axons per area (D) and myelin thickness (G).

To determine if the sciatic nerve abnormalities described above were accompanied by changes in the innervation of the TA muscle, the neuromuscular junctions (NMJs) of both genotypes were pre- and post-synaptically stained with synaptotagmin and α-btx, respectively. Figure 3 A-B shows representative images of presynaptic nerve terminals stained with Alexa 488 anti-synaptotagmin antibodies from WT and BACHD TA muscles, respectively. Figures 3A' (WT) and

11

B' (BACHD) show the post-synaptic acetylcholine receptors (AChRs) stained with Alexa 555 α-btx. Figure 3A'' (WT) and 3B'' (BACHD) show the merge of both green and red signals. Figures 3C and 3D show the graphic representation of the particle analysis for NMJs fragmentation. Figures 3C' and 3D' show the skeletonization process of the NMJs.

We found abnormal features in BACHD TA such as i) loss of colocalization between pre- and post-synaptic elements (BACHD: 87.5 ± 0.8 %; WT: 93.1 ± 1.2 % (mean ± SD); T_4=3.6; *p=0.02) (Figure 3E); ii) NMJs partial denervation were identified considering their colocalization with nAChR clusters. (BACHD: 27.6 ± 2.0 % Vs. WT: 5.6 ± 1.2 % (mean ± SD); T_4=9.3; ***p<0.0007) (Figure 3F); iii) decreased pre-synaptic terminal area (BACHD: 1231 ± 886 μm^2; WT: 1761 ± 964 μm^2 (median); ***p<0.0002), but not in postsynaptic area (Figure 3 G-H); iv) pronounced fragmentation of AChRs (BACHD: 85.6 ± 7.6 μm^2; WT: 47.6 ± 3.5 μm^2 (mean ± SD); T_4=7.8; **p<0.001) (Figure 3I). All abnormalities described above were augmented in BACHD NMJs but were absent or present only in few cases in WT NMJs. All these analyses provided evidence of the degenerative process that is taking place at the NMJs of TA muscles from BACHD animals.

BACHD TA muscle fibers are atrophic, with fiber type switching and show signs of degeneration at the ultrastructure level

We investigated if TA muscles, innervated by motoneurons from lumbar spinal cord segments, were affected in BACHD mice. To address this, cross-sections of TA muscles were stained with toluidine blue. Figure 4A-B show representative images of TA-muscle fibers from WT and BACHD animals, respectively. Quantitative analysis showed that the TA- muscle fibers CSA was smaller in BACHD mice compared WT (Figure 4K) (BACHD: 1535 ± 820.4 μm^2; WT: 1965 ± 779,4 μm^2 (median); ****p<0.0001). Ultrastructural analyses showed that WT- TA muscle fibers presented normal looking organelles such as mitochondria, well-preserved sarcomeres, triads and myofibrils (yellow rectangle, Figure 4E). However, the BACHD- TA muscle fibers were different in structure, showing severely disorganized sarcomeres (Figure 4F - dotted area). Figure 4G shows an enlarged view of the dotted area indicated in Figure 4F. Here, we observed atypical amounts of inter-myofibrillar glycogen (red arrow), loss of alignment among the sarcomeres (blue arrows), and invasion of the sarcoplasmic reticulum (SR) onto the myofibrils region (yellow asterisk). In addition, large vacuoles within the mitochondrial matrix were observed in the mitochondria of BACHD muscle fibers, a feature typically present in mitochondria enrolled in degeneration (Figure 4H, J and I).

Next, we investigated whether the BACHD muscle atrophy could be associated to changes in Myosin Heavy Chain (MyHC)- isoforms expression. To evaluate this, we used immunostaining for different fiber types through specific monoclonal antibodies against various MyHC- isoforms. The top panel represents staining for type I (Figure 4C), type IIA (Figure 4C'), type IIX (Figure 4C'') and type IIB (Figure 4C''') isoforms of muscle fibers from WT animals. The bottom panel shows the same staining but in this case for muscle fibers from BACHD animals (Figure 4D'-D'''). Quantitative analysis from individual animals showed a statistically significant decrease in the number of type IIB fibers (BACHD: 35.4 ± 5.1 %; WT: 46.8 ± 4.0 % (mean ± SD); T_6= 3.4; *p<0.01) and an increase in the number of type IIX muscle fibers (BACHD: 48.3 ± 8.3 %; WT: 32.5

12

568 ± 5.9 % (mean ± SD); T_4= 3.0; *p<0.02) in BACHD TA muscles (Figure 4L). Figure
569 4M shows that muscle fibers positive for type IIX and IIB isoforms presented a
570 decrease in fiber size (IIX: BACHD: 381.5 ± 171.9 μm^2; WT: 414.5 ± 173.3 μm^2
571 (mean ± SD); T_{61}= 2.3; *p<0.03) (IIB: BACHD: 634.3 ± 238.6 μm^2; WT: 672.3 ±
572 243.7 μm^2 (mean ± SD); T_{70}= 2.0; *p<0.03).

573 **Impaired motor behavior in BACHD mice**

574   Based on the nerve-muscle alterations described above, we examined if
575 BACHD mice indeed showed motor impairment. To assess motor performance,
576 mice from both genotypes were subjected to the following tests: paw print, wire
577 hanging, grip strength, and open field. Regarding the paw print test data we did
578 not find significant differences between WT and BACHD for any of the evaluated
579 standards: step length, step width and right / left pass (5A-D). In the open field
580 test, BACHD mice showed a significant decrease in exploratory behavior. For
581 example, the average distance traveled by BACHD mice was significantly shorter
582 than the distance traveled by the WT mice (BACHD: 5216 ± 481.8 cm; WT: 7647±
583 863.8 cm (mean ± SD); T_{26}= 2.6; p<0.01) (Figure 5A). In addition, the BACHD
584 mice scored worse than WT regarding the mean velocity traveled (BACHD: 4.2 ±
585 0.30 cm/s; WT: 6.2 ± 0.71 cm/s (mean ± SD); T_{26}= 2.9; p<0.003) (Figure 5B). The
586 wire hanging task revealed that BACHD mice presented more difficulty in
587 sustaining their weight while most WT mice kept hold of the grid over the entire
588 duration of the test (60 seconds) (BACHD: 0.4 ± 0.09 s; WT: 1.4 ± 0.09 s (mean
589 ± SD); T_{27}= 7.2; p<0.0001) (Figure 5C). However, we did not observe significant
590 differences in the grip strength test between the two genotypes BACHD and WT
591 mice (i.e., test to compare max strength) (Figure 5D).

592 **Discussion**

593   Although HD is mostly described as a neurological disorder, there is
594 growing evidence that a peripheral pathology participates in disease progression
595 (Ribchester et al., 2004; Van der burg et al., 2009; Mielcarek et al., 2015). Indeed,
596 HTT is normally expressed at high levels in a wide variety of mammalian tissues
597 (Li et al., 1993) and pathological aggregates of high molecular weight HTT have
598 been found in many non-central nervous system tissues including skeletal muscle
599 (Moffit et al., 2009). Recently, we have showed that MUs of a neck muscle (STM)
600 from BACHD mice presented morphological alterations in all its components i.e.,
601 motoneurons, axons, NMJs, and muscle fibers (Valadão et al., 2017).
602 Nevertheless, the connection between HD and the progressive disruption of
603 communication between motoneurons and skeletal muscles remains poorly
604 explored. Thus, in the present study, we investigated whether similar changes
605 were also present in MUs of the hind limb muscles such as the TA, which is
606 controlled by lumbar spinal cord segments and afflicted by many degenerative
607 disorders, including HD.

608   Previous works from other groups reported changes in NMJs and muscles
609 in R6/2 mouse model for HD that could be related to motoneurons degeneration
610 (Ribchester et al., 2004; Mielcarek and Isalan, 2015; Khedraki et al., 2017).
611 However, these authors did not look at the spinal cords to address whether
612 motoneurons were indeed affected in R6/2 mice. In our previous work using the
613 BACHD mouse model for HD, we examined this hypothesis. We observed that
614 CHAT-positive neurons from BACHD cervical spinal cord segments were

13

615 significantly fewer (~20%) and smaller in size than those in WT mice (Valadão et
616 al., 2017). In the current work, we showed, in another segment of the spinal cord
617 (Lumbar, L1-L5), that ChAT-positive neurons from BACHD lumbar segments
618 were also fewer (motoneurons number) and smaller (cell soma diameter)
619 compared to WT mice. Comparatively, these results show similar pathological
620 changes among cervical and lumbar spinal cord segments in BACHD mice of the
621 same age, suggesting that both spinal cord segments (cervical and lumbar)
622 undergo the same degree of impairment.

623   As in the cervical spinal cord segments (Valadão et al., 2017), here we
624 observed that BACHD lumbar spinal cords present approximately three times
625 more motoneurons positive for caspase-3 when compared to equivalent WT
626 spinal segments. Although it is not completely clear whether the neuronal death
627 seen in HD is due solely to apoptotic process, several lines of evidence indicate
628 that the activation of specific pathways can lead to neuronal death (Hickey and
629 Chesselet, 2003). In fact, Gervais et al., (2002), demonstrated that one of the
630 neuronal death pathways in HD occurs through the interaction of mHTT with
631 specific molecules that activate caspase-8, which in turns lead to mitochondrial
632 alterations with consequent activation of caspase-3, culminating in cell death by
633 apoptosis.

634   The qualitative analysis of electron micrographs of putative motoneurons
635 (large ventral horn neurons) from BACHD animals presented herein revealed
636 mitochondria with changes such as destruction of mitochondrial cristae and
637 vacuoles. These subcellular changes were similar to those identified in BACHD
638 cervical motoneurons (Valadão et al., 2017). In addition, we observed lipofuscin
639 granules in both lumbar genotypes WT and BACHD. However, this observation
640 was different from the cervical segments where we detected almost three times
641 more lipofuscin granules in BACHD compared to WT (Valadão et al., 2017).
642 Studies using TEM to evaluate damages in the brain of HD patients have pointed
643 out morphological alterations such as mitochondria with damaged cristae,
644 occasionally containing crystalline fibrillar structures within the matrix and
645 increase in lipofuscin granules (Tellez-Nagel et al., 1974; Goebel et al., 1978).
646 Moreover, it has been shown that the relationship of mHTT with mitochondrial
647 components leads to changes in its structure (Bossy-Wetzel et al., 2008; Song et
648 al., 2011; Shirendeb et al., 2012).

649   Although we observed a decrease in the number of motoneurons,
650 interestingly, the number of axons is not altered in BACHD animals. However, we
651 have shown changes in both the axon and axoplasm diameter, which leads us to
652 believe that these changes might be an earlier step in the process of total axonal
653 degeneration.

654   Our results also showed changes in the NMJs of TA muscles at 12 months
655 old in the BACHD animals. In this muscle, we identified a significant decrease in
656 presynaptic element area, but not in the postsynaptic element, which may be
657 explained by an initial denervation process, since we also observed locations
658 where there was a lack of overlap between the pre-synaptic terminal and nAChR.

659   Furthermore, we identified significant fragmentation of NMJs of BACHD
660 animals but little in control animals. Although recent data show that the age-
661 fragmentation process is not directly related to function (Willadt et al., 2016), we

14

662 believe that our data may indicate that structural changes such as fragmentation
663 are due to the genotype and not just related to age because the animals
664 evaluated were of the same age. It is known that mHTT interacts with
665 cytoskeletal synaptic vesicles proteins that are essential for the structure of NMJs
666 and for exocytosis and endocytosis of synaptic vesicles at the nerve terminals (Li
667 and Li, 2004; see review by Zuccato et al., 2010). Except for postsynaptic area
668 size, which was not statistically different for the TA muscle, all these
669 morphological changes were also observed in NMJs of STM muscle from 12
670 months old BACHD animals. This comparison is useful because we are dealing
671 with NMJs of two distinctive muscle groups that are affected differently in animals
672 of the same age in the BACHD murine model for HD.

673 We do not observe changes in the number of axons in the sciatic nerve,
674 despite the significant changes in the axons diameter. This result seems contrary
675 to the loss of motoneurons (~20%) observed in the lumbar segments of the
676 BACHD mice. There are several plausible explanations for this difference. It is
677 possible that axonal degeneration is a much slower process than the caspase
678 labeling observed at the spinal cord. This possibility finds support in the fact that
679 axons stay for much longer than motoneurons, a phenomenon previously
680 observed in ALS disease. Which it is consistent with the lower number of partial
681 denervation observed (10%). Another possibility is that the remaining
682 motoneurons, the caspase negative, are able to produce new branches, which
683 should travel within the nerve. These extra branches should account for a higher
684 number of axons at the sciatic nerve level. Since they are ramifications from the
685 main axonal branch, most of the new branches should be smaller in size. This is
686 consistent with the variability in axonal diameter observed in our sciatic nerve
687 analysis.

688 Another interesting finding is the change observed in skeletal muscle
689 fibers of the TA muscle from BACHD mice. First, we observed a decrease in CSA
690 in muscle fibers of BACHD animals suggesting muscle atrophy. A reduction in
691 the total number of fibers could also have contributed to muscle fiber atrophy in
692 the BACHD mouse. Indeed, it is well described that muscle atrophy is a common
693 factor in HD (Farrer and Meaney, 1985; Ribchester et al., 2004; Farrer, 2008).
694 Another point to be considered is the deleterious effects of mHTT in muscle fibers
695 of R6/2 mice (Sathasivam et al., 1999; Moffitt et al., 2009). The BACHD- STM
696 muscle also showed atrophy of muscle fibers (Valadão et al., 2017). However,
697 the atrophy seen in the BACHD- TA muscle was smaller compared to BACHD
698 STM muscle. However, the STM muscle has higher variability in fiber size mainly
699 because it has mixed features of contractility, consisting of fast and slow fibers.
700 In contrast, the TA muscle is a fast twitch muscle, usually presenting about 87%
701 of fast fiber type IIB muscle fibers (Bloemberg and Quadrilatero, 2012).

702 Previous studies revealed that muscle atrophy could be accompanied by
703 changes in expression of MyHC (Brown and Hasser, 1996; Carvalho et al., 2003;
704 Rice et al., 2005; Valadão et al., 2017b). Here, we show that the number of type
705 IIB muscle fibers was reduced in BACHD mice, indicating that the general atrophy
706 seen in this muscle relates to a change in MyHC isoform since in TA muscle type
707 IIB fibers are predominant (Bloemberg and Quadrilatero, 2012). These data are
708 in agreement with the work of Miranda et al., (2017)in which they showed the
709 same pattern of transition of the type of fiber in the TA muscle of animals R6 / 2,
710 however these authors did not investigate the protein expression of MyHC,

15

711 showing these changes only at the mRNA level through the qPCR technique.
712 Beside that, we had already identified changes in the expression pattern of MyHC
713 in the STM muscle with changes of type IIX muscle fibers was reduced in BACHD
714 mice (Valadão et al., 2017). Together, these results indicate that the atrophy seen
715 in both muscles was accompanied by alterations in the expression of MyHC,
716 differing only in the affected fast fiber type. The MyHC shift from Type IIB to IIX
717 seen in BACHD TA muscle might be explained by the observation that, in
718 denervated muscles, there is a change in the expression pattern of the faster
719 isoforms for the slower isoforms (d'Albis et al., 1995). We speculate that this fiber
720 type may be related to the NMJs denervation observed in the TA muscles from
721 BACHD mice. Data from the literature indicate that motoneurons and their NMJs
722 differ drastically in size, with biggest ones innervating fast muscle fibers with
723 largest NMJs (Burke et al., 1971; Mantilla et al., 2007). We hypothesize that the
724 changes in the motoneurons described herein, such as decrease in presynaptic
725 area and size of motoneurons in BACHD, cause a reduction in the number of IIB
726 muscle fibers in TA muscles from BACHD mice. However, we cannot rule out the
727 possibility that mHTT directly or indirectly alters muscle fiber type profile since
728 this has been described in R6/2 HD mice model and also in humans (Strand et
729 al., 2005; for a review see Zielonka et al., 2014). Further research will be needed
730 to clarify this matter.

731   Interestingly, we noted that the BACHD- TA muscles have greater
732 accumulation of glycogen in the inter-myofibrillar spaces and more mitochondrial
733 damage than the observed in STM muscles (Valadão et al., 2017). Moreover, in
734 the BACHD transgenic animals, the Z line did not follow a straight pattern as
735 observed in the control animals. Indeed, studies of denervated TA muscles of
736 transgenic rabbits also revealed Z-line misalignment and mitochondrial changes
737 (Ashley et al., 2007). In light of the information provided by these studies and
738 because we found greater changes in the mitochondria of BACHD TA muscles,
739 it is possible that these changes could be related to energy imbalance caused by
740 mitochondrial damage. However, it is important to mention that although the TEM
741 analysis revealing mitochondrial abnormalities is informative, caution should be
742 taken in the interpretation of the present data because our analysis was only
743 qualitative and not quantitative.

744   We evaluated the motor function of BACHD and WT mice to verify the
745 possible relationship between the morphological changes observed in TA MUs
746 and the alterations in motor behavior of BACHD animals. In the catwalk test, we
747 did not detect statiscally significant differences between WT and BACHD mice in
748 any of the gait patterns evaluated: step length, step width and right / left pass.
749 Interestingly, our results are in accordance with the data of Mantovani et al.,
750 (2016), who showed no significant differences in walking test between BACHD
751 animals and controls at 12 months old, even using another measuring device
752 [Noldus® Cat Walk apparatus (Wageningen, The Netherlands)]. These
753 observations may be related to the fact that the mice are quadruped animals,
754 which gives them greater stability. Interestingly, Menalled et al., 2009, using the
755 same method used by us, observed that 18-month-old BACHD mice presented
756 statistical differences as a larger extension and broader base. These changes
757 differ from the gait deficit found in humans, since the steps become shorter in
758 patients with HD (Koller and Trimble, 1985). However, even without presenting
759 significant changes in the gait, the 12-month-old BACHD mice showed a robust

16

760 phenotype in several behavioral tests that replicate and extend the published
761 results to date (Gray et al., 2008, Mantovani et al., 2016, Menalled et al., 2009).
762   The open field test revealed significant hypoactivity of BACHD mice, with
763 a significant reduction in locomotion, total distance traveled and mean velocity.
764 However, the number of rearing events was not significantly different when
765 compared to control mice. These findings are in accordance to the results
766 reported by Menalled et al., (2009), that showed that at 7 months of age, BACHD
767 mice presented locomotor hypoactivity. The same results (in 7 months old
768 BACHD) were previously observed by Gray et al., (2008). In the wire hanging
769 test, we observed that BACHD mice performed significantly worse than the WT
770 mice, similar to what Heng et al. (2007) and Brooks et al., (2012) noticed in 12
771 months old *Hdh* (CAG) 150 mice. In the wire hanging test, we observed that BACHD
772 mice performed worse than the WT mice even after normalizing the weight of the
773 animals to the time they were kept holding to the apparatus. In sum, the results
774 obtained showed that the BACHD mice has major motor alterations, which
775 directly influence their behavior.
776   The grip strength test did not show significant changes in the maximum
777 strength between BACHD and WT mice. Menalled et al. (2009) observed that
778 mice containing only a fragment of mutant HTT (R6/2) showed deficits in the
779 same motor test. However, animals expressing the full-length mHTT, including
780 BACHD, showed no significant differences in grip strength test. Accordingly,
781 Mantovani et al., (2016) showed that BACHD animals generated in a C57BL/6J
782 background (12 months old) did not present deficits in grip strength test, which
783 corroborate our results. It is also possible that the deficiencies in movement and
784 balance observed are due to aberrant connectivity or function in motor systems
785 of the brain, rather than brain stem or spinal motor neurons. Besides that, this
786 test are also open to interpretation as motivational rather than NMJ/muscle
787 physiological. Therefore, the case for NMJ involvement in MN/muscle atrophy
788 would be better made from isometric force measurements and intracellular
789 measurements of synaptic function.
790   Although the findings described herein are suggestive of axonal or NMJ
791 morphological differences in the BACHD mouse model, future research involving
792 corroborative nerve conduction measurements, muscle/motor unit tension data,
793 or electrophysiological analysis of NMJ function are necessary to establish
794 whether the abnormalities described at NMJs are biologically significant, or
795 whether they are primary consequences of CAG repeat expression or a
796 secondary change in response to, for example, muscle atrophy.
797
798   In summary, here we show that that motoneurons from BACHD lumbar
799 spinal cord are atrophic, reduced in size, and undergo apoptosis. The MUs
800 associated with the TA muscle from BACHD mice presents signs of degeneration
801 such as sciatic nerve reduced axon and axoplasm diameters, neuromuscular
802 junctions' fragmentation and partial denervation, skeletal muscle fibers atrophy,
803 and fiber type switching (Type 2B to Type 2X). Moreover, the present study
804 provides evidence that different MUs have similar degrees of impairment in this
805 animal model for HD. That is, regardless of innervation or muscle composition, it
806 appears that mHTT may be performing the same degree of degeneration of these
807 MUs investigated by us in the two studies. In addition, the changes seen in
808 different spinal cord segments indicate that, although the disease may be
809 Interestingly, our results are in accordance caused by neuronal death in the brain,

17

1
2
3
4
5
6
7
8
9
10
11
12
13
14
15
16
17
18
19
20
21
22
23
24
25
26
27
28
29
30
31
32
33
34
35
36
37
38
39
40
41
42
43
44
45
46
47
48
49
50
51
52
53
54
55
56
57
58
59
60

810 motoneurons at the lumbar spinal cord seems to be affected in HD, making room
811 for further studies to elucidate the molecular mechanisms underlying the
812 motoneuron cell death. Overall, our findings are important, and add further
813 support the hypothesis that cellular alterations occurring in peripheral tissues, in
814 this case skeletal muscles, occur independently of the progression of brain
815 dysfunction (Van der Burg et al., 2009). Thus, this work expands the perspectives
816 about the role of the MU in motor alterations seen in HD and the possibility that
817 clinical interventions targeting the MU could help treating signs of disease in
818 patients with Huntington's disease.
819

820 **Author Contributions**

821 P.A.C.V. was responsible for experimentation, data interpretation, and writing of
822 the article. B.C.A., M.P.S.M-G,J.N.A., G.F., J.V.J-S., were responsible for
823 experimentation and data interpretation. T.C.G.M and L.P. Were responsible for
824 data analysis. J.C.N, F.M.R. and J. C. T. were scientific consultant in all the
825 stages. C. G. was responsible for the conceptualization of the study data
826 interpretation and writing the article.

839

840 **Conflict of interest**
841

842 We declare no conflict of interest.
843

844 **References**
845 Ashley, Z., Salmons, S., Boncompagni, S., Protasi, F., Russold, M., Lanmuller,
846   H., Mayr, W., Sutherland, H., Jarvis, J.C., 2007. Effects of chronic electrical
847   stimulation on long-term denervated muscles of the rabbit hind limb. J.
848   Muscle Res. Cell Motil. 28, 203–217. https://doi.org/10.1007/s10974-007-
849   9119-4
850 Bilney, B., Morris, M.E., Churchyard, A., Chiu, E., Georgiou-Karistianis, N.,
851   2005. Evidence for a disorder of locomotor timing in Huntington's disease.
852   Mov. Disord. 20, 51–57. https://doi.org/10.1002/mds.20294
853 Bloemberg, D., Quadrilatero, J., 2012. Rapid determination of myosin heavy
854   chain expression in rat, mouse, and human skeletal muscle using
855   multicolor immunofluorescence analysis. PLoS One 7, e35273.
856   https://doi.org/10.1371/journal.pone.0035273
857 Bossy-Wetzel, E., Petrilli, A., Knott, A.B., 2008. Mutant huntingtin and

18

858 　mitochondrial dysfunction. Trends Neurosci. 31, 609–616.
859 　https://doi.org/10.1016/j.tins.2008.09.004
860 Brooks, S., Higgs, G., Jones, L., Dunnett, S.B., 2012. Longitudinal analysis of
861 　the behavioural phenotype in Hdh(CAG)150 Huntington's disease knock-in
862 　mice. Brain Res. Bull. 88, 182–188.
863 　https://doi.org/10.1016/j.brainresbull.2010.05.004
864 Brown, M., Hasser, E.M., 1996. Complexity of age-related change in skeletal
865 　muscle. J. Gerontol. A. Biol. Sci. Med. Sci. 51, B117-23.
866 　https://doi.org/10.1093/gerona/51a.2.b117
867 Burke, R.E., Levine, D.N., Zajac, F.E., 1971. Mammalian motor units:
868 　physiological-histochemical correlation in three types in cat gastrocnemius.
869 　Science 174, 709–12.
870 Busse, M.E., Khalil, H., Quinn, L., Rosser, A.E., 2008. Physical Therapy
871 　Intervention for People With Huntington Disease. Phys. Ther. 88, 820–831.
872 　https://doi.org/10.2522/ptj.20070346
873 Carroll, J.B., Bates, G.P., Steffan, J., Saft, C., Tabrizi, S.J., 2015. Treating the
874 　whole body in Huntington's disease. Lancet Neurol. 14, 1135–1142.
875 　https://doi.org/10.1016/S1474-4422(15)00177-5
876 Carvalho, R.F., Cicogna, A.C., Campos, G.E.R., De Assis, J.M.F., Padovani,
877 　C.R., Okoshi, M.P., Pai-Silva, M.D., 2003. Myosin heavy chain expression
878 　and atrophy in rat skeletal muscle during transition from cardiac
879 　hypertrophy to heart failure. Int. J. Exp. Pathol. 84, 201–206.
880 　https://doi.org/10.1046/j.1365-2613.2003.00351.x
881 Chau, W.K., So, K.-F., Tay, D., Dockery, P., 2000. A morphometric study of
882 　optic axons regenerated in a sciatic nerve graft of adult rats. Restor.
883 　Neurol. Neurosci. 16, 105–116.
884 Cruickshank, T., Reyes, A., Peñailillo, L., Thompson, J., Ziman, M., 2014.
885 　Factors that contribute to balance and mobility impairments in individuals
886 　with Huntington's disease. Basal Ganglia 4, 67–70.
887 　https://doi.org/10.1016/j.baga.2014.04.002
888 Cruickshank, T.M., Thompson, J.A., Domínguez D, J.F., Reyes, A.P., Bynevelt,
889 　M., Georgiou-Karistianis, N., Barker, R.A., Ziman, M.R., 2015. The effect of
890 　multidisciplinary rehabilitation on brain structure and cognition in
891 　Huntington's disease: an exploratory study. Brain Behav. 5, e00312.
892 　https://doi.org/10.1002/brb3.312
893 d'Albis, A., Couteaux, R., Goubel, F., Janmot, C., Mira, J.C., 1995. Relationship
894 　between muscle myosin isoforms and contractile features in rabbit fast-
895 　twitch denervated muscle. FEBS Lett. 375, 67–8.
896
897 Eisen, A., Kim, S., Pant, B., 1992. Amyotrophic lateral sclerosis (ALS): A
898 　phylogenetic disease of the corticomotoneuron? Muscle Nerve 15, 219–
899 　224. https://doi.org/10.1002/mus.880150215
900 Farrer, L.A., 2008. Diabetes mellitus in Huntington disease. Clin. Genet. 27, 62–
901 　67. https://doi.org/10.1111/j.1399-0004.1985.tb00185.x
902 Farrer, L.A., Meaney, F.J., 1985. An anthropometric assessment of
903 　Huntington's disease patients and families. Am. J. Phys. Anthropol. 67,
904 　185–194. https://doi.org/10.1002/ajpa.1330670304
905 Fischer, L. R., Culver, D. G., Tennant, P., Davis, A. A., Wang, M., Castellano-
906 　Sanchez, A., ... & Glass, J. D., 2004. Amyotrophic lateral sclerosis is a
907 　distal axonopathy: evidence in mice and man. Experimental neurology,

19

185(2), 232-240.

Fowler, S.C., Zarcone, T.J., Chen, R., Taylor, M.D., Wright, D.E., n.d. Low grip strength, impaired tongue force and hyperactivity induced by overexpression of neurotrophin-3 in mouse skeletal muscle. Int. J. Dev. Neurosci. 20, 303–8.

Gervais, F.G., Singaraja, R., Xanthoudakis, S., Gutekunst, C.-A., Leavitt, B.R., Metzler, M., Hackam, A.S., Tam, J., Vaillancourt, J.P., Houtzager, V., Rasper, D.M., Roy, S., Hayden, M.R., Nicholson, D.W., 2002. Recruitment and activation of caspase-8 by the Huntingtin-interacting protein Hip-1 and a novel partner Hippi. Nat. Cell Biol. 4, 95–105. https://doi.org/10.1038/ncb735

Goebel, H.H., Heipertz, R., Scholz, W., Iqbal, K., Tellez-Nagel, I., 1978. Juvenile Huntington chorea: clinical, ultrastructural, and biochemical studies. Neurology 28, 23–31.

Gray, M., Shirasaki, D., Cepeda, C., … V.A.-J. of, 2008, undefined, n.d. Full-length human mutant huntingtin with a stable polyglutamine repeat can elicit progressive and selective neuropathogenesis in BACHD mice. Soc Neurosci.

Gray, M., Shirasaki, D.I., Cepeda, C., Andre, V.M., Wilburn, B., Lu, X.-H., Tao, J., Yamazaki, I., Li, S.-H., Sun, Y.E., Li, X.-J., Levine, M.S., Yang, X.W., 2008. Full-Length Human Mutant Huntingtin with a Stable Polyglutamine Repeat Can Elicit Progressive and Selective Neuropathogenesis in BACHD Mice. J. Neurosci. 28, 6182–6195. https://doi.org/10.1523/JNEUROSCI.0857-08.2008

Heng, M.Y., Detloff, P.J., Albin, R.L., 2008. Rodent genetic models of Huntington disease. Neurobiol. Dis. 32, 1–9. https://doi.org/10.1016/j.nbd.2008.06.005

Heng, M.Y., Tallaksen-Greene, S.J., Detloff, P.J., Albin, R.L., 2007. Longitudinal Evaluation of the Hdh(CAG)150 Knock-In Murine Model of Huntington's Disease. J. Neurosci. 27, 8989–8998. https://doi.org/10.1523/JNEUROSCI.1830-07.2007

Hickey, M.A., Chesselet, M.-F., 2003. Apoptosis in Huntington's disease. Prog. Neuro-Psychopharmacology Biol. Psychiatry 27, 255–265. https://doi.org/10.1016/S0278-5846(03)00021-6

Joviano-Santos, J.V., Santos-Miranda, A., Botelho, A.F.M., de Jesus, I.C.G., Andrade, J.N., de Oliveira Barreto, T., Magalhães-Gomes, M.P.S., Valadão, P.A.C., Cruz, J. dos S., Melo, M.M., Guatimosim, S., Guatimosim, C., 2019. Increased oxidative stress and CaMKII activity contribute to electro-mechanical defects in cardiomyocytes from a murine model of Huntington's disease. FEBS J. 286, 110–123. https://doi.org/10.1111/febs.14706

Kazantsev, A., … E.P.-P. of the, 1999, undefined, n.d. Insoluble detergent-resistant aggregates form between pathological and nonpathological lengths of polyglutamine in mammalian cells. Natl. Acad Sci.

Khedraki, A., Reed, E., Romer, S., … Q.W.-J. of, 2017, undefined, n.d. Depressed Synaptic Transmission and Reduced Vesicle Release Sites in Huntington's Disease Neuromuscular Junctions. Soc Neurosci.

Koller, W.C., Trimble, J., 1985. The gait abnormality of Huntington's disease. Neurology 35, 1450–4. https://doi.org/10.1212/wnl.35.10.1450

Lagrán, M. de, Altafaj, X., Gallego, X., … E.M.-N. of, 2004, undefined, n.d.

20

958   Motor phenotypic alterations in TgDyrk1a transgenic mice implicate
959   DYRK1A in Down syndrome motor dysfunction. Elsevier.
960 Li, S.-H., Li, X.-J., 2004. Huntingtin–protein interactions and the pathogenesis of
961   Huntington's disease. Trends Genet. 20, 146–154.
962   https://doi.org/10.1016/j.tig.2004.01.008
963 Mantilla, C.B., Rowley, K.L., Zhan, W.-Z., Fahim, M.A., Sieck, G.C., 2007.
964   Synaptic vesicle pools at diaphragm neuromuscular junctions vary with
965   motoneuron soma, not axon terminal, inactivity. Neuroscience 146, 178–
966   189. https://doi.org/10.1016/j.neuroscience.2007.01.048
967 Mantovani, S., Gordon, R., Li, R., Christie, D.C., Kumar, V., Woodruff, T.M.,
968   2016. Motor deficits associated with Huntington's disease occur in the
969   absence of striatal degeneration in BACHD transgenic mice. Hum. Mol.
970   Genet. 25, 1780–1791. https://doi.org/10.1093/hmg/ddw050
971 Menalled, L., El-Khodor, B.F., Patry, M., Suárez-Fariñas, M., Orenstein, S.J.,
972   Zahasky, B., Leahy, C., Wheeler, V., Yang, X.W., MacDonald, M., Morton,
973   A.J., Bates, G., Leeds, J., Park, L., Howland, D., Signer, E., Tobin, A.,
974   Brunner, D., 2009. Systematic behavioral evaluation of Huntington's
975   disease transgenic and knock-in mouse models. Neurobiol. Dis. 35, 319–
976   336. https://doi.org/10.1016/j.nbd.2009.05.007
977 Menalled, L.B., Chesselet, M.-F., 2002. Mouse models of Huntington's disease.
978   Trends Pharmacol. Sci. 23, 32–9.
979 Mielcarek, M., Isalan, M., 2015. A shared mechanism of muscle wasting in
980   cancer and Huntington's disease. Clin. Transl. Med. 4, 34.
981   https://doi.org/10.1186/s40169-015-0076-z
982 Miranda, D.R., Wong, M., Romer, S.H., McKee, C., Garza-Vasquez, G.,
983   Medina, A.C., Bahn, V., Steele, A.D., Talmadge, R.J., Voss, A.A., 2017.
984   Progressive Cl$^-$ channel defects reveal disrupted skeletal muscle
985   maturation in R6/2 Huntington's mice. J. Gen. Physiol. 149, 55–74.
986   https://doi.org/10.1085/jgp.201611603
987 Moffitt, H., McPhail, G.D., Woodman, B., Hobbs, C., Bates, G.P., 2009.
988   Formation of Polyglutamine Inclusions in a Wide Range of Non-CNS
989   Tissues in the HdhQ150 Knock-In Mouse Model of Huntington's Disease.
990   PLoS One 4, e8025. https://doi.org/10.1371/journal.pone.0008025
991 Novak, M.J.U., Tabrizi, S.J., 2010. Huntington's disease. BMJ 340, c3109–
992   c3109. https://doi.org/10.1136/bmj.c3109
993 Pereira, L.M., Bastos, C.P., de Souza, J.M., Ribeiro, F.M., Pereira, G.S., 2014.
994   Estradiol enhances object recognition memory in Swiss female mice by
995   activating hippocampal estrogen receptor α. Neurobiol. Learn. Mem. 114,
996   1–9. https://doi.org/10.1016/j.nlm.2014.04.001
997 Piira, A., van Walsem, M.R., Mikalsen, G., Nilsen, K.H., Knutsen, S., Frich, J.C.,
998   2013. Effects of a One Year Intensive Multidisciplinary Rehabilitation
999   Program for Patients with Huntington's Disease: a Prospective Intervention
1000   Study. PLoS Curr. 5.
1001   https://doi.org/10.1371/currents.hd.9504af71e0d1f87830c25c394be47027
1002 Prado, V.F., Martins-Silva, C., de Castro, B.M., Lima, R.F., Barros, D.M.,
1003   Amaral, E., Ramsey, A.J., Sotnikova, T.D., Ramirez, M.R., Kim, H.-G.,
1004   Rossato, J.I., Koenen, J., Quan, H., Cota, V.R., Moraes, M.F.D., Gomez,
1005   M. V., Guatimosim, C., Wetsel, W.C., Kushmerick, C., Pereira, G.S.,
1006   Gainetdinov, R.R., Izquierdo, I., Caron, M.G., Prado, M.A.M., 2006. Mice
1007   Deficient for the Vesicular Acetylcholine Transporter Are Myasthenic and

21

Have Deficits in Object and Social Recognition. Neuron 51, 601–612. https://doi.org/10.1016/j.neuron.2006.08.005

Pratt, S.J.P., Shah, S.B., Ward, C.W., Inacio, M.P., Stains, J.P., Lovering, R.M., 2013. Effects of *in vivo* injury on the neuromuscular junction in healthy and dystrophic muscles. J. Physiol. 591, 559–570. https://doi.org/10.1113/jphysiol.2012.241679

Reiner, A., Albin, R.L., Anderson, K.D., D'amato, C.J., Penneyt, J.B., Youngt, A.B., 1988. Differential loss of striatal projection neurons in Huntington disease. Neurobiology 85, 5733–5737. https://doi.org/10.1073/pnas.85.15.5733

Reinius, B., Blunder, M., Brett, F.M., Eriksson, A., Patra, K., Jonsson, J., Jazin, E., Kullander, K., 2015. Conditional targeting of medium spiny neurons in the striatal matrix. Front. Behav. Neurosci. 9, 71. https://doi.org/10.3389/fnbeh.2015.00071

Ribchester, R.R., Thomson, D., Wood, N.I., Hinks, T., Gillingwater, T.H., Wishart, T.M., Court, F.A., Morton, A.J., 2004. Progressive abnormalities in skeletal muscle and neuromuscular junctions of transgenic mice expressing the Huntington's disease mutation. Eur. J. Neurosci. 20, 3092–3114. https://doi.org/10.1111/j.1460-9568.2004.03783.x

Rice, K.M., Linderman, J.K., Kinnard, R.S., Blough, E.R., 2005. The Fischer 344/NNiaHSd X Brown Norway/BiNia is a Better Model of Sarcopenia than the Fischer 344/NNiaHSd: a Comparative Analysis of Muscle Mass and Contractile Properties in Aging Male Rat Models. Biogerontology 6, 335–343. https://doi.org/10.1007/s10522-005-4808-0

Rodrigues, H.A., Fonseca, M. de C., Camargo, W.L., Lima, P.M.A., Martinelli, P.M., Naves, L.A., Prado, V.F., Prado, M.A.M., Guatimosim, C., 2013. Reduced Expression of the Vesicular Acetylcholine Transporter and Neurotransmitter Content Affects Synaptic Vesicle Distribution and Shape in Mouse Neuromuscular Junction. PLoS One 8, e78342. https://doi.org/10.1371/journal.pone.0078342

Sango, K., McDonald, M.P., Crawley, J.N., Mack, M.L., Tifft, C.J., Skop, E., Starr, C.M., Hoffmann, A., Sandhoff, K., Suzuki, K., Proia, R.L., 1996. Mice lacking both subunits of lysosomal β–hexosaminidase display gangliosidosis and mucopolysaccharidosis. Nat. Genet. 14, 348–352. https://doi.org/10.1038/ng1196-348

Sathasivam, K., Hobbs, C., Mangiarini, L., Mahal, A., Turmaine, M., Doherty, P., Davies, S.W., Bates, G.P., 1999. Transgenic models of Huntington'sdisease. Philos. Trans. R. Soc. London B Biol. Sci. 354.

Shirendeb, U.P., Calkins, M.J., Manczak, M., Anekonda, V., Dufour, B., McBride, J.L., Mao, P., Reddy, P.H., 2012. Mutant huntingtin's interaction with mitochondrial protein Drp1 impairs mitochondrial biogenesis and causes defective axonal transport and synaptic degeneration in Huntington's disease. Hum. Mol. Genet. 21, 406–420. https://doi.org/10.1093/hmg/ddr475

Song, W., Chen, J., Petrilli, A., Liot, G., Klinglmayr, E., Zhou, Y., Poquiz, P., Tjong, J., Pouladi, M.A., Hayden, M.R., Masliah, E., Ellisman, M., Rouiller, I., Schwarzenbacher, R., Bossy, B., Perkins, G., Bossy-Wetzel, E., 2011. Mutant huntingtin binds the mitochondrial fission GTPase dynamin-related protein-1 and increases its enzymatic activity. Nat. Med. 17, 377–382. https://doi.org/10.1038/nm.2313

22

1058 Strand, A.D., Aragaki, A.K., Shaw, D., Bird, T., Holton, J., Turner, C., Tapscott,
1059   S.J., Tabrizi, S.J., Schapira, A.H., Kooperberg, C., Olson, J.M., 2005. Gene
1060   expression in Huntington's disease skeletal muscle: a potential biomarker.
1061   Hum. Mol. Genet. 14, 1863–1876. https://doi.org/10.1093/hmg/ddi192

1062 Tellez-Nagel, I., Johnson, A.B., Terry, R.D., 1974. Studies on brain biopsies of
1063   patients with Huntington's chorea. J. Neuropathol. Exp. Neurol. 33, 308–32.

1064 Thaut, M.H., Miltner, R., Lange, H.W., Hurt, C.P., Hoemberg, V., 1999. Velocity
1065   modulation and rhythmic synchronization of gait in Huntington's disease.
1066   Mov. Disord. 14, 808–19.

1067 Valadão, P., Gomes, M., … B.A.-N., 2018, undefined, n.d. Neuromuscular
1068   synapse degeneration without muscle function loss in the diaphragm of a
1069   murine model for Huntington's Disease. Elsevier.

1070 Valadão, P.A.C., de Aragão, B.C., Andrade, J.N., Magalhães-Gomes, M.P.S.,
1071   Foureaux, G., Joviano-Santos, J.V., Nogueira, J.C., Ribeiro, F.M., Tapia,
1072   J.C., Guatimosim, C., 2017a. Muscle atrophy is associated with cervical
1073   spinal motoneuron loss in BACHD mouse model for Huntington's disease.
1074   Eur. J. Neurosci. 45, 785–796. https://doi.org/10.1111/ejn.13510

1075 Valadão, P.A.C., de Aragão, B.C., Andrade, J.N., Magalhães-Gomes, M.P.S.,
1076   Foureaux, G., Joviano-Santos, J.V., Nogueira, J.C., Ribeiro, F.M., Tapia,
1077   J.C., Guatimosim, C., 2017b. Muscle atrophy is associated with cervical
1078   spinal motoneuron loss in BACHD mouse model for Huntington's disease.
1079   Eur. J. Neurosci. 45, 785–796. https://doi.org/10.1111/ejn.13510

1080 Valdez, G., Tapia, J.C., Kang, H., Clemenson, G.D., Gage, F.H., Lichtman,
1081   J.W., Sanes, J.R., 2010. Attenuation of age-related changes in mouse
1082   neuromuscular synapses by caloric restriction and exercise. Proc. Natl.
1083   Acad. Sci. 107, 14863–14868. https://doi.org/10.1073/pnas.1002220107

1084 Valdez, G., Tapia, J.C., Lichtman, J.W., Fox, M.A., Sanes, J.R., 2012. Shared
1085   Resistance to Aging and ALS in Neuromuscular Junctions of Specific
1086   Muscles. PLoS One 7, e34640.
1087   https://doi.org/10.1371/journal.pone.0034640

1088 Van den Bos, M. A., Geevasinga, N., Higashihara, M., Menon, P., & Vucic, S.,
1089   2019. Pathophysiology and Diagnosis of ALS: Insights from Advances in
1090   Neurophysiological Techniques. International Journal of Molecular
1091   Sciences, 20(11), 2818.

1092 Van der Burg, J.M., Björkqvist, M., Brundin, P., 2009. Beyond the brain:
1093   widespread pathology in Huntington's disease. Lancet Neurol. 8, 765–774.
1094   https://doi.org/10.1016/S1474-4422(09)70178-4

1095 Wheelock, V.L., Tempkin, T., Marder, K., Nance, M., Myers, R.H., Zhao, H.,
1096   Kayson, E., Orme, C., Shoulson, I., Huntington Study Group, 2003.
1097   Predictors of nursing home placement in Huntington disease. Neurology
1098   60, 998–1001. https://doi.org/10.1212/01.wnl.0000052992.58107.67

1099 Willadt, S., Nash, M., Slater, C.R., 2016. Age-related fragmentation of the motor
1100   endplate is not associated with impaired neuromuscular transmission in the
1101   mouse diaphragm. Sci. Rep. 6, 24849. https://doi.org/10.1038/srep24849

1102 William Yang, X., Gray, M., 2011. Mouse Models for Validating Preclinical
1103   Candidates for Huntington's Disease, Neurobiology of Huntington's
1104   Disease: Applications to Drug Discovery. CRC Press/Taylor & Francis.

1105 Yang, X.W., Model, P., Heintz, N., 1997. Homologous recombination based
1106   modification in Esherichia coli and germline transmission in transgenic mice
1107   of a bacterial artificial chromsome. Nat. Biotechnol. 15, 859–865.
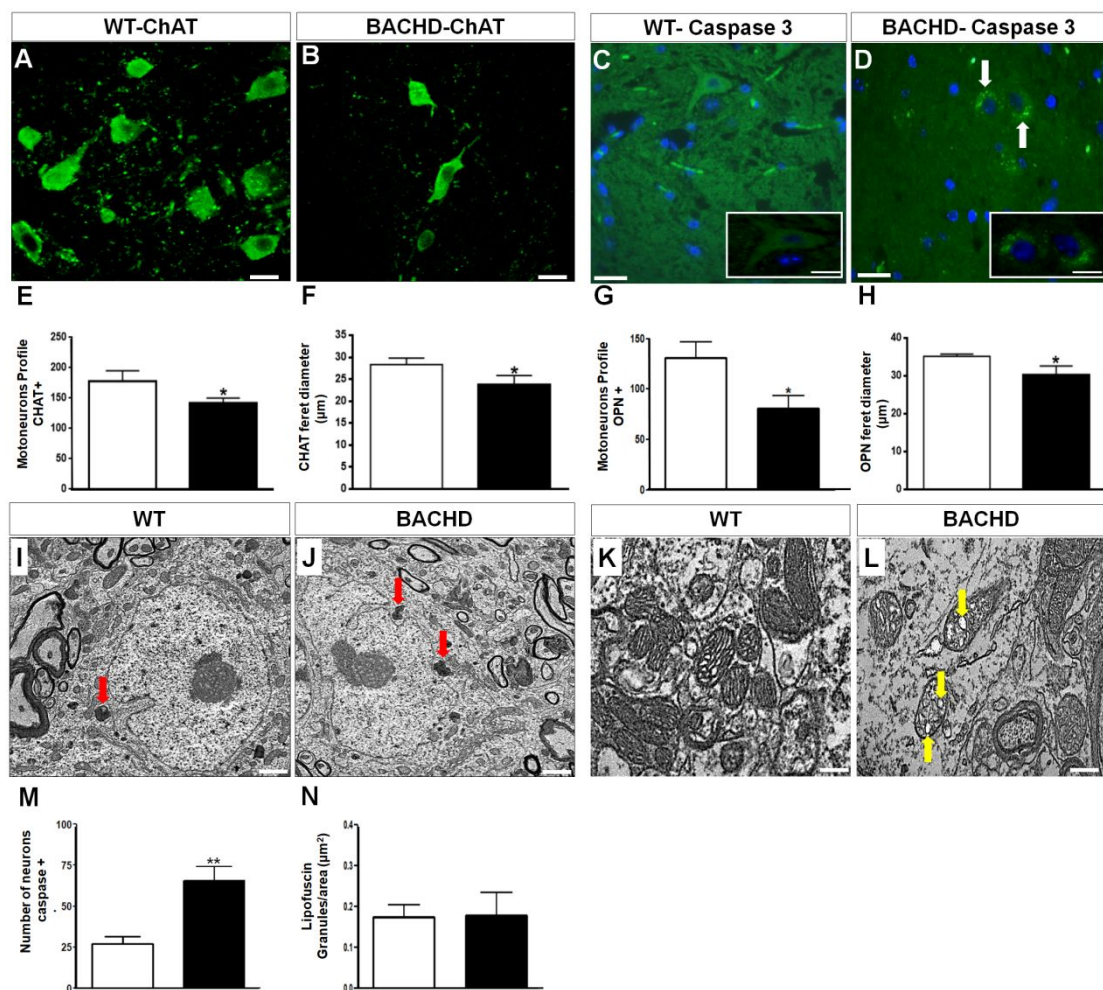
23

1108   https://doi.org/10.1038/nbt0997-859

1109   Yap, F., Bui, J., Knuttinen, M., … N.W.-D. and, 2013, undefined, n.d.
1110   Quantitative morphometric analysis of hepatocellular carcinoma:
1111   development of a programmed algorithm and preliminary application.
1112   researchgate.net.

1113   Zuccato, C., Valenza, M., Cattaneo, E., 2010. Molecular Mechanisms and
1114   Potential Therapeutical Targets in Huntington's Disease. Physiol. Rev. 90,
1115   905–981. https://doi.org/10.1152/physrev.00041.2009

1116

1117

1118

1119

Figure 1: Atrophy in BACHD lumbar motoneurons.

1121

1122

1123

Figure 2: BACHD mice present alterations in sciatic nerve morphology

1133

Figure 3: NMJs from TA muscles are partially denervated and fragmented in BACHD mice.
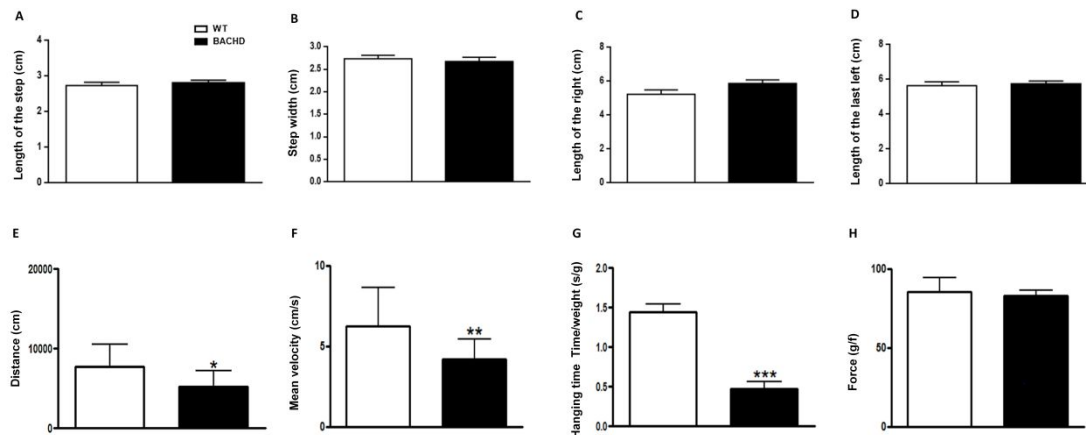

Figure 4: Muscle atrophy, muscle fiber switching and ultrastructural abnormalities in BACHD.

Figure 5: Motor behavior alterations in BACHD.

Figure Legends

Figure 1: Atrophy in BACHD lumbar motoneurons. A–B: Representative images of motoneurons from lumbar spinal cord sections stained with ChAT from 12 -months-old WT (A) and BACHD (B) animals. Scale bar: 50 µm. C-D: Fluorescence images of putative motoneurons stained with caspase-3 in WT (C) and BACHD (D- white arrows). Nuclei were stained with DAPI. Insert: putative motoneurons positive for caspase-3 in BACHD. Scale bar: 50 µm. E and G: Quantification of ChAT and OPN-positive motoneurons profiles in WT and BACHD lumbar spinal cords (~150 neurons analyzed per genotype). Feret diameter for CHAT (F) and for OPN (H) (unpaired student's t-test; *p < 0.05; n=3 animals per genotype). I–J: Ultrastructure images showing a motoneuron with more lipofuscin granules (red arrows) in BACHD (J) compared to WT (I). K-L: Representative images normal and vacuolated mitochondria in WT and BACHD, respectively. Scale bar: 500 nm. M: Graphical quantification of motoneurons stained positively for caspase-3 in WT and BACHD (~150 neurons analyzed per genotype; unpaired student's t-test; **p<0.002; *n*=3 animals per genotype. N: Quantification of the number of lipofuscin granules/area in WT and BACHD motoneurons (Total from 30 motoneurons per genotype; unpaired Student's t-test; p=0.4; *n*=3 animals per genotype). All results described here are from *n*=3 individual animals per genotype and were expressed as mean ± SD.

27

1
2
3   1175
4
5   1176   **Figure 2: BACHD mice present alterations in sciatic nerve morphology**. A-
6   1177   B: Representative images of transversal sections of the sciatic nerve from 12
7   1178   months old WT and BACHD mice, respectively. Note the difference between the
8   1179   size of the axons on inserts in A (WT) and B (BACHD). Scale bar: 10µm. C-H:
9   1180   Quantification of nerve area (C), number of axons per nerve area (D), axon's
10   1181   diameter (E)(**p<0.001; Mann-Whitney test), axoplasm diameter (***p<0.0001;
11   1182   Mann-Whitney test) (F); myelin thickness (G), G-ratio (G=d/D, where G is the G-
12   1183   ratio, d is the inner diameter, and D is the outer diameter) (****p<0.0001; Mann-
13   1184   Whitney test) (H). *n*=3 animals per group. We analyzed 2.874 axons in WT and
14   1185   2.573 in BACHD. Unpaired Student's t-test, p > 0.05 (C and D).
15
16   1186
17
18
19   1187   **Figure 3: NMJs from TA muscles are partially denervated and fragmented**
20   1188   **in BACHD mice**. A–B: Representative images of TA NMJs obtained from 12
21   1189   months old WT and BACHD mice. A and B: Presynaptic terminals labeled with
22   1190   an Alexa-488 anti-synaptotagmin antibody (green). A' and B': Postsynaptic
23   1191   AChRs labeled with Alexa-555 α-btx (red). A″ and B″: Merged images. Scale bar:
24   1192   50 µm. C and D: Representation of particle analysis for both genotypes (red
25   1193   numbers). C' and D': Skeletonization rendering of fragmentation in endplates
26   1194   from WT and BACHD. E–I: Graphs showing the degree of colocalization (E) (*p
27   1195   =0.02; unpaired Student's t-test); partial denervation (F) (***p < 0.0007 unpaired
28   1196   student t-test); pre-synaptic area (G) (***p < 0.0002; Mann-Whitney test); post-
29   1197   synaptic area (H) (p>0.05; Mann-Whitney test); and fragmentation of the
30   1198   endplates (I) (**p=0.001; unpaired student t-test). The results represent the mean
31   1199   ± SD from 50 NMJs per genotype. *n*=3 individual animals per genotype.
32
33   1200   **Figure 4: Muscle atrophy, muscle fiber switching and ultrastructural**
34   1201   **abnormalities in BACHD.** A–B: Representative images of TA skeletal muscle
35   1202   fibers from 12 months old WT and BACHD mice. Scale bar: 50 µm. C–C''' to D–
36   1203   D''': Representative images of TA fiber typing from 12 months old WT and
37   1204   BACHD mice. Scale bar: 50 µm. E–J: Representative electron micrographs of TA
38   1205   fibers from WT and BACHD animals. Observe a normal triad in WT (Figure E,
39   1206   yellow box). G: High magnification view of the area in F showing marked glycogen
40   1207   accumulation in the inter-myofibrillar spaces (red arrows), SR enlargement
41   1208   (yellow asterisk) and Z-line discontinuity (blue arrows) in BACHD animals. H-J:
42   1209   Observe profound mitochondrial changes (green arrows). Scale bar: 500 nm. We
43   1210   analyzed 90 images per genotype from six individual animals (three per
44   1211   genotype). K: Quantitative analysis shows the CSA mean values for WT and
45   1212   BACHD TA muscle fibers. These results represent the mean ± SD of more than
46   1213   4.000 muscle fibers per genotype (****p<0.0001; Mann-Whitney test); *n*=3
47   1214   animals per genotype). L: Quantitative analysis of the fiber typing showing
48   1215   decreased number of IIB isoform and increase of IIX in BACHD TA muscle fibers
49   1216   compared to WT (*p= 0.01 and *p=0.02; unpaired Student's t-test; *n*=3 animals
50   1217   per genotype). M: Quantitative analysis of the CSA from fiber typing (*p= 0.03;
51   1218   unpaired Student's t-test; *n*=3 animals per genotype). The results represent the
52   1219   mean ± SD (unpaired Student's t-test, *p<0.05; *n*=3 animals per genotype).
53
54   1220

28

1221 **Figure 5: Motor behavior alterations in BACHD.** A-D: Graphical quantification
1222 of pattern of gait of WT and BACHD mice. A: Length of the step (p=0.54; unpaired
1223 Student's t-test). B: Step width (p=0.51; unpaired Student's t-test). C: Length of
1224 the rigth(p=0.07; unpaired Student's t-test). D: Length of the left (p=0.70; unpaired
1225 Student's t-test). E:Graphical quantification of the total distance traveled by WT
1226 and BACHD mice, showing hypoactivity in transgenic animals (*p=0.01; unpaired
1227 Student's t-test). F: Graphical quantification of the average speed traveled by
1228 both genotypes with a decrease in BACHD animals (**p=0.003; unpaired
1229 Student's t-test). G: Graphical quantification of the total time the animals kept
1230 holding their own weight in the test apparatus (time/weigth = time corrected for
1231 weight) (***p=0.0001; unpaired Student's t-test) H: Maximum force quantification
1232 in the test of grip strength exerted by WT animals and BACHD when a constant
1233 and opposite force is applied (p=0.39; unpaired Student's t-test). The results
1234 express the mean ± SD from 11 WT and 17 BACHD animals.

1235

29

Abstract

Huntington's disease (HD) is a disorder characterized by chronic involuntary movements, dementia, and psychiatric symptoms. It is caused by a mutation in the gene that encodes for huntingtin protein (HTT), leading to the formation of mutant proteins expressed in various tissues. Although brain pathology has become the hallmark for HD, recent studies suggest that damage of peripheral structures also contributes to HD progression. We previously identified severe alterations in the motor units (MUs) that innervate cervical muscles in 12 months old BACHD mice, a well-established mouse model for HD. Here, we studied lumbar motoneurons and their projections onto hind limb fast-twitch skeletal muscles (Tibialis Anterior, TA), which control balance and gait in HD patients. We found that lumbar motoneurons were altered in the HD mouse model; the number and size of lumbar motoneurons were reduced in BACHD. Structural alterations were also present in the sciatic nerve, and neuromuscular junctions (NMJs). Acetylcholine receptors (AChRs) were organized in several small patches (AChR fragmentation), many of which were partially innervated. In BACHD mice, we observed atrophy of TA muscles, decreased expression of glycolytic fast type IIB fibers, and at the ultrastructural level, alterations of sarcomeres and mitochondria. Corroborating all these findings, BACHD animals performed worse on motor behavior tests. Our results provide additional evidences that nerve-muscle communication is impaired in HD and that motoneurons from distinct spinal cord locations are similarly affected in the disease.

Summary statement

This study evaluates the morphology of the motor unit of the tibilais anterior muscle. The main finding is that Huntington's disease can affect the motor unit in all its components, from the motoneuron to the skeletal muscle.

1
2
3   48
4
5   49   **Introduction**
6
7   50   Skeletal muscle loss and dysfunction are found in Huntington's disease
8   51   (HD), which is a progressive neurodegenerative disorder caused by an
9   52   autosomal dominant condition leading to motor, cognitive, and psychiatric
10   53   impairment. In 1993, the Huntington's Disease Collaborative Research Group
11   54   identified a mutation in the short arm of chromosome 4, an unstable expansion in
12   55   the number of CAG repeats in the Huntingtin (HTT) protein (The Huntington's
13   56   Disease Collaborative Research Group, 1993). Historically, HD has been studied
14   57   in the central nervous system (CNS), mainly in neurons from the basal ganglia
15   58   and cerebral cortex (Reiner et al., 1988; Novak and Tabrizi, 2010; Reinius et al.,
16   59   2015).
17   60   The discovery of HTT gene mutation opened a new scenario for scientific
18   61   research enabling the generation of numerous animal models for the disease
19   62   (Menalled and Chesselet, 2002; Heng et al., 2008; Menalled et al., 2009; Yang
20   63   and Gray, 2011). Experiments performed in these animal models allowed the
21   64   identification of mutant Huntingtin protein (mHTT) not only in the CNS but also in
22   65   peripheral structures, such as skeletal muscles (Van der Burg et al., 2009;
23   66   Zielonka et al., 2014; Mielkarek et al., 2017). In fact, mouse HD models exhibited
24   67   pronounced skeletal muscle atrophy, a pathophysiological finding that could be
25   68   due to accumulation of mHTT in skeletal muscles, motoneurons or both (Khedraki
26   69   et al., 2017). This prompted the question of whether a primary defect in the
27   70   neuromuscular system contributes to the motor deterioration observed in patients
28   71   with HD, independently of the striatal degeneration (Van der Burg et al., 2009).
29   72   Consistent with this hypothesis, Ribchester et al., (2004), using the R6/2 mouse
30   73   model, identified physiological and morphological alterations on neuromuscular
31   74   junctions (NMJs), a result that suggested a progressive disruption of the
32   75   communication between motoneurons and skeletal muscles. However, it is
33   76   important to note that these authors did not investigate whether there is
34   77   denervation in the NMJs of R6 / 2 mice.
35
36   78   Recently, using a different mouse model for HD (BACHD), which
37   79   expresses the full-length human mHTT in a BAC vector, we reported alterations
38   80   in cervical motor units (MUs), such as the reduction in the number and size of
39   81   motoneurons, axonal degeneration, and fragmentation of NMJs. Furthermore,
40   82   marked muscle atrophy and fiber-type switching were observed in BACHD-
41   83   sternomastoid (STM) muscles (Valadão et al., 2017). In addition, we also
42   84   described abnormal neuromuscular junctions in the diaphragm of BACHD mice
43   85   (Valadão et al.,2018). Nonetheless, the hypothesis that HD may have a more
44   86   direct connection with progressive disruption of communication between
45   87   motoneurons and skeletal muscles remains poorly explored.
46   88   Following the trail initiated in our previous studies, we investigated whether
47   89   mHTT-mediated alterations were restricted to cervical motoneurons, or spread
48   90   over other spinal cord segments like the lumbar segment. This comparison has
49   91   clinical importance, since in Amyotrophic lateral sclerosis (ALS), which is a
50   92   disease that affects the motoneurons, there are evidences that upper and lower
51   93   motor neurons are differently affected during the course of the disease (Eisen et
52   94   al., 1992;Fischer et al., 2004, reviewed by Van den Bos et al., 2019). Thus,
53   95   studying two different segments of the spinal cord in the BACHD animal model,
54   96   which shows clear loss of motoneurons, is an important study in the sense of
55   97   identifying possible differences in these two regions (cervical and lumbar
56
57
58
59
60

98 segments) in this HD model. To this end, we chose to look at the lumbar spinal
99 cord segment and the MU of the lower hindlimb muscle Tibialis Anterior (TA).
100 This muscle controls movement and balance that are severely impaired in HD
101 such as decreased walking speed, difficulties in starting the steps and variable
102 pattern of step. In addition, motor neurons of the lumbar spinal cord segment and
103 TA muscle are also involved in gait, which is considered to be one of the main
104 factors of disability in patients with HD (Piira et al., 2013). It is noteworthy that,
105 with the progression of the disease, the mobility is affected, increasing the risk of
106 falls and directly impacting the functionality of the patients who end up needing
107 constant help in their daily living activities (Bilney et al., 2005; Carroll et al., 2015;
108 Cruickshank et al., 2015; Koller and Trimble, 1985; Thaut et al., 1999; Wheelock
109 et al., 2003).
110 In this way, this study adds to our previous work, since the focus now is
111 to examine another segment of the spinal cord, with motoneurons that are
112 involved in the innervation of muscle groups with function (TA is dorsiflexion and
113 inversion of the foot) and composition (predominantly a fast contraction muscle)
114 different from the STM muscle previously studied by us.

115
116 **Materials and methods**
117 **BACHD mice**

118 All experiments were performed according to the rules established by the
119 local animal care committee (Ethics Committee on Animal Experiments of the
120 Universidade Federal de Minas Gerais - CEUA / UFMG); approved protocol
121 #036/2013. All efforts were made to minimize animal suffering and to reduce the
122 number of animals used. This study was not pre-registered.

123 The FVB/NJ (wild-type) and FVB/N-Tg (HTT*97Q)IXwy/J (BACHD)
124 transgenic mice (male) were purchased from Jackson Laboratory (Barl Harbor,
125 ME, USA) (JAX stock #008197) and used to establish a new colony. Mice were
126 held in a place with controlled temperature (23 °C) in a 12-12h light-dark cycle.
127 Food and water were provided *ad libitum* in an animal care facility of the
128 Department of Physiology and Biophysics, UFMG. All animals used in this study
129 were genotyped ten days after birth using multiplex Polymerase Chain Reaction
130 (PCR) (HTT-Forward: CCGCTCAGGTTCTGCTTTTA/HTT-Reverse:
131 GGTCGGTGCAGCGGCTCCTC; Actin-Forward:
132 TGGAATCGTGTGGCATCCATCA/Actin-Reverse:
133 AATGCCTGGGTACATGGGGTA).

134 The BACHD mouse model, unlike the R6 / 2 model, expresses the total length of
135 human mHtt inserted into the BAC (Bacterial Artificial Chromosome (Gray et
136 al.,2018). Compared to the R6 / 2 model, BACHD has an expressive vantage,
137 because in addition to presenting behavioral and pathological characteristics of
138 the disease, it also has the polyglutamine sequence "CAA / CAG" in a more stable
139 form, thus the length of the CAA / CAG repeat in BACHD mice is stable in 97
140 replicates over several generations (Yang et al., 1997). In this way, this model is
141 reliability for the study of long-term phenotypic characteristics as we did in 12-
142 month-old animals (Kazantsev et al., 1999.; Yang et al., 1997). In addition to
143 these characteristics, this model has a normal life span with slow disease
144 progression, allowing more detailed longitudinal studies when compared to other
145 rapid progression models, such as R6 / 2, for example (Yang and Gray, 2011).

3

146 Animals were identified by numbers according to their genotype (WT or BACHD).
147 They were separated into mini-isolator cages with a maximum of 4 animals per
148 cage. In this study, we used WT and BACHD mice (24 grams). Using a table of
149 random numbers, animals were randomly divided into two groups. Our
150 experiments were performed on 12 months old WT and BACHD animals, as
151 previous studies using this model demonstrated pronounced neurodegenerative
152 signals in the cerebral cortex and deficits in motor behavior in mice of this age
153 (Gray et al., 2008); for review see (Yang and Gray, 2011). Also, this age
154 corresponds to middle age in humans, when it is supposed to appear HD
155 symptoms. In addition, previous work from our research group have shown that
156 12 months old BACHD mice present alterations in cardiac cells and other
157 muscles such as sternomastoid and diaphragm (Joviano-Santos et al., 2019;
158 Valadão et al., 2017b); Valadão et al., 2018).

159 For all experiments involving morphology and immunofluorescence
160 techniques, mice from both genotypes (WT and BACHD) were deeply
161 anesthetized with ketamine/xylazine (0.1mL/20g) in accordance to the
162 CEUA/UFMG protocol. All surgical procedures were described in the
163 appropriated sections. The experimental procedures were performed in the
164 afternoon and, by the end of each surgical procedure, the animals were
165 euthanized by an over-dosage of anesthetics.

166 The experimental procedures were performed in the Departments of
167 Morphology and Pharmacology at the UFMG. The experimental groups
168 remained constant from the beginning to the end of the study, and the exact
169 numbers for all experiments are provided in the figure captions/results section.

170

171 Lumbar Spinal Cord immunofluorescence
172 All immunofluorescence experiments were performed according to the
173 protocol described by Valadão et al., (2017). For the identification of alpha-
174 motoneurons, lumbar spinal cords slices were stained with Choline
175 Acetyltransferase (ChAT) antibody (1:100, Cat #AB1582 RRID: AB_11211009)
176 and with osteopontin (OPN) (1:100, R&D Systems Cat #MAB14331
177 RRID:AB_2194980) Lumbar spinal cord (L1-L5 segments) were removed and
178 fixed with 4% PFA for 48 hours. Next, the spinal cord segments were kept in 30%
179 sucrose for 24 hours. Samples were then frozen in isopentane (Sigma-Aldrich),
180 cooled with liquid nitrogen, and stored at -80°C. The lumbar spinal cords cross-
181 sections (30μm) were cut on a cryostat (Leica CM3050S), and collected on
182 gelatin-coated slides. The sections were blocked (60 minutes, room temperature)
183 in solution containing 3% bovine serum albumin (BSA), 5% donkey serum, and
184 0.1% Triton X-100. Samples were then incubated overnight at 4 °C with the
185 following primary antibodies diluted in 3% BSA, 5% donkey serum, 5% goat
186 serum: goat anti-ChAT and mouse anti-OPN. Slides were washed three times
187 with PBS 1x, and incubated for 2 hours at room temperature with the secondary
188 antibodies Alexa 488 donkey anti-goat IgG1 for anti-CHAT (1:800, Molecular
189 Probes Cat.#A-11055 RRID: AB_142672) and Alexa 488 goat anti-mouse for
190 anti-OPN (1:1000;Thermo Fisher Scientific Cat. #A-21042 RRID: AB_2535711).
191 Samples were washed three times with PBS 1x and mounted using ProLong®
192 Gold antifade (Thermo Scientific Invitrogen™). Images were acquired using a 63x
193 oil immersion (NA 1.4) objective attached to a laser-scanning confocal

4

194 microscope (Zeiss LSM 510 Meta, Zeiss GmbH, Jena, Germany). An Argon (488
195 nm) laser was used for excitation of lumbar spinal cord slides marked with anti-
196 ChAT and anti-OPN. The Z series of optical sections were collected at 2.0μm
197 intervals. All digital images were quantitatively analyzed using Image J software
198 (Wayne Rasband, National Institutes of Health, USA).

199 Caspase-3 staining in BACHD mice spinal cords lumbar segments (L1-L5)
200 was performed by immersing the spinal cord in neutral-buffered formalin (NBF)
201 for 24 hours. The samples were then dehydrated in ethanol (70%, 80%, 90%,
202 95%, and 100%), cleared in xylene, embedded in paraffin and cut (thin sections
203 -5μm) using a microtome (model HM335E; Microm, Inc., Minneapolis, MN).
204 Nonspecific blockade was performed by incubation of the samples in a solution
205 containing 2% BSA, 0.1% Tween-20 for 1 hour in a moist chamber. Samples
206 were incubated with the primary antibody (1:100 polyclonal rabbit anti-caspase-
207 3, Sigma-Aldrich, Saint Louis, MO) diluted in blocking solution (overnight at 4°C
208 in a moist chamber)and then washed 3 times with PBS following incubation with
209 the secondary antibody (1:1000, Alexa Fluor 488 goat anti-rabbit; Invitrogen,
210 Eugene, OR) for 1 hour. To allow nuclei identification, sections were washed 3
211 times with PBS and stained with DAPI (1:1000; Invitrogen, Eugene, OR). The
212 stained sections were imaged using a NIKON ECLIPSE Ti microscope (100X
213 objective, N.A: 1.49). All digital images were quantitatively analyzed using Image
214 J software (Wayne Rasband, National Institutes of Health, USA).

215 To perform the counting of motoneurons marked with CHAT, OPN and
216 caspase-3, only those with evident nuclei were measured. Since the
217 motoneurons are variable and not perfect circles, we chose to use the "Feret
218 diameter" present in the Image J software (Feret diameter) to measure the
219 diameter of these cells. This tool uses mathematical calculations to correct the
220 diameter of figures that are not totally spherical. In general, it can be defined as
221 the common base of a group of diameters derived from the distance of two
222 tangents to the particle contour in a well-defined orientation (Yap et al., 2012).

NMJ immunofluorescence and confocal microscopy analysis

224 Six mice were anesthetized (three per genotype) as previously described
225 with ketamine/xylazine (0.1mL/20g) and transcardially perfused with iced-cold
226 4% PFA (paraformaldehyde) in 0.1M PBS (phosphate-buffered saline; pH 7.4).
227 The TA muscles were dissected, blocked in 3% BSA + 5% goat serum + 0.5%
228 Triton X-100 for 30 minutes at room temperature and stained with anti-
229 synaptotagmin antibody (1:250, Anti-synaptotagmin, anti-mouse, IgG2A, DSHB;
230 Cat #3H2 2D7 RRID: AB_528483) in the blocking solution. The samples were
231 then incubated overnight at 4°C, washed three times with PBS and incubated for
232 1 hour at room temperature with Alexa 555-α-bungarotoxin (α-btx) (1:1000; Cat#
233 T1175 Molecular Probes, Eugene, OR; T1175 RRID: AB_2313931) together with
234 secondary antibody (1:1000, Alexa-488 goat anti-mouse IgG2A; Invitrogen; Cat
235 #A-21141 also A21141 RRID: AB_141626). The Muscles were washed three
236 times with PBS and whole-mounted using Vectashield (Vector Laboratories,
237 Eching, Germany). Images of NMJs were acquired using a 63x oil immersion
238 (N.A: 1.4) objective attached to a laser-scanning confocal microscope (Zeiss
239 LSM 510 Meta, Zeiss GmbH, Jena, Germany. We used an argon (488 nm) and

240 helium-neon (He-Ne, 543 nm) lasers to excite the samples. The Z series optical
241 sections were collected at 2.0 μm intervals, and the whole TA muscle samples
242 were scanned. The nerve terminals were identified considering their
243 colocalization near the AChR clusters. Images were converted to a grayscale
244 format (8 bits), and each synaptic element was individually evaluated. The
245 NMJs- fragmentation index was obtained using the particles analysis method
246 described in Valadão et al. (2017). Briefly, the images were converted into a
247 binary image pattern and were skeletonized. Next, to describe the connectivity
248 for each pixel in the image, a histogram was generated using the
249 BinaryConnectivityClass plugin from IMAGEJ (Pratt et al., 2013). We analyzed
250 the degree of fragmentation in pre- and postsynaptic elements comparing the
251 muscle samples from WT and BACHD mice. The parameters adopted for
252 fragmentation were defined according to the evaluation criteria described by
253 (Valdez et al., 2010), which establishes fragmentation by five or more islands
254 both in the presynaptic and postsynaptic membranes. We analyzed 50 NMJs for
255 each animal.

Morphology and morphometric analysis of sciatic nerve and TA muscle
fibers

258 The TA muscle was dissected-out and fixed in 4% glutaraldehyde diluted
259 in PBS (0.2 M) for 24 hours at room temperature. After dehydration in an
260 ascending series of alcohols (70%, 80%, 90%, 95% 2X), samples were
261 embedded in glycolmethacrylate resin (Leica) and sectioned (5μm) in a
262 microtome (Reichert Jung). Sections from the TA muscle were stained with
263 toluidine blue (EMS), and the cross-sectional area (CSA) of individual myofibers
264 imaged using a light microscope (10X oil objective -Leica DM2500) coupled to
265 a CCD camera (Leica DFC345FX).

266 Samples containing the sciatic nerve were histologically analyzed. Semi-
267 thin cross sections (300 nm) were obtained and stained with toluidine blue.
268 Images of whole sciatic nerve cross-sections from WT and BACHD mice were
269 captured using a 20x objective in a ZEISS Axio Lab.A1 microscope. The total
270 CSA of the nerve was measured using ImageJ plugins (NIH), and the total
271 number of axons was counted. Like the motoneurons, the axons are not perfect
272 circles and we also used the Feret diameter (described above) for the calculation
273 of the total diameter (axon diameter). To quantify axonal myelination, we used
274 the G-ratio, which was calculated measuring the axonal inner diameter and
275 dividing it by the outer diameter following the formula: G=d/D, where G is the G-
276 ratio, d is the inner diameter and D is the outer diameter (Chau et al., 2000).

TA muscle fiber typing

278 TA muscle fiber typing was performed according to the protocol described
279 by Valdez et al., (2012). TA samples were put in freezing molds covered with
280 *optimum cutting temperature* (OCT) freezing medium (Easy Path), and fresh
281 frozen in isopentane (Sigma-Aldrich) cooled with liquid nitrogen and stored at -
282 80°C. The mid-belly region of the TA muscle was cut on a cryostat (Leica
283 CM3050S), and the cross-sections (10μm) collected on gelatin-coated slides.
284 Slides containing muscle sections were then blocked for 30 minutes at room
285 temperature (RT) with 3% BSA (Sigma-Aldrich), 5% goat serum (Sigma-Aldrich)

6

286 and 0.1% Triton X-100 (Sigma-Aldrich) diluted in PBS 1x. Muscle sections were
287 incubated overnight at 4°C with the following primary antibodies: type 1 (1:250,
288 Leica Microsystems Cat# NCL-MHCs RRID: AB_563898); type 2A (1:100, DSHB
289 Cat# SC-71 RRID:AB_2147165), type 2X (1:100, DSHB Cat# BF-35
290 RRID:AB_2274680, which recognizes all types of muscles fibers except 2X), and
291 type 2B (1:100, DSHB Cat# BF-F3 RRID:AB_2266724). All antibodies were
292 diluted in 3% BSA, 5% goat serum prepared in PBS 1x. Slides were washed three
293 times with PBS 1x and incubated for 1 hour at room temperature with secondary
294 antibodies Alexa 488 goat anti-mouse IgG1 (Thermo Fisher Scientific Cat # A-
295 21121 RRID: AB_2535764. It recognizes type 1, 2A and 2X antibodies) and Alexa
296 488 goat anti-mouse IgM (Thermo Fisher Scientific Cat #A-21042 RRID:
297 AB_2535711 It recognizes type 2B antibody). The samples were washed three
298 times with PBS 1x and mounted using VectaShield antifade solution (Vector
299 Laboratories Cat #H-1000 RRID: AB_2336789). Images were acquired using an
300 air objective (10x, 0.25NA) in an epi-fluorescence microscope (Leica DM2500)
301 equipped with a Leica DFC 345FX camera and visualized in a computer. The
302 excitation light came from a 100W Hg lamp, and a FITC filter cube was used to
303 collect the emitted light. Whole muscle cross-sections were imaged for analysis.
304 Each fiber type was expressed as a percentage of the total number of fibers.
305 Validation for each antibody was obtained from the datasheets provided by the
306 company. The CSA of individual myofibers from each fiber type was measured.

Transmission electron microscopy (TEM)

308 For the ultrastructural studies, we used the protocol previously described
309 by us (Rodrigues et al., 2013). Briefly, mice were anesthetized with
310 ketamine/xylazine (0.1mL/20 g), and the heart left ventricle perfused with ice-cold
311 modified Karnovsky fixative (4% PFA and 2.5% glutaraldehyde in 0.1 M sodium
312 cacodylate buffer at 4°C), and maintained in the solution for at least 24 hours at
313 4ºC. Lumbar spinal cord segments (L1-L5) and TA muscles from WT and BACHD
314 transgenic mice were then collected. After fixation, samples were washed with
315 cacodylate buffer (0.1 M), cut into several fragments (300 nm), post-fixed in
316 reduced osmium (1% osmium tetroxide containing 1.6% potassium ferrocyanide),
317 contrasted *en bloc* with uranyl acetate (UA, 2% in deionized water), dehydrated
318 through an ascending series of ethanol solutions and embedded in EPON. After
319 several days in the oven at 60ºC, the resin blocks were sectioned (50 nm), and
320 the ultra-thin sections collected on 200 or 300 mesh copper grids and contrasted
321 with lead citrate. The ultra-thin sections were viewed with a Tecnai- G2-Spirit
322 FEI/Quanta electron microscope (120 kV Philips).
323 To quantify the lipofuscin granules in the motoneurons, we used 30
324 electron micrographs of the lumbar spinal cord motoneurons for each genotype
325 (WT, BACHD). The counting was performed using the ImageJ software plugins
326 (NIH). Data were presented as granules/area using the GraphPad Prism 6.

Motor behavioral tests

330 We used the test paw print test to examine the pattern of steps of mice
331 hind limbs during the locomotion (adapted from de Lagrán et al., 2004). Briefly,
332 the apparatus consisted of a narrow wooden tunnel (10x10x70cm), lined with
333 white paper, containing a dark box at one of its ends (positive reinforcement) and
334 positioned in an illuminated room (aversive stimulus). Rodents naturally seek to

7

335 be lodged in safer and dimly lit environments, so when the animal were placed at
336 the end of the corridor opposite the box, they naturally tended to walk towards it.
337 The hind legs of the animals were previously painted with non-toxic black ink, so
338 that when walking on paper, the footprints of their legs were printed / recorded.
339 This procedure was repeated at least three times (3 trials) for each animal.
340   The gait pattern of each animal was recorded through four gait cycles
341 for each trial and data were expressed as the mean of at least three trials. A
342 complete gait cycle was previously defined by de Lagrán et al., (2004), as the
343 distance from one pair of hind legs to the next pair of hind legs. Three parameters
344 were evaluated: the length and the width of the step and the size of the step (right
345 and left). The length of the pitch was measured as the average distance of
346 locomotion between one leg and the next immediately ahead. The width was
347 measured as the mean distance between the right and left hind legs. The length
348 of the stride was considered as the distance between each cycle (right and left).
349 These variables were expressed in centimeters.
350   The data obtained through the behavioral tests were plotted in Microsoft
351 Excel® and converted to graphical representations through the program
352 GraphPad Prisma 7.0 (San Diego, CA, USA).
353
354   Spontaneous locomotor activity was evaluated by means of a automatic
355 open field (LE 8811 IR Motor Activity MonitorsPANLAB /HARVARD
356 APPARATUS), with acrylic box dimensions 450x450x200mm (width x depth x
357 height) (Pereira et al., 2014). The WT and BACHD animals were habituated in
358 the behavioral testing room for the minimum time of 60 minutes. The activities
359 detected in the horizontal plane (distance traveled and mean velocity) was
360 measured for 60 min. The measure of activity total was calculated using the
361 ACTITRACK program and the statistical analyzes were performed using
362 GraphPad Prism 6 software.
363   For the wire hang test is a measure of the force muscle (fore and hind
364 limbs) analysis in rodents and the experiments were conducted according to
365 protocol described by (Sango et al., 1996) and (Prado et al., 2006). The animals
366 were accustomed to the experimental room and manipulated by the researcher
367 at least 2 hours before of the test. The apparatus used consisted of a metal grid
368 with spacing of 1 cm between the 0.8 mm diameter bars. The test was conducted
369 in a single session, in which the animal was individually placed on the grid until
370 the hold. The grid was then inverted and maintained at 20 cm above a foam. It is
371 important to note that this height is sufficient for the animal to remain attached to
372 the grid, however is unable to injure it in the event of fall. The latency, which is
373 the time until the animal disengaged and fell off the inverted grid for 60 seconds
374 observation, was measured, and three observations per animal were considered.
375 It is important to emphasize that we use Time/weight (time corrected for weight),
376 since the BACHD mice presented weight gain and for this reason we corrected
377 the time spent in the apparatus by the weight of the animal. The time was counted
378 in seconds and the weight in grams.
379   The grip strength test was performed according to Fowler et al., 2002.
380 To this end, the power transducer was connected to a small metal bracket that
381 could be grasped by the mouse. The force transducer was coupled to a computer
382 that recorded the maximum grip force in fore limbs exerted by the mouse. The
383 animals were used to the test room and handled by only one researcher.

8

384   During the test, the experimenter gently manipulated the animals by the
385 tail to allow adhesion of the animal with the front legs to the apparatus maintaining
386 the body of the animal parallel to the surface. After holding for two seconds in this
387 position, the experimenter continuously increased the force until the animals lost
388 their grip. The peak of the force automatically recorded at the time the animals
389 lost their adhesion was recorded and expressed in grams / force (g / f). The test
390 was performed three times for each animal for a maximum period of 60 seconds.
391 The mean values of three trials were calculated for each animal and used for
392 further analysis.
393
394 **Statistical Analysis**

395   We used Microsoft Excel for analyzes and all data were plotted using the
396 program GRAPHPAD PRISM 6. For data with normal distribution, values were
397 represented as the standard error of the mean (S.E.M.). Statistical significance
398 was evaluated using the unpaired Student's t-test. As described in the text, when
399 data were not normally distributed, values were represented as the median, and
400 the Mann-Whitney test was used to evaluate statistical significance. Values of p
401 < 0.05 were considered statistically significant. Exact p-values were provided in
402 the figure captions. During analysis, the investigators were blinded for both
403 animal genotype and experimental group. A specific number was assigned to
404 each of the genotyped animals, and the identifier was announced to the
405 researchers only all the analyses were completed.
406   In this work, we used a minimum of three animals per genotype for each
407 data set to obtain statistical difference with 95% of confidence (a = 0.05) and 0.8
408 power. The exact *n* for each experimental procedure is described in the figures'
409 captions.
410
411 **Results**

412 **Lumbar spinal cord motoneurons are reduced in size, number and are**
413 **caspase-positive in BACHD mice**

414   Reduced lower limb muscle strength has been described in HD patients
415 and this contribute significantly to mobility and balance problems in HD (Busse et
416 al., 2008; Cruickshank et al., 2014)**.** Herein, we investigated if the lumbar spinal
417 cord motoneurons that innervate lower limb muscles are affected in 12 months
418 old BACHD mouse model for HD.

419   We began by investigating the number, size, and morphology of the
420 motoneurons from the ventral spinal cord lumbar segments (L1-L5). Figure 1 A-
421 B shows representative images of ChAT-positive (a motoneuron marker) neurons
422 located in the ventral portion of the lumbar segments of the spinal cord of WT and
423 BACHD animals, respectively. Quantitative analysis of ChAT-positive neurons
424 showed a significant decrease in the total number of ChAT-positive cells in the
425 lumbar segments of BACHD animals when compared to WT animals (BACHD:
426 142.0 ± 8.0 number; WT: 178.0 ± 17.6 number (mean ± SD); T_4= 3.3; *p<0.02)
427 (Figure 1E). We also noticed a significant decrease in the diameter of these
428 neurons, with ChAT positive-BACHD neurons being smaller than WT (BACHD:
429 23.7 ± 2.0 µm; WT: 28.3 ± 1.4 µm (mean ± SD); T_4= 3.1; *p<0.03) (Figure 1F). A
430 similar trend in number and size was observed when the antibody against OPN
431 (a specific marker for alpha motoneuron type) was used in the lumbar spinal cord

9

432 segments. A statistically significant decrease in the number (BACHD: 80.5 ± 25.3
433 number; WT: 131.0 ± 31.4 number (mean ± SD); T_6=2.5; *p<0.02) and diameter
434 (BACHD: 30.2 ± 2.3 μm; WT: 35.1 ± 0.6 μm; T_4=3.5 *p<0.02) of OPN-positive
435 neurons was observed in BACHD mice compared to WT (Figure 1 G-H).

436 It is possible that BACHD ChAT/OPN- positive neurons were dying at 12
437 months old. Thus, we immunostained lumbar spinal cord sections (40μm) of
438 BACHD and WT animals for caspase-3 to investigate if these motoneurons were
439 undergoing apoptosis. Figure 1C shows representative images of WT lumbar
440 segments incubated with the antibody anti-caspase-3. Very little caspase staining
441 was observed in all WT lumbar sections. On the other hand, lumbar spinal cord
442 sections of BACHD animals showed a clear presence of caspase-3 labeling with
443 the majority was in ventral horn neurons, mostly in motoneurons (white arrows)
444 (Figure 1D). These observations were confirmed by quantitative analyses of
445 several lumbar spinal cord sections for both genotypes (BACHD: 65.6 ± 8.3
446 number; WT: 27.0 ± 4.3 number (mean ± SD); T_4=7.1; **p<0.002) (Figure 1M).
447 Overall, these results indicate that the activation of the apoptotic cascade can be
448 part of the degenerative changes seen in motoneurons of BACHD animals.

449 We next asked if motoneurons from BACHD lumbar spinal cord presented
450 any abnormal feature at the ultrastructure level. Qualitative analysis of electron
451 micrographs showed that typical motoneurons in WT animals were large in size
452 (Figure 1I), whereas motoneurons from BACHD animals looked significantly
453 smaller (Figure 1J, compare to 1I). At the subcellular level, we observed
454 abnormalities in the mitochondria from BACHD lumbar spinal cord motoneurons,
455 such as cristae disruption and presence of vacuoles (Figure 1L, yellow arrows),
456 whereas in WT animals this organelle was well preserved (Figure 1K). We also
457 identified the presence of lipofuscin granules in motoneurons from BACHD
458 (Figure 1J) and WT (Figure 1I) animals (red arrows). However, the number of
459 these granules was not significantly different between the genotypes (BACHD:
460 0.17 ± 0.05 μm^2; WT: 0.17 ± 0.03 μm^2 (mean ± SD); T_4= 0.08; p= 0.4) (Figure
461 1N).

462 **Abnormities in sciatic nerve and NMJs from BACHD mice**

463 We next performed histological analysis of the sciatic nerve, which projects
464 to the lower hind limb TA muscle (Figure 2A and B). We found statistically
465 significant differences in the following morphological parameters between
466 BACHD and WT mice: i) axon diameter (BACHD: 10.9 ± 3.5 μm; WT: 11.4 ± 4.02
467 μm (median); **p<0.001) (E); ii) axoplasm diameter (BACHD: 6.8 ± 2.6 μm; WT:
468 7.5 ± 2.8 μm (median); ***p<0.0001) (F) and iii) G-ratio (BACHD: 0.6 ± 0.07; WT:
469 0.6 ± 0.07 (median); ****p<0.0001) (H). However, no significant differences were
470 observed between WT and BACHD sciatic nerves in terms of nerve area (C),
471 number of axons per area (D) and myelin thickness (G).

472

473 To determine if the sciatic nerve abnormalities described above were
474 accompanied by changes in the innervation of the TA muscle, the neuromuscular
475 junctions (NMJs) of both genotypes were pre- and post-synaptically stained with
476 synaptotagmin and α-btx, respectively. Figure 3 A-B shows representative
477 images of presynaptic nerve terminals stained with Alexa 488 anti-synaptotagmin
478 antibodies from WT and BACHD TA muscles, respectively. Figures 3A' (WT) and

10

B' (BACHD) show the post-synaptic acetylcholine receptors (AChRs) stained with Alexa 555 α-btx. Figure 3A'' (WT) and 3B'' (BACHD) show the merge of both green and red signals. Figures 3C and 3D show the graphic representation of the particle analysis for NMJs fragmentation. Figures 3C' and 3D' show the skeletonization process of the NMJs.

We found abnormal features in BACHD TA such as i) loss of colocalization between pre- and post-synaptic elements (BACHD: 87.5 ± 0.8 %; WT: 93.1 ± 1.2 % (mean ± SD); T_4=3.6; *p=0.02) (Figure 3E); ii) NMJs partial denervation were identified considering their colocalization with nAChR clusters. (BACHD: 27.6 ± 2.0 % Vs. WT: 5.6 ± 1.2 % (mean ± SD); T_4=9.3; ***p<0.0007) (Figure 3F); iii) decreased pre-synaptic terminal area (BACHD: 1231 ± 886 μm^2; WT: 1761 ± 964 μm^2 (median); ***p<0.0002), but not in postsynaptic area (Figure 3 G-H); iv) pronounced fragmentation of AChRs (BACHD: 85.6 ± 7.6 μm^2; WT: 47.6 ± 3.5 μm^2 (mean ± SD); T_4=7.8; **p<0.001) (Figure 3I). All abnormalities described above were augmented in BACHD NMJs but were absent or present only in few cases in WT NMJs. All these analyses provided evidence of the degenerative process that is taking place at the NMJs of TA muscles from BACHD animals.

BACHD TA muscle fibers are atrophic, with fiber type switching and show signs of degeneration at the ultrastructure level

We investigated if TA muscles, innervated by motoneurons from lumbar spinal cord segments, were affected in BACHD mice. To address this, cross-sections of TA muscles were stained with toluidine blue. Figure 4A-B show representative images of TA-muscle fibers from WT and BACHD animals, respectively. Quantitative analysis showed that the TA- muscle fibers CSA was smaller in BACHD mice compared WT (Figure 4K) (BACHD: 1535 ± 820.4 μm^2; WT: 1965 ± 779,4 μm^2 (median); ****p<0.0001). Ultrastructural analyses showed that WT- TA muscle fibers presented normal looking organelles such as mitochondria, well-preserved sarcomeres, triads and myofibrils (yellow rectangle, Figure 4E). However, the BACHD- TA muscle fibers were different in structure, showing severely disorganized sarcomeres (Figure 4F - dotted area). Figure 4G shows an enlarged view of the dotted area indicated in Figure 4F. Here, we observed atypical amounts of inter-myofibrillar glycogen (red arrow), loss of alignment among the sarcomeres (blue arrows), and invasion of the sarcoplasmic reticulum (SR) onto the myofibrils region (yellow asterisk). In addition, large vacuoles within the mitochondrial matrix were observed in the mitochondria of BACHD muscle fibers, a feature typically present in mitochondria enrolled in degeneration (Figure 4H, J and I).

Next, we investigated whether the BACHD muscle atrophy could be associated to changes in Myosin Heavy Chain (MyHC)- isoforms expression. To evaluate this, we used immunostaining for different fiber types through specific monoclonal antibodies against various MyHC- isoforms. The top panel represents staining for type I (Figure 4C), type IIA (Figure 4C'), type IIX (Figure 4C'') and type IIB (Figure 4C''') isoforms of muscle fibers from WT animals. The bottom panel shows the same staining but in this case for muscle fibers from BACHD animals (Figure 4D'-D'''). Quantitative analysis from individual animals showed a statistically significant decrease in the number of type IIB fibers (BACHD: 35.4 ± 5.1 %; WT: 46.8 ± 4.0 % (mean ± SD); T_6= 3.4; *p<0.01) and an increase in the number of type IIX muscle fibers (BACHD: 48.3 ± 8.3 %; WT: 32.5

11

527 ± 5.9 % (mean ± SD); T_4= 3.0; *p<0.02) in BACHD TA muscles (Figure 4L). Figure
528 4M shows that muscle fibers positive for type IIX and IIB isoforms presented a
529 decrease in fiber size (IIX: BACHD: 381.5 ± 171.9 μm^2; WT: 414.5 ± 173.3 μm^2
530 (mean ± SD); T_{61}= 2.3; *p<0.03) (IIB: BACHD: 634.3 ± 238.6 μm^2; WT: 672.3 ±
531 243.7 μm^2 (mean ± SD); T_{70}= 2.0; *p<0.03).

Impaired motor behavior in BACHD mice

533   Based on the nerve-muscle alterations described above, we examined if
534 BACHD mice indeed showed motor impairment. To assess motor performance,
535 mice from both genotypes were subjected to the following tests: paw print, wire
536 hanging, grip strength, and open field. Regarding the paw print test data we did
537 not find significant differences between WT and BACHD for any of the evaluated
538 standards: step length, step width and right / left pass (5A-D). In the open field
539 test, BACHD mice showed a significant decrease in exploratory behavior. For
540 example, the average distance traveled by BACHD mice was significantly shorter
541 than the distance traveled by the WT mice (BACHD: 5216 ± 481.8 cm; WT: 7647±
542 863.8 cm (mean ± SD); T_{26}= 2.6; p<0.01) (Figure 5A). In addition, the BACHD
543 mice scored worse than WT regarding the mean velocity traveled (BACHD: 4.2 ±
544 0.30 cm/s; WT: 6.2 ± 0.71 cm/s (mean ± SD); T_{26}= 2.9; p<0.003) (Figure 5B). The
545 wire hanging task revealed that BACHD mice presented more difficulty in
546 sustaining their weight while most WT mice kept hold of the grid over the entire
547 duration of the test (60 seconds) (BACHD: 0.4 ± 0.09 s; WT: 1.4 ± 0.09 s (mean
548 ± SD); T_{27}= 7.2; p<0.0001) (Figure 5C). However, we did not observe significant
549 differences in the grip strength test between the two genotypes BACHD and WT
550 mice (i.e., test to compare max strength) (Figure 5D).

Discussion

552   Although HD is mostly described as a neurological disorder, there is
553 growing evidence that a peripheral pathology participates in disease progression
554 (Ribchester et al., 2004; Van der burg et al., 2009; Mielcarek et al., 2015). Indeed,
555 HTT is normally expressed at high levels in a wide variety of mammalian tissues
556 (Li et al., 1993) and pathological aggregates of high molecular weight HTT have
557 been found in many non-central nervous system tissues including skeletal muscle
558 (Moffit et al., 2009). Recently, we have showed that MUs of a neck muscle (STM)
559 from BACHD mice presented morphological alterations in all its components i.e.,
560 motoneurons, axons, NMJs, and muscle fibers (Valadão et al., 2017).
561 Nevertheless, the connection between HD and the progressive disruption of
562 communication between motoneurons and skeletal muscles remains poorly
563 explored. Thus, in the present study, we investigated whether similar changes
564 were also present in MUs of the hind limb muscles such as the TA, which is
565 controlled by lumbar spinal cord segments and afflicted by many degenerative
566 disorders, including HD.

567   Previous works from other groups reported changes in NMJs and muscles
568 in R6/2 mouse model for HD that could be related to motoneurons degeneration
569 (Ribchester et al., 2004; Mielcarek and Isalan, 2015; Khedraki et al., 2017).
570 However, these authors did not look at the spinal cords to address whether
571 motoneurons were indeed affected in R6/2 mice. In our previous work using the
572 BACHD mouse model for HD, we examined this hypothesis. We observed that
573 CHAT-positive neurons from BACHD cervical spinal cord segments were

12

574 significantly fewer (~20%) and smaller in size than those in WT mice (Valadão et
575 al., 2017). In the current work, we showed, in another segment of the spinal cord
576 (Lumbar, L1-L5), that ChAT-positive neurons from BACHD lumbar segments
577 were also fewer (motoneurons number) and smaller (cell soma diameter)
578 compared to WT mice. Comparatively, these results show similar pathological
579 changes among cervical and lumbar spinal cord segments in BACHD mice of the
580 same age, suggesting that both spinal cord segments (cervical and lumbar)
581 undergo the same degree of impairment.

582 As in the cervical spinal cord segments (Valadão et al., 2017), here we
583 observed that BACHD lumbar spinal cords present approximately three times
584 more motoneurons positive for caspase-3 when compared to equivalent WT
585 spinal segments. Although it is not completely clear whether the neuronal death
586 seen in HD is due solely to apoptotic process, several lines of evidence indicate
587 that the activation of specific pathways can lead to neuronal death (Hickey and
588 Chesselet, 2003). In fact, Gervais et al., (2002), demonstrated that one of the
589 neuronal death pathways in HD occurs through the interaction of mHTT with
590 specific molecules that activate caspase-8, which in turns lead to mitochondrial
591 alterations with consequent activation of caspase-3, culminating in cell death by
592 apoptosis.

593 The qualitative analysis of electron micrographs of putative motoneurons
594 (large ventral horn neurons) from BACHD animals presented herein revealed
595 mitochondria with changes such as destruction of mitochondrial cristae and
596 vacuoles. These subcellular changes were similar to those identified in BACHD
597 cervical motoneurons (Valadão et al., 2017). In addition, we observed lipofuscin
598 granules in both lumbar genotypes WT and BACHD. However, this observation
599 was different from the cervical segments where we detected almost three times
600 more lipofuscin granules in BACHD compared to WT (Valadão et al., 2017).
601 Studies using TEM to evaluate damages in the brain of HD patients have pointed
602 out morphological alterations such as mitochondria with damaged cristae,
603 occasionally containing crystalline fibrillar structures within the matrix and
604 increase in lipofuscin granules (Tellez-Nagel et al., 1974; Goebel et al., 1978).
605 Moreover, it has been shown that the relationship of mHTT with mitochondrial
606 components leads to changes in its structure (Bossy-Wetzel et al., 2008; Song et
607 al., 2011; Shirendeb et al., 2012).

608 Although we observed a decrease in the number of motoneurons,
609 interestingly, the number of axons is not altered in BACHD animals. However, we
610 have shown changes in both the axon and axoplasm diameter, which leads us to
611 believe that these changes might be an earlier step in the process of total axonal
612 degeneration.

613 Our results also showed changes in the NMJs of TA muscles at 12 months
614 old in the BACHD animals. In this muscle, we identified a significant decrease in
615 presynaptic element area, but not in the postsynaptic element, which may be
616 explained by an initial denervation process, since we also observed locations
617 where there was a lack of overlap between the pre-synaptic terminal and nAChR.

618 Furthermore, we identified significant fragmentation of NMJs of BACHD
619 animals but little in control animals. Although recent data show that the age-
620 fragmentation process is not directly related to function (Willadt et al., 2016), we

13

621 believe that our data may indicate that structural changes such as fragmentation
622 are due to the genotype and not just related to age because the animals
623 evaluated were of the same age. It is known that mHTT interacts with
624 cytoskeletal synaptic vesicles proteins that are essential for the structure of NMJs
625 and for exocytosis and endocytosis of synaptic vesicles at the nerve terminals (Li
626 and Li, 2004; see review by Zuccato et al., 2010). Except for postsynaptic area
627 size, which was not statistically different for the TA muscle, all these
628 morphological changes were also observed in NMJs of STM muscle from 12
629 months old BACHD animals. This comparison is useful because we are dealing
630 with NMJs of two distinctive muscle groups that are affected differently in animals
631 of the same age in the BACHD murine model for HD.

632 We do not observe changes in the number of axons in the sciatic nerve,
633 despite the significant changes in the axons diameter. This result seems contrary
634 to the loss of motoneurons (~20%) observed in the lumbar segments of the
635 BACHD mice. There are several plausible explanations for this difference. It is
636 possible that axonal degeneration is a much slower process than the caspase
637 labeling observed at the spinal cord. This possibility finds support in the fact that
638 axons stay for much longer than motoneurons, a phenomenon previously
639 observed in ALS disease. Which it is consistent with the lower number of partial
640 denervation observed (10%). Another possibility is that the remaining
641 motoneurons, the caspase negative, are able to produce new branches, which
642 should travel within the nerve. These extra branches should account for a higher
643 number of axons at the sciatic nerve level. Since they are ramifications from the
644 main axonal branch, most of the new branches should be smaller in size. This is
645 consistent with the variability in axonal diameter observed in our sciatic nerve
646 analysis.

647 Another interesting finding is the change observed in skeletal muscle
648 fibers of the TA muscle from BACHD mice. First, we observed a decrease in CSA
649 in muscle fibers of BACHD animals suggesting muscle atrophy. A reduction in
650 the total number of fibers could also have contributed to muscle fiber atrophy in
651 the BACHD mouse. Indeed, it is well described that muscle atrophy is a common
652 factor in HD (Farrer and Meaney, 1985; Ribchester et al., 2004; Farrer, 2008).
653 Another point to be considered is the deleterious effects of mHTT in muscle fibers
654 of R6/2 mice (Sathasivam et al., 1999; Moffitt et al., 2009). The BACHD- STM
655 muscle also showed atrophy of muscle fibers (Valadão et al., 2017). However,
656 the atrophy seen in the BACHD- TA muscle was smaller compared to BACHD
657 STM muscle. However, the STM muscle has higher variability in fiber size mainly
658 because it has mixed features of contractility, consisting of fast and slow fibers.
659 In contrast, the TA muscle is a fast twitch muscle, usually presenting about 87%
660 of fast fiber type IIB muscle fibers (Bloemberg and Quadrilatero, 2012).

661 Previous studies revealed that muscle atrophy could be accompanied by
662 changes in expression of MyHC (Brown and Hasser, 1996; Carvalho et al., 2003;
663 Rice et al., 2005; Valadão et al., 2017b). Here, we show that the number of type
664 IIB muscle fibers was reduced in BACHD mice, indicating that the general atrophy
665 seen in this muscle relates to a change in MyHC isoform since in TA muscle type
666 IIB fibers are predominant (Bloemberg and Quadrilatero, 2012). These data are
667 in agreement with the work of Miranda et al., (2017)in which they showed the
668 same pattern of transition of the type of fiber in the TA muscle of animals R6 / 2,
669 however these authors did not investigate the protein expression of MyHC,

14

670 showing these changes only at the mRNA level through the qPCR technique.
671 Beside that, we had already identified changes in the expression pattern of MyHC
672 in the STM muscle with changes of type IIX muscle fibers was reduced in BACHD
673 mice (Valadão et al., 2017). Together, these results indicate that the atrophy seen
674 in both muscles was accompanied by alterations in the expression of MyHC,
675 differing only in the affected fast fiber type. The MyHC shift from Type IIB to IIX
676 seen in BACHD TA muscle might be explained by the observation that, in
677 denervated muscles, there is a change in the expression pattern of the faster
678 isoforms for the slower isoforms (d'Albis et al., 1995). We speculate that this fiber
679 type may be related to the NMJs denervation observed in the TA muscles from
680 BACHD mice. Data from the literature indicate that motoneurons and their NMJs
681 differ drastically in size, with biggest ones innervating fast muscle fibers with
682 largest NMJs (Burke et al., 1971; Mantilla et al., 2007). We hypothesize that the
683 changes in the motoneurons described herein, such as decrease in presynaptic
684 area and size of motoneurons in BACHD, cause a reduction in the number of IIB
685 muscle fibers in TA muscles from BACHD mice. However, we cannot rule out the
686 possibility that mHTT directly or indirectly alters muscle fiber type profile since
687 this has been described in R6/2 HD mice model and also in humans (Strand et
688 al., 2005; for a review see Zielonka et al., 2014). Further research will be needed
689 to clarify this matter.

690   Interestingly, we noted that the BACHD- TA muscles have greater
691 accumulation of glycogen in the inter-myofibrillar spaces and more mitochondrial
692 damage than the observed in STM muscles (Valadão et al., 2017). Moreover, in
693 the BACHD transgenic animals, the Z line did not follow a straight pattern as
694 observed in the control animals. Indeed, studies of denervated TA muscles of
695 transgenic rabbits also revealed Z-line misalignment and mitochondrial changes
696 (Ashley et al., 2007). In light of the information provided by these studies and
697 because we found greater changes in the mitochondria of BACHD TA muscles,
698 it is possible that these changes could be related to energy imbalance caused by
699 mitochondrial damage. However, it is important to mention that although the TEM
700 analysis revealing mitochondrial abnormalities is informative, caution should be
701 taken in the interpretation of the present data because our analysis was only
702 qualitative and not quantitative.

703   We evaluated the motor function of BACHD and WT mice to verify the
704 possible relationship between the morphological changes observed in TA MUs
705 and the alterations in motor behavior of BACHD animals. In the catwalk test, we
706 did not detect statiscally significant differences between WT and BACHD mice in
707 any of the gait patterns evaluated: step length, step width and right / left pass.
708 Interestingly, our results are in accordance with the data of Mantovani et al.,
709 (2016), who showed no significant differences in walking test between BACHD
710 animals and controls at 12 months old, even using another measuring device
711 [Noldus® Cat Walk apparatus (Wageningen, The Netherlands)]. These
712 observations may be related to the fact that the mice are quadruped animals,
713 which gives them greater stability. Interestingly, Menalled et al., 2009, using the
714 same method used by us, observed that 18-month-old BACHD mice presented
715 statistical differences as a larger extension and broader base. These changes
716 differ from the gait deficit found in humans, since the steps become shorter in
717 patients with HD (Koller and Trimble, 1985). However, even without presenting
718 significant changes in the gait, the 12-month-old BACHD mice showed a robust

15

phenotype in several behavioral tests that replicate and extend the published results to date (Gray et al., 2008, Mantovani et al., 2016, Menalled et al., 2009).

The open field test revealed significant hypoactivity of BACHD mice, with a significant reduction in locomotion, total distance traveled and mean velocity. However, the number of rearing events was not significantly different when compared to control mice. These findings are in accordance to the results reported by Menalled et al., (2009), that showed that at 7 months of age, BACHD mice presented locomotor hypoactivity. The same results (in 7 months old BACHD) were previously observed by Gray et al., (2008). In the wire hanging test, we observed that BACHD mice performed significantly worse than the WT mice, similar to what Heng et al. (2007) and Brooks et al., (2012) noticed in 12 months old Hdh (CAG) 150 mice. In the wire hanging test, we observed that BACHD mice performed worse than the WT mice even after normalizing the weight of the animals to the time they were kept holding to the apparatus. In sum, the results obtained showed that the BACHD mice has major motor alterations, which directly influence their behavior.

The grip strength test did not show significant changes in the maximum strength between BACHD and WT mice. Menalled et al. (2009) observed that mice containing only a fragment of mutant HTT (R6/2) showed deficits in the same motor test. However, animals expressing the full-length mHTT, including BACHD, showed no significant differences in grip strength test. Accordingly, Mantovani et al., (2016) showed that BACHD animals generated in a C57BL/6J background (12 months old) did not present deficits in grip strength test, which corroborate our results. It is also possible that the deficiencies in movement and balance observed are due to aberrant connectivity or function in motor systems of the brain, rather than brain stem or spinal motor neurons. Besides that, this test are also open to interpretation as motivational rather than NMJ/muscle physiological. Therefore, the case for NMJ involvement in MN/muscle atrophy would be better made from isometric force measurements and intracellular measurements of synaptic function.

Although the findings described herein are suggestive of axonal or NMJ morphological differences in the BACHD mouse model, future research involving corroborative nerve conduction measurements, muscle/motor unit tension data, or electrophysiological analysis of NMJ function are necessary to establish whether the abnormalities described at NMJs are biologically significant, or whether they are primary consequences of CAG repeat expression or a secondary change in response to, for example, muscle atrophy.

In summary, here we show that that motoneurons from BACHD lumbar spinal cord are atrophic, reduced in size, and undergo apoptosis. The MUs associated with the TA muscle from BACHD mice presents signs of degeneration such as sciatic nerve reduced axon and axoplasm diameters, neuromuscular junctions' fragmentation and partial denervation, skeletal muscle fibers atrophy, and fiber type switching (Type 2B to Type 2X). Moreover, the present study provides evidence that different MUs have similar degrees of impairment in this animal model for HD. That is, regardless of innervation or muscle composition, it appears that mHTT may be performing the same degree of degeneration of these MUs investigated by us in the two studies. In addition, the changes seen in different spinal cord segments indicate that, although the disease may be Interestingly, our results are in accordance caused by neuronal death in the brain,

16

769 motoneurons at the lumbar spinal cord seems to be affected in HD, making room
770 for further studies to elucidate the molecular mechanisms underlying the
771 motoneuron cell death. Overall, our findings are important, and add further
772 support the hypothesis that cellular alterations occurring in peripheral tissues, in
773 this case skeletal muscles, occur independently of the progression of brain
774 dysfunction (Van der Burg et al., 2009). Thus, this work expands the perspectives
775 about the role of the MU in motor alterations seen in HD and the possibility that
776 clinical interventions targeting the MU could help treating signs of disease in
777 patients with Huntington's disease.
778

792 **Conflict of interest**
793
794 We declare no conflict of interest.
795

796 **References**
797 Ashley, Z., Salmons, S., Boncompagni, S., Protasi, F., Russold, M., Lanmuller,
798   H., Mayr, W., Sutherland, H., Jarvis, J.C., 2007. Effects of chronic electrical
799   stimulation on long-term denervated muscles of the rabbit hind limb. J.
800   Muscle Res. Cell Motil. 28, 203–217. https://doi.org/10.1007/s10974-007-
801   9119-4
802 Bilney, B., Morris, M.E., Churchyard, A., Chiu, E., Georgiou-Karistianis, N.,
803   2005. Evidence for a disorder of locomotor timing in Huntington's disease.
804   Mov. Disord. 20, 51–57. https://doi.org/10.1002/mds.20294
805 Bloemberg, D., Quadrilatero, J., 2012. Rapid determination of myosin heavy
806   chain expression in rat, mouse, and human skeletal muscle using
807   multicolor immunofluorescence analysis. PLoS One 7, e35273.
808   https://doi.org/10.1371/journal.pone.0035273
809 Bossy-Wetzel, E., Petrilli, A., Knott, A.B., 2008. Mutant huntingtin and
810   mitochondrial dysfunction. Trends Neurosci. 31, 609–616.
811   https://doi.org/10.1016/j.tins.2008.09.004
812 Brooks, S., Higgs, G., Jones, L., Dunnett, S.B., 2012. Longitudinal analysis of
813   the behavioural phenotype in Hdh(CAG)150 Huntington's disease knock-in
814   mice. Brain Res. Bull. 88, 182–188.
815   https://doi.org/10.1016/j.brainresbull.2010.05.004
816 Brown, M., Hasser, E.M., 1996. Complexity of age-related change in skeletal
817   muscle. J. Gerontol. A. Biol. Sci. Med. Sci. 51, B117-23.
818   https://doi.org/10.1093/gerona/51a.2.b117

17

819   Burke, R.E., Levine, D.N., Zajac, F.E., 1971. Mammalian motor units:
820   physiological-histochemical correlation in three types in cat gastrocnemius.
821   Science 174, 709–12.
822   Busse, M.E., Khalil, H., Quinn, L., Rosser, A.E., 2008. Physical Therapy
823   Intervention for People With Huntington Disease. Phys. Ther. 88, 820–831.
824   https://doi.org/10.2522/ptj.20070346
825   Carroll, J.B., Bates, G.P., Steffan, J., Saft, C., Tabrizi, S.J., 2015. Treating the
826   whole body in Huntington's disease. Lancet Neurol. 14, 1135–1142.
827   https://doi.org/10.1016/S1474-4422(15)00177-5
828   Carvalho, R.F., Cicogna, A.C., Campos, G.E.R., De Assis, J.M.F., Padovani,
829   C.R., Okoshi, M.P., Pai-Silva, M.D., 2003. Myosin heavy chain expression
830   and atrophy in rat skeletal muscle during transition from cardiac
831   hypertrophy to heart failure. Int. J. Exp. Pathol. 84, 201–206.
832   https://doi.org/10.1046/j.1365-2613.2003.00351.x
833   Chau, W.K., So, K.-F., Tay, D., Dockery, P., 2000. A morphometric study of
834   optic axons regenerated in a sciatic nerve graft of adult rats. Restor.
835   Neurol. Neurosci. 16, 105–116.
836   Cruickshank, T., Reyes, A., Peñailillo, L., Thompson, J., Ziman, M., 2014.
837   Factors that contribute to balance and mobility impairments in individuals
838   with Huntington's disease. Basal Ganglia 4, 67–70.
839   https://doi.org/10.1016/j.baga.2014.04.002
840   Cruickshank, T.M., Thompson, J.A., Domínguez D, J.F., Reyes, A.P., Bynevelt,
841   M., Georgiou-Karistianis, N., Barker, R.A., Ziman, M.R., 2015. The effect of
842   multidisciplinary rehabilitation on brain structure and cognition in
843   Huntington's disease: an exploratory study. Brain Behav. 5, e00312.
844   https://doi.org/10.1002/brb3.312
845   d'Albis, A., Couteaux, R., Goubel, F., Janmot, C., Mira, J.C., 1995. Relationship
846   between muscle myosin isoforms and contractile features in rabbit fast-
847   twitch denervated muscle. FEBS Lett. 375, 67–8.
848
849   Eisen, A., Kim, S., Pant, B., 1992. Amyotrophic lateral sclerosis (ALS): A
850   phylogenetic disease of the corticomotoneuron? Muscle Nerve 15, 219–
851   224. https://doi.org/10.1002/mus.880150215
852   Farrer, L.A., 2008. Diabetes mellitus in Huntington disease. Clin. Genet. 27, 62–
853   67. https://doi.org/10.1111/j.1399-0004.1985.tb00185.x
854   Farrer, L.A., Meaney, F.J., 1985. An anthropometric assessment of
855   Huntington's disease patients and families. Am. J. Phys. Anthropol. 67,
856   185–194. https://doi.org/10.1002/ajpa.1330670304
857   Fischer, L. R., Culver, D. G., Tennant, P., Davis, A. A., Wang, M., Castellano-
858   Sanchez, A., ... & Glass, J. D., 2004. Amyotrophic lateral sclerosis is a
859   distal axonopathy: evidence in mice and man. Experimental neurology,
860   185(2), 232-240.
861   Fowler, S.C., Zarcone, T.J., Chen, R., Taylor, M.D., Wright, D.E., n.d. Low grip
862   strength, impaired tongue force and hyperactivity induced by
863   overexpression of neurotrophin-3 in mouse skeletal muscle. Int. J. Dev.
864   Neurosci. 20, 303–8.
865   Gervais, F.G., Singaraja, R., Xanthoudakis, S., Gutekunst, C.-A., Leavitt, B.R.,
866   Metzler, M., Hackam, A.S., Tam, J., Vaillancourt, J.P., Houtzager, V.,
867   Rasper, D.M., Roy, S., Hayden, M.R., Nicholson, D.W., 2002. Recruitment
868   and activation of caspase-8 by the Huntingtin-interacting protein Hip-1 and

18

869 a novel partner Hippi. Nat. Cell Biol. 4, 95–105.
870 https://doi.org/10.1038/ncb735
871 Goebel, H.H., Heipertz, R., Scholz, W., Iqbal, K., Tellez-Nagel, I., 1978.
872 Juvenile Huntington chorea: clinical, ultrastructural, and biochemical
873 studies. Neurology 28, 23–31.
874 Gray, M., Shirasaki, D., Cepeda, C., … V.A.-J. of, 2008, undefined, n.d. Full-
875 length human mutant huntingtin with a stable polyglutamine repeat can
876 elicit progressive and selective neuropathogenesis in BACHD mice. Soc
877 Neurosci.
878 Gray, M., Shirasaki, D.I., Cepeda, C., Andre, V.M., Wilburn, B., Lu, X.-H., Tao,
879 J., Yamazaki, I., Li, S.-H., Sun, Y.E., Li, X.-J., Levine, M.S., Yang, X.W.,
880 2008. Full-Length Human Mutant Huntingtin with a Stable Polyglutamine
881 Repeat Can Elicit Progressive and Selective Neuropathogenesis in BACHD
882 Mice. J. Neurosci. 28, 6182–6195.
883 https://doi.org/10.1523/JNEUROSCI.0857-08.2008
884 Heng, M.Y., Detloff, P.J., Albin, R.L., 2008. Rodent genetic models of
885 Huntington disease. Neurobiol. Dis. 32, 1–9.
886 https://doi.org/10.1016/j.nbd.2008.06.005
887 Heng, M.Y., Tallaksen-Greene, S.J., Detloff, P.J., Albin, R.L., 2007. Longitudinal
888 Evaluation of the Hdh(CAG)150 Knock-In Murine Model of Huntington's
889 Disease. J. Neurosci. 27, 8989–8998.
890 https://doi.org/10.1523/JNEUROSCI.1830-07.2007
891 Hickey, M.A., Chesselet, M.-F., 2003. Apoptosis in Huntington's disease. Prog.
892 Neuro-Psychopharmacology Biol. Psychiatry 27, 255–265.
893 https://doi.org/10.1016/S0278-5846(03)00021-6
894 Joviano-Santos, J.V., Santos-Miranda, A., Botelho, A.F.M., de Jesus, I.C.G.,
895 Andrade, J.N., de Oliveira Barreto, T., Magalhães-Gomes, M.P.S.,
896 Valadão, P.A.C., Cruz, J. dos S., Melo, M.M., Guatimosim, S., Guatimosim,
897 C., 2019. Increased oxidative stress and CaMKII activity contribute to
898 electro-mechanical defects in cardiomyocytes from a murine model of
899 Huntington's disease. FEBS J. 286, 110–123.
900 https://doi.org/10.1111/febs.14706
901 Kazantsev, A., … E.P.-P. of the, 1999, undefined, n.d. Insoluble detergent-
902 resistant aggregates form between pathological and nonpathological
903 lengths of polyglutamine in mammalian cells. Natl. Acad Sci.
904 Khedraki, A., Reed, E., Romer, S., … Q.W.-J. of, 2017, undefined, n.d.
905 Depressed Synaptic Transmission and Reduced Vesicle Release Sites in
906 Huntington's Disease Neuromuscular Junctions. Soc Neurosci.
907 Koller, W.C., Trimble, J., 1985. The gait abnormality of Huntington's disease.
908 Neurology 35, 1450–4. https://doi.org/10.1212/wnl.35.10.1450
909 Lagrán, M. de, Altafaj, X., Gallego, X., … E.M.-N. of, 2004, undefined, n.d.
910 Motor phenotypic alterations in TgDyrk1a transgenic mice implicate
911 DYRK1A in Down syndrome motor dysfunction. Elsevier.
912 Li, S.-H., Li, X.-J., 2004. Huntingtin–protein interactions and the pathogenesis of
913 Huntington's disease. Trends Genet. 20, 146–154.
914 https://doi.org/10.1016/j.tig.2004.01.008
915 Mantilla, C.B., Rowley, K.L., Zhan, W.-Z., Fahim, M.A., Sieck, G.C., 2007.
916 Synaptic vesicle pools at diaphragm neuromuscular junctions vary with
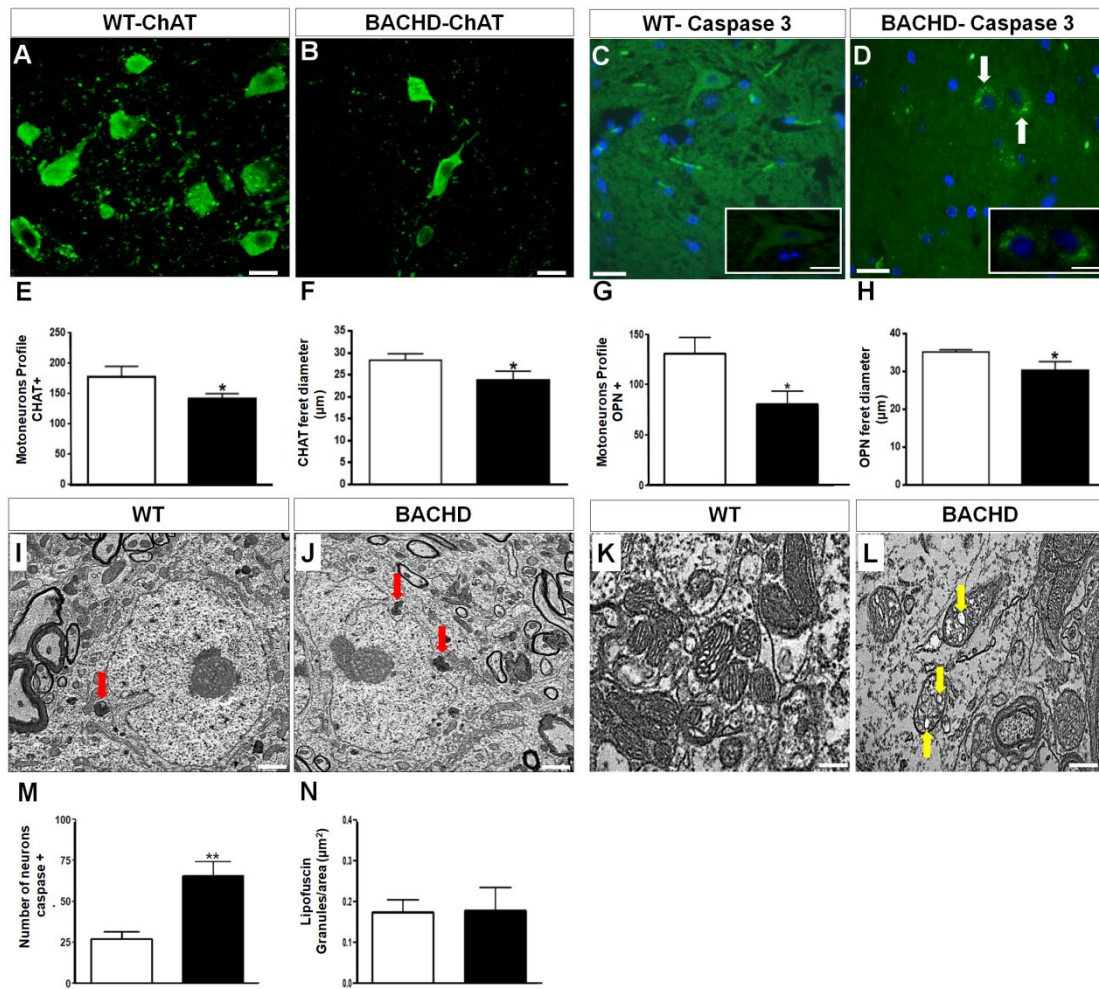917 motoneuron soma, not axon terminal, inactivity. Neuroscience 146, 178–
918 189. https://doi.org/10.1016/j.neuroscience.2007.01.048

19

919   Mantovani, S., Gordon, R., Li, R., Christie, D.C., Kumar, V., Woodruff, T.M.,
920   2016. Motor deficits associated with Huntington's disease occur in the
921   absence of striatal degeneration in BACHD transgenic mice. Hum. Mol.
922   Genet. 25, 1780–1791. https://doi.org/10.1093/hmg/ddw050
923   Menalled, L., El-Khodor, B.F., Patry, M., Suárez-Fariñas, M., Orenstein, S.J.,
924   Zahasky, B., Leahy, C., Wheeler, V., Yang, X.W., MacDonald, M., Morton,
925   A.J., Bates, G., Leeds, J., Park, L., Howland, D., Signer, E., Tobin, A.,
926   Brunner, D., 2009. Systematic behavioral evaluation of Huntington's
927   disease transgenic and knock-in mouse models. Neurobiol. Dis. 35, 319–
928   336. https://doi.org/10.1016/j.nbd.2009.05.007
929   Menalled, L.B., Chesselet, M.-F., 2002. Mouse models of Huntington's disease.
930   Trends Pharmacol. Sci. 23, 32–9.
931   Mielcarek, M., Isalan, M., 2015. A shared mechanism of muscle wasting in
932   cancer and Huntington's disease. Clin. Transl. Med. 4, 34.
933   https://doi.org/10.1186/s40169-015-0076-z
934   Miranda, D.R., Wong, M., Romer, S.H., McKee, C., Garza-Vasquez, G.,
935   Medina, A.C., Bahn, V., Steele, A.D., Talmadge, R.J., Voss, A.A., 2017.
936   Progressive Cl⁻ channel defects reveal disrupted skeletal muscle
937   maturation in R6/2 Huntington's mice. J. Gen. Physiol. 149, 55–74.
938   https://doi.org/10.1085/jgp.201611603
939   Moffitt, H., McPhail, G.D., Woodman, B., Hobbs, C., Bates, G.P., 2009.
940   Formation of Polyglutamine Inclusions in a Wide Range of Non-CNS
941   Tissues in the HdhQ150 Knock-In Mouse Model of Huntington's Disease.
942   PLoS One 4, e8025. https://doi.org/10.1371/journal.pone.0008025
943   Novak, M.J.U., Tabrizi, S.J., 2010. Huntington's disease. BMJ 340, c3109–
944   c3109. https://doi.org/10.1136/bmj.c3109
945   Pereira, L.M., Bastos, C.P., de Souza, J.M., Ribeiro, F.M., Pereira, G.S., 2014.
946   Estradiol enhances object recognition memory in Swiss female mice by
947   activating hippocampal estrogen receptor α. Neurobiol. Learn. Mem. 114,
948   1–9. https://doi.org/10.1016/j.nlm.2014.04.001
949   Piira, A., van Walsem, M.R., Mikalsen, G., Nilsen, K.H., Knutsen, S., Frich, J.C.,
950   2013. Effects of a One Year Intensive Multidisciplinary Rehabilitation
951   Program for Patients with Huntington's Disease: a Prospective Intervention
952   Study. PLoS Curr. 5.
953   https://doi.org/10.1371/currents.hd.9504af71e0d1f87830c25c394be47027
954   Prado, V.F., Martins-Silva, C., de Castro, B.M., Lima, R.F., Barros, D.M.,
955   Amaral, E., Ramsey, A.J., Sotnikova, T.D., Ramirez, M.R., Kim, H.-G.,
956   Rossato, J.I., Koenen, J., Quan, H., Cota, V.R., Moraes, M.F.D., Gomez,
957   M. V., Guatimosim, C., Wetsel, W.C., Kushmerick, C., Pereira, G.S.,
958   Gainetdinov, R.R., Izquierdo, I., Caron, M.G., Prado, M.A.M., 2006. Mice
959   Deficient for the Vesicular Acetylcholine Transporter Are Myasthenic and
960   Have Deficits in Object and Social Recognition. Neuron 51, 601–612.
961   https://doi.org/10.1016/j.neuron.2006.08.005
962   Pratt, S.J.P., Shah, S.B., Ward, C.W., Inacio, M.P., Stains, J.P., Lovering, R.M.,
963   2013. Effects of *in vivo* injury on the neuromuscular junction in healthy and
964   dystrophic muscles. J. Physiol. 591, 559–570.
965   https://doi.org/10.1113/jphysiol.2012.241679
966   Reiner, A., Albin, R.L., Anderson, K.D., D 'amato, C.J., Penneyt, J.B., Youngt,
967   A.B., 1988. Differential loss of striatal projection neurons in Huntington
968   disease. Neurobiology 85, 5733–5737.

https://doi.org/10.1073/pnas.85.15.5733

Reinius, B., Blunder, M., Brett, F.M., Eriksson, A., Patra, K., Jonsson, J., Jazin, E., Kullander, K., 2015. Conditional targeting of medium spiny neurons in the striatal matrix. Front. Behav. Neurosci. 9, 71. https://doi.org/10.3389/fnbeh.2015.00071

Ribchester, R.R., Thomson, D., Wood, N.I., Hinks, T., Gillingwater, T.H., Wishart, T.M., Court, F.A., Morton, A.J., 2004. Progressive abnormalities in skeletal muscle and neuromuscular junctions of transgenic mice expressing the Huntington's disease mutation. Eur. J. Neurosci. 20, 3092–3114. https://doi.org/10.1111/j.1460-9568.2004.03783.x

Rice, K.M., Linderman, J.K., Kinnard, R.S., Blough, E.R., 2005. The Fischer 344/NNiaHSd X Brown Norway/BiNia is a Better Model of Sarcopenia than the Fischer 344/NNiaHSd: a Comparative Analysis of Muscle Mass and Contractile Properties in Aging Male Rat Models. Biogerontology 6, 335–343. https://doi.org/10.1007/s10522-005-4808-0

Rodrigues, H.A., Fonseca, M. de C., Camargo, W.L., Lima, P.M.A., Martinelli, P.M., Naves, L.A., Prado, V.F., Prado, M.A.M., Guatimosim, C., 2013. Reduced Expression of the Vesicular Acetylcholine Transporter and Neurotransmitter Content Affects Synaptic Vesicle Distribution and Shape in Mouse Neuromuscular Junction. PLoS One 8, e78342. https://doi.org/10.1371/journal.pone.0078342

Sango, K., McDonald, M.P., Crawley, J.N., Mack, M.L., Tifft, C.J., Skop, E., Starr, C.M., Hoffmann, A., Sandhoff, K., Suzuki, K., Proia, R.L., 1996. Mice lacking both subunits of lysosomal β–hexosaminidase display gangliosidosis and mucopolysaccharidosis. Nat. Genet. 14, 348–352. https://doi.org/10.1038/ng1196-348

Sathasivam, K., Hobbs, C., Mangiarini, L., Mahal, A., Turmaine, M., Doherty, P., Davies, S.W., Bates, G.P., 1999. Transgenic models of Huntington'sdisease. Philos. Trans. R. Soc. London B Biol. Sci. 354.

Shirendeb, U.P., Calkins, M.J., Manczak, M., Anekonda, V., Dufour, B., McBride, J.L., Mao, P., Reddy, P.H., 2012. Mutant huntingtin's interaction with mitochondrial protein Drp1 impairs mitochondrial biogenesis and causes defective axonal transport and synaptic degeneration in Huntington's disease. Hum. Mol. Genet. 21, 406–420. https://doi.org/10.1093/hmg/ddr475

Song, W., Chen, J., Petrilli, A., Liot, G., Klinglmayr, E., Zhou, Y., Poquiz, P., Tjong, J., Pouladi, M.A., Hayden, M.R., Masliah, E., Ellisman, M., Rouiller, I., Schwarzenbacher, R., Bossy, B., Perkins, G., Bossy-Wetzel, E., 2011. Mutant huntingtin binds the mitochondrial fission GTPase dynamin-related protein-1 and increases its enzymatic activity. Nat. Med. 17, 377–382. https://doi.org/10.1038/nm.2313

Strand, A.D., Aragaki, A.K., Shaw, D., Bird, T., Holton, J., Turner, C., Tapscott, S.J., Tabrizi, S.J., Schapira, A.H., Kooperberg, C., Olson, J.M., 2005. Gene expression in Huntington's disease skeletal muscle: a potential biomarker. Hum. Mol. Genet. 14, 1863–1876. https://doi.org/10.1093/hmg/ddi192

Tellez-Nagel, I., Johnson, A.B., Terry, R.D., 1974. Studies on brain biopsies of patients with Huntington's chorea. J. Neuropathol. Exp. Neurol. 33, 308–32.

Thaut, M.H., Miltner, R., Lange, H.W., Hurt, C.P., Hoemberg, V., 1999. Velocity modulation and rhythmic synchronization of gait in Huntington's disease. Mov. Disord. 14, 808–19.

21

1019 Valadão, P., Gomes, M., … B.A.-N., 2018, undefined, n.d. Neuromuscular
1020   synapse degeneration without muscle function loss in the diaphragm of a
1021   murine model for Huntington's Disease. Elsevier.
1022 Valadão, P.A.C., de Aragão, B.C., Andrade, J.N., Magalhães-Gomes, M.P.S.,
1023   Foureaux, G., Joviano-Santos, J.V., Nogueira, J.C., Ribeiro, F.M., Tapia,
1024   J.C., Guatimosim, C., 2017a. Muscle atrophy is associated with cervical
1025   spinal motoneuron loss in BACHD mouse model for Huntington's disease.
1026   Eur. J. Neurosci. 45, 785–796. https://doi.org/10.1111/ejn.13510
1027 Valadão, P.A.C., de Aragão, B.C., Andrade, J.N., Magalhães-Gomes, M.P.S.,
1028   Foureaux, G., Joviano-Santos, J.V., Nogueira, J.C., Ribeiro, F.M., Tapia,
1029   J.C., Guatimosim, C., 2017b. Muscle atrophy is associated with cervical
1030   spinal motoneuron loss in BACHD mouse model for Huntington's disease.
1031   Eur. J. Neurosci. 45, 785–796. https://doi.org/10.1111/ejn.13510
1032 Valdez, G., Tapia, J.C., Kang, H., Clemenson, G.D., Gage, F.H., Lichtman,
1033   J.W., Sanes, J.R., 2010. Attenuation of age-related changes in mouse
1034   neuromuscular synapses by caloric restriction and exercise. Proc. Natl.
1035   Acad. Sci. 107, 14863–14868. https://doi.org/10.1073/pnas.1002220107
1036 Valdez, G., Tapia, J.C., Lichtman, J.W., Fox, M.A., Sanes, J.R., 2012. Shared
1037   Resistance to Aging and ALS in Neuromuscular Junctions of Specific
1038   Muscles. PLoS One 7, e34640.
1039   https://doi.org/10.1371/journal.pone.0034640
1040 Van den Bos, M. A., Geevasinga, N., Higashihara, M., Menon, P., & Vucic, S.,
1041   2019. Pathophysiology and Diagnosis of ALS: Insights from Advances in
1042   Neurophysiological Techniques. International Journal of Molecular
1043   Sciences, 20(11), 2818.
1044 Van der Burg, J.M., Björkqvist, M., Brundin, P., 2009. Beyond the brain:
1045   widespread pathology in Huntington's disease. Lancet Neurol. 8, 765–774.
1046   https://doi.org/10.1016/S1474-4422(09)70178-4
1047 Wheelock, V.L., Tempkin, T., Marder, K., Nance, M., Myers, R.H., Zhao, H.,
1048   Kayson, E., Orme, C., Shoulson, I., Huntington Study Group, 2003.
1049   Predictors of nursing home placement in Huntington disease. Neurology
1050   60, 998–1001. https://doi.org/10.1212/01.wnl.0000052992.58107.67
1051 Willadt, S., Nash, M., Slater, C.R., 2016. Age-related fragmentation of the motor
1052   endplate is not associated with impaired neuromuscular transmission in the
1053   mouse diaphragm. Sci. Rep. 6, 24849. https://doi.org/10.1038/srep24849
1054 William Yang, X., Gray, M., 2011. Mouse Models for Validating Preclinical
1055   Candidates for Huntington's Disease, Neurobiology of Huntington's
1056   Disease: Applications to Drug Discovery. CRC Press/Taylor & Francis.
1057 Yang, X.W., Model, P., Heintz, N., 1997. Homologous recombination based
1058   modification in Esherichia coli and germline transmission in transgenic mice
1059   of a bacterial artificial chromsome. Nat. Biotechnol. 15, 859–865.
1060   https://doi.org/10.1038/nbt0997-859
1061 Yap, F., Bui, J., Knuttinen, M., … N.W.-D. and, 2013, undefined, n.d.
1062   Quantitative morphometric analysis of hepatocellular carcinoma:
1063   development of a programmed algorithm and preliminary application.
1064   researchgate.net.
1065 Zuccato, C., Valenza, M., Cattaneo, E., 2010. Molecular Mechanisms and
1066   Potential Therapeutical Targets in Huntington's Disease. Physiol. Rev. 90,
1067   905–981. https://doi.org/10.1152/physrev.00041.2009
1068

22

1069

1070

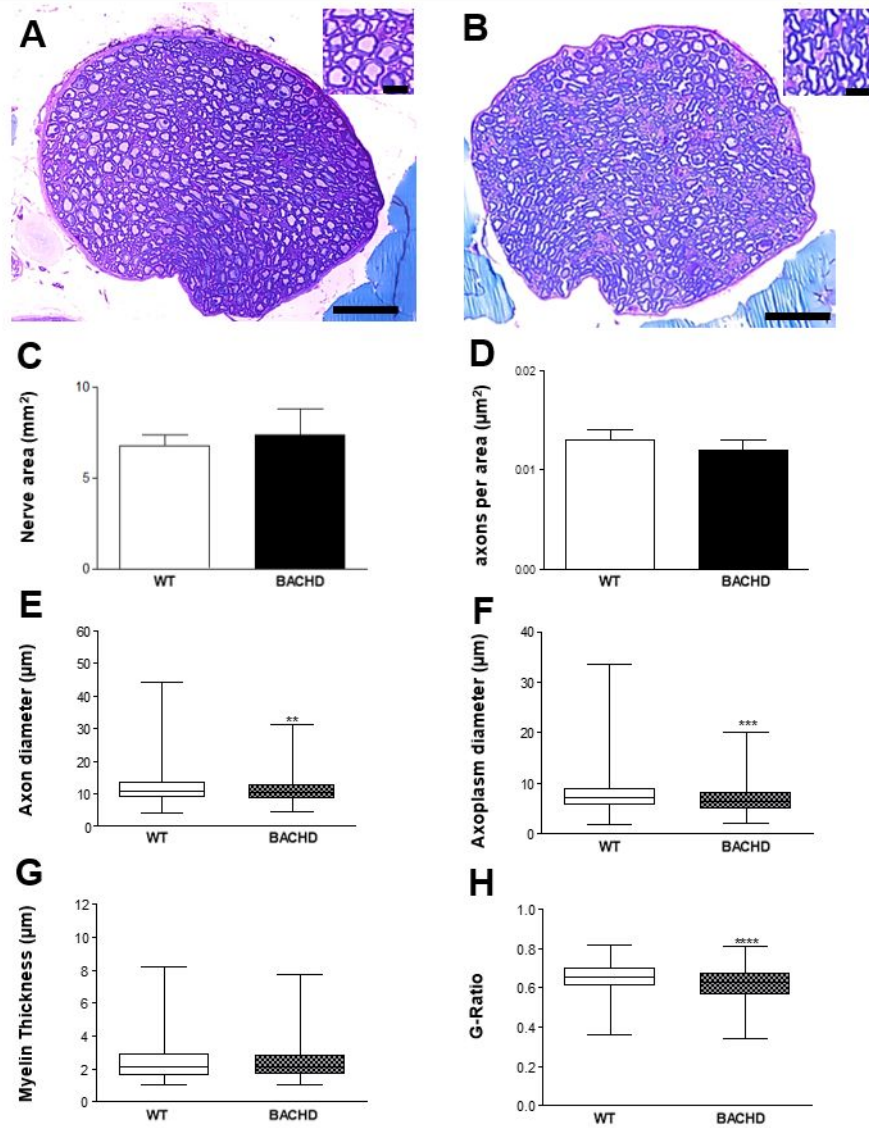Figure 1: Atrophy in BACHD lumbar motoneurons.

1071

1072

1073

1074

1075

23

Figure 2: BACHD mice present alterations in sciatic nerve morphology

1085

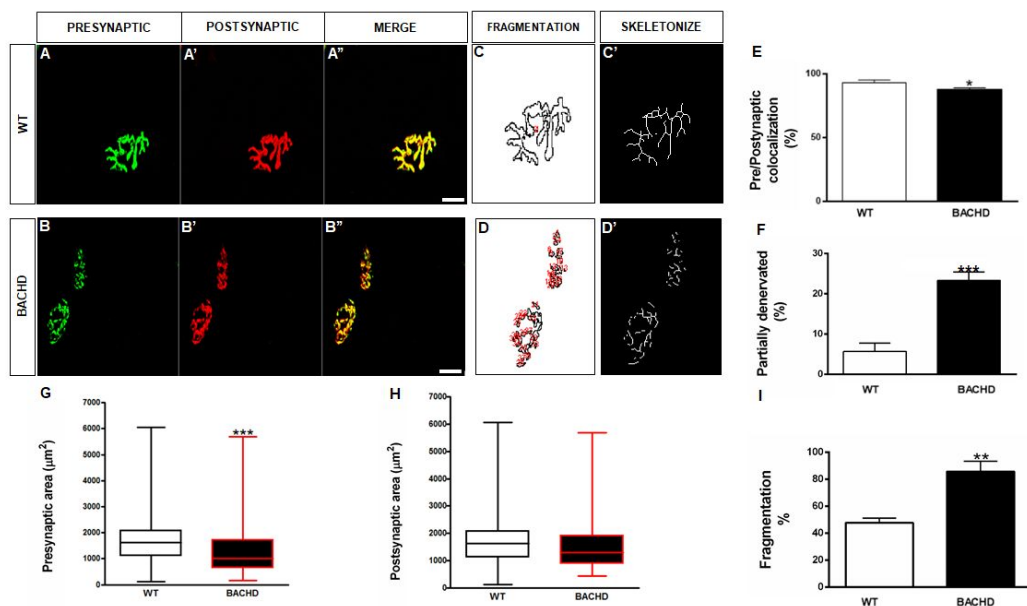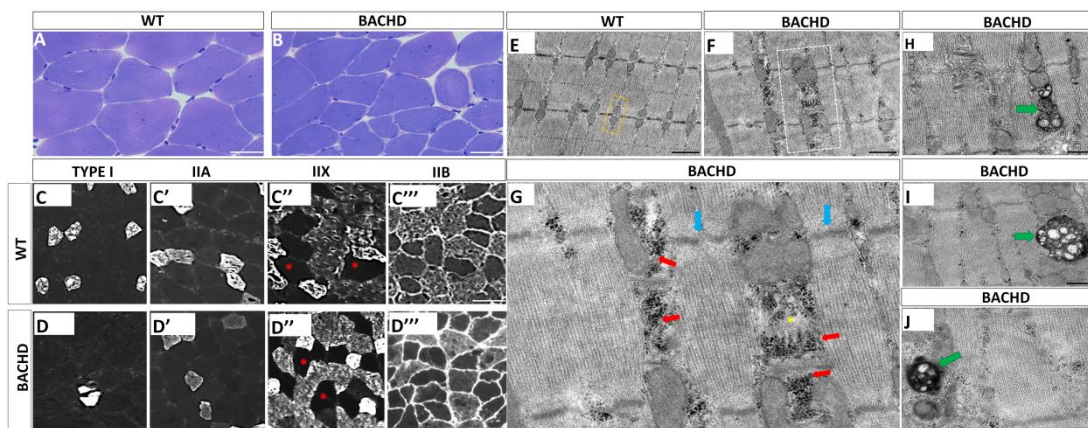

Figure 3: NMJs from TA muscles are partially denervated and fragmented in BACHD mice.
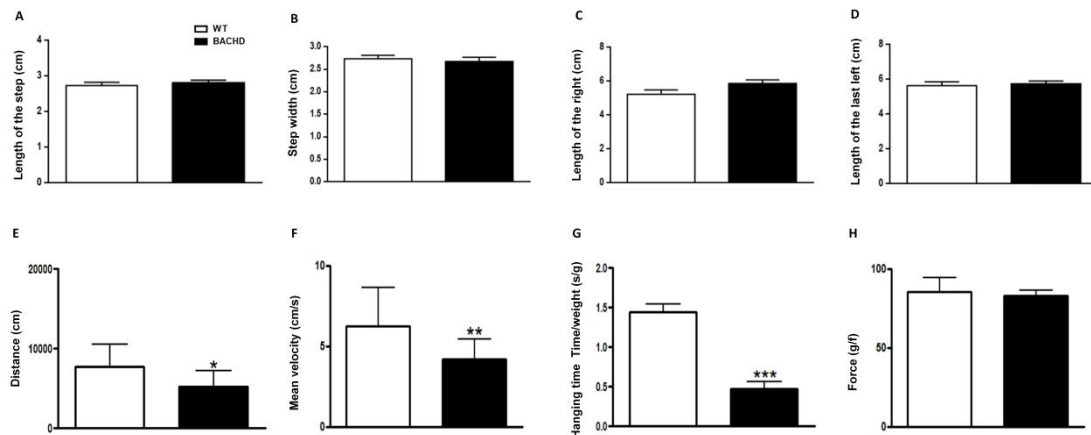
1086
1087
1088

1089

1090

1091

Figure 4: Muscle atrophy, muscle fiber switching and ultrastructural abnormalities in BACHD.

1092

1093
1094

1095

25

Figure 5: Motor behavior alterations in BACHD.

Figure Legends

Figure 1: Atrophy in BACHD lumbar motoneurons. A–B: Representative images of motoneurons from lumbar spinal cord sections stained with ChAT from 12 -months-old WT (A) and BACHD (B) animals. Scale bar: 50 µm. C-D: Fluorescence images of putative motoneurons stained with caspase-3 in WT (C) and BACHD (D- white arrows). Nuclei were stained with DAPI. Insert: putative motoneurons positive for caspase-3 in BACHD. Scale bar: 50 µm. E and G: Quantification of ChAT and OPN-positive motoneurons profiles in WT and BACHD lumbar spinal cords (~150 neurons analyzed per genotype). Feret diameter for CHAT (F) and for OPN (H) (unpaired student's t-test; *p < 0.05; n=3 animals per genotype). I–J: Ultrastructure images showing a motoneuron with more lipofuscin granules (red arrows) in BACHD (J) compared to WT (I). K-L: Representative images normal and vacuolated mitochondria in WT and BACHD, respectively. Scale bar: 500 nm. M: Graphical quantification of motoneurons stained positively for caspase-3 in WT and BACHD (~150 neurons analyzed per genotype; unpaired student's t-test; **p<0.002; *n*=3 animals per genotype. N: Quantification of the number of lipofuscin granules/area in WT and BACHD motoneurons (Total from 30 motoneurons per genotype; unpaired Student's t-test; p=0.4; *n*=3 animals per genotype). All results described here are from *n*=3 individual animals per genotype and were expressed as mean ± SD.

26

1
2
3   1127
4
5   1128   **Figure 2: BACHD mice present alterations in sciatic nerve morphology**. A-
6   1129   B: Representative images of transversal sections of the sciatic nerve from 12
7   1130   months old WT and BACHD mice, respectively. Note the difference between the
8   1131   size of the axons on inserts in A (WT) and B (BACHD). Scale bar: 10µm. C-H:
9   1132   Quantification of nerve area (C), number of axons per nerve area (D), axon's
10   1133   diameter (E)(**p<0.001; Mann-Whitney test), axoplasm diameter (***p<0.0001;
11   1134   Mann-Whitney test) (F); myelin thickness (G), G-ratio (G=d/D, where G is the G-
12   1135   ratio, d is the inner diameter, and D is the outer diameter) (****p<0.0001; Mann-
13   1136   Whitney test) (H). *n*=3 animals per group. We analyzed 2.874 axons in WT and
14   1137   2.573 in BACHD. Unpaired Student's t-test, p > 0.05 (C and D).
15
16   1138
17
18
19   1139   **Figure 3: NMJs from TA muscles are partially denervated and fragmented**
20   1140   **in BACHD mice**. A–B: Representative images of TA NMJs obtained from 12
21   1141   months old WT and BACHD mice. A and B: Presynaptic terminals labeled with
22   1142   an Alexa-488 anti-synaptotagmin antibody (green). A' and B': Postsynaptic
23   1143   AChRs labeled with Alexa-555 α-btx (red). A″ and B″: Merged images. Scale bar:
24   1144   50 µm. C and D: Representation of particle analysis for both genotypes (red
25   1145   numbers). C' and D': Skeletonization rendering of fragmentation in endplates
26   1146   from WT and BACHD. E–I: Graphs showing the degree of colocalization (E) (*p
27   1147   =0.02; unpaired Student's t-test); partial denervation (F) (***p < 0.0007 unpaired
28   1148   student t-test); pre-synaptic area (G) (***p < 0.0002; Mann-Whitney test); post-
29   1149   synaptic area (H) (p>0.05; Mann-Whitney test); and fragmentation of the
30   1150   endplates (I) (**p=0.001; unpaired student t-test). The results represent the mean
31   1151   ± SD from 50 NMJs per genotype. *n*=3 individual animals per genotype.
32
34   1152   **Figure 4: Muscle atrophy, muscle fiber switching and ultrastructural**
35   1153   **abnormalities in BACHD.** A–B: Representative images of TA skeletal muscle
36   1154   fibers from 12 months old WT and BACHD mice. Scale bar: 50 µm. C–C''' to D–
37   1155   D''': Representative images of TA fiber typing from 12 months old WT and
38   1156   BACHD mice. Scale bar: 50 µm. E–J: Representative electron micrographs of TA
39   1157   fibers from WT and BACHD animals. Observe a normal triad in WT (Figure E,
40   1158   yellow box). G: High magnification view of the area in F showing marked glycogen
41   1159   accumulation in the inter-myofibrillar spaces (red arrows), SR enlargement
42   1160   (yellow asterisk) and Z-line discontinuity (blue arrows) in BACHD animals. H-J:
43   1161   Observe profound mitochondrial changes (green arrows). Scale bar: 500 nm. We
44   1162   analyzed 90 images per genotype from six individual animals (three per
45   1163   genotype). K: Quantitative analysis shows the CSA mean values for WT and
46   1164   BACHD TA muscle fibers. These results represent the mean ± SD of more than
47   1165   4.000 muscle fibers per genotype (****p<0.0001; Mann-Whitney test); *n*=3
48   1166   animals per genotype). L: Quantitative analysis of the fiber typing showing
49   1167   decreased number of IIB isoform and increase of IIX in BACHD TA muscle fibers
50   1168   compared to WT (*p= 0.01 and *p=0.02; unpaired Student's t-test; *n*=3 animals
51   1169   per genotype). M: Quantitative analysis of the CSA from fiber typing (*p= 0.03;
52   1170   unpaired Student's t-test; *n*=3 animals per genotype). The results represent the
53   1171   mean ± SD (unpaired Student's t-test, *p<0.05; *n*=3 animals per genotype).
54
55   1172
56
57
58
59
60

27

1
2
3   1173   **Figure 5: Motor behavior alterations in BACHD.** A-D: Graphical quantification
4   1174   of pattern of gait of WT and BACHD mice. A: Length of the step (p=0.54; unpaired
5   1175   Student's t-test). B: Step width (p=0.51; unpaired Student's t-test). C: Length of
6   1176   the rigth(p=0.07; unpaired Student's t-test). D: Length of the left (p=0.70; unpaired
7   1177   Student's t-test). E:Graphical quantification of the total distance traveled by WT
8   1178   and BACHD mice, showing hypoactivity in transgenic animals (*p=0.01; unpaired
9   1179   Student's t-test). F: Graphical quantification of the average speed traveled by
10 1180   both genotypes with a decrease in BACHD animals (**p=0.003; unpaired
11 1181   Student's t-test). G: Graphical quantification of the total time the animals kept
12 1182   holding their own weight in the test apparatus (time/weigth = time corrected for
13 1183   weight) (***p=0.0001; unpaired Student's t-test) H: Maximum force quantification
14 1184   in the test of grip strength exerted by WT animals and BACHD when a constant
15 1185   and opposite force is applied (p=0.39; unpaired Student's t-test). The results
16 1186   express the mean ± SD from 11 WT and 17 BACHD animals.
17
18 1187
19
20 1188
21
22
23
24
25
26
27
28
29
30
31
32
33
34
35
36
37
38
39
40
41
42
43
44
45
46
47
48
49
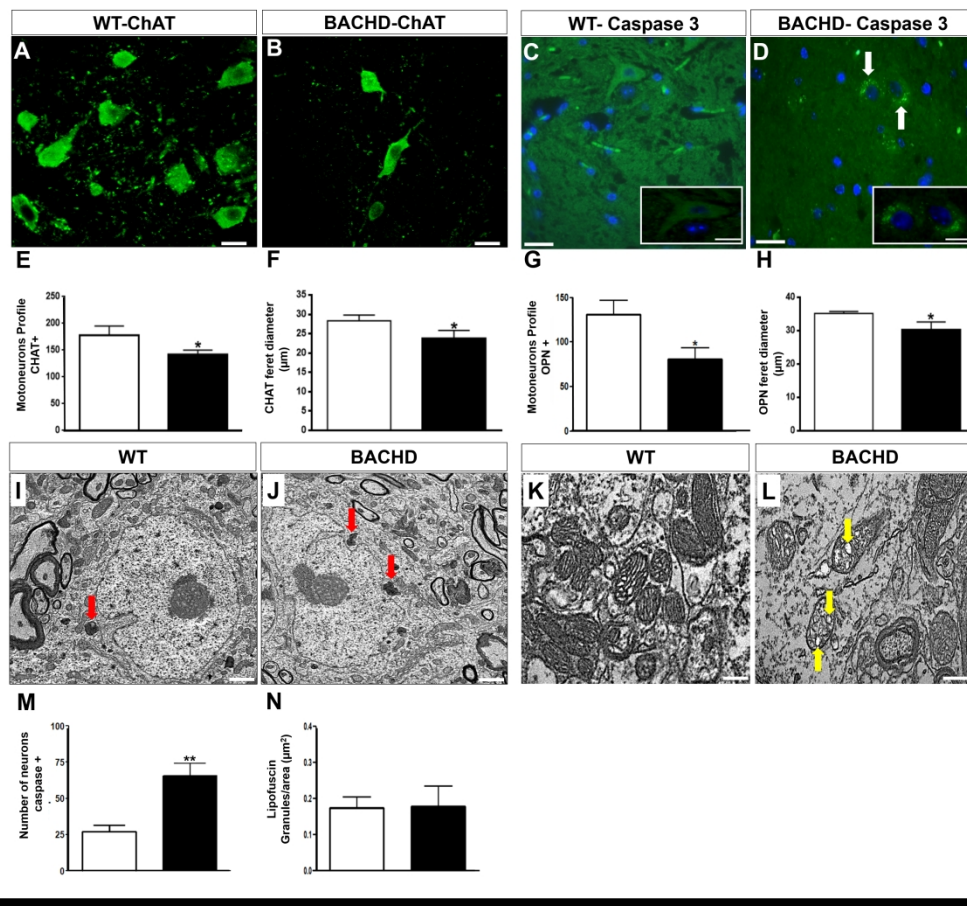50
51
52
53
54
55
56
57
58
59
60

28

Figure 1: Atrophy in BACHD lumbar motoneurons. A–B: Representative images of motoneurons from lumbar spinal cord sections stained with ChAT from 12 -months-old WT (A) and BACHD (B) animals. Scale bar: 50 μm. C-D: Fluorescence images of putative motoneurons stained with caspase-3 in WT (C) and BACHD (D- white arrows). Nuclei were stained with DAPI. Insert: putative motoneurons positive for caspase-3 in BACHD. Scale bar: 50 μm. E and G: Quantification of ChAT and OPN-positive motoneurons profiles in WT and BACHD lumbar spinal cords (~150 neurons analyzed per genotype). Feret diameter for CHAT (F) and for OPN (H) (unpaired student's t-test; *p < 0.05; n=3 animals per genotype). I–J: Ultrastructure images showing a motoneuron with more lipofuscin granules (red arrows) in BACHD (J) compared to WT (I). K-L: Representative images normal and vacuolated mitochondria in WT and BACHD, respectively. Scale bar: 500 nm. M: Graphical quantification of motoneurons stained positively for caspase-3 in WT and BACHD (~150 neurons analyzed per genotype; unpaired student's t-test; **p<0.002; n=3 animals per genotype. N: Quantification of the number of lipofuscin granules/area in WT and BACHD motoneurons (Total from 30 motoneurons per genotype; unpaired Student's t-test; p=0.4; n=3 animals per genotype). All results described here are from n=3 individual animals per genotype and were expressed as mean ± SD.
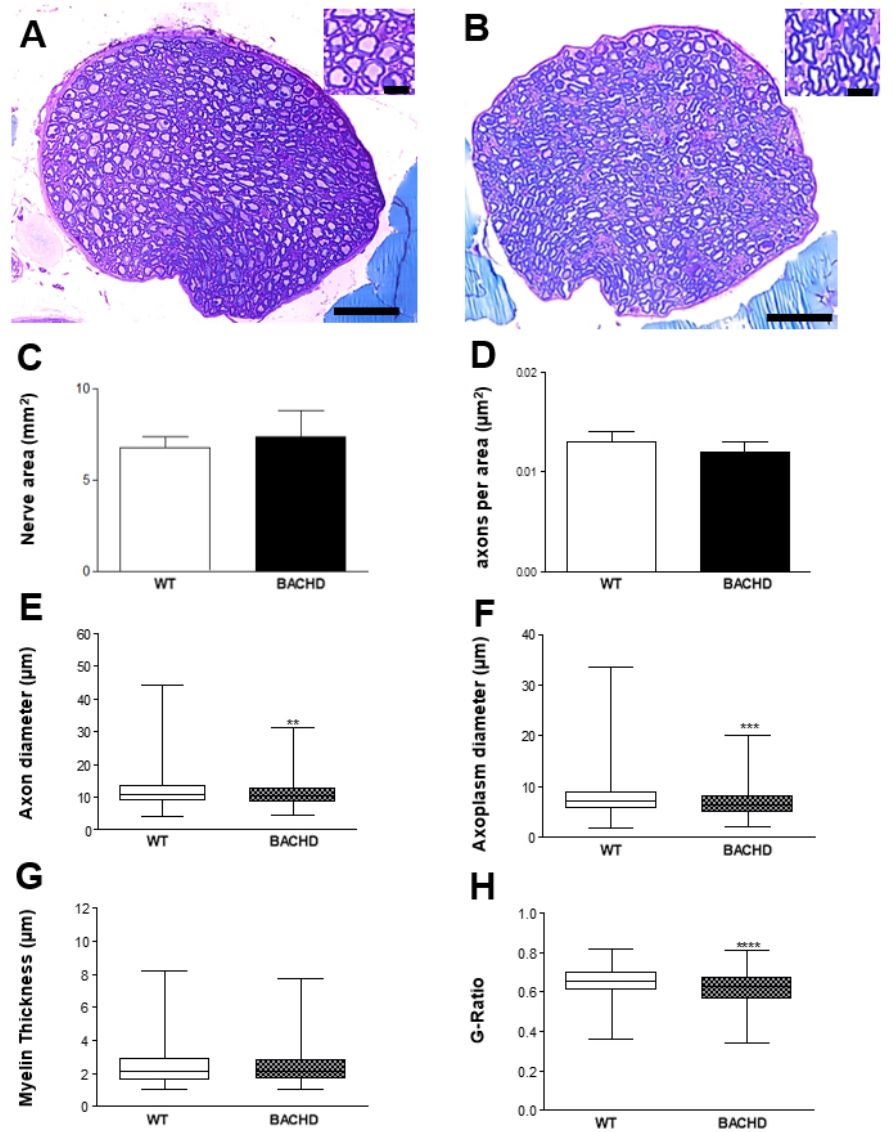
303x281mm (300 x 300 DPI)

Figure 2: BACHD mice present alterations in sciatic nerve morphology. A- B: Representative images of transversal sections of the sciatic nerve from 12 months old WT and BACHD mice, respectively. Note the difference between the size of the axons on inserts in A (WT) and B (BACHD). Scale bar: 10μm. C-H: Quantification of nerve area (C), number of axons per nerve area (D), axon's diameter (E)(**p<0.001; Mann-Whitney test), axoplasm diameter (***p<0.0001; Mann-Whitney test) (F); myelin thickness (G), G-ratio (G=d/D, where G is the G-ratio, d is the inner diameter, and D is the outer diameter) (****p<0.0001; Mann-Whitney test) (H). n=3 animals per group. We analyzed 2.874 axons in WT and 2.573 in BACHD. Unpaired Student's t-test, p > 0.05 (C and D).
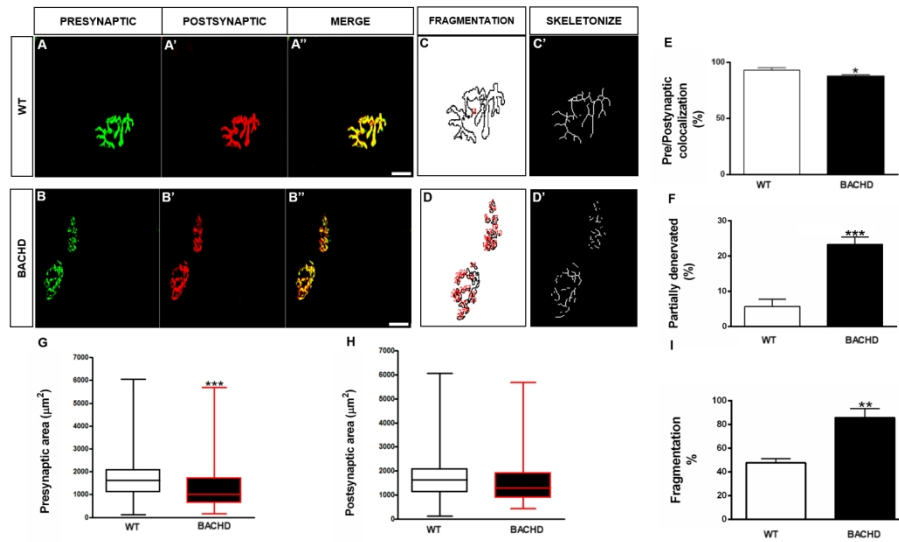
62x78mm (300 x 300 DPI)

Figure 3: NMJs from TA muscles are partially denervated and fragmented in BACHD mice. A–B: Representative images of TA NMJs obtained from 12 months old WT and BACHD mice. A and B: Presynaptic terminals labeled with an Alexa-488 anti-synaptotagmin antibody (green). A' and B': Postsynaptic AChRs labeled with Alexa-555 α-btx (red). A" and B": Merged images. Scale bar: 50 µm. C and D: Representation of particle analysis for both genotypes (red numbers). C' and D': Skeletonization rendering of fragmentation in endplates from WT and BACHD. E–I: Graphs showing the degree of colocalization (E) (*p =0.02; unpaired Student's t-test); partial denervation (F) (***p < 0.0007 unpaired student t-test); pre-synaptic area (G) (***p < 0.0002; Mann-Whitney test); post-synaptic area (H) (p>0.05; Mann-Whitney test); and fragmentation of the endplates (I) (**p=0.001; unpaired student t-test). The results represent the mean ± SD from 50 NMJs per genotype. n=3 individual animals per genotype.
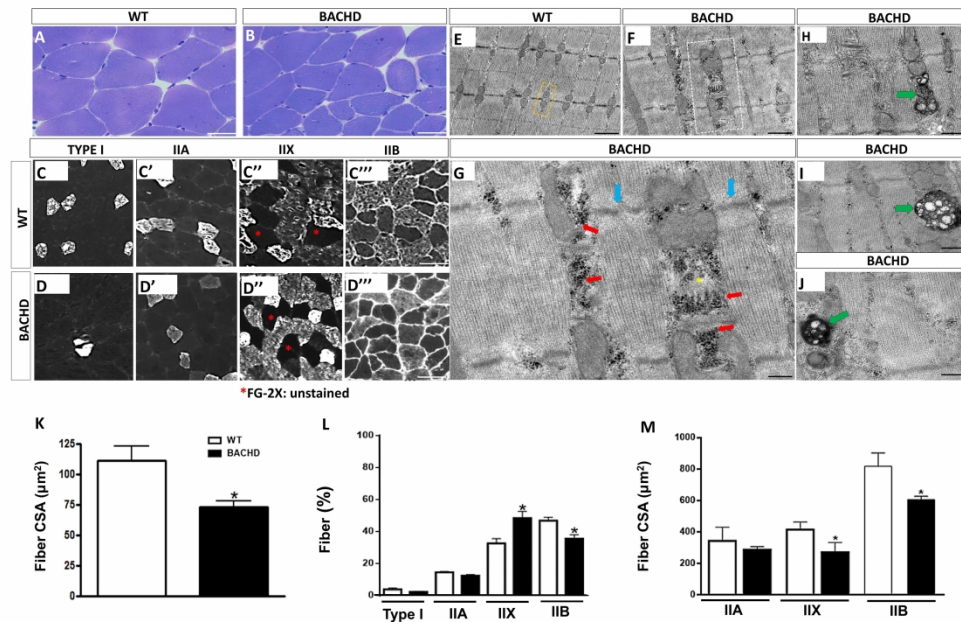
162x90mm (300 x 300 DPI)

Figure 4: Muscle atrophy, muscle fiber switching and ultrastructural abnormalities in BACHD. A–B: Representative images of TA skeletal muscle fibers from 12 months old WT and BACHD mice. Scale bar: 50 µm. C–C''' to D–D''': Representative images of TA fiber typing from 12 months old WT and BACHD mice. Scale bar: 50 µm. E–J: Representative electron micrographs of TA fibers from WT and BACHD animals. Observe a normal triad in WT (Figure E, yellow box). G: High magnification view of the area in F showing marked glycogen accumulation in the inter-myofibrillar spaces (red arrows), SR enlargement (yellow asterisk) and Z-line discontinuity (blue arrows) in BACHD animals. H-J: Observe profound mitochondrial changes (green arrows). Scale bar: 500 nm. We analyzed 90 images per genotype from six individual animals (three per genotype). K: Quantitative analysis shows the CSA mean values for WT and BACHD TA muscle fibers. These results represent the mean ± SD of more than 4.000 muscle fibers per genotype (****$p<0.0001$; Mann-Whitney test); n=3 animals per genotype). L: Quantitative analysis of the fiber typing showing decreased number of IIB isoform and increase of IIX in BACHD TA muscle fibers compared to WT (*$p= 0.01$ and *$p=0.02$; unpaired Student's t-test; n=3 animals per genotype). M: Quantitative analysis of the CSA from fiber typing (*$p= 0.03$; unpaired Student's t-test; n=3 animals per genotype). The results represent the mean ± SD (unpaired Student's t-test, *$p<0.05$; n=3 animals per genotype).
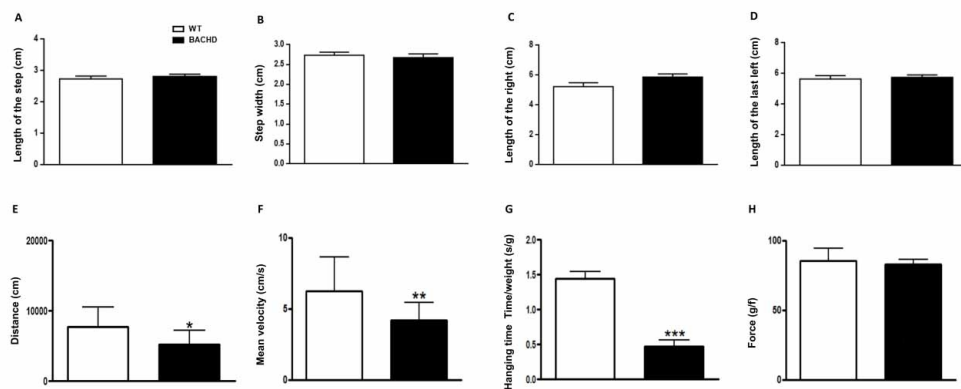
438x283mm (300 x 300 DPI)

Figure 5: Motor behavior alterations in BACHD. A-D: Graphical quantification of pattern of gait of WT and BACHD mice. A: Length of the step (p=0.54; unpaired Student's t-test). B: Step width (p=0.51; unpaired Student's t-test). C: Length of the rigth(p=0.07; unpaired Student's t-test). D: Length of the left (p=0.70; unpaired Student's t-test). E:Graphical quantification of the total distance traveled by WT and BACHD mice, showing hypoactivity in transgenic animals (*p=0.01; unpaired Student's t-test). F: Graphical quantification of the average speed traveled by both genotypes with a decrease in BACHD animals (**p=0.003; unpaired Student's t-test). G: Graphical quantification of the total time the animals kept holding their own weight in the test apparatus (time/weigth = time corrected for weight) (***p=0.0001; unpaired Student's t-test) H: Maximum force quantification in the test of grip strength exerted by WT animals and BACHD when a constant and opposite force is applied (p=0.39; unpaired Student's t-test). The results express the mean ± SD from 11 WT and 17 BACHD animals.

109x46mm (300 x 300 DPI)
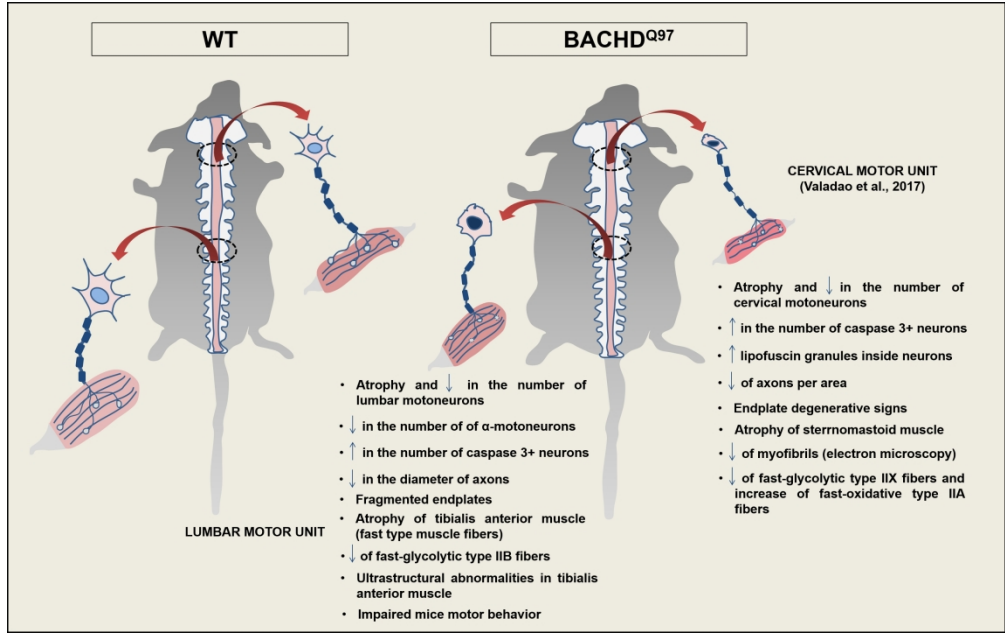
247x156mm (300 x 300 DPI)

8- REFERÊNCIAS

1.   Brown, R. C., Lockwood, A. H. & Sonawane, B. R. Neurodegenerative diseases: an overview of environmental risk factors. *Env. Heal. Perspect* **113,** 1250–1256 (2005).

2.   Meek, P. D., Mckeithan, K. & Schumock, G. T. Economic Considerations in Alzheimer's Disease. *Pharmacotherapy* **18,** 68–73 (1998).

3.   Schrag, A., Jahanshahi, M. & Quinn, N. What contributes to quality of life in patients with Parkinson's disease? *J Neurol Neurosurg Psychiatry* **69,** 308–312 (2000).

4.   Schenkman, M., Wei Zhu, C., Cutson, T. M. & Whetten-goldstein, K. Longitudinal evaluation of economic and physical impact of Parkinsons disease. *Park. Relat Disord* **8,** 41–50 (2001).

5.   Haddad, M. & Cummings, J. Huntington's Disease. *Psychiatr Clin North Am* **20,** 791–807 (1997).

6.   Bates, G. P. The molecular genetics of Huntington disease — a history. *Nat Rev Genet* **6,** 766–773 (2005).

7.   Albin, R. L. & Tagle, D. A. Genetics and molecular biology of Huntington's disease. *Trends Neurosci* **18,** 11–14 (1995).

8.   Margolis, R. L. & Ross, C. A. Diagnosis of Huntington disease. *Clin Chem* **49,** 1726–1732 (2003).

9.   Yu, S. *et al.* A novel gene containing a trinucleotide repeat that is expanded and unstable on Huntington's disease chromosomes. The Huntington's Disease Collaborative Research Group. *Cell* **72,** 971–83 (1993).

10.   Bean, L. & Bayrak-toydemir, P. ACMG Standards and Guidelines American College of Medical Genetics and Genomics Standards and Guidelines for Clinical Genetics Laboratories , 2014 edition : technical standards and guidelines for Huntington disease ACMG Standards and Guidelines. *Genet. Med.* **16,** e2 (2014).

11.   Pringsheim, T. *et al.* The incidence and prevalence of Huntington's disease: a systematic review and meta-analysis. *Mov Disord* **27,** 1083–1091 (2012).

12.   Baig, S. S., Strong, M. & Quarrell, O. W. The global prevalence of Huntington's disease: a systematic review and discussion. *Neurodegener Dis Manag* **6,** 331–343 (2016).

13.   De Andrade Agostinho, L. *et al.* A Study of a Geographical Cluster of Huntington's Disease in a Brazilian Town of Zona da Mata, Minas Gerais State. *Eur Neurol* **74,** 62–68 (2015).

14.   Prospero, N. A. Di & Fischbeck, K. H. Therapeutics Development for Triplet Repeat Expansion Diseases. *Nat Rev Genet* **6,** 756–765 (2005).

15.   Saudou, F. & Humbert, S. Review The Biology of Huntingtin. *Neuron* **89,** 910–926 (2016).

16. Rozas, J. L., Gómez-Sánchez, L., Tomás-Zapico, C., Lucas, J. J. & Fernández-Chacón, R. Increased Neurotransmitter Release at the Neuromuscular Junction in a Mouse Model of Polyglutamine Disease. *Neurobiol. Dis.* **31,** 1106–1113 (2011).

17. Smith, R., Brundin, P. & Li, J. Cellular and Molecular Life Sciences Synaptic dysfunction in Huntington ' s disease : a new perspective. *Cell. Mol. Life Sci.* **62,** 1901–1912 (2005).

18. Morfini, G., Pigino, G. & Brady, S. T. Polyglutamine expansion diseases: failing to deliver. *TRENDS Mol. Med.* **11,** 64–70 (2005).

19. Morfini, G. A. *et al.* Pathogenic Huntingtin Inhibits Fast Axonal Transport by Activating JNK3 and Phosphorylating Kinesin. *Nat Neurosci* **12,** 864–871 (2010).

20. Browne, S. E., Ferrante, R. J. & Beal, M. F. Oxidative stress in Huntington's disease. *Brain Pathol* **9,** 147–163 (1999).

21. Sepers, M. D. & Raymond, L. A. Mechanisms of synaptic dysfunction and excitotoxicity in Huntington's disease. *Drug Discov Today* **19,** 990–996 (2014).

22. Zeron, M. M. *et al.* Increased sensitivity to N-methyl-D-aspartate receptor-mediated excitotoxicity in a mouse model of Huntington's disease. *Neuron* **33,** 849–860 (2002).

23. Graham, R. K. *et al.* Differential susceptibility to excitotoxic stress in YAC128 mouse models of Huntington disease between initiation and progression of disease. *Neurobiol. Dis.* **29,** 2193–2204 (2009).

24. Molero, A. E., Arteaga-bracho, E. E., Chen, C. H. & Gulinello, M. Selective expression of mutant huntingtin during development recapitulates characteristic features of Huntington ' s disease. *Proc Natl Acad Sci U S A* **113,** 5736–5741 (2016).

25. Doble, A. The role of excitotoxicity in neurodegenerative disease: implications for therapy. *Pharmacol Ther* **81,** 163–221 (1999).

26. Curtis, D. R., Phillis, J. W. & Watkins, J. C. Chemical excitation of spinal neurones. *Nature* **183,** 611–612 (1959).

27. Watkins, J. C. & Evans, R. H. Excitatory amino acid transmitters. *Annu. Rev. Pharmacol. Toxicol.* **21,** 165–204 (1981).

28. Weber, A. & Backes, L. Excitotoxicity glutamatergic in Huntington's disease. *Rev. Context. Saúde* **16,** 96–103 (2016).

29. Grewer, C. & Rauen, T. Electrogenic glutamate transporters in the CNS: molecular mechanism, pre-steady-state kinetics, and their impact on synaptic signaling. *J Membr Biol* **203,** 1–20 (2005).

30. Featherstone, D. E. Intercellular glutamate signaling in the nervous system and beyond. *ACS Chem Neurosci* **1,** 4–12 (2010).

31. Choi, D. W. Neurodegeneration: cellular defences destroyed. *Nature* **433,** 696–698 (2005).

32. Suzuki, K., Hata, S., Kawabata, Y. & Sorimachi, H. Structure , Activation , and Biology of Calpain. *Diabetes* **53,** S12-8 (2004).

33. Kurokawa, M. & Kornbluth, S. Caspases and Kinases in a Death Grip Manabu. *Cell* **138,** 838–854 (2009).

34. Simms, B. A. & Zamponi, G. W. Review Neuronal Voltage-Gated Calcium Channels : Structure, Function, and Dysfunction. *Neuron* **82,** 24–45 (2014).

35. Graveland, G. A., Williams, R. S. & DiFiglia, M. Evidence for degenerative and regenerative changes in neostriatal spiny neurons in Huntington's disease. *Science (80-.).* **227,** 770–773 (1985).

36. Beal, M. F., Ferrante, R. J., Swartz, K. J. & Kowall, N. W. Chronic quinolinic acid lesions in rats closely resemble Huntington's disease. *J Neurosci* **11,** 1649–1659 (1991).

37. Ferrante, R. J., Kowall, N. W. & Richardson, E. P. Proliferative and degenerative changes in striatal spiny neurons in Huntington's disease: a combined study using the section-Golgi method and calbindin D28k immunocytochemistry. *J Neurosci* **11,** 3877–3887 (1991).

38. McGeer, E. G. & McGeer, P. L. Duplication of biochemical changes of Huntington's chorea by intrastriatal injections of glutamic and kainic acids. *Nature* **263,** 517–519 (1976).

39. Isacson, O., Brundin, P., Gage, F. H. & Björklund, A. Neural grafting in a rat model of Huntington's disease: progressive neurochemical changes after neostriatal ibotenate lesions and striatal tissue grafting. *Neuroscience* **16,** 799–817 (1985).

40. Arzberger, T., Krampfl, K., Leimgruber, S. & Weindl, A. Changes of NMDA receptor subunit (NR1, NR2B) and glutamate transporter (GLT1) mRNA expression in Huntington's disease--an in situ hybridization study. *J Neuropathol Exp Neurol* **56,** 440–454 (1997).

41. Liévens, J. C. *et al.* Impaired glutamate uptake in the R6 Huntington's disease transgenic mice. *Neurobiol Dis* **8,** 807–821 (2001).

42. Behrens, P. F., Franz, P., Woodman, B., Lindenberg, K. S. & Landwehrmeyer, G. B. Impaired glutamate transport and glutamate-glutamine cycling: downstream effects of the Huntington mutation. *Brain* **125,** 1908–1922 (2002).

43. Hassel, B., Tessler, S., Faull, R. L. M. & Emson, P. C. Glutamate uptake is reduced in prefrontal cortex in Huntington's disease. *Neurochem Res* **33,** 232–237 (2008).

44. Shin, J. Y. *et al.* Expression of mutant huntingtin in glial cells contributes to neuronal excitotoxicity. *J Cell Biol* **171,** 1001–1012 (2005).

45. Guidetti, P., Luthi-Carter, R. E., Augood, S. J. & Schwarcz, R. Neostriatal and cortical quinolinate levels are increased in early grade Huntington's disease. *Neurobiol Dis* **17,** 455–461 (2004).

46. Crook, Z. R. & Housman, D. Huntington's Disease: Can Mice Lead the Way to Treatment? *Neuron* **69,** 423–435 (2015).

47. Pouladi, M. A., Morton, A. J. & Hayden, M. R. Choosing an animal model for the study of Huntington's disease. *Nat Rev Neurosci* **14,** 708–721 (2013).

48. Mangiarini, L. *et al.* Exon 1 of the HD Gene with an Expanded CAG Repeat Is Sufficient to Cause a Progressive Neurological Phenotype in Transgenic Mice. *Cell* **87,** 493–506 (1996).

49. Menalled, L. *et al.* Systematic behavioral evaluation of Huntington's disease transgenic and knock-in mouse models. *Neurobiol Dis* **35,** 319–336 (2010).

50. van der Burg, J. M., Björkqvist, M. & Brundin, P. Beyond the brain: widespread pathology in Huntington's disease. *Lancet Neurol* **8,** 765–774 (2009).

51. Carter, R. J. *et al.* Characterization of progressive motor deficits in mice transgenic for the human Huntington's disease mutation. *J. Neurosci.* **19,** 3248–3257 (1999).

52. Li, J. Y., Popovic, N. & Brundin, P. The use of the R6 transgenic mouse models of Huntington's disease in attempts to develop novel therapeutic strategies. *NeuroRx* **2,** 447–464 (2005).

53. Gray, M. *et al.* Full-length human mutant huntingtin with a stable polyglutamine repeat can elicit progressive and selective neuropathogenesis in BACHD mice. *J Neurosci* **28,** 6182–6195 (2008).

54. Fink, K. D. *et al.* Developing stem cell therapies for juvenile and adult-onset Huntington's disease. *Regen Med* **10,** 623–646 (2015).

55. Walker, F. O. Huntington's disease. *Lancet* **369,** 218–228 (2007).

56. Haber, S. N. Corticostriatal circuitry. *Dialogues Clin Neurosci* **18,** 7–21 (2016).

57. Ferrante, R. J., Kowall, N. W., Jr, E. P. & Edward, D. Topography of enkephalin, substance P and acetylcholinesterase staining in Huntington's disease striatum. *Neurosci Lett* **71,** 283–288 (1986).

58. Ferrante, R. J., Beal, M. F., Kowall, N. W., Richardson, E. P. & Martin, J. B. Sparing of acetylcholinesterase-containing striatal neurons in Huntington's disease. *Brain Res* **411,** 162–166 (1987).

59. Vincent, S. R., Staines, W. A. & Fibiger, H. C. Histochemical demonstration of separate populations of somatostatin and cholinergic neurons in the rat striatum. *Neurosci Lett* **35,** 111–114 (1983).

60. Reiner, A., Medina, L. & Veenman, C. L. Structural and functional evolution of the basal ganglia in vertebrates. *Brain Res Brain Res Rev* **28,** 235–285 (1998).

61. Li, S., Schilling, G., Foktein, S. E., Hedreen, J. C. & Ross, C. A. Huntington's disease gene (IT15) is widely expressed in human and rat tissues. *Neuron* **11,** 985–993 (1993).

62. Fry, B. G. *et al.* The toxicogenomic multiverse: convergent recruitment of proteins into animal venoms. *Annu Rev Genomics Hum Genet.* **10,** 483–511 (2009).

63. Heading, C. E. Ziconotide (Elan Pharmaceuticals). *Idrugs* **4,** 339–350 (2001).

64. Mcgivern, J. G. Ziconotide: a review of its pharmacology and use in the treatment of pain. *Neuropsychiatr Dis Treat* **3,** 69–85 (2007).

65. Rocha E Silva, M., Beraldo, W. T. & Rosenfeld, G. Bradykinin, a hypotensive and smooth muscle stimulating factor released from plasma globulin by snake venoms and by trypsin. *Am J Physiol* **156,** 261–273 (1949).

66. Ferreira, S. H., Bartelt, D. C. & Greene, L. J. Isolation of bradykinin-potentiating peptides from Bothrops jararaca venom. *Biochemistry* **9,** 2583–2593 (1970).

67. de Souza, J. M., Goncalves, B. D. C., Gomez, M. V., Vieira, L. B. & Ribeiro, F. M. Animal Toxins as Therapeutic Tools to Treat Neurodegenerative Diseases. *Front. Pharmacol.* **9,** eCollection 2018 (2018).

68. Silva, F. R. *et al.* The Phoneutria nigriventer spider toxin, PnTx4-5-5, promotes neuronal survival by blocking NMDA receptors. *Toxicon* **112,** 16–21 (2016).

69. Frank, S. Treatment of Huntington's disease. *Neurotherapeutics* **11,** 153–160 (2014).

70. Killoran, A. & Biglan, K. M. Current therapeutic options for Huntington's disease: good clinical practice versus evidence-based approaches? *Mov Disord* **29,** 1404–1413 (2014).

71. Evans, R. M. & Zamponi, G. W. Presynaptic Ca 2+ channels – integration centers for neuronal signaling pathways. *TRENDS Neurosci.* **29,** 617–624 (2006).

72. Gomez, M. V, Kalapothakis, E., Guatimosim, C. & Prado, M. A. M. Phoneutria nigriventer Venom : A Cocktail of Toxins That Affect Ion Channels. *Cell. Mol. Neurobiol.* **22,** 579–588 (2002).

73. Lucas, S. Spiders in Brazil. *Toxicon* **26,** 759–772 (1988).

74. Rezende Júnior, L., Cordeiro, M. N., Oliveira, E. B. & Diniz, C. R. Isolation of neurotoxic peptides from the venom of the "armed" spider Phoneutria nigriventer. *Toxicon* **29,** 1255–1233 (1991).

75. Mafra, R. A. *et al.* PhTx4, a new class of toxins from Phoneutria nigriventer spider venom, inhibits the glutamate uptake in rat brain synaptosomes. *Brain Res.* **831,** 297–300 (1999).

76. Cordeiro, M. N. *et al.* Purification and amino acid sequences of six Tx3 type neurotoxins from the venom of the Brazilian "armed" spider Phoneutria nigriventer (Keys). *Toxicon* **31,** 35–42 (1993).

77. Prado, M. A. M. *et al.* A novel tool for the investigation of glutamate release from rat cerebrocortical synaptosomes: the toxin Tx3-3 from the venom of the spider Phoneutria nigriventer. *Biochem J* **314,** 145–150 (1996).

78. Guatimosim, C. *et al.* A toxin from the spider Phoneutria nigriventer that blocks calcium channels coupled to exocytosis. *Br J Pharmacol* 591–597 (1997).

79. Kushmerick, C. *et al.* Phoneutria nigriventer Toxin Tx3-1 Blocks A-TypeK+ Currents Controlling Ca2+ Oscillation Frequency in GH3 Cells. *J. Neurochem.* **72,** 1472–1481 (1999).

80. Reis, H. J. *et al.* Inhibition of glutamate uptake by a polypeptide toxin (phoneutriatoxin 3-4) from the spider Phoneutria nigriventer. *Biochem J* **343,** 413–418 (1999).

81. Sorensen, S. A. & Fenger, K. Causes of death in patients with Huntington's disease and in unaffected first degree relatives. *J. Med. Genet.* **29,** 911–914 (1992).

82. Bradford, J. W., Li, S. & Li, X.-J. Polyglutamine toxicity in non-neuronal cells. *Cell Res* **20,** 400–407 (2010).

83. Moffitt, H., McPhail, G. D., Woodman, B., Hobbs, C. & Bates, G. P. Formation of polyglutamine inclusions in a wide range of non-CNS tissues in the HdhQ150 knock-in mouse model of Huntington's disease. *PLoS One* **4,** e8025 (2009).

84. Wood, N. I. *et al.* Direct evidence of progressive cardiac dysfunction in a transgenic mouse model of Huntington's disease. *J. Huntingtons. Dis.* **1,** 57–64 (2012).

85. Aziz, N. A., Anguelova, G. V., Marinus, J., Van Dijk, J. G. & Roos, R. A. C. Autonomic symptoms in patients and pre-manifest mutation carriers of Huntington's disease. *Eur. J. Neurol.* **17,** 1068–1074 (2010).

86. Kobal, J. *et al.* Autonomic dysfunction in presymptomatic and early symptomatic Huntington's disease. *Acta Neurol. Scand.* **121,** 392–399 (2010).

87. Algra, A., Tijssen, J., Roelandt, J., Pool, J. & Lubsen, J. Heart Rate Variabilit From 24-Hour Electrocardiography and the 2-Year Risk for Sudden Death. *Circulation* **88,** 180–185 (1993).

88. Schroeder, A., Loh, D., Jordan, M., Roos, K. & Colwell, C. Baroreceptor reflex dysfunction in the BACHD mouse model of Huntington's disease. *PLoS Curr.* **4,** RRN1266 (2011).

89. Pinheiro, A. C. N. *et al.* Neuroprotective effect on brain injury by neurotoxins from the spider Phoneutria nigriventer. *Neurochem. Int.* **49,** 543–547 (2006).

90. Pinheiro, A. C. N. *et al.* Phoneutria Spider Toxins Block Ischemia-Induced Glutamate Release, Neuronal Death, and Loss of Neurotransmission in Hippocampus. *Hippocampus* **19,** 1123–1129 (2009).

91. Agostini, R. *et al.* Ischemia-Induced Glutamate Release and Neuronal Death of Cell Layers of the Retina. *Retina* **31,** 1392–1399 (2011).

92. Binda, N. S. *et al.* PhTx3-4, a Spider Toxin Calcium Channel Blocker, Reduces NMDA-Induced Injury of the Retina. *Toxins (Basel).* **8,** 1–14 (2016).

93. Vieira, L. B. *et al.* Inhibition of High Voltage-Activated Calcium Channels by Spider Toxin PnTx3-6. *J Pharmacol Exp Ther* **314,** 1370–1377 (2005).

94. Rigo, F. K. *et al.* Pharmacology, Biochemistry and Behavior Effect of ω-conotoxin MVIIA

and Ph α 1 β on paclitaxel-induced acute and chronic pain. *Pharmacol. Biochem. Behav.* **114–115,** 16–22 (2013).

95. de Souza, A. H. *et al.* Antiallodynic effect and side effects of Phα1β, a neurotoxin from the spider Phoneutria nigriventer: comparison with ω-conotoxin MVIIA and morphine. *Toxicon* **58,** 626–633 (2011).

96. Rosa, F. *et al.* Phα1β, a Peptide from the Venom of the Spider Phoneutria Nigriventer Shows Antinociceptive Effects after Continuous Infusion in a Neuropathic Pain Model in Rats. *Anesth Analg* **119,** 196–202 (2014).

97. Diniz, D. M. *et al.* Effects of the calcium channel blockers Phα1β and ω-conotoxin MVIIA on capsaicin and acetic acid-induced visceral nociception in mice. *Pharmacol. Biochem. Behav.* **126,** 97–102 (2014).

98. de Souza, A. *et al.* An Evaluation of the Antinociceptive Effects of Pha1b, a Neurotoxin from the Spider Phoneutria nigriventer , and u-Conotoxin MVIIA, a Con Snail Conus magus Toxin, in Rat Model of Inflammatory and Neuropathic Pain. *Cell Mol Neurobiol* **33,** 59–67 (2013).

99. Rosa, F. *et al.* Phα1β, a peptide from the venom of the spider Phoneutria nigriventer shows antinociceptive effects after continuous infusion in a neuropathic pain model in rats. *Anesth Analg* **119,** 196–202 (2014).

100. Souza, A. H. *et al.* Analgesic effect in rodents of native and recombinant Ph alpha 1beta toxin, a high-voltage-activated calcium channel blocker isolated from armed spider venom. *Pain* **140,** 115–126 (2008).

101. Rigo, F. K. *et al.* The spider toxin Phα1β recombinant possesses strong analgesic activity. *Toxicon* **133,** 145–152 (2017).

102. Ross A, C. & Tabrizi, S. J. Huntington's disease: From molecular pathogenesis to clinical treatment. *Lancet* **10,** 83–98 (2011).

103. Gilissen, E. P. & Staneva-dobrovski, L. Distinct types of lipofuscin pigment in the hippocampus and cerebellum of aged cheirogaleid primates. *Anat Rec* **296,** 1895–1906 (2013).

104. Chandra, A. *et al.* Enhanced mitochondrial biogenesis ameliorates disease phenotype in a full-length mouse model of Huntington's disease. *Hum Mol Genet* **25,** 2269–2282 (2016).

105. Choo, Y. S., Johnson, G. V. W., Macdonald, M., Detloff, P. J. & Lesort, M. Mutant huntingtin directly increases susceptibility of mitochondria to the calcium-induced permeability transition and cytochrome c release. *Hum Mol Genet* **13,** 1407–1420 (2004).

106. Reddy, P. H., Mao, P. & Manczak, M. Mitochondrial structural and functional dynamics in Huntington's disease. *Brain Res. Rev.* **61,** 33–48 (2009).

107. Bossy-wetzel, E., Petrilli, A. & Knott, A. B. Mutant huntingtin and mitochondrial dysfunction. *Trends Neurosci* **31,** 609–616 (2008).

108. Song, W. *et al.* Mutant huntingtin binds the mitochondrial fission GTPase dynamin-related protein-1 and increases its enzymatic activity. *Nat Med* **17,** 377–382 (2011).

109. Swaminathan, P. D., Purohit, A., Hund, T. J. & Anderson, M. E. Calmodulin-dependent protein kinase II: linking heart failure and arrhythmias. *Circ Res* **110,** 1661–1677 (2012).

110. Zhang, T. *et al.* The cardiac-specific nuclear delta(B) isoform of Ca2+/calmodulin-dependent protein kinase II induces hypertrophy and dilated cardiomyopathy associated with increased protein phosphatase 2A activity. *J Biol Chem* **277,** 1261–1267 (2002).

111. Bers, D. Cardiac excitation–contraction coupling. *Nature* **415,** 198–205 (2002).

112. Bers, D. M. Calcium Cycling and Signaling in Cardiac Myocytes. *Annu Rev Physiol* **70,** 23–49 (2008).

113. Rokita, A. G. & Anderson, M. E. New Therapeutic Targets in Cardiology : Arrhythmias and CaMKII. *Circulation* **126,** 2125–2139 (2012).

114. Mustroph, J., Neef, S. & Maier, L. S. CaMKII as a target for arrhythmia suppression. *Pharmacol. Ther.* (2016). doi:10.1016/j.pharmthera.2016.10.006

115. Cuello, F. & Lorenz, K. Inhibition of cardiac CaMKII to cure heart failure: step by step towards translation? *Basic Res Cardiol.* **111,** 66 (2016).

116. Johnson, W. M., Wilson-delfosse, A. L. & Mieyal, J. J. Dysregulation of glutathione homeostasis in neurodegenerative diseases. *Nutrients* **4,** 1399–1440 (2012).

117. Stack, E. C., Matson, W. R. & Ferrante, R. J. Evidence of oxidant damage in Huntington's disease: translational strategies using antioxidants. *Ann N Y Acad Sci* **92,** 79–92 (2008).

118. Michaelis, E. K. Molecular biology of glutamate receptors in the central nervous system and their role in excitotoxicity, oxidative stress and aging. *Prog Neurobiol* **54,** 369–415 (1998).

119. Diniz, D. M. *et al.* Effects of the calcium channel blockers Phα1β and ω-conotoxin MVIIA on capsaicin and acetic acid-induced visceral nociception in mice. *Pharmacol Biochem Behav* **126,** 97–102 (2014).

120. Gomez, M. V, Kalapothakis, E., Guatimosim, C. & Prado, M. A. Phoneutria nigriventer venom: a cocktail of toxins that affect ion channels. *Cell Mol Neurobiol* **22,** 579–588 (2002).

121. Mochida, S., Sheng, Z. H., Baker, C., Kobayashi, H. & Catterall, W. A. Inhibition of neurotransmission by peptides containing the synaptic protein interaction site of N-type Ca2+channels. *Neuron* **17,** 781–788 (1996).

122. Mcdonough, S. I., Boland, L. M., Mintz, I. M. & Bean, B. P. Interactions among toxins that inhibit N-type and P-type calcium channels. *J. Gen. Physiol* **119,** 313–328 (2002).

123. Vieira, L. B. *et al.* PnTx3-6 a spider neurotoxin inhibits K+-evoked increase in [Ca2+](i) and Ca2+-dependent glutamate release in synaptosomes. *Neurochem Int* **42,** 277–282

(2003).

124. Valadão, P. A. C. *et al.* Muscle atrophy is associated with cervical spinal motoneuron loss in BACHD mouse model for Huntington's disease. *Eur. J. Neurosci.* **45,** 785–796 (2017).

125. Riedl, S. J. & Shi, Y. Molecular mechanisms of caspase regulation during apoptosis. *Nat Rev Mol Cell Biol* **5,** 897–907 (2004).

126. Heemskerk, A. W. & Roos, R. A. Dysphagia in Huntington's disease: a review. *Dysphagia* **26,** 62–66 (2011).

127. Jones, K. *et al.* Interventions for dysphagia in long-term, progressive muscle disease. *Cochrane Database Syst Rev* **2016,** CD004303 (2016).

128. Ribchester, R. R. *et al.* Progressive abnormalities in skeletal muscle and neuromuscular junctions of transgenic mice expressing the Huntington's disease mutation. *Eur J Neurosci* **20,** 3092–3114 (2004).

129. Dauber, J. Estimating the number of motor units in a muscle. *J Clin Neurophysiol* **12,** 585–594 (1995).